

This electronic thesis or dissertation has been downloaded from the King's Research Portal at <https://kclpure.kcl.ac.uk/portal/>

## Investigating allostery in IgE-Fc using a panel of anti-IgE antibodies

Allan, Elizabeth

*Awarding institution:*  
King's College London

The copyright of this thesis rests with the author and no quotation from it or information derived from it may be published without proper acknowledgement.

### END USER LICENCE AGREEMENT



Unless another licence is stated on the immediately following page this work is licensed

under a Creative Commons Attribution-NonCommercial-NoDerivatives 4.0 International

licence. <https://creativecommons.org/licenses/by-nc-nd/4.0/>

You are free to copy, distribute and transmit the work

Under the following conditions:

- Attribution: You must attribute the work in the manner specified by the author (but not in any way that suggests that they endorse you or your use of the work).
- Non Commercial: You may not use this work for commercial purposes.
- No Derivative Works - You may not alter, transform, or build upon this work.

Any of these conditions can be waived if you receive permission from the author. Your fair dealings and other rights are in no way affected by the above.

### Take down policy

If you believe that this document breaches copyright please contact [librarypure@kcl.ac.uk](mailto:librarypure@kcl.ac.uk) providing details, and we will remove access to the work immediately and investigate your claim.

# Investigating allostery in IgE-Fc using a panel of anti-IgE antibodies

Elizabeth Allan

A thesis submitted in fulfilment of the requirements for the  
degree of Doctor of Philosophy at King's College London



Randall Division of Cell and Molecular Biophysics  
Faculty of Life Sciences and Medicine  
King's College London  
December 2016

# Abstract

The interactions between immunoglobulin E (IgE) and its receptors, FcεRI and CD23, regulate a number of important processes in allergic disorders. The Fc fragment of IgE, which binds the receptors, has a high degree of conformational plasticity and can be allosterically modulated. A comprehensive understanding of IgE-Fc dynamics and allosteric modulation could provide insights that enable the development of novel therapeutics for asthma and allergy.

Using UCB's Core Antibody Discovery Process we screened the immune repertoire of rabbits immunized against IgE-Fc for antibodies that bind IgE-Fc and affect the IgE-Fc/CD23 interaction. Surface plasmon resonance (SPR) was used to identify a subset of antibodies that elicit their effect on IgE-Fc-receptor binding allosterically. Kinetic and thermodynamic interaction studies of these antibodies are helping to elucidate the mechanisms of allostery in IgE-Fc. Allosteric communication in IgE-Fc has previously only been demonstrated between two sites within the same domain; here we show for the first time that allostery in IgE-Fc can occur across different domains over long distances. We suggest that allostery in IgE-Fc is not binary in character; certain domain orientations cannot always be attributed to inhibition of receptor binding. Rather, we advocate an ensemble treatment of allostery, in which allosteric phenomena are due to the intrinsic dynamic properties of the IgE-Fc protein. X-ray crystallographic structures of transiently populated conformations of IgE-Fc trapped by anti-IgE antibodies will provide insights into the energy landscape of IgE-Fc and the importance of IgE-Fc dynamics in receptor engagement.

*To Mum and Dad.*

*Thank you.*

# Acknowledgements

I owe my sincerest gratitude to the many people who have contributed to this thesis. To begin, my colleagues in the Randall Division of King's College London. I want to thank my PhD committee: my supervisor, Professor James McDonnell, my second supervisor, Professor Brian Sutton and my PhD coordinator, Dr Baljinder Mankoo. Without your support and encouragement this thesis would not have been possible. In particular, I am truly indebted to Professor James McDonnell who has been an inspirational academic mentor to me since I was an undergraduate, and who has taught me more than I could ever give him credit for here. I am truly lucky to have had such a patient supervisor who has nurtured my skills, built my confidence and got me here!

I would like to thank the current and past members of the McDonnell laboratory, in particular Dr Daniel O'Loughlin and Dr Seema Mayank, who made my time in the group so enjoyable. I am also deeply thankful to those members who contributed work presented in this thesis: Dr Seema Mayank, Miss Virginia Casablancas Antras and Mr Scott Isherwood. In addition I owe particular thanks to Dr Anna Davies and Dr Sneha Ramaswamy for their much appreciated help with X-ray crystallography. I wish to extend my gratitude to the Allergy and Asthma Group: I have greatly benefited from the support of the group and it has been a real privilege to work alongside such experienced and dedicated scientists. I extend my thanks even further to the entire Randall Division and to King's College London: it has been a pleasure working for my PhD here.

I am deeply grateful to our industrial collaborators, UCB, who helped fund my studentship, welcomed me into their laboratories and provided many materials integral to my work. In particular, I would like to express my deepest appreciation to my industrial supervisor, Dr Alistair Henry. Dr Alistair Henry's suggestions

---

were invaluable, his support was boundless and his energy was inspiring.

My PhD project was only possible because UCB kindly provided me access to their equipment and because the staff so generously gave up their time to show me how to use it. I would like to offer my special thanks to Ms Victoria O'Dowd, Dr Michael Wright, and Dr Lena D'hooghe for teaching me so much and making me a better scientist. I also owe much to Dr Hanna Hailu and Dr Jean Dalgarno for the work they contributed towards this thesis.

Finally, I would like to thank the Biotechnology and Biological Sciences Research Council (BBSRC) for their funding as part of their industrial cooperative awards in science and technology (CASE) studentship programme.

# Contents

<b>1</b>	<b>Introduction</b>	<b>18</b>
1.1	IgE in allergy and asthma . . . . .	18
1.1.1	The role of IgE/receptor interactions in allergy and asthma .	19
1.1.2	Targeting IgE/receptor interactions in the treatment of al- lergy and asthma . . . . .	25
1.2	The structural and biophysical basis of the IgE/receptor interactions . . . . .	28
1.2.1	The structure and dynamics of IgE . . . . .	28
1.2.2	The IgE/Fc $\epsilon$ RI interaction . . . . .	30
1.2.3	The IgE/CD23 interaction . . . . .	33
1.3	Allosteric regulation of IgE-Fc interactions . . . . .	37
1.3.1	Reciprocal allosteric inhibition of IgE-receptor binding . . . . .	37
1.3.2	Allosteric enhancement of the IgE/Fc $\epsilon$ RI interaction by the C $\epsilon$ 2 domain pair . . . . .	38
1.3.3	Allosteric inhibition of the IgE/Fc $\epsilon$ RI interaction by a $\epsilon$ Fab1	39
1.3.4	Allosteric inhibition of the IgE/Fc $\epsilon$ RI interaction by Xolair .	41
1.3.5	Accelerated dissociation of IgE-Fc:Fc $\epsilon$ RI complexes . . . . .	43
1.4	The ensemble model allostery . . . . .	45
1.4.1	The ensemble model of allostery . . . . .	48
1.4.2	The ensemble model of allostery and IgE . . . . .	52
1.5	Rationale . . . . .	54
<b>2</b>	<b>Materials and methods</b>	<b>58</b>
2.1	Materials . . . . .	58
2.1.1	Buffers and media . . . . .	58
2.1.2	Recombinant proteins . . . . .	59
2.2	General deoxyribonucleic acid (DNA) analysis and manipulation techniques . . . . .	60
2.2.1	Spectroscopic quantitation of DNA . . . . .	60
2.2.2	Agarose gel electrophoresis of DNA . . . . .	60
2.2.3	Heat-shock transformation of <i>E. coli</i> . . . . .	60
2.3	General protein analysis techniques . . . . .	61
2.3.1	Spectroscopic determination of protein concentration . . . . .	61
2.3.2	SDS-PAGE analysis . . . . .	61
2.4	derCD23 production and purification . . . . .	62
2.4.1	DNA and vectors . . . . .	62

2.4.2	Transformation . . . . .	63
2.4.3	Bacterial expression . . . . .	63
2.4.4	Purification of insoluble inclusion bodies . . . . .	63
2.4.5	Protein refolding . . . . .	64
2.4.6	Heparin-sepharose chromatography . . . . .	64
2.4.7	Size exclusion chromatography . . . . .	64
2.4.8	Positive electrospray mass spectrometry . . . . .	65
2.4.9	One dimensional $^1\text{H}$ NMR spectroscopy . . . . .	65
2.5	Anti-IgE antibody discovery . . . . .	65
2.5.1	IgE-Fc immunisations . . . . .	66
2.5.2	UCB's core antibody discovery platform . . . . .	66
2.5.3	B cell culture . . . . .	67
2.5.4	The primary fluorescence-based homogeneous screening assay . . . . .	68
2.5.5	Hit-picking . . . . .	68
2.5.6	The secondary fluorescence-based screening assay . . . . .	68
2.5.7	Foci-picking . . . . .	69
2.5.8	Reverse transcription PCR (RT-PCR) . . . . .	70
2.5.9	Transcriptionally active PCR (TAP) . . . . .	70
2.5.10	Cloning of variable region genes . . . . .	71
2.5.11	Small scale transient expression of anti-IgE antibodies and Fabs Expi293 <sup>TM</sup> expression system . . . . .	71
2.5.12	Large-scale transient expression of anti-IgE Fabs using the electroporation . . . . .	72
2.5.13	$\alpha\epsilon$ Fab purification . . . . .	73
2.6	Surface plasmon resonance . . . . .	74
2.6.1	The SPR phenomenon . . . . .	75
2.6.2	The SPR experiment . . . . .	76
2.6.3	Performing kinetic experiments using SPR . . . . .	83
2.6.4	Performing steady-state experiments using SPR . . . . .	86
2.6.5	Using $K_D$ and $B_{\text{max}}$ to characterise interactions . . . . .	88
2.7	Flow cytometry . . . . .	89
2.7.1	An introduction to flow cytometry . . . . .	89
2.7.2	Experimental details of cell-based assays using flow cytometry	91
2.8	Intramolecular fluorescence resonance energy transfer (FRET) . . .	92
2.8.1	An introduction to FRET . . . . .	92
2.8.2	Experimental details of intramolecular FRET experiments . . . . .	96
<b>3</b>	<b>Allosteric modulation of the IgE-Fc/CD23 interaction by <math>\alpha\epsilon</math>Fab1</b>	<b>99</b>
3.1	Introduction . . . . .	99
3.2	Results . . . . .	100
3.2.1	Production and purification of derCD23 . . . . .	100
3.2.2	Production of His-tagged IgE-Fc . . . . .	104
3.2.3	SPR studies of the effect of $\alpha\epsilon$ Fab1 on the interaction be- tween IgE-Fc and CD23 . . . . .	106
3.2.4	Inhibition studies on the surface of B cells . . . . .	110



3.2.5	Structural comparisons of derCD23-bound IgE-Fc and aεFab1-bound IgE-Fc . . . . .	114
3.2.6	The effect of Cε3 rigidification on allosteric communication between aεFab1 and CD23 binding sites . . . . .	119
3.3	Discussion . . . . .	123
<b>4</b>	<b>Anti-IgE antibody discovery</b>	<b>127</b>
4.1	Introduction . . . . .	127
4.2	Results . . . . .	130
4.2.1	Primary fluorescence-based homogeneous screening . . . . .	130
4.2.2	Secondary fluorescence-based homogeneous screening . . . . .	131
4.2.3	Cloning of variable region genes and DNA sequencing . . . . .	137
4.2.4	Investigating the effect of the full-length antibodies on the interaction between IgE-Fc and derCD23 using SPR . . . . .	142
4.3	Discussion . . . . .	146
<b>5</b>	<b>Anti-IgE Fab selection and generation</b>	<b>149</b>
5.1	Introduction . . . . .	149
5.2	Results . . . . .	150
5.2.1	Investigating binding of IgE-Fc to aεFabs using SPR . . . . .	150
5.2.2	Investigating the effect of one aεFab molecule on the IgE-Fc/derCD23 interaction using SPR. . . . .	153
5.2.3	Investigating the effect of one aεFab molecule on the IgE-Fc/sFcεRIα interaction using SPR. . . . .	158
5.2.4	aεFab competition experiments using SPR. . . . .	161
5.2.5	Selection of six aεFabs . . . . .	164
5.2.6	Expression of the selected aεFabs in CHOSXE cells . . . . .	168
5.2.7	Purification of the aεFabs . . . . .	172
5.2.8	aεFab mass determination mass spectrometry . . . . .	175
5.3	Discussion . . . . .	179
<b>6</b>	<b>Characterisation of the anti-IgE Fab/IgE interactions</b>	<b>182</b>
6.1	Introduction . . . . .	182
6.2	Results . . . . .	186
6.2.1	Determining the stoichiometry of the aεFab/IgE-Fc interactions using SEC . . . . .	186
6.2.2	Determining the equilibrium dissociation constants of the aεFab/IgE-Fc interactions using SPR . . . . .	187
6.2.3	IgE-Fc heterogeneity . . . . .	191
6.2.4	Intramolecular FRET experiments . . . . .	201
6.2.5	The binding of different IgE-Fc subfragments to the aεFabs . . . . .	206
6.3	Discussion . . . . .	211
<b>7</b>	<b>Modulation of the IgE/CD23 interaction by anti-IgE Fabs</b>	<b>215</b>
7.1	Introduction . . . . .	215
7.2	Results . . . . .	219

7.2.1	Modulation of the IgE/CD23 interaction on the surface of cells by aεFabs . . . . .	219
7.2.2	SPR investigations into the binding of derCD23 to different aεFab:IgE-Fc complexes . . . . .	228
7.2.3	Models for how each aεFab modulates the interaction between IgE and CD23 . . . . .	239
7.3	Discussion . . . . .	246
<b>8</b>	<b>Discussion</b>	<b>251</b>
		<b>271</b>
A.1	IgE-Fc protein sequence . . . . .	271
A.2	SPR analysis of the interaction between IgE-Fc and unpurified aεFabs 272	
A.3	SPR analysis of the interactions between derCD23 and IgE-Fc bound to unpurified aεFabs . . . . .	274
A.4	SPR analysis of the interactions between FcεRIα and IgE-Fc bound to unpurified aεFabs . . . . .	276
A.5	SPR analysis to investigate aεFab competition . . . . .	277
A.6	Investigating the stoichiometry of the aεFab/IgE-Fc interactions . . . . .	278
A.7	SPR analysis of the interaction between IgE-Fc and purified aεFabs	279
A.8	Repeat SPR experiment for the binding of IgE-Fc (3-4) to aεFab12	280
A.9	Repeat SPR experiment for the binding of the Cε2 dimer to aεFab12	281
A.10	IgE/mCD23 inhibition assays . . . . .	282
A.11	SPR experiments investigating the binding of derCD23 to aεFab:IgE-Fc (1:1) complexes . . . . .	283
A.12	Analytical HPLC SEC analysis of aεFab:IgE-Fc (2:1) complex preparative SEC fractions . . . . .	284
A.13	SPR experiments investigating the binding of derCD23 to aεFab:IgE-Fc (2:1) complexes . . . . .	285
A.14	Protein sequence alignment of human and rabbit IgE-Fc . . . . .	286

# List of Figures

1.1	Schematic representations of IgE and its receptors . . . . .	20
1.2	IgE/receptor interactions are important in the initiation and propagation of allergic disease . . . . .	23
1.3	The mechanisms of CD23-mediated IgE homoeostasis . . . . .	26
1.4	A schematic representation of IgG and IgE . . . . .	28
1.5	The crystal structures of IgE-Fc suggest that IgE-Fc is asymmetric and bent . . . . .	29
1.6	IgE-Fc(3-4) exists in a range of open and closed conformations . . . . .	30
1.7	IgE-Fc can adopt extended and partially extended conformations . . . . .	31
1.8	A molecular dynamics simulation of IgE-Fc extension . . . . .	32
1.9	The interaction between IgE-Fc and sFcεRIα . . . . .	33
1.10	sFcεRIα binds to an open conformation of IgE-Fc whereas derCD23 binds a closed state . . . . .	34
1.11	The crystal structure of the derCD23:IgE-Fc(3-4) 2:1 complex . . . . .	35
1.12	The crystal structure of the derCD23:IgE-Fc 1:1 complex . . . . .	36
1.13	The structural basis for the allosteric and mutual incompatibility of IgE-Fc receptor binding . . . . .	38
1.14	αεFab1 allosterically inhibits the IgE/FcεRI interaction . . . . .	40
1.15	Crystal structures of Xolair Fab:IgE-Fc complexes . . . . .	42
1.16	αεFabXol3 allosterically disrupts the interaction between IgE-Fc and FcεRIα . . . . .	43
1.17	The concerted and sequential models of allostery . . . . .	46
1.18	The MWC/Perutz model for the cooperative transition from ‘T’ state to ‘R’ state haemoglobin . . . . .	47
1.19	A schematic representation of the ensemble model of allostery . . . . .	49
1.20	An ensemble description of the allosteric cooperativity of substrate binding to cyclic to cAMP-dependent protein kinase (cAPK) . . . . .	51
1.21	A change in entropy upon binding a ligand alters the width of the free-energy basin without affecting its position . . . . .	52
2.1	A schematic representation of the principles of SPR . . . . .	76
2.2	A schematic representation of an SPR sensorgram . . . . .	81
2.3	A schematic representation of a flow cytometry experiment . . . . .	89
2.4	A schematic representation of forward and side scattered light . . . . .	90
2.5	simplified Jablonski diagram illustrating the basic principles of FRET . . . . .	93
2.6	A schematic illustration of the Förster principle . . . . .	94
2.7	An illustration of the terbium chelate and Alexa Fluor 488 emission and excitation spectra . . . . .	95

---

3.1	Induced expression of derCD23 in <i>E. coli</i> BL21 (DE3) cells . . . . .	101
3.2	derCD23 over-expression into insoluble inclusion bodies and purification . . . . .	102
3.3	Chromatogram of derCD23 purified by heparin-sepharose chromatography . . . . .	102
3.4	Chromatogram of derCD23 purified by size exclusion . . . . .	103
3.5	Positive ion electrospray mass spectrometry of purified derCD23 . .	104
3.6	1D <sup>1</sup> H NMR spectroscopy of purified derCD23 . . . . .	105
3.7	The SPR sensorgrams profiles for the binding of un-purified His-tagged IgE-Fc to immobilised alpha-gamma . . . . .	106
3.8	SPR sensorgrams of derCD23 binding to His-tagged IgE-Fc and aεFab1-bound IgE-Fc . . . . .	109
3.9	IgE-Fc bound to aεFab1 has a lower capacity and affinity for derCD23	110
3.10	aεFab1 caused dose-dependent inhibition of the IgE/CD23 interaction on the surface of B cells . . . . .	112
3.11	The aεFab1 dose-dependent inhibition of the IgE/CD23 interaction on the surface of (RPMI 8866) B cells is statistically significant . .	113
3.12	Superposition of derCD23-bound IgE-Fc onto aεFab1-bound IgE-Fc upon the Cε4 domains . . . . .	115
3.13	Superposition of the derCD23 bound IgE-Fc (3-4) and aεFab1-bound IgE-Fc (3-4) . . . . .	116
3.14	Superposition images of the derCD23 and aεFab1 complexes with IgE-Fc(3-4) . . . . .	117
3.15	Superposition images of the Cε3 of derCD23-bound IgE-Fc (3-4) and aεFab1-bound IgE-Fc . . . . .	118
3.16	Model of the Cε3 disulphide-stabilised IgE-Fc . . . . .	119
3.17	SPR sensorgrams showing derCD23-mediated accelerated dissociation of wildtype IgE-Fc from aεFab1 . . . . .	122
3.18	Rigidifying the Cε3 domain of IgE-Fc reduces the effect of derCD23-mediated accelerated dissociation from aεFab1 . . . . .	123
4.1	Schematic representation of a full-length IgG antibody and an IgG Fab . . . . .	128
4.2	Schematic representation of the workflow for UCB's Core Antibody Discovery Process . . . . .	130
4.3	Schematic representation of the primary fluorescence-based homogeneous assay . . . . .	131
4.4	Schematic representation of the secondary fluorescence-based homogeneous assay . . . . .	132
4.5	Secondary screen development in HEPES buffer . . . . .	134
4.6	Secondary screen development in non-'hit' B cell supernatant . . . .	135
4.7	Secondary homogeneous fluorescence-based assay results . . . . .	136
4.8	Workflow for transcriptionally active PCR of variable region genes .	139
4.9	1 % agarose gel of secondary TAP products . . . . .	140
4.10	Heavy and light chain variable domains were cloned into UCB in-house plasmids using restriction enzymes . . . . .	141

---

4.11	Protein sequence alignment of the (a) heavy and (b) kappa CDR3s of ‘secondary hit’ antibodies . . . . .	143
4.12	Protein sequence alignment and phylogenetic analysis of the CDR3s of ‘secondary hit’ antibodies using the online MUSCLE tool . . . . .	144
4.13	A schematic representation of SPR experiments performed to ascertain the effect of the antibody/IgE-Fc interaction on the binding of derCD23 to IgE-Fc . . . . .	145
5.1	Example sensorgrams from SPR experiments to investigate the binding of IgE-Fc to $\alpha$ Fabs in transient transfection supernatant . . . . .	152
5.2	The binding of IgE-Fc to the different $\alpha$ Fabs show varied kinetics as determined by SPR . . . . .	152
5.3	Example of fitting kinetic data for the $\alpha$ Fab/IgE-Fc interaction as determined by SPR . . . . .	154
5.4	Example sensorgrams from SPR experiments to investigate the binding of derCD23 to $\alpha$ Fab-bound IgE-Fc in transient transfection supernatant . . . . .	156
5.5	The binding curve for the interaction between derCD23 and $\alpha$ Fab2-bound IgE-Fc . . . . .	157
5.6	derCD23 accelerates the dissociation of IgE-Fc from $\alpha$ Fab13 as shown by SPR experiments using $\alpha$ Fab transient transfected supernatants . . . . .	158
5.7	Example sensorgrams from SPR experiments to investigate the binding of sFc $\epsilon$ R1 $\alpha$ to $\alpha$ Fab-bound IgE-Fc . . . . .	159
5.8	Different $\alpha$ Fab:IgE-Fc (1:1) complexes bind sFc $\epsilon$ R1 $\alpha$ with different kinetics . . . . .	160
5.9	An example sensorgram from SPR experiments to investigate $\alpha$ Fab competition . . . . .	163
5.10	An overview of the results from the $\alpha$ Fab SPR competition experiments . . . . .	166
5.11	Sequence alignment of the six $\alpha$ Fabs selected for large scale expression and purification . . . . .	171
5.12	$\alpha$ Fab12 purification using protein G affinity chromatography . . . . .	172
5.13	Purification of $\alpha$ Fabs by size exclusion chromatography . . . . .	173
5.14	An HPLC SEC chromatogram for purified $\alpha$ Fab12 . . . . .	174
5.15	The ES-MS mass spectra of (a) $\alpha$ Fab2 and (b) $\alpha$ Fab12 . . . . .	176
5.16	The mechanism of N-terminal glutamine conversion to N-terminal pyroglutamate . . . . .	176
6.1	X-ray crystal structures of IgE-Fc bound to the different anti-IgE-Fc ligands . . . . .	183
6.2	Different IgE-Fc complexes show that IgE-Fc is flexible and can adopt a wide range of conformations . . . . .	184
6.3	Molecular dynamic simulations of IgE-Fc extension . . . . .	185
6.4	A representative size exclusion chromatogram for $\alpha$ Fab, IgE-Fc and $\alpha$ Fab:IgE-Fc complexes . . . . .	187
6.5	SPR sensorgrams for the binding of IgE-Fc to the different immobilised $\alpha$ Fabs . . . . .	189

---

6.6	The binding of 64 nM IgE-Fc to immobilised $\alpha$ Fab2 is well described by single $k_{on}$ and $k_{off}$ kinetic models . . . . .	190
6.7	The binding of 2 $\mu$ M IgE-Fc to immobilised $\alpha$ Fab2 is well described by biphasic kinetic models . . . . .	191
6.8	The $\alpha$ Fab12/IgE-Fc interaction has multiphasic binding kinetics at high IgE-Fc concentrations . . . . .	193
6.9	The extensive and largely hydrophobic sFc $\epsilon$ RI $\alpha$ :IgE-Fc binding interface . . . . .	194
6.10	Capturing His-IgE-Fc via its His-tag provides a straightforward way of deconvoluting the $K_D$ and $B_{max}$ of IgE-Fc/analyte interactions .	195
6.11	Binding curves of sFc $\epsilon$ RI $\alpha$ and derCD23 binding to His-tagged IgE-Fc.	196
6.12	SPR sensorgrams for the binding of sFc $\epsilon$ RI $\alpha$ to His-tagged IgE-Fc .	197
6.13	Solution-based stopped-flow experiments show the IgE-Fc/sFc $\epsilon$ RI $\alpha$ has multiphasic binding characteristics . . . . .	198
6.14	The Boltzmann distribution suggests that for each weakly-bound IgE-Fc:sFc $\epsilon$ RI $\alpha$ complex, there should be 11,000 strongly-bound Fc:sFc $\epsilon$ RI $\alpha$ complexes . . . . .	200
6.15	A schematic representation of the proposed IgE-Fc:sFc $\epsilon$ RI $\alpha$ energy landscape . . . . .	201
6.16	Our current best description of the IgE-Fc/sFc $\epsilon$ RI $\alpha$ binding equation	202
6.17	A schematic representation of the experimental setup for the IgE-Fc intramolecular FRET assays . . . . .	203
6.18	IgE-Fc intramolecular FRET experiments suggest that binding of $\alpha$ Fab2, $\alpha$ Fab12 and $\alpha$ Fab13 to IgE-Fc is associated with a conformational change in IgE-Fc . . . . .	205
6.19	Schematic representation IgE-Fc and different subfragments of IgE-Fc	206
6.20	The five selected $\alpha$ Fabs bind to the C $\epsilon$ 2 domains of IgE-Fc . . . . .	209
6.21	SPR sensorgrams for the binding of C $\epsilon$ 2 dimer and C $\epsilon$ 2 monomer to the five selected $\alpha$ Fab surfaces . . . . .	210
6.22	Intramolecular FRET studies suggested that the binding of some of the $\alpha$ Fabs results in IgE-Fc unbending . . . . .	213
7.1	Each C $\epsilon$ 3 domain of IgE-Fc can bind one CD23 head domain . . . . .	216
7.2	A schematic representation of the different types of IgE/CD23 inhibition that are theoretically possible by $\alpha$ Fabs . . . . .	218
7.3	Fc $\epsilon$ RI, $\alpha$ Fab1 and Xolair <sup>®</sup> bind IgE-Fc and inhibit the IgE-Fc/CD23 interaction . . . . .	219
7.4	rIgE-A647 binds to mCD23 with nanomolar binding affinity . . . . .	220
7.5	Schematic representation of the rIgE-A647/mCD23 binding assays .	222
7.6	The FITC-labeled MHM6-monoclonal antibody indicated the levels of mCD23 expression on RPMI 8866 cells . . . . .	224
7.7	Xolair Fab mutant 3, a Fab that binds to IgE and orthosterically inhibits CD23 binding, showed concentration-dependent inhibition of the rIgE-A647/CD23 interaction on the surface of RPMI 8866 cells	225
7.8	$\alpha$ Fab3 showed no dose-dependent inhibition of the rIgE-A647/CD23 interaction on the surface of RPMI 8866 cells . . . . .	226

---

7.9	$\alpha\epsilon$ Fab2 showed concentration-dependent inhibition of the rIgE-A647/CD23 interaction on the surface of RPMI 8866 cells . . . . .	227
7.10	The concentration-dependent inhibition of the rIgE-A647/CD23 interaction on the surface of RPMI 8866 cells by $\alpha\epsilon$ Fab2 and $\alpha\epsilon$ Fab13 is statistically significant . . . . .	229
7.11	The equilibrium effect of the $\alpha\epsilon$ Fabs on the interaction between 12 nM rIgE-A647 and CD23 on the surface of RPMI 8866 cells is a combination of the effects of each of the sites . . . . .	230
7.12	A schematic representation of the SPR experiments performed to assess the binding of a single molecule of derCD23 to different $\alpha\epsilon$ Fab:IgE-Fc complexes . . . . .	230
7.13	Example sensorgrams from SPR experiments performed to investigate the binding of derCD23 to $\alpha\epsilon$ Fab-bound IgE-Fc (1:1) complexes. . . . .	234
7.14	Binding plots for the interaction between derCD23 and His-IgE-Fc and derCD23 and the $\alpha\epsilon$ Fab2:IgE-Fc (1:1) complex . . . . .	234
7.15	Histograms shown the dissociation constants ( $K_D$ ) and $B_{max}$ values for the binding of derCD23 to $\alpha\epsilon$ Fab:IgE-Fc complexes as determined by SPR . . . . .	236
7.16	Analytical HPLC SEC analysis of $\alpha\epsilon$ Fab2:IgE-Fc (2:1) complex preparative SEC fractions . . . . .	237
7.17	Example sensorgrams from SPR experiments performed to investigate the binding of derCD23 to $\alpha\epsilon$ Fab:IgE-Fc (2:1) complexes . . . . .	238
7.18	Binding curves for the interactions between derCD23 and His-IgE-Fc and between derCD23 and $\alpha\epsilon$ Fab:IgE-Fc (2:1) complexes . . . . .	239
7.19	Schematic representations of the proposed models for the affect of each $\alpha\epsilon$ Fab on the IgE/CD23 interaction . . . . .	240
7.20	derCD23-induced accelerated dissociation of $\alpha\epsilon$ Fab13 from IgE-Fc occurs when $\alpha\epsilon$ Fab13 is in a 1:1 complex with IgE-Fc but not a 2:1 complex . . . . .	245
8.1	A partially-solved crystal structure of the $\alpha\epsilon$ Fab2:IgE-Fc (2:1) complex . . . . .	265
1	The protein sequence of a single IgE-Fc chain (N265Q, N371Q background) . . . . .	271
2	Reference-subtracted sensorgrams from SPR experiments investigating the binding of IgE-Fc to $\alpha\epsilon$ Fabs in transient transfection supernatant . . . . .	272
3	Fitting the kinetic data for the interaction between IgE-Fc and $\alpha\epsilon$ Fabs in transient transfection supernatant . . . . .	273
4	Reference-subtracted sensorgrams from SPR experiments investigating the binding of derCD23 to $\alpha\epsilon$ Fab-bound IgE-Fc . . . . .	274
5	Binding curves for the interactions between derCD23 and $\alpha\epsilon$ Fab-bound IgE-Fc . . . . .	275
6	Reference-subtracted sensorgrams from SPR experiments investigating the binding of sFc $\epsilon$ RI $\alpha$ to $\alpha\epsilon$ Fab-bound IgE-Fc . . . . .	276
7	SPR analysis to investigate $\alpha\epsilon$ Fab competition . . . . .	277
8	Size exclusion chromatograms for each $\alpha\epsilon$ Fab, IgE-Fc and $\alpha\epsilon$ Fab:IgE-Fc complexes . . . . .	278

## List of Figures

---

9	Fitting the kinetic data for the interaction between IgE-Fc and purified $\alpha\epsilon$ Fabs . . . . .	279
10	IgE-Fc (3-4) binds $\alpha\epsilon$ Fab12 in a repeated SPR binding experiment.	280
11	The C $\epsilon$ 2 dimer binds $\alpha\epsilon$ Fab12 in a repeated SPR binding experiment.	281
12	IgE/mCD23 inhibition assays . . . . .	282
13	SPR experiments investigating the binding of derCD23 to $\alpha\epsilon$ Fab:IgE-Fc (1:1) complexes . . . . .	283
14	Analytical HPLC SEC analysis of $\alpha\epsilon$ Fab:IgE-Fc (2:1) complex preparative SEC fractions . . . . .	284
15	Double-subtracted SPR sensorgrams for the binding of derCD23 to $\alpha\epsilon$ Fab:IgE-Fc (2:1) complexes . . . . .	285
16	Protein sequence alignment of human and rabbit ( <i>Oryctolagus cuniculus</i> ) IgE-Fc . . . . .	286



# List of Tables

2.1	A list of buffers frequently used for the purposes of this thesis . . .	58
2.2	A list of recombinant proteins used for the purposes of this thesis .	59
2.3	SDS-PAGE gel recipe . . . . .	62
4.1	An overview of the screening and sequencing data from the different ‘secondary hit’ antibodies . . . . .	138
4.2	Agreement between the secondary screen measurements of the supernatants of presumed clones . . . . .	141
5.1	Summary of the association and dissociation rate constants, and the dissociation constants for IgE-Fc binding to $\alpha$ εFabs as determined by SPR . . . . .	155
5.2	Summary of the dissociation constants and $B_{\max}$ values for derCD23 binding to $\alpha$ εFab-bound IgE-Fc as determined by SPR using transiently transfected $\alpha$ εFab supernatants . . . . .	157
5.3	Summary of the association and dissociation rate constants and the dissociation constants for sFcεRIα binding to $\alpha$ εFab-bound IgE-Fc as determined by SPR . . . . .	161
5.4	Protein G HPLC analysis of $\alpha$ εFab transfection supernatants . . . .	170
5.5	The estimated level of aggregated $\alpha$ εFab contaminants in each of the the purified $\alpha$ εFab samples as determined by HPLC SEC . . . . .	174
5.6	Reconciling the differences between the ES-MS-determined $\alpha$ εFab single chain masses and the ProtPram-predicted $\alpha$ εFab single chain masses . . . . .	178
5.7	The differences between the ES-MS-determined whole $\alpha$ εFab masses and the ProtPram-predicted whole $\alpha$ εFab masses . . . . .	179
5.8	A summary of the binding characteristics of the selected $\alpha$ εFabs as determined by SPR experiments of transient transfection supernatants	180
6.1	The equilibrium dissociation constants of the (a) higher- and (b) lower-affinity $\alpha$ εFab/IgE-Fc interactions as derived from kinetic binding experiments . . . . .	192
7.1	Maximum inhibition of the IgE/CD23 interaction on the surface of RPMI 8866 cells under saturating conditions of different $\alpha$ εFabs . .	228

# Abbreviations

A488	Alexa Fluor® 488
A647	Alexa Fluor® 647
aεAb	Anti-IgE antibody
aεFab	Anti-IgE Fab
aεFabXol3	Xolair Fab mutant 3
ANS	8-Anilinoanthracene-1-sulfonic acid
APCs	Antigen presenting cells
APS	Ammonium persulfate
BSA	Bovine serum albumin
cAMP	Cyclic adenosine monophosphate
CAP	Catabolite activator protein
CAPK	cAMP-dependent protein kinase
cDNA	Copy deoxyribonucleic acid
Cε	IgE constant domain
C <sub>H</sub>	Constant heavy domain
DARPin	Designed ankyrin repeat proteins
DMSO	Dimethyl sulfoxide
DNA	Deoxyribonucleic Acid
DTT	Dithiothreitol
EDC	1-ethyl-3-(3-dimethylaminopropyl)-carbodiimide hydrochloride
ES-MS	Electrospray mass spectrometry
Fab	Fragment antigen-binding
FAP	Facilitated antigen presentation
Fc	Fragment crystallizable region
FCS	Fetal calf serum
FSC	Forward scattered light
FDA	US Food and Drug Administration
FITC	Fluorescein isothiocyanate
FRET	Fluorescence resonance energy transfer
FSC	Forward scattered light
HBS	HEPES buffered saline
HEK	Human embryonic kidney

HMCV	Human cytomegalovirus
HPLC	High performance liquid chromatography
Ig	Immunoglobulin
IgE	Immunoglobulin E
IL	Interlukin
IPTG	Isopropyl $\beta$ -D-1-thiogalactopyranoside
ITC	Isothermal calorimetry
$K_D$	Dissociation constant
$k_{off}$	Dissociation rate constant
$k_{on}$	Association rate constant
LB	Luria Broth
mAb	Monoclonal antibody
mCD23	Membrane CD23
MFI	Mean fluorescence intensity
MHC	Major histocompatibility complex
MS	Mass spectrometry
MWCO	Molecular weight cut off
NHS	<i>N</i> -hydroxysuccinimide
NMR	Nuclear magnetic resonance
PBS	Phosphate buffered saline
PCR	Polymerase chain reaction
PDB	Protein Data Bank
PMT	Photomultiplier tube
PPI	Protein-protein interaction
RMSD	Root mean squared deviation
RNA	Ribonucleic acid
rpm	Revolutions per minute
RT-PCR	Reverse transcription polymerase chain reaction
RU	Resonance units
sCD23	Soluble CD23
SDS	Sodium dodecyl sulfate
SDS-PAGE	Sodium dodecyl sulfate polyacrylamide gel electrophoresis
SEC	Size exclusion chromatography
SPR	Surface plasmon resonance
SSC	Side scattered light
TAP	Transcriptionally active PCR
TBS	Tris buffered saline
TEMED	Tetramethylethylenediamine
$T_H2$ cells	T helper 2 cells
TR-FRET	Time resolved fluorescence energy transfer
VH	Variable heavy domain
VK	Variable kappa domain

# Chapter 1

## Introduction

### 1.1 IgE in allergy and asthma

The immune system responds to pathogenic invasions through the coordinated action of cellular and molecular defence systems. The antibody response is a molecular defence system that plays a crucial role in the fight against infection. B cells undergo heavy chain class switching to become plasma cells dedicated to the production of a specific antibody isotype: IgG, IgE, IgA, IgM or IgD. The different antibody isotypes can specifically stimulate a range of cellular activities vital in the immune response, including the killing of infected cells, lysis of the pathogen's cells and inflammation [1]. Antibodies trigger these responses through interactions with their cognate receptors that are expressed on the surfaces of the effector cells. The cellular distribution of the various antibody receptors, and the specificity and affinity of the different antibody isotype/receptor interactions contribute to the range of different response mechanism that occur upon the encounter of distinct antigens [2]. Different antibody isotype responses are associated with different types of immune responses to infection. Evidence suggests that IgE evolved to help fight parasitic infections [3], however it is better known for the central role that it plays in allergic disease through interactions with its two principle receptors, FcεRI and CD23 [4].

Allergies occur when the body's immune system mounts a response against an otherwise innocuous foreign antigen (an allergen). A majority of allergens are proteins or glycoproteins from sources as diverse as animal danders, pollen, dust mite feces, venoms and foods [1]. The number of people suffering from allergic diseases

worldwide has reached epidemic proportions: one in three people have at least one allergy and approximately half of all school-aged children in the developed world are sensitised to at least one allergen [5]. The global economic burden of asthma has been estimated to be greater than that of tuberculosis and HIV combined [6], and is likely to increase as the young population reaches adulthood, and as ambient temperatures and air pollution rise [5].

Anti-histamines and immunotherapy are often effective treatments for mild allergic diseases such as allergic rhinitis [5]. More severe forms of allergic disease, such as allergic asthma and atopic dermatitis, are often treated with drugs that suppress the immune system and can have serious side effects such as glucose and gastrointestinal intolerance, hypertension and increased susceptibility to infections [7]. It has also been reported that 5 - 10 % of asthmatics are unresponsive to usual immunosuppressant treatment [8]. Furthermore, the number of people suffering from food allergies, for which there are no approved therapeutics, is increasing at an alarming rate [9]. It is hoped that alternative and superior therapeutics for allergy and asthma will better treat the growing number of allergic patients, as well as the sufferers that are unresponsive to the current therapies.

There are ongoing efforts to find ways of specifically targeting cells and molecules involved in the allergic response, including mast cells [10] and various cytokines [11]. Recently, the US Food and Drug Administration (FDA) approved two monoclonal antibodies that target the proallergic cytokine, interleukin-5 (IL-5), for the treatment of persistent eosinophilic allergic asthma: reslizumab (CINQAIR<sup>®</sup>, Teva) and mepolizumab (Nucala<sup>®</sup>, GSK). Since most allergic responses to allergens are mediated by IgE, IgE is also highly regarded as an important therapeutic target.

### **1.1.1 The role of IgE/receptor interactions in allergy and asthma**

In 1966 IgE was identified as the component in the sera of allergic individuals capable of transferring immediate hypersensitivity to the skin of normally un-reactive persons [12]. IgE antibodies are produced and secreted by B cells that have undergone heavy-chain class switching from IgM to IgE plasma cells [1]. The serum

levels of IgE are very low compared to other antibody classes [13], and IgE exists predominantly in mucosal tissues as part of an IgE-Fc $\epsilon$ RI complex on the surface of mast cells and basophils [14]. As for other antibody isotypes, IgE antibodies are composed of two identical heavy and light chains [1]. The IgE molecule has two antigen/allergen-specific fragment antigen-binding regions (Fabs) and a single fragment crystallizable (Fc) region (Figure 1.1). The interaction between IgE-Fc and its canonical cell-surface receptors, Fc $\epsilon$ RI and CD23, are important in many aspects of allergic disease [4].

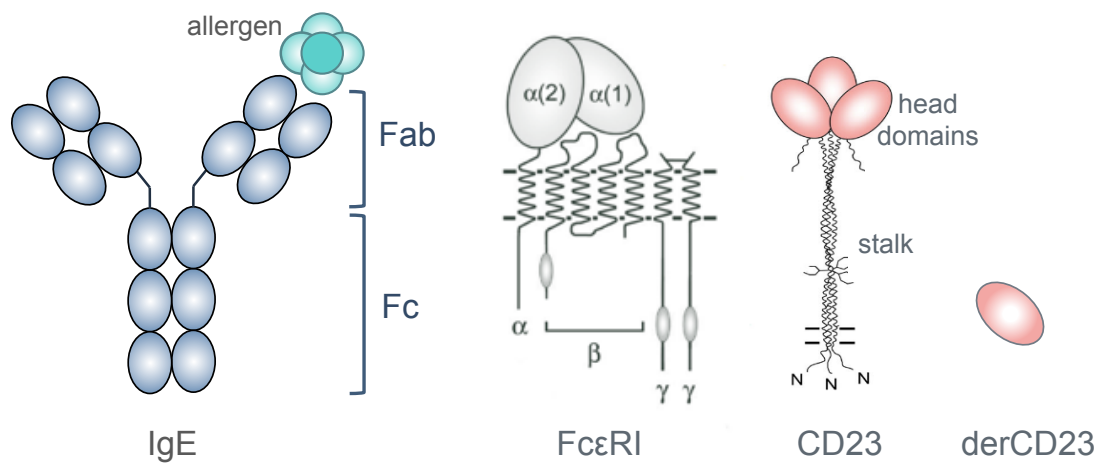


Figure 1.1: **Schematic representations of IgE and its receptors.** IgE has a typical antibody architecture; it is composed of two identical heavy and light chains. The two Fab regions bind to specific epitopes on antigens, or in the case of allergic disease, allergens. The Fc region binds the receptors, Fc $\epsilon$ RI and CD23, and through these interactions, IgE elicits its effector functions. The extracellular domains of the alpha chain of Fc $\epsilon$ RI bind IgE-Fc, whereas the C-type lectin head domains of CD23 contain the IgE-Fc binding activity. Cleavage of membrane trimeric CD23 by the der p1 protease results in the release of single soluble CD23 head domains (derCD23).

Fc $\epsilon$ RI is expressed on the surface of mast cells and basophils as an  $\alpha\beta\gamma_2$  tetramer and on a variety of human antigen presenting cells (APCs) as an  $\alpha\gamma_2$  trimer (Figure 1.1). Fc $\epsilon$ RI binds to IgE-Fc via the extracellular domains of the  $\alpha$  chain (sFc $\epsilon$ RI $\alpha$ ), whereas the  $\beta$  and  $\gamma$  chains are involved in signal transduction [14, 15].

CD23 is expressed as trimer on the surface of B cells, epithelial cells and a range of inflammatory cells types [16]. Three C-type lectin domain heads are tethered to the surface of the cell via an  $\alpha$ -helical coiled-coil stalk [17] (Figure 1.1). The IgE-Fc

binding activity is located in C-type lectin head domains, but does not recognise carbohydrate [18]. Carbohydrate is, however, involved in the binding of CD23 to CD21, an interaction that links the IgE-antibody system to the complement pathway [16]. The stalk of trimeric membrane CD23 (mCD23) can be cleaved in various places by a range of endogenous and exogenous proteases, resulting in the release of soluble CD23 (sCD23) with different stalk lengths and oligomeric states [19]. Der p1 is a protease found in house dust mite feces, which cleaves human mCD23, releasing single soluble head domains (derCD23) (Figure 1.1) [20].

The IgE/Fc $\epsilon$ RI interaction is crucial in the sensitisation of individuals to allergens and in triggering the initial allergic response. Both IgE/Fc $\epsilon$ RI and IgE/CD23 interactions are also involved in processes that propagate and exacerbate allergic reactions (Figure 1.2) [4].

### **Immediate hypersensitivity**

Mast cells and basophils of sensitised individuals are primed with allergen-specific IgE through interactions with Fc $\epsilon$ RI on their surfaces. Since mast cells and basophils exist primarily in mucosal tissues, Fc $\epsilon$ RI-bound IgE is one of the first immunological molecules an allergen may encounter [4]. Cross-linking of Fc $\epsilon$ RI-bound IgE-Fc on the surface of mast cells results in downstream signalling that triggers mast cell activation and the consequential release of a diverse set of pro-inflammatory cytokines and lipid mediators (Figure 1.2 (1)) [21]. Within minutes, this ‘early phase’ of the allergic reaction causes vasodilation and increased vascular permeability, and results in either localised or systemic reactions. Some of the mediators that are released during the ‘early phase’ of the allergic reaction initiate the ‘late phase’ of an allergic response, which peaks around 6 – 9 hours after allergen exposure. The ‘late phase’ involves the recruitment and activation of T helper 2 (T<sub>H</sub>2) cells, eosinophils and other inflammatory cell-types to the affected site, as well as the persistent production of pro-inflammatory mediators by mast cells and basophils [21, 15].

### **Antigen presentation**

Both FcεRI and CD23 have important roles in allergen presentation to T cells, which drive the immune response to allergen. FcεRI is expressed by a variety of APCs that patrol the body's surface in search of foreign antigens. The APCs process and present allergens that have been captured by IgE/FcεRI complexes on their surfaces to T helper cells, which increase the activity of other immune cells and propagates the allergic response [22].

Antigen-activated B cells express CD23 on their surface and present allergen to T cells in a process known as facilitated antigen presentation (FAP). IgE/CD23 complexes on the surface of antigen-activated B cells act as allergen receptors. Allergen-IgE-CD23 complexes are internalised and processed by the antigen-activated B cells, and the resulting peptides are displayed on their cell surfaces for T cell recognition by MHC class II proteins (Figure 1.2 (2)) [23, 22, 24, 25]. FAP allows antigen-activated B cells to concurrently process and present unrelated antigens and allergens to cognate T cells, and is thought to be responsible for the phenomenon of epitope spreading [4]. Epitope spreading is when an antibody response for one epitope leads to the production of antibodies specific for another epitope on the same antigen, or a different antigen, and may contribute to the 'Atopic March', whereby individuals become sensitized to an increasing number of allergens [26].

### **IgE-mediated cytotoxicity**

Eosinophils, monocytes and macrophages are amongst the cells that are recruited to the site of allergic inflammation [21]. Once activated, these cells express CD23 and FcεRI on their surfaces [27]. The capture of allergen:IgE complexes by receptors on the surfaces of these cells triggers the lysis of target cells and phagocytosis of cell fragments [28]. Although beneficial in the fight against a parasitic infection, the release of cytotoxic mediators by these cells can result in damage to surrounding tissues, and in the context of allergy and asthma contributes to the inflammation of tissues at the site of allergen encounter [3] (Figure 1.2 (3)).



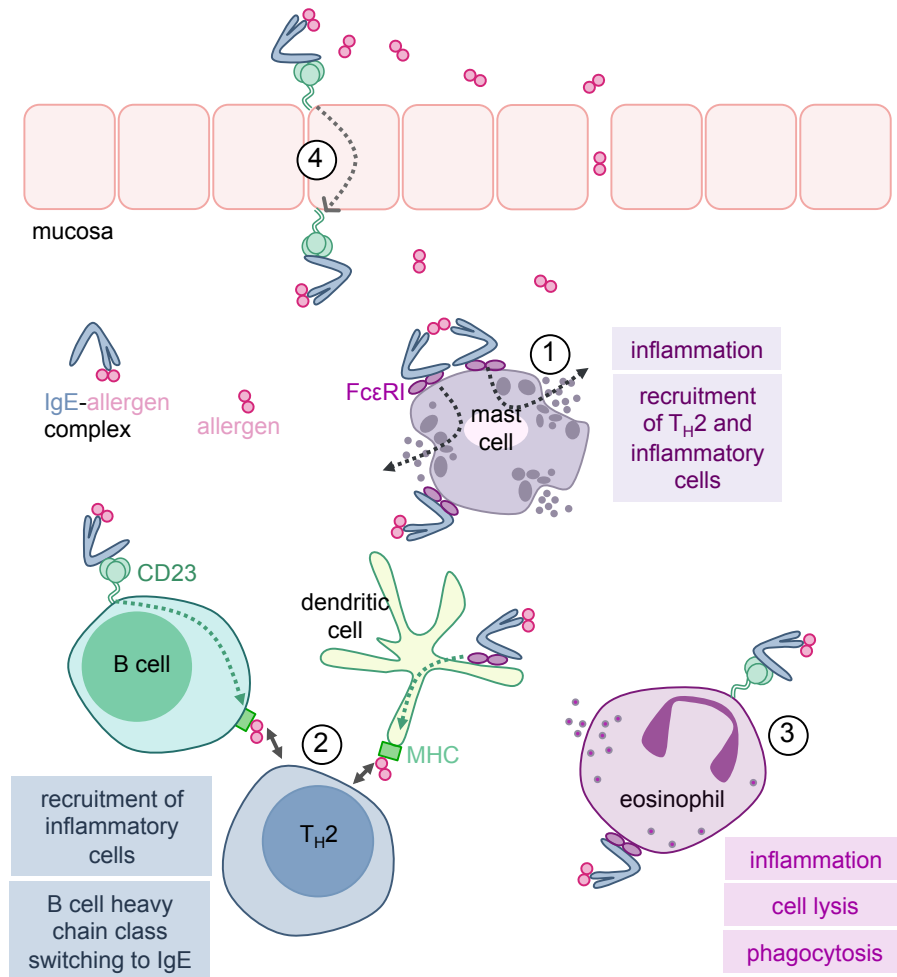


Figure 1.2: **IgE/receptor interactions are important in the initiation and propagation of allergic disease.** IgE, secreted by IgE-switched B cells, binds to FcεRI on the surface of mast cells and sensitises them to the allergen to which they are specific. (1) Cross-linking of FcεRI-bound IgE on the surface of mast cells activates the mast cells and triggers their degranulation. The release of pro-inflammatory mediators causes an allergic response. Secreted IgE also binds to IgE-receptors expressed on the surface of antigen presenting cells, and CD23 on B cells. Allergen-IgE complexes on the surface of APCs, such as dendritic cells, are processed and presented to TH2 cells (2). The allergen activated TH2 cells subsequently produce and secrete type 2 cytokines such as IL-4, which help to recruit and maintain the TH2 cell population and are also required for heavy chain class switching to IgE, thereby increasing the local IgE concentration. Eosinophils are recruited to the site of allergen encounter by the mediators and cytokines released from activated TH2 cells and from mast cell degranulation. Allergen-IgE complexes bind to IgE-receptors on the surface of eosinophils, resulting in the release of inflammatory messengers and molecules that lyse cells. CD23 on the surface of epithelial cells binds allergen-IgE complexes and transports them across the epithelia of the gut, nose and lungs into the mucosa (4) where they can bind the effector cells, and exacerbate the allergic reaction. The resulting inflammation compromises the tight junctions of the epithelia and allows further allergen entry.

### **CD23-dependent allergen transcytosis**

The epithelial cells of the respiratory tract [29], intestine [30] and nasal passages [31] constitutively express CD23. Through interactions with IgE, CD23 on the surfaces of epithelial cells can facilitate the apical to basal transcytosis of allergen-IgE complexes into the mucosa (Figure 1.2 (4)) [32, 33, 29]. Once in the mucosa, it has been suggested that the IgE-allergen complexes are capable of binding and activating immune cells, for example it has been proposed that the IgE-allergen complexes can bind Fc $\epsilon$ RI on the surface of mast cells where they can trigger the acute phase of an allergic response [33, 29]. Similarly, the IgE-allergen complexes may bind Fc $\epsilon$ RI on the surface of dendritic cells, ultimately resulting in the activation of IgE class switching in local B cells. Inflammation occurs as a result of an allergic response, and damages the epithelium, which in turn allows more allergen into the mucosa and intensifies the allergic reaction [4]. CD23-mediated transcytosis is therefore thought to play important roles in the initiation and exacerbation of allergic disease, and may also partly explain why allergic reactions occur so quickly after allergen challenge (Figure 1.2).

### **CD23-mediated IgE homoeostasis**

CD23 is regarded as a natural regulator of IgE synthesis but the exact mechanisms through which it acts to control levels of IgE are not fully understood [4]. The different states of CD23 appear to have differential effects on IgE homoeostasis. Numerous studies have demonstrated that soluble oligomeric CD23 acts to increase IgE synthesis [34, 35, 36, 37], whereas soluble monomeric CD23 has been shown to decrease levels of IgE synthesis [35, 36, 37]. The interaction between CD23 and the complement receptor, CD21, expressed on the surface of B cells, was shown to be necessary for the positive effect of soluble trimeric CD23 on IgE synthesis [34]. The formation of large signalling platforms that lower the B cell activation threshold are generated by the cross-linking of CD21 and IgM on the surface of B cells by the complement component C3 [38]. CD23 can bind IgE and CD21 simultaneously [39], and it has been proposed that trimeric sCD23 could act in an analogous way to C3, and cross-link CD21 and IgE on the surface of B cells, resulting in the formation

of a signalling platform that promotes B cell proliferation and differentiation [36] (Figure 1.3). Monomeric sCD23, which binds IgE with a 2:1 stoichiometry, would be unable to form these extended arrays, and it is suggested that their negative effect on IgE synthesis is a result of competition with trimeric sCD23 for IgE [36]. There is also evidence from several studies in mice suggesting that stabilising mCD23 is associated with a reduction in IgE synthesis [40, 41, 42, 43, 25, 44]. It has been proposed that a negative signal for B cell proliferation and differentiation could be delivered by the co-ligation of IgE and mCD23 by IgE-allergen complexes [4] (Figure 1.3).

Evidence for and against specific models of CD23-mediated IgE homeostasis is relatively sparse and there is a lack of substantiating structural data. Nevertheless, the importance of the CD23/IgE interaction in IgE synthesis is undisputed and because of the role that IgE plays in allergic disease, CD23 is considered a potential therapeutic target. Antibodies that bind the head domain of CD23 have indeed been shown *in vitro* [45, 46, 47, 48], in animals [49, 50, 51] and in humans [52] to reduce IgE production.

### **1.1.2 Targeting IgE/receptor interactions in the treatment of allergy and asthma**

Since the IgE/receptor interactions play a major role in the initiation and propagation of allergic disease, modulating these interactions may provide a way of treating allergic disease. Inhibition of these interactions is, in fact, a proven therapeutic strategy: in 2003 Omalizumab (Xolair<sup>®</sup>, Novartis), which blocks IgE/receptor interactions, became the first anti-IgE monoclonal antibody (mAb) to be approved by the FDA for the treatment of severe and persistent allergic asthma [53], and in 2014 Xolair was also licensed for the treatment of chronic idiopathic urticaria. Xolair works principally by reducing the serum levels of free IgE by as much as 97 % [54], and also by down-regulating the expression of FcεRI on the surface of mast cells, basophils [55, 56, 57] and dendritic cells [58]. The depletion of free IgE and the reduction FcεRI expression both contribute to reduced levels of IgE/FcεRI on the surface of mast cells, basophils and dendritic cells, which subsequently pre-

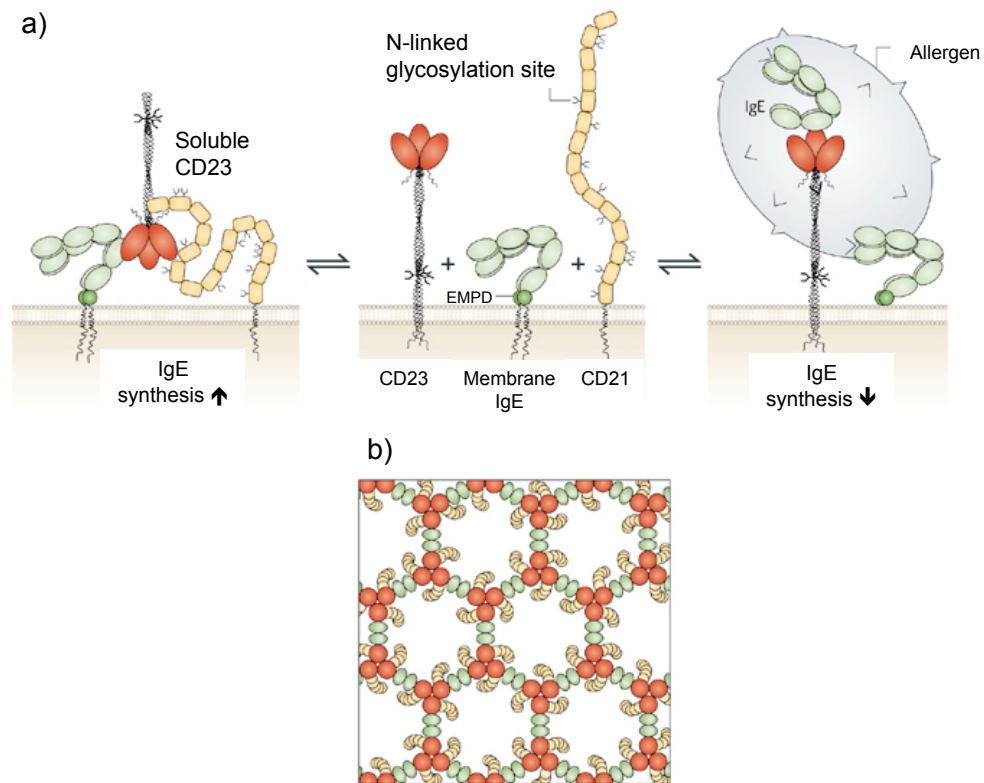


Figure 1.3: **The mechanisms of CD23-mediated IgE homeostasis.** The exact mechanisms of IgE regulation by CD23 in humans are disputed. (a) One popular model suggests that cross-linking of membrane IgE and CD21 expressed on the surface of B cells, by soluble CD23, results in the up-regulation of IgE synthesis. IgE synthesis is thought to be suppressed by the cross-linking of membrane IgE and membrane CD23 on the surface of B cells by a IgE-allergen complex. (b) Large networks, formed through the co-ligation of IgE (green) and CD21 (yellow) by soluble, trimeric CD23 (red) may act as signalling platforms for the survival and differentiation of IgE-B cells. Adapted from Gould and Sutton, 2008 [4].

vents IgE-mediated activation of these cells and thereby limits immediate type I hypersensitivity reactions and antigen presentation [54].

Clinical trials of an anti-CD23 mAb, lumiliximab, also showed promise: lumiliximab improved patient outcomes by reducing the levels of serum IgE and inhibiting allergen-specific T cell responses as a result of limiting antigen-presentation [59]. Further development of lumiliximab however, was discontinued after the merger of the companies involved in its discovery [60].

Therapeutic mAbs, like Xolair and lumiliximab, are the fastest growing class of therapeutic molecules [61]. mAbs can be produced with high specificity and high affinity for an almost infinite number of targets, without requiring structural rationalisation. However, biologics like mAbs are generally more delicate than small

molecules and are sensitive to heat, light, agitation and contamination [62]. In the past, manufacturing large quantities of pure and active monoclonal antibodies has been a very costly process [63], but a rapid increase in demand of therapeutic mAbs has driven efforts to increase production and improve purification. The resulting increase in titers has led to a significant reduction in production costs, which in the future may become a relatively small proportion of the sales price [64].

Another major consideration of any therapy is immunogenicity- where the therapeutic entity elicits an immune response and results in the production of anti-drug antibodies (ADAs) and/or the initiation of pro-inflammatory cytokines [65]. Immunogenicity can affect the efficacy of the drug, for example ADAs may increase its clearance thereby reducing its plasma half-life. ADAs may also bind and neutralise the drug's pharmacological activity. Immunogenicity can also alter a drug's safety, for example a therapeutic agent may initiate IgE-hypersensitivity reactions or 'cytokine storms' [65]. Immunogenicity arises because the immune system recognises the therapeutic agent as 'non-self'. The larger size and greater chemical complexity of mAbs, compared to small molecules, in general renders them more immunogenic [66]. All therapeutic mAbs in clinical use have shown signs of immunogenicity [67]. Because of the safety risks associated with immunogenicity, Xolair has to be administered in a healthcare setting under the supervision of a healthcare professional trained to manage life-threatening anaphylaxis. Fortunately Xolair-related anaphylaxis is uncommon and has been seen in less than 0.1 % of patients [68].

Small molecule therapeutics are generally considered less expensive to manufacture than mAbs and can be administered orally, however, because of their small size they are generally poor protein-protein interaction (PPI) inhibitors. Typically small molecules bind deep cavities on proteins ( $\sim 300\text{--}500 \text{ \AA}^2$ ) [69], whereas PPI surfaces are usually flat and large ( $\sim 1,000\text{--}2,000 \text{ \AA}^2$  per side) [70]. Generating small molecule PPI inhibitors that target the interactions between IgE and its receptors would be very challenging, but could be a valuable alternative treatment for sufferers of severe and persistent allergic diseases.

## 1.2 The structural and biophysical basis of the IgE/receptor interactions

### 1.2.1 The structure and dynamics of IgE

IgE binds to its receptors via its Fc region, which is composed of two identical chains, each comprised of three C-domains: C $\epsilon$ 2, C $\epsilon$ 3 and C $\epsilon$ 4. C $\epsilon$ 3 and C $\epsilon$ 4 have homologous sequences and similar structures to the equivalent domains in the Fc region of IgG, however, IgG has flexible linkers in place of the C $\epsilon$ 2 domains of IgE [4] (Figure 1.4).

Crystal structures of IgE-Fc show that the C $\epsilon$ 2 domains fold back upon the C $\epsilon$ 3 domains in an asymmetric manner [71, 72] (Figure 1.5), such that the C $\epsilon$ 2 domain pair interacts with the C $\epsilon$ 3 and C $\epsilon$ 4 domains of the chain it folds back onto. Solution studies using fluorescence resonance energy transfer (FRET) [73, 74, 75] and X-ray and neutron scattering [76] also allude to a bent IgE structure that is distinct from the extended Y-shape of the IgG molecule.

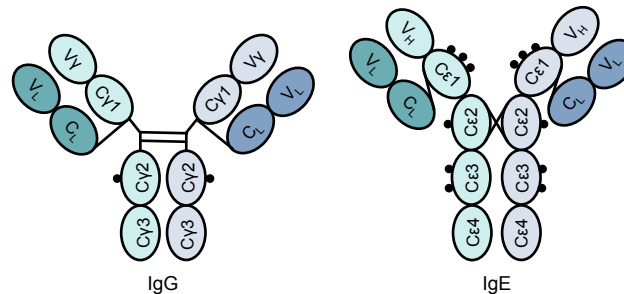


Figure 1.4: **A schematic representation of IgG and IgE.** IgE shares a common architecture with IgG. The Fc regions of both IgG and IgE are composed of two identical heavy chains. The C $\gamma$ 2 and C $\gamma$ 3 domains of IgG-Fc are homologous to the C $\epsilon$ 3 and C $\epsilon$ 4 domains of IgE, respectively. The two chains of IgE-Fc each have an additional C-domain (C $\epsilon$ 2) compared to IgG, which instead has a flexible linker joining the Fc region to the Fabs. Inter-chain disulphide bonds form in both IgG and IgE (lines) and both molecules contain multiple glycosylation sites (circles).

Despite forming a more compact structure than IgG in solution, IgE displays a large degree of conformational flexibility. Different crystal forms of the C $\epsilon$ 3-C $\epsilon$ 4 sub-fragment of IgE-Fc (IgE-Fc(3-4)) show that the molecule can exist in a range of ‘open’ and ‘closed’ structures, in which a rigid-body motion of the C $\epsilon$ 3 domains upon the C $\epsilon$ 4 domains changes the relative disposition of the two C $\epsilon$ 3 domains to

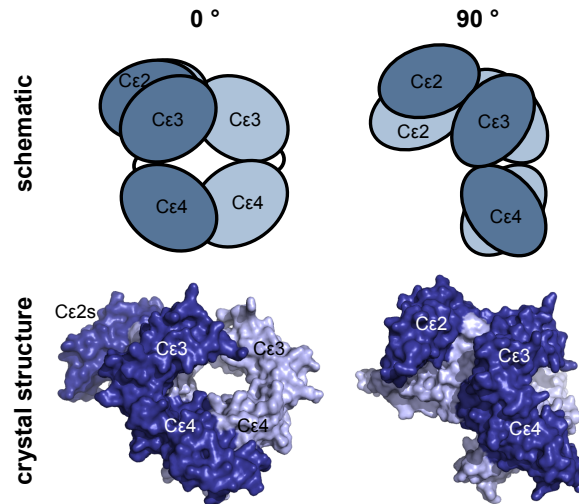


Figure 1.5: **The crystal structures of IgE-Fc suggest that IgE-Fc is asymmetric and bent.** The crystal structures of IgE-Fc show that it exists in a conformation in which the Cε2 domains fold back over onto one side of the molecule [71, 72]. The crystal structure of IgE-Fc (PDB: 2WQR [72]) is shown here in surface representation.

one another (Figure 1.6) [77].

The Cε3 domains, to which IgE receptors bind, are also intrinsically dynamic and in isolation they have a molten globule character [78, 79]. The Cε3 domain is unlike any other immunoglobulin domain in regards to its loose hydrophobic packing and low thermostability, which are responsible for the relatively low melting temperature of IgE compared to other classes of antibody [80].

Studies investigating various IgE-Fc/ligand interactions have further demonstrated the extraordinary conformational diversity of IgE-Fc. The crystal structure of IgE-Fc bound to an anti-IgE Fab (αεFab1) revealed a conformation of IgE-Fc in which the Cε2 domain pair is unbent, and IgE-Fc exists in an almost entirely extended and symmetric state [81] (Figure 1.7).

Saturating concentrations of αεFab1 were shown to inhibit the FRET signal between donor and acceptor fluorophores in the N and C-termini of IgE-Fc, indicating that αεFab1 stabilises an extended conformation of IgE-Fc in solution. Isothermal titration calorimetry (ITC) and stopped-flow kinetics suggested that αεFab1 selects for an extended conformation of IgE-Fc that is already present in a pre-existing equilibrium of IgE-Fc states [81]. A free-energy landscape of IgE-Fc, produced from molecular dynamics simulations, also suggested that IgE-Fc exists

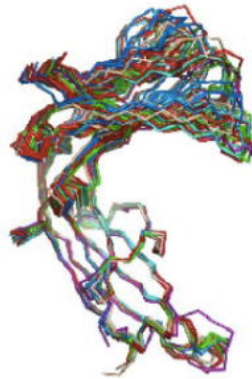


Figure 1.6: **IgE-Fc(3-4) exists in a range of open and closed conformations.** Wurzburg *et al.* solved X-ray structures of IgE-Fc(3-4) from different crystal forms [77]. An overlay, in which the IgE-Fc(3-4) chains were aligned on C $\epsilon$ 4 domain residues (441-541), shows that the C $\epsilon$ 3 domains move as a rigid-body upon the C $\epsilon$ 4 domains, adopting a range of ‘open’ and ‘closed’ conformations. (Figure adapted from Wurzburg *et al.* [77].)

in a range of extended conformations along an ‘unbending pathway’ (Figure 1.8). The energy difference between the apo-bent conformation and the fully extended state was approximated to be 20 kJ mol<sup>-1</sup> (8 k<sub>B</sub>T), meaning that although fully extended states of IgE-Fc may be rarely populated, the C $\epsilon$ 2 domain pair can ‘flip’ from one side of the molecule to the other [81].

Recently, the structure of IgE-Fc bound to a mutant Xolair Fab (Xolair Fab mutant 3) was determined in our laboratory, and shows the C $\epsilon$ 2 domains in a partially extended conformation [82] (Figure 1.7). Determining other intermediates along the ‘unbending pathway’ and alternative states of this dynamic molecule will help to understand the structure and dynamics of IgE-Fc in the context of its conformational ensemble.

### 1.2.2 The IgE/Fc $\epsilon$ RI interaction

The interaction between IgE and Fc $\epsilon$ RI has an unusually high affinity compared to other immunoglobulin/receptor interactions [14]. Kinetic studies performed using surface plasmon resonance (SPR) show that the high affinity of the interaction is largely the consequence of an exceptionally slow off-rate [83, 84]. The slow dissociation of IgE from Fc $\epsilon$ RI on the surface of mast cells and basophils accounts for the long half life of IgE in mucosal tissue, and consequently the the long-term



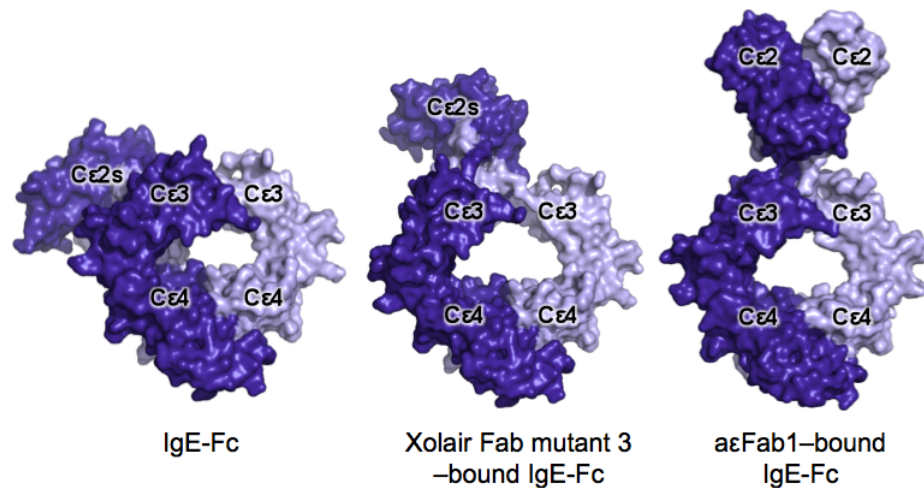


Figure 1.7: **IgE-Fc can adopt extended and partially extended conformations.** Crystal structures of free IgE-Fc suggest it exists predominately in a bent asymmetric conformation. The crystal structure of IgE-Fc when it is bound to Xolair Fab mutant 3 [82] shows the C $\epsilon$ 2 domains adopt partially extended conformations. The crystal structure of IgE-Fc bound to a $\epsilon$ Fab1 (PDB: 4J4P [81]) demonstrates that IgE-Fc can adopt an almost fully extended, symmetric conformation. All three crystal structures of IgE-Fc are shown in surface representation, with the two identical chains in different shades of blue.

sensitisation of these cells and the immediacy of the allergic reaction upon allergen exposure [85]. The off-rate of the interaction sFc $\epsilon$ RI $\alpha$  and a subfragment of IgE-Fc lacking the C $\epsilon$ 2 domains (IgE-Fc(3-4)) has a significantly increased off-rate compared to IgE-Fc or whole IgE, suggesting that the C $\epsilon$ 2 domains of IgE-Fc play an important role in stabilising the IgE/receptor interaction [83].

Several crystal structures of IgE-Fc and IgE-Fc(3-4) bound to sFc $\epsilon$ RI $\alpha$  have been solved [86, 87, 72] and allow an atomic description of this high affinity interaction. The  $\alpha$ 2 domain, and a linker between the  $\alpha$ 1 and  $\alpha$ 2 domains of Fc $\epsilon$ RI, bind to two C $\epsilon$ 3 subsites on IgE-Fc that are non-identical but overlapping (Figure 1.9). The largely hydrophobic interaction surface runs across both C $\epsilon$ 3 domains of IgE-Fc, close to the C $\epsilon$ 3-C $\epsilon$ 2 linker. Two salt-bridges and three hydrogen bonds form between sFc $\epsilon$ RI $\alpha$  and C $\epsilon$ 3 residues in subsite 1, and packing interactions form between a proline of IgE-Fc sandwiched between two sFc $\epsilon$ RI $\alpha$  tryptophan residues in subsite 2. There are no specific contacts between at sFc $\epsilon$ RI $\alpha$  and the C $\epsilon$ 2 domains [72]. Thermodynamic data demonstrate that the binding of Fc $\epsilon$ RI to IgE-Fc(3-4) is enthalpically driven, whereas the IgE-Fc/Fc $\epsilon$ RI interaction is entropically driven

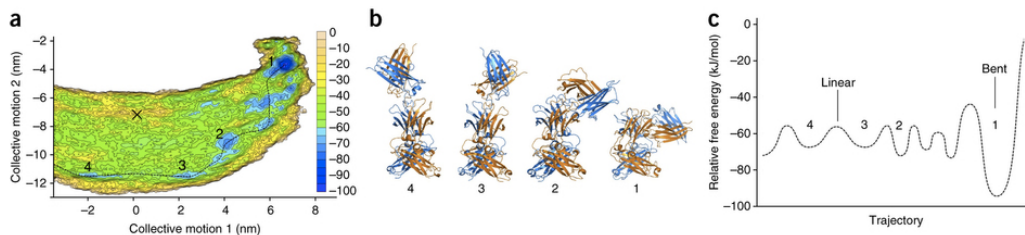


Figure 1.8: **A molecular dynamics simulation of IgE-Fc extension.** A multiple-walker metadynamics simulation was performed to look at the unbending and twisting of the C $\epsilon$ 2 domain pair in IgE-Fc. These two collective variables were extracted from preliminary unbiased and biased simulations through principle component analysis. The final multiple-walker simulation provided a full-atomic description of IgE-Fc, starting from the bent structure (1O0V), and converged after 3755 ns using Gaussians of height 4 kJ/mol added every 4 ps (for more detail see [81]). (a) The free-energy surface diagram generated from the metadynamics simulation suggests that IgE-Fc exists predominantly in a bent conformation but that it may also transiently populate extended states (collective motion 1: IgE-Fc bending/extension, collective motion 2: C $\epsilon$ 2 domain pair twisting in relation to (C $\epsilon$ 3-C $\epsilon$ 4)<sub>2</sub>). A dotted line between energy minima shows a suggested ‘unbending’ pathway. A cross marks the position of the  $\alpha$ Fab1-bound IgE-Fc structure in the energy surface, which deviates from the proposed pathway due to a twisting of the C $\epsilon$ 2 domain pair, presumably stabilised by  $\alpha$ Fab binding. Models for the conformations of IgE-Fc that exist in the minima along the ‘unbending pathway’ are shown in (b), and a sketch of the suggested pathway is illustrated in (c). (Figure taken from Drinkwater *et al.* [81].)

[83].

The crystal structures demonstrate that conformational flexibility of IgE-Fc is important in how it interacts with sFc $\epsilon$ RI $\alpha$ . The binding of sFc $\epsilon$ RI $\alpha$  to IgE-Fc results in considerable conformational changes in IgE-Fc, although there are almost no observable rearrangements in the structure of Fc $\epsilon$ RI $\alpha$  as a result of the interaction [86, 87, 72]. The C $\epsilon$ 2 domains fold back even further onto the C $\epsilon$ 3 and C $\epsilon$ 4 domains than in the apo-IgE crystal structures [72], and evidence from intramolecular FRET data suggests that this more compact shape is also adopted upon binding sFc $\epsilon$ RI $\alpha$  in solution [74, 75]. Furthermore, to accommodate the simultaneous engagement of sFc $\epsilon$ RI $\alpha$  with both subsites on IgE-Fc, both C $\epsilon$ 3 domains adopt ‘open’ conformations in which they are further from one another than in the apo-IgE structures (Figure 1.10). The crystal structures also suggest that conformational changes in the Fc $\epsilon$ RI binding loops occur in order to correctly coordinate the receptor [86, 87, 72].

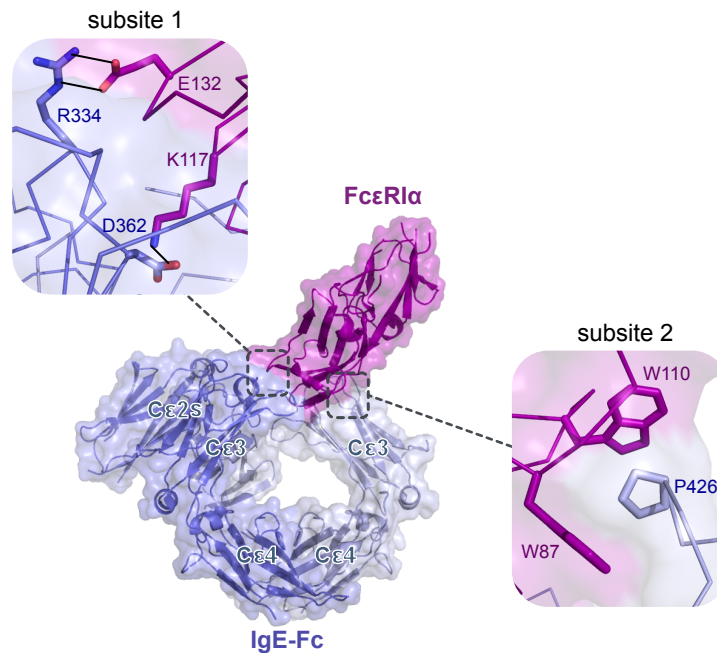


Figure 1.9: **The interaction between IgE-Fc and sFc $\epsilon$ RI $\alpha$ .** The crystal structure of sFc $\epsilon$ RI $\alpha$  bound to IgE-Fc (PDB: 2YZQ [72]) shows sFc $\epsilon$ RI $\alpha$  binds to IgE-Fc with a 1:1 stoichiometry. sFc $\epsilon$ RI $\alpha$  contacts both C $\epsilon$ 3 domains of IgE-Fc, forming two different interaction subsites. A network of hydrogen bonds and salt bridges form at subsite 1, whereas stacking interactions between an IgE-Fc proline, sandwiched between two sFc $\epsilon$ RI $\alpha$  tryptophan residues, stabilise the interaction at the subsite 2.

The crystal structures of free IgE-Fc show that one of the C $\epsilon$ 3 domains already exists in the ‘open’ conformation required for Fc $\epsilon$ RI binding. It has been proposed that the C $\epsilon$ 2 domains of IgE, which are absent in IgG, stabilise the flexible C $\epsilon$ 3 domains, thereby reducing the entropic penalty that occurs as a result of Fc $\epsilon$ RI binding [83, 72].

### 1.2.3 The IgE/CD23 interaction

A single chain of CD23 binds IgE with a  $K_D$  of  $10^{-7}$  -  $10^{-6}$  M, [88, 39, 89, 90] but because CD23 exists as a trimer on the surface of cells, avidity increases the affinity of the interaction such that its binding affinity is roughly comparable to that of the IgE/Fc $\epsilon$ RI interaction [91, 92, 36, 90]. The structure of IgE-Fc(3-4) bound to recombinant derCD23 confirms previous reports that two CD23 head domains bind one molecule of IgE [88]. In the context of trimeric CD23, two head domains from the same CD23 molecule cannot simultaneously coordinate one molecule of

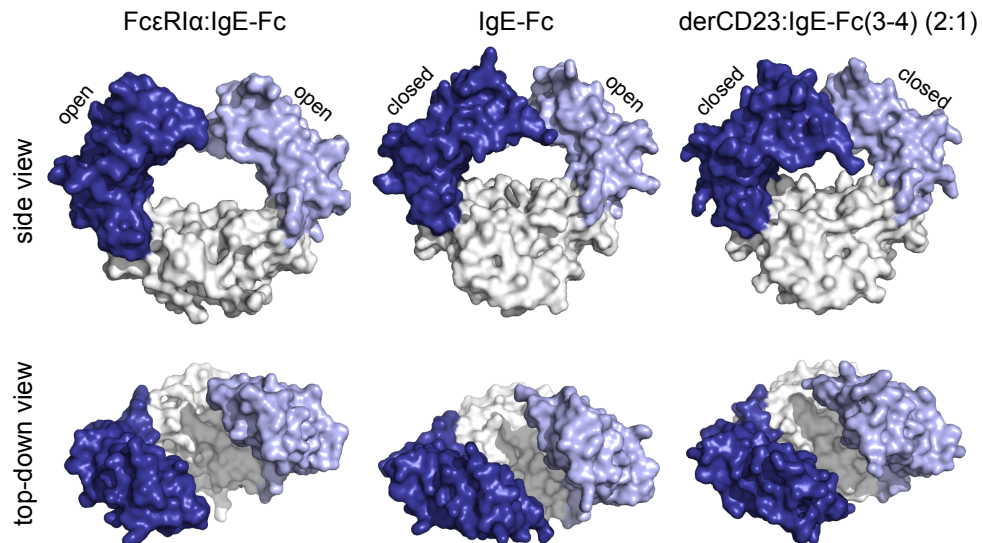


Figure 1.10: **sFcεRIα binds to an open conformation of IgE-Fc whereas derCD23 binds a closed state.** The crystal structure of sFcεRIα bound to IgE-Fc (PDB: 2YZQ [72]) shows sFcεRIα binds to IgE-Fc in which both Cε3 domains are in an ‘open’ conformation. For clarity only the Cε3 (blue) and Cε4 (white) domains are shown in the surface representation. In the crystal structure of IgE-Fc (PDB: 2WQR [72]), one Cε3 domain is in an ‘open’ conformation and the other is in a ‘closed’ conformation. Again, for clarity only the Cε3 (blue) and Cε4 (white) domains are shown in the surface representation. The crystal structure of IgE-Fc(3-4) bound to two molecules of derCD23 (PDB: 4EZM [18]) shows both Cε3 domains adopt ‘closed’ conformations.

IgE since simultaneous engagement would require a very significant ‘unzipping’ of the CD23 stalk [88, 85]. Two head domains from two different CD23 molecules could, however, simultaneously engage one molecule of IgE, further adding to the avidity of the interaction [85].

Each CD23 head domain binds a separate chain of IgE-Fc(3-4) at symmetrically equivalent binding sites (Figure 1.11). Both crystallography [18, 93] and nuclear magnetic resonance (NMR) [89] have confirmed the location and composition of the CD23 binding sites, which primarily involve the Cε3 domains, although the Cε3-Cε4 domain linkers and the Cε4 domains do make some smaller contributions to the interaction. The interaction interface is mainly hydrophilic and a network of salt bridges and hydrogen bonds form between IgE-Fc and flexible loops of the CD23 molecule (Figure 1.11.b) [18, 93]. CD23 belongs to the C-type lectin superfamily: a family of calcium-dependent carbohydrate-binding proteins, however calcium is not essential for binding of CD23 to human IgE [39, 93] and the interaction is

independent of carbohydrate [94]. Although not essential for the interaction, the presence of calcium increases the affinity of the interaction by about 30 fold (at 37 °C) [93]. The crystal structure of the IgE-Fc(3-4):derCD23 (2:1) complex in the presence of  $\text{Ca}^{2+}$  shows that it binds to a loop that is partially disordered in the absence of  $\text{Ca}^{2+}$ . The stabilisation of the loop by  $\text{Ca}^{2+}$  permits the formation of two additional hydrogen bonds between this loop and IgE-Fc, and accounts for the entropic contribution to binding that is observed in the presence of calcium [93].

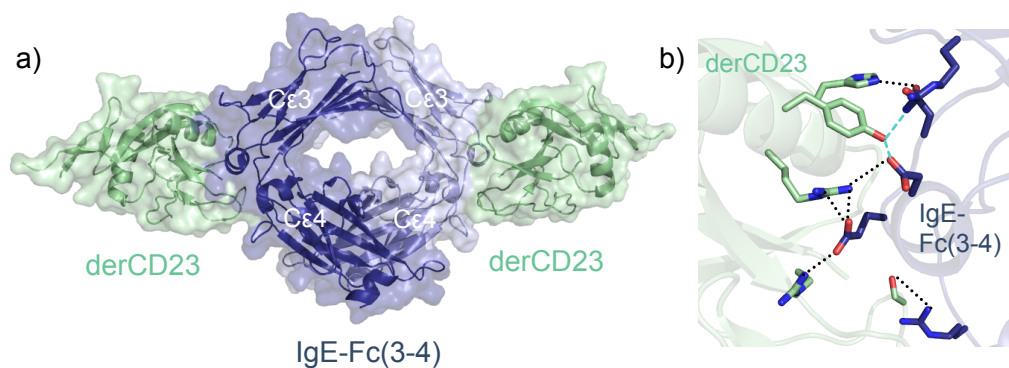


Figure 1.11: **The crystal structure of the derCD23:IgE-Fc(3-4) 2:1 complex (PDB: 4EZM [18]).** (a) Two molecules of derCD23 bind one molecule of IgE. Each binding site is comprised predominantly of residues from loops in the CD23 head domain and residues from the C $\epsilon$ 3 domain. (b) A network of salt bridges (black dotted lines) and hydrogen bonds (green dashed lines) form at the interaction interface.

Conformational dynamics also play a key role in the interaction between IgE and CD23. Unlike sF $\epsilon$ cRI $\alpha$ , the CD23 head domain has a degree of plasticity: structures of the CD23 head domain demonstrate that the loops involved in binding IgE are dynamic [85], and as illustrated by the stabilising effect of calcium on one of these loops, their plasticity is important for the interaction. Similarly, the conformational variability of IgE-Fc is a crucial aspect of the IgE/CD23 interaction. The C $\epsilon$ 3 domains in the IgE-Fc(3-4):derCD23 (2:1) crystal structures are closer to one another than in the apo IgE-Fc and IgE-Fc(3-4) structures [18, 93]. The various derCD23-bound IgE-Fc(3-4) structures all adopt relatively ‘closed’ conformations compared to apo-IgE-Fc (Figure 1.10), however, the C $\epsilon$ 3-C $\epsilon$ 4 interdomain angles vary, indicating that even when complexed to derCD23, the C $\epsilon$ 3 domains still retain a degree of conformational flexibility [18, 93].

Recently, the crystal structure of full-length IgE-Fc in complex with a single

derCD23 head was solved (Figure 1.12). This structure has not yet been published but it shows that the binding interface is very similar to those described in the crystal structure of IgE-Fc(3-4) bound to derCD23. IgE-Fc remains asymmetrically bent in the presence of the derCD23 molecule, but the C $\epsilon$ 2 domains are slightly more extended than in the apo-structures. The C $\epsilon$ 2 domains fold over onto the chain that is bound to derCD23 and consequently make a close approach to the receptor molecule. Nevertheless, the C $\epsilon$ 2 domain pair does not appear to make significant specific interactions with derCD23, and only a single hydrogen bond forms between derCD23 and the C $\epsilon$ 2 domain of the same chain to which it is bound. As anticipated, the C $\epsilon$ 3 domain to which the derCD23 molecule is bound is in a ‘closed’ conformation, but the unbound C $\epsilon$ 3 domain adopts a more ‘open’ conformation [95]. It is possible that this asymmetry is responsible for a difference observed in the affinity of the binding interaction of the first and second CD23 molecules to IgE-Fc ( $K_{D1} = 1.2 \mu\text{M}$ ,  $K_{D2} = 14.4 \mu\text{M}$ ) as determined by isothermal calorimetry (ITC) [95]. The binding of CD23 to the more ‘open’ C $\epsilon$ 3 domain of IgE-Fc may be responsible for the observed lower affinity component of the interaction, but further research is required to support this hypothesis: at present we are still unable to definitively attribute the different binding affinities to particular CD23 binding sites.

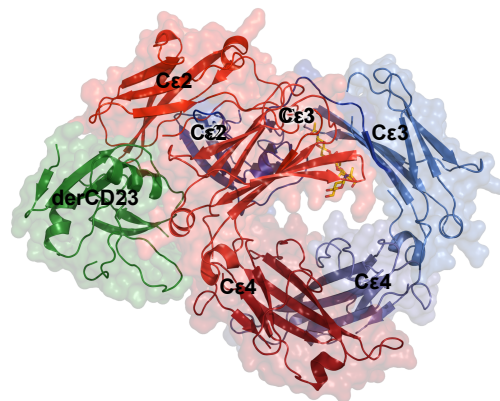


Figure 1.12: **The crystal structure of the derCD23:IgE-Fc 1:1 complex [95].** derCD23 binds an asymmetrically bent conformation of IgE-Fc. derCD23 binds a ‘closed’ C $\epsilon$ 3 domain, but the other C $\epsilon$ 3 domain adopts a more ‘open’ structure. The C $\epsilon$ 2 domain pair is slightly more extended than in crystal structures of apo IgE-Fc.

## 1.3 Allosteric regulation of IgE-Fc interactions

Allostery is the process in which a perturbation by an effector at one site of a biological macromolecule results in a functional change at a distal site, through alterations in conformation and/or dynamics. Allostery has a fundamental role in the regulation of many biological processes, including cell signalling, metabolism and gene regulation [96, 97]. Because allostery is integral to many aspects of biology, its dysregulation can result in disease, however allostery can also be harnessed in the development of therapeutics [98]. Allosteric effectors are diverse: they can be biological molecules such as proteins, lipids and nucleic acids that bind to the allosteric macromolecule, covalent modifications such as phosphorylation and point mutations, and even structural disturbances as a result of changes in the physical environment, for example irradiation and light exposure [98]. It has been suggested that all dynamic proteins are allosteric [99]. IgE-Fc is a highly dynamic protein capable of large scale conformational movements (Section 1.2.1) and it has been shown that IgE-Fc-receptor interactions can be allosterically modulated.

### 1.3.1 Reciprocal allosteric inhibition of IgE-receptor binding

Fc $\epsilon$ RI and CD23 are unable to bind IgE simultaneously [100, 101]. The mutual inhibition of the two IgE receptors may have evolved to prevent the cross-linking of Fc $\epsilon$ RI-bound IgE-Fc on the surface of mast cells and basophils by CD23, which would result in systemic anaphylaxis [4]. Before the receptor binding sites had been mapped, it was suggested that their mutual inhibition was a result of steric overlap [4]. It is now evident, however, that their respective binding sites are spatially distinct and are located at opposite ends of the C $\epsilon$ 3 domains [18]. Consequently the two receptors must be allosteric inhibitors of one another, and comparisons of the structures of IgE-Fc bound to Fc $\epsilon$ RI and IgE-Fc(3-4) bound to CD23 suggest that the rigid-body motion of the C $\epsilon$ 3 domains upon the C $\epsilon$ 4 domains plays an important role in the allosteric mechanism [18]. In the ‘open’ structure of IgE-Fc that is adopted when bound to sFc $\epsilon$ RI $\alpha$ , the CD23 binding sites are partly inaccessible,

and in the ‘closed’ derCD23-bound state, the two FcεRI subsites are incorrectly coordinated for binding (Figure 1.13) [18]. Given the intrinsic flexibility of the Cε3 domain, it is also possible that conformational changes within the receptor-binding domain itself may contribute towards the mutual allosteric exclusion of IgE-Fc receptor binding and may be revealed by additional crystal structures and NMR data.

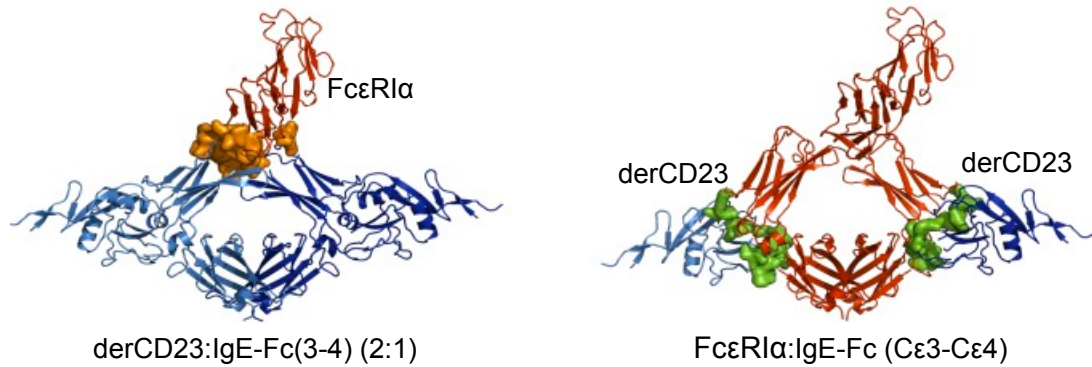


Figure 1.13: **The structural basis for the allosteric and mutual incompatibility of IgE-Fc receptor binding.** Steric clashes (orange) would prevent sFcεRIα binding the ‘closed’ derCD23-bound IgE-Fc(3-4) (PDB: 4EZM). Steric clashes (green) would also prevent derCD23 binding the ‘open’ sFcεRIα-bound IgE-Fc(3-4) (PDB: 1F6A). (Figure taken from Dhaliwal *et al.*, 2012, [18].)

### 1.3.2 Allosteric enhancement of the IgE/FcεRI interaction by the Cε2 domain pair

Crystal structures of apo-IgE-Fc(3-4) show that the molecule can adopt a range of ‘open’ and ‘closed’ conformations [77], whereas the crystal structures of apo IgE-Fc show that the presence of the Cε2 domains limits this dynamism: one of the Cε3 domains adopts an ‘open’ conformation whereas the other adopts a ‘closed’ conformation [86, 72]. The Cε3 domains in the crystal structures of both sFcεRIα:IgE-Fc(3-4) and sFcεRIα:IgE-Fc show that the two Cε3 domains adopt ‘open’ conformations [71, 72]. It has therefore been suggested that the presence of the Cε2 domain pair acts to limit the entropic penalty that is incurred upon binding of FcεRI, which requires both Cε2 domains to adopt ‘open’ conformations [72]. This is supported by thermodynamic data, which suggest that the sFcεRIα/IgE-Fc interaction is entropically driven and has around a 20 fold slower off-rate than the



enthalpically driven interaction between sFcεRIα and IgE-Fc(3-4) [83, 72]. Because the Cε2 domain pair of IgE is not directly involved in the interaction between IgE-Fc and FcεRI, but functions to increase the affinity of the interaction, the domain pair can be thought of as an allosteric enhancer of the IgE/FcεRI interaction. Whereas reciprocal allosteric inhibition of receptor binding is thought principally to be the result of conformational changes, here the allosteric mechanism appears to be largely driven by changes in dynamics.

### 1.3.3 Allosteric inhibition of the IgE/FcεRI interaction by aεFab1

The anti-IgE Fab fragment, aεFab1, was produced by phage display technology in an effort to find Fabs that block FcεRI binding. aεFab1 binds IgE-Fc with a 2:1 stoichiometry ( $K_{D1} = 76$  nM,  $K_{D2} = 1.5$  μM), each aεFab1 molecule binds predominantly to a single IgE-Fc chain, and each binding interface is centred on the Cε3 domain (Figure 1.14.a) [81]. As described earlier, the crystal structure of the aεFab1:IgE-Fc (2:1) complex demonstrated that IgE-Fc is capable of undergoing a remarkable conformational change (Section 1.2.1). In the structure, the Cε2 domains have extended from the asymmetrically bent conformation (observed for apo-IgE-Fc) so that there is a complete loss of contacts between the Cε2 domain pair and the Cε3-Cε4 domains. ITC analysis indicated that both aεFab1 binding sites on IgE-Fc are occupied in solution and intermolecular FRET studies indicated that the binding of both aεFab1 molecules also results in an extended conformation in solution [81]. Moreover, the Cε3 domains in the crystal structure of the complex are both in ‘open’ conformations and even further apart from each other than in the crystal structures of IgE-Fc bound to sFcεRIα. The Cε4 domains, however, appear unchanged.

aεFab1 acts as an allosteric inhibitor of IgE/FcεRI interaction: the conformational changes associated with the binding of the Fab are incompatible with the binding of the receptor. The extension of the Cε2 domain pair is accompanied by a significant shift in the linker region that joins the Cε2 and Cε3 domains (Figure 1.14) [81]. Arg334, which forms important salt-bridges with FcεRI is located in the

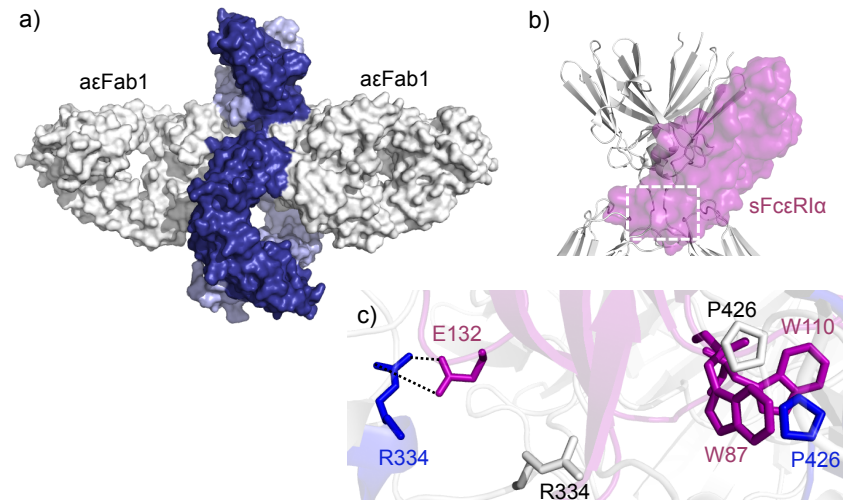


Figure 1.14: **αεFab1 allosterically inhibits the IgE/FcεRI interaction.** (a) The crystal structure of IgE-Fc (blue) bound to two molecules of αεFab1 (white) in surface representation (PDB: 4J4P [81]). αεFab1 binds to an extended conformation of IgE-Fc, in which the newly adopted position of the Cε2 domains blocks binding of FcεRI. (b) The crystal structure of the IgE-Fc:sFcεRIα complex (PDB: 2Y7Q, [72]) was aligned to the crystal structure of the αεFab1 complex upon the Cε4 domain pair, and shows that sFcεRIα (purple representation) overlaps with the Cε2 domains of αεFab1-bound IgE-Fc (white cartoon representation). Cε2 domain extension also causes conformational changes in the Cε2-Cε3 linker region (white dashed box) of IgE-Fc, which shifts key residues involved in the IgE-Fc/sFcεRIα interaction. (c) R334 is positioned in the linker region of IgE-Fc and forms salt bridges (black dotted lines) with E132 of sFcεRIα (purple) in the IgE-Fc:sFcεRIα complex (Fc of this complex in blue). In αεFab1-bound IgE-Fc (white) R334 is significantly shifted such that it can no longer form salt-bridges with E132. Furthermore, P426 (blue), is packed between two tryptophans of FcεRI in the IgE-Fc:sFcεRIα complex, but a shift in the position of P426 in αεFab1-bound IgE-Fc (white) prevents these stabilising interactions.

linker region, and accordingly when binding αεFab1, this salt-bridge cannot form. Additionally, the proline residue involved in the stacking interactions at subsite 2 of the IgE-Fc/FcεRI interaction interface (Figure 1.9) is shifted by 6 Å upon the binding of αεFab1 (Figure 1.14.c). Even if these perturbations were not sufficient to prevent the binding of FcεRI, the extended Cε2 domain pair blocks the FcεRI binding site, and the further opening of the Cε3 domains prevents optimal engagement of both subsites on IgE-Fc by FcεRI (Figure 1.14.b) [81]. Presumably the ‘open’ conformation of αεFab1-bound IgE-Fc would prevent binding of CD23, which binds a relatively closed conformation of IgE-Fc, however this has not yet been investigated.

### 1.3.4 Allosteric inhibition of the IgE/Fc $\epsilon$ RI interaction by Xolair

The clinical benefits of Xolair in the treatment of asthma are well recognised and have been attributed to its ability to inhibit the interactions between IgE-Fc and its receptors [53, 102, 103]. In particular, Xolair is thought to function by binding to IgE in the serum and preventing it from binding to Fc $\epsilon$ RI on the surface of mast cells and basophils [104, 105]. It has been shown that Xolair binds to IgE with a 2:1 stoichiometry and through a combination of peptide inhibition and molecular modeling its binding site has been mapped to the C $\epsilon$ 3 domains of IgE, which also bind the receptors [106, 105]. Difficulties in crystallisation of the the IgE-Fc:Xolair Fab complex have lead to a delay in our structural understanding of Xolair's mechanism of action [107]. Very recently, two crystal structures of different IgE-Fc:Xolair Fab complexes have been solved (Figure 1.15). One structure is of Xolair Fab bound to a constrained IgE-Fc(3-4) construct held in a 'closed' conformation with limited C $\epsilon$ 3 conformational freedom [108], the other is of a mutant Xolair Fab (called Xolair Fab mutant 3, containing three non-CDR mutations, designed to disrupt Fab-only crystal packing) bound to IgE-Fc [82].

The Xolair:IgE-Fc binding interface is similar in both crystal structures, and partly agrees with the previously determined binding site mapping data [106]. One molecule of Xolair binds to a single C $\epsilon$ 3 domain and its binding site is centred between the Fc $\epsilon$ RI and CD23 binding sites [108]. Comparisons of the crystal structures with the structures of IgE-Fc(3-4):derCD23 complexes show that the Xolair and CD23 binding sites coincide and there is also substantial steric overlap (Figure 1.15).

Whereas the data clearly suggests that Xolair acts as an orthosteric inhibitor of the IgE/CD23 interaction, there is some ambiguity about how Xolair inhibits Fc $\epsilon$ RI binding. In both Xolair complexes, the Xolair binding site does not encroach upon the Fc $\epsilon$ RI binding site and as such Xolair does not inhibit binding of the receptor to IgE-Fc by engaging the same residues. Pennington *et al.* suggest that the binding of Xolair has no substantial effect on the conformation of the residues at the Fc $\epsilon$ RI binding site, and instead suggest that Fc $\epsilon$ RI cannot bind Xolair-bound

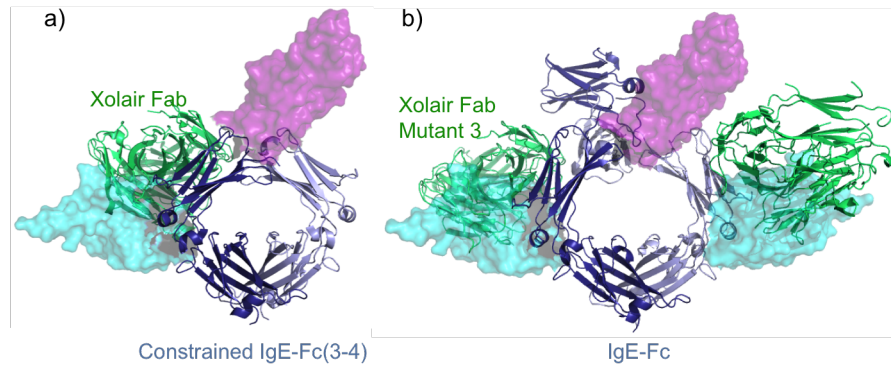


Figure 1.15: **Crystal structures of Xolair Fab:IgE-Fc complexes demonstrate that Xolair binds to a site in the Cε3 domain that is between the two receptor binding sites. Xolair sterically blocks CD23 binding but the Xolair binding site does not overlap with the FcεRI binding site.** (a) The crystal structure of Xolair Fab bound to a constrained IgE-Fc(3-4) construct held in ‘closed’ state (PDB: 5HYS [108]). (b) The crystal structure of Xolair Fab Mutant 3 bound to IgE-Fc with a 2:1 stoichiometry [82]. The crystal structure of IgE-Fc(3-4):derCD23 (PDB: 4EZM [18]) and the crystal structure of IgE-Fc:sFcεRIα (PDB: 2Y7Q, [72]) were aligned by the Cε4 domains to the Xolair Fab complex structures. The resulting placement of the derCD23 (green) and sFcεRIα (purple) are shown in surface representations.

IgE-Fc because of atomic overlap [108]. Davies *et al.*, however, suggest that Xolair acts allosterically to prevent the binding of FcεRI to IgE-Fc [82].

The structure produced by Davies *et al.* is of a Xolair Fab construct binding to full length, unconstrained IgE-Fc, and consequently can report on conformational changes that may occur in the whole of IgE-Fc upon Xolair binding. The crystal structure demonstrates that Xolair Fab mutant 3 (αεFabXol3) binds to a partially extended conformation of IgE-Fc, with its Cε3 domains further apart from each other than in any structure of IgE-Fc published to date. In this extremely ‘open’ conformation FcεRI would be unable to simultaneously coordinate both subsites required for binding to IgE-Fc (Figure 1.16) [82].

Time resolved fluorescent resonance energy transfer (TR-FRET) studies showed that both the apparent affinity (given by  $K_D$ ) and the number of available binding site (given by  $B_{max}$ ) for the interaction between IgE-Fc and sFcεRIα were reduced in the presence of increasing concentrations of αεFabXol3. Whereas a reduction in the apparent affinity can be the result of orthosteric or allosteric inhibition, a reduction in the available binding sites is generally indicative of allosteric inhibition.

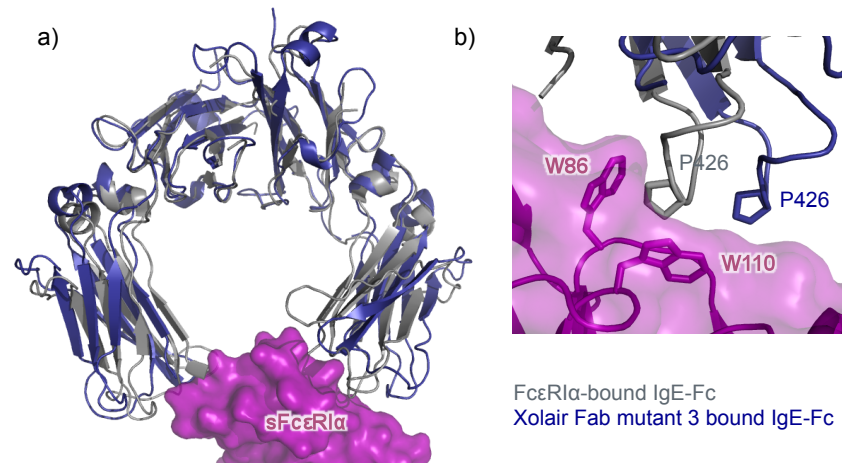


Figure 1.16:  $\alpha\epsilon$ FabXol3 allosterically disrupts the interaction between IgE-Fc and Fc $\epsilon$ RI $\alpha$  (a) The crystal structure of the IgE-Fc: $\alpha\epsilon$ FabXol3 complex [82] indicates that when IgE-Fc binds  $\alpha\epsilon$ FabXol3 it adopts a very ‘open’ conformation (grey cartoon representation). sFc $\epsilon$ RI $\alpha$  (purple surface representation) binds a conformation of IgE-Fc in which the C $\epsilon$ 3 domains are closer together (blue cartoon representation). In the more ‘open’  $\alpha\epsilon$ FabXol3-bound structure, subsites 1 and 2 are too far apart for simultaneous engagement by Fc $\epsilon$ RI. The structure of IgE-Fc in complex with sFc $\epsilon$ RI (PDB: 2Y7Q [72]) was superposed onto the  $\alpha\epsilon$ FabXol3-bound structure upon the C $\epsilon$ 4 domains. (b) A substantial displacement of Pro426 in the  $\alpha\epsilon$ FabXol3-bound structure moves the residue out from between two sFc $\epsilon$ RI $\alpha$  tryptophans that usually provide stabilising contacts at subsite 2.

Although the crystal structure of IgE-Fc bound to  $\alpha\epsilon$ FabXol3 does not provide evidence that the Xolair construct acts sterically to block Fc $\epsilon$ RI binding, it does not rule it out. Consequently Davies *et al.* suggest that although it is possible that Xolair acts as a steric inhibitor of interaction between IgE-Fc and Fc $\epsilon$ RI, Xolair elicits its effect on the interaction predominately through allosteric processes.

### 1.3.5 Accelerated dissociation of IgE-Fc:Fc $\epsilon$ RI complexes

In 2012 Kim *et al.* published a paper demonstrating that a designed ankyrin repeat protein (DARPin E2\_79) not only inhibited binding of free IgE to Fc $\epsilon$ RI but also actively disrupted pre-formed IgE:Fc $\epsilon$ RI complexes *in vitro* [109]. Later it was shown that DARPin E2\_79 could also accelerate the dissociation of IgE:receptor complexes on the surface of human allergic effector cells both *ex vivo* and *in vivo* [110]. Furthermore, it has been shown that Xolair can also facilitate dissociation of Fc $\epsilon$ RI-bound IgE, although only at very high concentrations that are substantially greater than therapeutic doses [110]. SPR experiments performed by Davies *et*

*al.* demonstrated that aεFabXol3 can accelerate the dissociation of IgE-Fc from sFcεRIα, immobilised on a SPR sensor surface, with greater efficiency than either full-length Xolair antibody or Xolair Fab [82]. The group also showed that the occupation of both Xolair binding sites is required for mediating accelerated dissociation.

Because IgE-Fc binds FcεRI on the surface of mast cells and basophils with unusually high affinity, and because of the exceptionally slow off-rate of the interaction [14, 15], mast cells in allergic individuals are almost always sensitised, and cross-linking of IgE on their surface instantly triggers immediate hypersensitivity allergic reactions [4]. Consequently, understanding mechanisms that cause accelerated dissociation of IgE:FcεRIα complexes could provide exciting insights into a new therapeutic approach that reduces the lifetime of IgE:FcεRI complexes on the surface of cells that mediate allergic disease.

The mechanisms by which Xolair and DARPin E2.79 mediate the accelerated dissociation of IgE/FcεRI complexes have been studied using structural and kinetic data from SPR experiments [109, 110, 108, 82]. The structure of DARPin E2.79 bound to a constrained IgE-Fc(3-4) construct locked in the ‘closed’ conformation showed the DARPin bound to IgE-Fc with a 2:1 stoichiometry and that each DARPin bound a separate Cε3 domain [109]. The two DARPin molecules bind to non-equivalent binding sites on Cε3; one DARPin molecule is distant from FcεRI binding site, whereas the other molecule is thought to partially overlap with FcεRI. Although the crystal structure indicated little about the mechanism of DARPin E2.79-mediated accelerated dissociation, a study of the binding kinetics suggested that it occurred through the molecular process of facilitated dissociation [109].

Facilitated dissociation is the consequence of competition between the effector and the ligand for attachment points within a ligand binding site, which become partially exposed during the natural complex dissociation process [109]. Based on the complex of Xolair Fab bound to a constrained IgE-Fc(3-4) construct, Pennington *et al.* suggest that Xolair also accelerates the dissociation of IgE-Fc:FcεRI complexes through the process of facilitated dissociation [108]. They propose that the lower disruptive capacity of Xolair compared to DARPin E2.79 is the result

of a larger degree of spatial-overlap with IgE-bound Fc $\epsilon$ RI, which would reduce Xolair's ability to access attachment points during the dissociation process [108].

SPR studies demonstrate that a $\epsilon$ FabXol3 can bind IgE-Fc:Fc $\epsilon$ RI $\alpha$  complexes with almost the same affinity that it binds uncomplexed IgE-Fc, but that only 10 % of the a $\epsilon$ FabXol3 binding sites are available on the IgE-Fc:sFc $\epsilon$ RI $\alpha$  complex. Consequently, Davies *et al.* suggest that Xolair-mediated accelerated dissociation of IgE:Fc $\epsilon$ RI complexes occurs via allosteric processes [82].

## 1.4 The ensemble model allostery

Historically two main models have been used to describe allosteric processes, the sequential model (KNF model) posited by Koshland Némethy and Filmer, and the concerted model (MWC model) put forward by Monod, Wyman and Changeux [111]. Both models interpret allostery in terms of conformational changes that occur between two functional states ('T' and 'R') of a macromolecule upon binding of an allosteric modulator, and initially described these changes in oligomeric proteins. The MWC model proposed that the binding of an allosteric modulator to a macromolecule shifts the pre-existing equilibrium of the 'T' and 'R' states in such a way that the symmetry of the oligomer is conserved [112]. The KNF model, however suggested that the binding of an allosteric effector induces conformational changes in the macromolecule between 'T' and 'R' states (Figure 1.17) [113]. Both models allow for a description of positive cooperativity - where the binding of ligand to a macromolecule increases the affinity of further ligand binding sites, but only the KNF model allows for a description of negative cooperativity - where the binding of a ligand to a macromolecule decreases the affinity of further ligand binding sites. This difference lies in the fact that the MWC model insists that conformational changes of subunits are concerted: if ligand binds and stabilises the 'R' state of a protein, each subunit (and therefore each binding site) must be in the 'R' state.

Both the MWC and KNF these models have been used to describe allosteric systems [114] and were initially proposed to describe the cooperative binding of oxygen to haemoglobin [112, 113]. The landmark X-ray crystallographic studies of deoxy-haemoglobin ('T' state) and oxy-haemoglobin ('R' state) by Perutz led

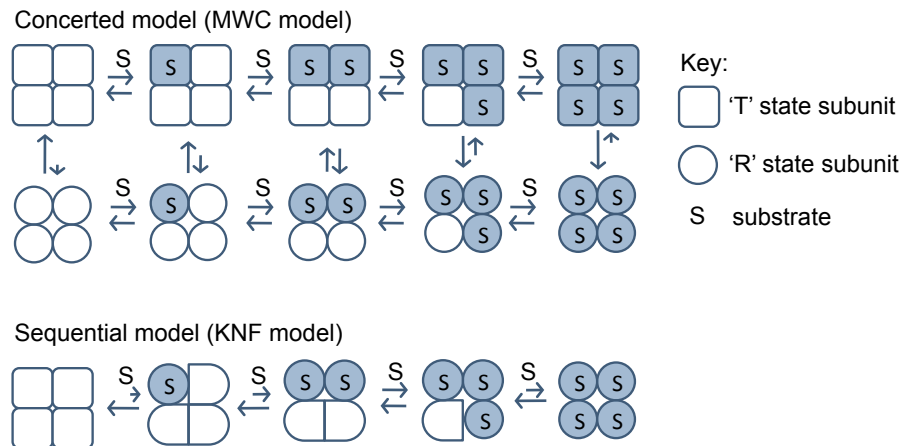


Figure 1.17: **The concerted and sequential models of allostery.** These models propose that in an allosteric oligomer, made of symmetrically related subunits, the subunits exist in equilibrium between tensed ‘T’ states and relaxed ‘R’ states. A substrate can bind both ‘T’ and ‘R’ states, but has different affinities for the distinct conformations. In this example the substrate has a greater affinity for the ‘R’ state. The binding of an effector shifts the equilibrium either one way or the other, depending on whether it acts an inhibitor or enhancer of substrate binding. Here, it is the substrate itself that acts as an enhancer of further substrate binding. In the concerted model, the symmetry of the oligomer must be maintained and consequently a change in conformation is simultaneously conferred to symmetrically related subunits [112]. In the sequential model, the subunits are not connected to the same extent, instead changes in conformation of the different subunits occur sequentially through an induced fit [113].

to the first structural description of allostery in the context of the MWC model (Figure 1.18) [115], which for decades remained the paradigm for studying allostery. In 1992, however, two papers were published that questioned the legitimacy of a two-state structure-based description of allostery in haemoglobin. Silva and co-workers published the structure of an alternative ‘R’ state structure of haemoglobin, showing that the molecule is capable of existing in more than two-states [116]. Additionally, Colombo *et al.* published thermodynamic data that suggested the the ‘T’ to ‘R’ state transition must be accompanied by the preferential binding of 60 water molecules to the ‘R’ state, which could not be determined from the crystal structure [117].

Recent advances in techniques that probe protein structural dynamics and thermodynamics such as NMR, have cast further doubt on the ability of two-state structural-based models to accurately describe allostery [111]. It is now well established that proteins are dynamic entities that experience thermal fluctuations,



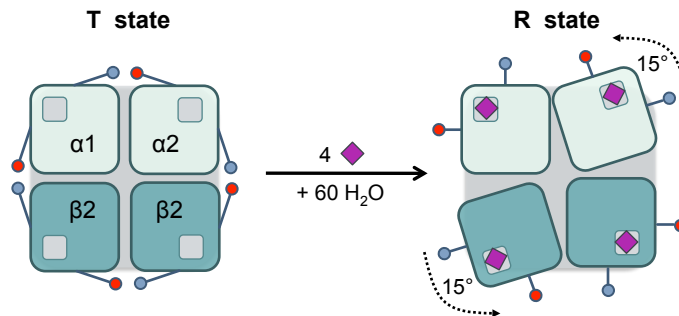


Figure 1.18: **The MWC/Perutz model for the cooperative transition from ‘T’ state to ‘R’ state haemoglobin.** Tetrameric haemoglobin can be considered as a dimer of  $\alpha\beta$  dimers. Each subunit has their own heme group (grey boxes). Perutz suggested that the salt bridges between positively charged residues (blue circles) and negatively charged residues (red circles) hold haemoglobin in the ‘T’ conformation. The binding of oxygen (purple diamonds) is accompanied by a  $15^\circ$  turn in one dimer relative to the other, which releases the salt bridges, resulting in the ‘R’ conformation [115]. Perutz hypothesised that ‘T’ state has a lower affinity for oxygen compared to the ‘R’ state because of strain in the heme moiety [115]. Even decades after Perutz proposed this model, however, no structural feature has actually been identified that has sufficient energy to account for the observed level of oxygen binding cooperativity [118], and it has been demonstrated that thermodynamic appreciation of the whole system is necessary: without additional solvation of the ‘R’ state it is unlikely it would even exist [117].

respond to their environment and are capable of undergoing conformational rearrangements on a variety of scales [119, 120, 121, 122]. Since protein structure and function are tightly coupled, it is reasonable to assume that allosteric processes in dynamic molecules may not be described completely by the differences between only one main ‘T’ state and one main ‘R’ state [123]. Furthermore, there are reports of allostery occurring in macromolecules without an obvious change in structure, where allostery is instead manifested through changes in entropy [124, 125, 126, 111]. This form of ‘dynamic allostery’ was first proposed by Cooper and Dryden in 1984 and suggests that changes in the frequency and amplitudes of thermal fluctuations that occur upon binding of an allosteric effector can result in either a positive or negative contribution to the entropy of ligand binding [127].

Over the years various other models have been used to describe allostery including those that use statistical and thermodynamic approaches [128]. In recent years there has been a revolution in the way we approach allostery: a new unifying model was proposed which, unlike previous models, encompasses thermodynamics, the

dynamic behaviour of proteins, and structural considerations in the context of allostery. The ensemble model of allostery, as it has come to be named, is also able to explain how the same allosteric modulator may have different, or even completely opposing, effects under distinct sets of conditions [123].

### 1.4.1 The ensemble model of allostery

Proteins are dynamic and exist as conformational ensembles that include the many different states that a protein may adopt, including the native state, folding intermediates, numerous active functional states and different inactive functional states [120, 121, 129]. Depending on the intrinsic dynamics of a protein, these different conformations may be very closely linked or they may be relatively diverse in their form [98]. The different conformations of a protein have distinct energies and are described by the protein's free-energy landscape under a certain set of conditions [129]. The free-energy landscape of a protein is dependent on its inherent physiochemical properties in its environment [98]. The energy minima in a free-energy landscape represent the possible conformations that a protein can adopt, the depth of a minimum represents the stability of that conformer and the breadth represents the entropic spread of that state [129]. The populations of the different conformations are distributed according to statistical thermodynamics, such that the lowest energy conformations are the most occupied. A protein's function is not simply described by the most populated state, but is the collective and weighted outcome of the conformational ensemble [98].

Moving between the different conformations requires 'climbing' over the energy barrier between the different states, and how long a protein spends in a certain conformation depends upon the height of the energy barrier. Changes in the environment of a protein can cause a change in the free-energy landscape and results in the redistribution of conformational populations. In the ensemble model of allostery, allosteric modulators acting at a site distal to the functional site of a protein, act to change the functionality of the protein not by creating new conformations, but by stabilising certain conformations and thereby redistributing the populations of the conformational ensemble (Figure 1.19). For example, a protein may adopt a

number of conformations that are functionally ‘on’ and others that are ‘off’. In the absence of an allosteric inhibitor, the weighting of the conformations favours those in the ‘on’ state, resulting in a functional activity. The binding of an allosteric inhibitor, however may stabilise certain conformers but not others, reshaping the energy landscape in such a way that the ‘off’ states become more populated and the protein’s functionality decreases. The level of reduction in protein function is dependent upon the relative stabilisation of ‘off’ states to ‘on’ states in the presence of the allosteric inhibitor, and consequently the effects of allosteric modulators can be subtler than the binary switch provided by orthosteric inhibitors. Furthermore, the relative stabilisation of different states by allosteric effectors depends upon the initial distribution of molecules in the free energy landscape, which can be distinct under different environmental conditions. Accordingly, under different sets of conditions (e.g. temperature, pH, presence of other effectors) the effects of allosteric modulators can be altered, allowing the fine-tuning of regulatory systems [123, 130, 98, 111].

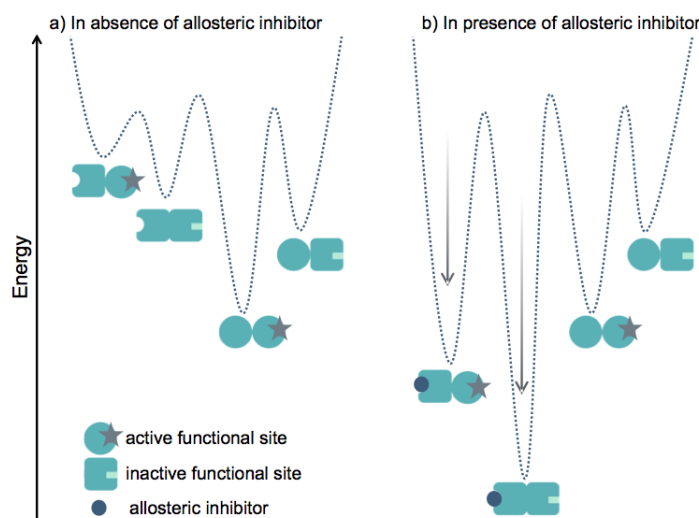


Figure 1.19: **A schematic representation of the ensemble model of allostery.** Proteins are dynamic and exist as an ensemble of conformations. The free energy diagrams here represent the different energies of the distinct conformations of a protein (a) before and (b) after binding of an allosteric inhibitor. The protein has an effector subunit that binds the inhibitor and a functional subunit at a distal site. Both subunits can exist in active and inactive conformations. Binding of the inhibitor to active effector subunits stabilises certain conformations (arrows). The resulting shift in the free-energy landscape leads to an increase in the population of inactive functional subunits. Consequently, the overall effect of the shift is negative in terms of the functionality of the protein.

The ensemble model has been useful in understanding allostery in various different systems including those where multiple conformations are involved in the allosteric process, and in those where conformational changes are mediated through dynamic fluctuations rather than conformational perturbations [130]. The allosteric cooperation of ligand binding to cAMP-dependent protein kinase (cAPK) is a good example of the former. cAMP catalyses the phosphorylation of various proteins, consequently altering their specific cellular activities. In order to catalyse phosphoryl transfer cAPK must first bind adenosine and its peptide substrate. The binding of adenosine to cAPK results in a 3 - 4 fold increase in the affinity in the interaction of cAPK with its substrate, and similarly the binding to protein substrate to cAPK increases the affinity of adenosine/cAPK interaction [125].

X-ray crystallography has revealed that cAPK exists in at least three distinct conformations that differ in the relation of the large and small lobes of the protein [131, 132]. An ‘open conformation’ refers to apo-cAPK, the ‘intermediate conformation’ refers to cAPK bound to either adenosine or peptide substrate, and the ‘closed conformation’ is bound to both adenosine and substrate (Figure 1.20) [131, 133, 132, 134]. According to the ensemble model of allostery, free cAPK largely populates the ‘open conformation’, but binding of adenosine (or peptide substrate) to apo-cAPK causes a shift in the free energy landscape that favours the population of the ‘intermediate conformation’. The ‘intermediate conformation’ has a higher affinity for peptide substrate (or adenosine) than the ‘open conformation’. The subsequent binding of the peptide substrate (or adenosine) stabilise the ‘closed conformation’ and consequently results in a redistribution of the cAPK population, such that the enzymatically active ‘closed conformation’ is the most populated state (Figure 1.20) [135, 98]. Although the conformational changes observed in the crystal structures are clearly important in understanding the cooperative binding of its two ligands, NMR and molecular dynamic simulations indicate that entropic changes that occur on binding peptide or adenosine also contribute to the observed cooperativity in cAPK [125].

When a ligand binds to a protein it affects both its thermodynamic and dynamic properties [98]. Changes in the amplitude and frequency of protein motions affect the entropic spread of a conformational minimum, and thereby changes the width of

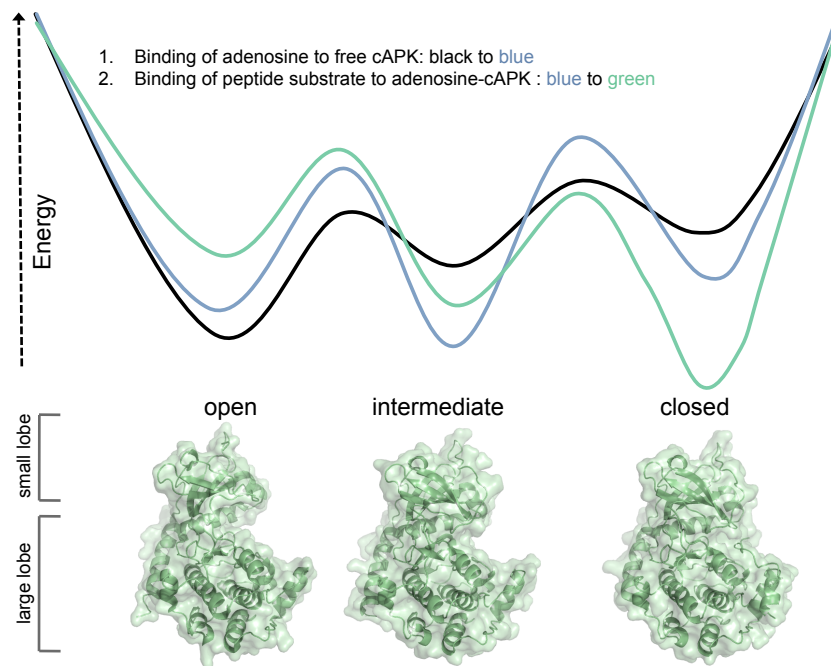


Figure 1.20: **An ensemble description of the allosteric cooperativity of substrate binding to cyclic to cAMP-dependent protein kinase (cAPK).** cAPK exists as an ‘open conformation’ (apo structure, PDB: 1J3H [134]), an ‘intermediate conformation’ (adenosine-bound (adenosine-5’-monophosphate), PDB: 1BKX [132]) and a ‘closed’ conformation (adenosine (adenoside-5’-triphosphate) and peptide-bound, PDB: 1ATP [131]). The binding of adenosine to cAPK causes a population shift in the free energy landscape in favour of the intermediate conformation, which has a greater affinity for peptide substrate. The binding of peptide substrate stabilises the ‘closed’ conformation required for phosphoryl transfer activity [98].

the free energy basin without affecting its position (Figure 1.21) [136]. The binding of cyclic adenosine monophosphate (cAMP) to catabolite activator protein (CAP) is negatively cooperative, and it was the first allosteric process to be explained almost entirely in terms of changes in entropy. CAP is a homodimeric transcription factor composed of a DNA binding domain and a substrate binding domain. The substrate binding domain binds to two molecules of cAMP, and the binding of the two cAMP is negatively cooperative. The crystal structures of the substrate binding domain in the apo state ( $\text{CAP}^{\text{N}}$ ), the singly liganded state ( $\text{cAMP1-CAP}^{\text{N}}$ ) and the doubly-bound state ( $\text{cAMP2-CAP}^{\text{N}}$ ) indicate that the binding of the first molecule of cAMP has no significant effect on the binding-site of the second cAMP molecule. NMR analysis of backbone dynamics, however, suggests that the binding of the first ligand increases the dynamics of the protein, and thermodynamic analysis using

ITC indicates the negative cooperativity is entropically driven. It is proposed that the binding of the first cAMP molecule increases entropy of CAP<sup>N</sup>, thereby increasing the entropic penalty incurred upon binding of the second cAMP molecule [124]. Molecular dynamic simulations have also provided data supporting the role of entropy in the negative cooperativity of cAMP binding in CAP, however, the simulations also suggested that side chain movements at the cAMP binding pocket and the protomer-protomer interface also contribute to the mechanism of negative allostery [137]. Since this initial demonstration of dynamic allostery many other examples of entropically driven allostery have been described [138, 125, 126, 111, 139], including the allosteric enhancement of the IgE-Fc/FcεRI interaction by the Cε2 domain pair (Section 1.3.2).

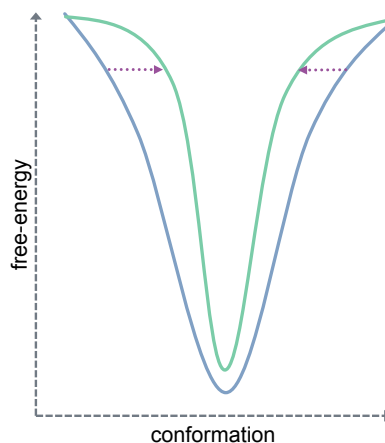


Figure 1.21: **A change in entropy upon binding a ligand alters the width of the free-energy basin without affecting its position.** The conformation of a protein under given conditions is represented as a minimum in a free-energy landscape. The depth of the minimum corresponds to its free-energy and therefore its stability, whereas its width indicates the level of conformational spread (or entropy). If binding of a ligand to a particular conformation of a protein (blue minimum) decreases the amplitude and frequency of its thermal fluctuations then the entropic spread of the conformation reduces (purple dotted arrows), and consequently the width of the energy minimum decreases, but not its position (green minimum).

### 1.4.2 The ensemble model of allostery and IgE

As described in Section 1.2.1, IgE-Fc is a dynamic molecule: it can ‘open’ and ‘close’, and ‘bend’ and ‘extend’ to varying degrees, and IgE-Fc’s conformational

flexibility has a considerable impact on how it interacts with its receptors (Section 1.2). Additionally, binding of various anti-IgE proteins distal to the receptor binding sites have been shown to stabilise certain conformers of IgE with altered affinities for FcεRI and CD23 (Section 1.3). In this way, the allosteric regulation of IgE-receptor interactions fits inside the framework of an ensemble model of allostery - it is consistent with a model whereby allosteric modulation is the consequence of perturbing the distribution of IgE ensemble states, in which ‘open’ and ‘closed’, and ‘bent’ and ‘extended’ conformations are the extremes. Accordingly, if we are to gain a deeper understanding of the allosteric regulation of IgE-receptor binding it will be necessary to achieve a wider appreciation of the conformations that IgE-Fc can adopt, the energy barriers between them, and their relative receptor affinities under well-defined conditions.

Because NMR spectroscopy can provide information about the structure, dynamics and thermodynamics of a protein at atomic detail, it has played a major role in understanding conformational ensembles of proteins and the dynamic changes coupled to allostery [140, 111, 141]. Relaxation dispersion techniques can describe conformational heterogeneity and transitions between different conformational states, and residual dipolar couplings and magnetization transfer techniques can be used to characterise dynamic processes on a range of timescales [141]. NMR spectroscopy could therefore provide a wealth of information about the ensemble nature of IgE-Fc and the dynamic changes that occur upon binding allosteric modulators. Significant amounts of isotopically-labeled protein are required to investigate protein dynamics using NMR spectroscopy. IgE-Fc is produced in mammalian or insect cell-lines that allow correct disulphide bond formation and glycosylation [142]. Isotopic labelling, however, is usually performed in a bacterial or cell-free system [143], and to date there have been no reports of the successful generation of functional IgE-Fc in either system. Production of isotopically-labeled IgE-Fc is a major hurdle in the investigation of the structural and dynamic properties of IgE-Fc using NMR spectroscopy, and currently no NMR data has been published for IgE-Fc.

Multi-dimensional NMR experiments are most commonly performed on proteins that have been uniformly labelled with  $^{15}\text{N}$  and  $^{13}\text{C}$ . Uniform labeling in

large proteins can generate very complex NMR signals. Signal complexity can be reduced by labeling only certain amino acids, which then act as site-specific probes. Site-specific labeling has been useful in investigating ligand interactions and conformational changes of relatively large proteins by NMR and could be a further option for NMR studies of IgE-Fc (75 kDa) [144].

Generally, X-ray crystallography produces a static structure of a protein that is an average of its dynamic, heterogeneous ensemble within a crystal. Consequently, X-ray crystallography provides a snapshot representation of the most populated state under certain conditions, which for the most part cannot be deconvoluted to determine ensemble properties of a protein [145]. It is possible, however, to trap transiently populated conformations of a protein through ligand stabilisation: an extended, open conformation of IgE-Fc was trapped, for example, by  $\alpha$ εFab1. Using this approach it may be possible to gain a greater understanding of IgE-Fc's conformational ensemble. As demonstrated in the studies of  $\alpha$ εFab1 [81] and  $\alpha$ εFabXol3 [82], crystal structures of anti-IgE Fab:IgE-Fc complexes, in combination with solution-based binding studies, can help understand allosteric regulation of IgE-Fc/receptor interactions.

## 1.5 Rationale

The dynamic behaviour of IgE-Fc's conformational ensemble is instrumental in the IgE/receptor interactions (Section 1.2), which are fundamental to the mechanisms of allergic disease (Section 1.1.1). Understanding the conformational versatility of IgE-Fc is therefore crucial to understanding its immunological role. IgE-Fc has evolved a dynamic structure that, through allostery, allows it to separate the functionality of its two different receptors (Section 1.3.5), and to bind its FcεRI receptor with an affinity unparalleled by any other antibody/receptor interaction (Section 1.2.2). By learning about the dynamic conformational ensemble of IgE-Fc we can understand more about IgE's function in immunology, as well as how we can exploit it in the design of therapeutics that target the IgE/receptor interactions.

Allosteric drugs have several main advantages over orthosteric drugs that target the functional site of the protein. One such advantage is their specificity: allosteric



modulators do not bind to the the functional sites of proteins, which are generally more conserved than other parts of the protein, and are usually highly conserved in proteins of the same family [98]. Moreover, because allosteric drugs work by shifting the distribution of equilibrium conformations, their binding can simultaneously effect multiple functionalities, and in the case of inhibitors, they allow modulation of function rather than only providing total elimination of function [98]. Allosteric inhibitors are also an interesting and exciting proposition in the design of small molecules that target protein-protein interactions PPIs. Because of their size, small molecule inhibitors are poorly equipped to disrupt the large surface interfaces of PPIs sterically (Section 1.1.2), the size of an allosteric molecule, however, does not affect its ability to inhibit PPIs allosterically. Understanding more about allosteric sites and mechanisms of IgE could therefore provide insights useful in the development of novel therapeutics for asthma and allergy. Furthermore, the accelerated dissociation of IgE/Fc $\epsilon$ RI complexes (Section 1.3.5), indicates that modulators can destabilise the very tight interaction between IgE and Fc $\epsilon$ RI on the surface of effector cells, which is responsible for long-term sensitization to allergen and the immediacy of allergic interactions (Section 1.2.2). Accelerating the dissociation of IgE/Fc $\epsilon$ RI complexes could be a new way to target allergic disease therapeutically, and understanding the potentially allosteric mechanisms of this process is therefore of great interest.

It is only in recent years that we have started to uncover the extent of IgE-Fc's conformational dynamism, and only in the very recent past have we learnt that IgE-Fc can adopt extended conformations (Section 1.2.1). Much remains to be learnt about the conformational ensemble of IgE-Fc and how it relates to the functions of IgE. Rigid-body domain movements in IgE-Fc have been shown to result in a range of 'open', 'closed', 'bent' and 'extended' conformations that have different affinities for Fc $\epsilon$ RI and CD23 (Section 1.2). There is also some suggestion that intradomain movements within the intrinsically dynamic C $\epsilon$ 3 domain may also contribute towards changes in receptor-binding (Section 1.2.2). The conformational ensemble of IgE-Fc is likely to include numerous other IgE-Fc conformers that, when increasingly populated, affect receptor binding activity. Other conformations of IgE-Fc may be 'open' or 'extended' to varying degrees, or they could indicate

the existence of different rigid-body motions that have not yet been described in IgE. Additionally, a greater description of the conformational ensemble could uncover dynamic processes on a smaller scale, such as backbone and side-chain dynamics that affect IgE/receptor interactions. In addition to understanding more about the conformational ensemble itself, questions remain about how to target it allosterically: how can we stabilise conformations in order to modulate a certain receptor-binding functionality?

When significant amounts of a isotopically-labeled IgE-Fc have been produced, NMR spectroscopy will reveal much about the conformational ensemble of IgE-Fc and its dynamic properties. Until then, there is still a lot that can be learnt through molecular dynamic simulations and X-ray crystallography. The crystal structure of  $\alpha$ Fab1-bound IgE-Fc revealed an unexpected IgE-Fc conformation and revealed a novel strategy of allosteric inhibition of IgE/receptor interaction (Section 1.3.3). Based upon the success of the  $\alpha$ Fab1 project, King's and UCB are working in collaboration to generate a whole panel of  $\alpha$ Fabs that trap IgE-Fc in a variety of transiently populated conformations. We will use UCB's new antibody discovery platform [146, 147, 148] to screen the immune repertoires of rabbits immunised against IgE in order to find antibodies that bind to IgE-Fc and thereby affect IgE/receptor interactions. This project will involve screening for antibodies that affect the IgE-Fc/CD23 interaction. Through the biophysical and structural characterisation of the  $\alpha$ Fab/IgE-Fc interactions we hope to learn more about the different conformations that IgE-Fc can adopt, how they relate to different receptor-binding activities and accordingly gain a greater comprehension of allostery in IgE-Fc.

Herein we describe the discovery and biophysical characterisation of antibodies selected for their ability to alter the CD23/IgE interaction. Using SPR and cell-binding assays we investigated how the selected  $\alpha$ Fabs affect the binding of CD23 to IgE, and determine if they work allosterically. Ultimately, with structural data, we aim to understand the mechanisms through which the selected  $\alpha$ Fabs modulate CD23 binding. By linking structure and function in the context of IgE-Fc's conformational ensemble we hope to provide insights into new ways of allosterically targeting the IgE-receptor interactions for the development of novel therapeutics

for asthma and allergy.

# Chapter 2

## Materials and methods

### 2.1 Materials

#### 2.1.1 Buffers and media

Buffer/Media	Abbreviation	Description
2xYT growth medium	2x YT	16 g/L tryptone, 10 g/L yeast extract, 5 g/L NaCl
Luria Broth	LB	10 g/L tryptone, 5g/L yeast extract, 10 g/L NaCl
HEPES buffer saline	HBS	25 mM HEPES, 150 mM NaCl, 4 mM CaCl <sub>2</sub> , pH 7.4
Phosphate buffer saline	PBS	140 mM NaCl, 2.7 mM KCl, 1.5 mM KH <sub>2</sub> PO <sub>4</sub> , 8 mM Na <sub>2</sub> HPO <sub>4</sub> , pH 7.4
SDS-PAGE resolving gel buffer		1500 mM Tris-HCl, pH 8.8, 0.4 % SDS
SDS running buffer (10 x)		30 g/L Tris-HCl, pH 8.3, 144 g/L glycine, 10 g/L SDS
SDS-PAGE stacking gel buffer		500 mM Tris-HCl, pH 6.8, 0.4 % SDS
Super optimal broth with catabolite repression	SOC	20 g/L tryptone, 5 g/L yeast extract, 5 g/L NaCl, 2.5 mM KCl, 10 mM MgCl <sub>2</sub> , 10 mM MgSO <sub>4</sub>
SPR running buffer		10 mM HEPES, 150 mM NaCl pH 7.4, 0.005 % surfactant P20, 4 mM CaCl <sub>2</sub>
Tris-acetate-EDTA	1 x TAE	40 mM Tris, 20 mM acetic acid, 1 mM EDTA.
Tris buffer saline	TBS	25 mM Tris, 125 mM NaCl, 4 mM CaCl <sub>2</sub> pH 7.4

Table 2.1: A list of buffers frequently used for the purposes of this thesis.

## 2.1.2 Recombinant proteins

Protein	Description	Molecular weight (kDa)	Extinction coefficient ( $M^{-1}cm^{-1}$ )	Reference
$\alpha\epsilon$ Fab1	Anti-epsilon fragment antigen binding 1	52	111895	Drinkwater <i>et al.</i> , 2014
$\alpha\gamma$	Immunoglobulin G subclass 4 constant domains fused with soluble domains of the alpha chain of Fc $\epsilon$ RI ( $\alpha$ 1 and $\alpha$ 2) in place of fragment antigen binding regions	93	89440	Shi <i>et al.</i> , 1997
<b>derCD23*</b>	<b>Soluble head domain of the IgE receptor, CD23</b>	<b>16</b>	<b>45430</b>	<b>Shi <i>et al.</i>, 1997</b>
derCD23-A488	Alexa Fluor <sup>®</sup> 488-labelled	16	45430	
<b>IgE-Fc</b>	<b>C<math>\epsilon</math>2-C<math>\epsilon</math>4 fragment of the IgE constant region, N265Q and N371Q background</b>	<b>75</b>	<b>48830</b>	<b>Young <i>et al.</i>, 1995</b>
dssIgE-Fc**	L340C and R341C mutations	75	48830	
His-IgE-Fc*	6x His-tag at C terminus	75	48830	
IgE-Fc (E289C)-Biotinylated	E289C mutation and biotinylated via a BirA tag at the C terminus	75	48830	
IgE-Fc(3-4)	C $\epsilon$ 3-C $\epsilon$ 4 fragment of the IgE constant region, N265Q and N371Q background	53	64565	Shi <i>et al.</i> , 1997
C $\epsilon$ 2 dimer	C $\epsilon$ 2 domain pair of IgE constant region	24	31315	
C $\epsilon$ 2 monomer***	C $\epsilon$ 2 domain of IgE constant region	12	15595	McDonnell <i>et al.</i> , 2001
sFc $\epsilon$ RI $\alpha$	Soluble domains of the alpha chain ( $\alpha$ 1 and $\alpha$ 2) of the IgE receptor, Fc $\epsilon$ RI.	22	53650	Cooke <i>et al.</i> , 1997
rIgE-A647	Phl p 7 allergen-specific immunoglobulin E, Alexa Fluor <sup>®</sup> 647-labelled	190	297000	James <i>et al.</i> , 2012
Xolair Fab Mutant 3	Xolair <sup>®</sup> fragment antigen binding with three mutations: S81R, N83R and L158P	48	78895	Davies <i>et al.</i> , 2017

Table 2.2: **A list of recombinant proteins used for the purposes of this thesis.** All proteins were generously donated by UCB, except those denoted by \* that were produced as part of the project, those denoted by \*\* which were kindly donated by Seema Mayank, and those denoted \*\*\* which were kindly donated by Virginia Casablanca Antras.

## 2.2 General deoxyribonucleic acid (DNA) analysis and manipulation techniques

### 2.2.1 Spectroscopic quantitation of DNA

Absorbance readings at 260 nm were used to estimate DNA concentrations, taking  $0.020 (\mu\text{g}/\text{ml})^{-1} \text{ cm}^{-1}$  to be the the average extinction coefficient for double-stranded DNA. A260/A280 nm and A260/A230 nm ratios were used to estimate the level of DNA purity in terms of protein and organic compounds respectively, with a tolerance of  $\sim 1.8$  and 2.0-2.2 for A260/A280 nm and A260/A230 nm ratios, respectively.

### 2.2.2 Agarose gel electrophoresis of DNA

Agarose gel electrophoresis was used to separate DNA fragments on the basis of their size. To make a gel, agarose (Biolone) was added to 1 x TAE buffer to a final concentration of 1 % and dissolved by heating. After cooling, 0.5  $\mu\text{g}/\text{ml}$  ethidium bromide (Sigma-Aldrich) was added and the mixture was poured into a gel tray with a plastic comb. Once set, the gel was placed in an electrophoresis tank and submerged in 1 x TAE. 5-50  $\mu\text{l}$  of samples were pre-mixed with Gel Loading Dye, Blue (6X) (New England Biolabs). The comb was removed and the samples were placed in the wells alongside a molecular weight marker. A voltage of 100 V was applied across the gel until the DNA fragments were sufficiently separated. DNA bands were visualised under UV illumination. In order to recover DNA, bands were excised from the gel under UV illumination and purified from the agarose using the Qiagen gel extraction kit, according to manufacturers instructions.

### 2.2.3 Heat-shock transformation of *E. coli*

Plasmid DNA was introduced into *E. coli* using the heat-shock method. 45  $\mu\text{l}$  of frozen chemically competent *E. coli* were gently thawed on ice. 1  $\mu\text{l}$  of 100  $\mu\text{g}/\text{ml}$  DNA solution was added to the thawed cells, mixed gently and incubated on ice for 20 minutes. The cells were immersed in a water bath at 42 °C for 45 seconds

and subsequently returned to the ice for 2 minutes before the addition of 250  $\mu$ l of pre-warmed Super Optimal broth with catabolite repression (SOC) media (New England Biolabs). The cells were incubated at 37 °C with orbital agitation at 225 rpm for 1 hr before plating onto selective LB agar and overnight incubation at 37 °C.

## 2.3 General protein analysis techniques

### 2.3.1 Spectroscopic determination of protein concentration

Protein concentrations were determined using spectrophotometry. Absorption of UV/visible light was measured from 200-700 nm. Absorbance measurements at 280 nm (from tryptophan and tyrosine residues, and disulphide bonds) were used to derive protein concentrations using the Beer-Lambert law (Equation 2.1). The extinction coefficients of different proteins were determined by the number of tyrosines, tryptophans and cysteine residues in the amino acid sequence using (Equation 2.2). Protein concentrations in mg/ml were calculated through multiplication of the protein concentration (M) by molecular weight (Da). A list of relevant protein extinction coefficients and molecular weights are given in Table 2.2.

$$A_{280} = \epsilon_{280}cl \quad (2.1)$$

$A_{280}$  = absorption at 280 nm,  $\epsilon_{280}$  = extinction coefficient ( $M^{-1} \text{ cm}^{-1}$ )

$c$  = protein concentration (M)  $l$  = path length of sample (cm)

$$\epsilon_{280} = 5690n_w + 1280n_y + 120n_c \quad (2.2)$$

$\epsilon_{280}$  = absorption at 280 nm ( $M^{-1} \text{ cm}^{-1}$ )  $n_w$  = number of tryptophans

$n_y$  = number of tyrosines  $n_c$  = number of cysteines

### 2.3.2 SDS-PAGE analysis

Electrophoresis was used to assess the presence and purity of protein in a sample. Gels were cast according to the recipe in Table 2.3. Samples were prepared in

2x Laemmli sample buffer (BioRad), with or without 5%  $\beta$ -mercaptoethanol as appropriate. Samples were heated at 95 °C for 3 minutes . For protein samples, 5 – 10  $\mu$ g of protein in 20  $\mu$ L was loaded into each well alongside appropriate molecular weight markers. The gel was placed in a tank containing SDS running buffer and a voltage of 120 V was applied to the gel until the dye reached the bottom of the plate. Gels were stained in Instant Blue (Generon) for 1 hr or until protein bands were clearly visible and then excess dye was removed by washing with distilled water.

	<b>Resolving gel (15%)</b>	<b>Stacking gel</b>
Resolving gel buffer (ml)	2.5	1.25
30 % acrylamide (ml)	5	1
Water (ml)	2.36	3.18
10 % APS (ml)	0.075	0.050
TEMED (ml)	0.011	0.025

Table 2.3: **SDS-PAGE gel recipe.** APS is ammonium persulphate, TEMED is tetramethylethylenediamine.

## 2.4 derCD23 production and purification

### 2.4.1 DNA and vectors

The Swiss-Prot accession code for the human low affinity IgE-Fc receptor is P06734. The derCD23 construct comprises the amino acids Ser156 to Glu298 of P066734. The derCD23 construct was previously cloned into the pET5a expression vector [149]. The pET5a expression vector is under the control of the T7 bacteriophage promoter, and the T7 RNA polymerase is under control of the lacUV5 promoter. The lacUV5 promoter can be induced using  $\beta$ -D-1- thiogalactopyranoside (IPTG). The pET5a vector also encodes a gene for ampicillin resistance, which allows positive selection of transformed host cells.



### 2.4.2 Transformation

Frozen chemically competent BL21(DE3) (New England Biolabs) *E. coli* were transformed with derCD23 plasmid DNA using the heat-shock (Section 2.2.3) and plated onto LB agar plates supplemented with ampicillin (Melfords Laboratories) (25 µg/ml). 5 ml over-night cultures were set up from single ampicillin-resistant colonies in LB broth supplemented with ampicillin (100 µg/ml). DNA from the cultures was extracted using the QIAprep Spin Miniprep Kit (Qiagen) and sequenced using primers specific for the T7 promoter.

### 2.4.3 Bacterial expression

A 5 ml culture was set up from a single derCD23-transformed ampicillin-resistant BL21 (DE3) colony, in LB brother supplemented with ampicillin (100 µg/ml). The culture was used to inoculate 50 ml of LB supplemented with 100 µg/ml ampicillin. This starter culture was incubated at 37 °C, with orbital agitation at 180 rpm over-night. Over-night culture was added to 500 ml of LB supplemented with 100 µg/ml ampicillin at a volume sufficient to give an absorbance of approximately 0.1 at 600 nm. The culture was incubated at 37 °C, with orbital agitation at 225 rpm in a 2 L baffled conical flask. Expression of derCD23 was induced when the absorbance of the culture at 600 nm reached 0.7 through the addition of IPTG (Sigma) to a final concentration of 1 mM. After induction, the culture was left to incubate at 37 °C, with orbital agitation at 225 rpm for a further 3 hours. The cultures were spun at 4,000  $xg$  for 30 minutes in order to harvest the cells. The cell pellet was then re-suspended in 40 ml of PBS pH 7.4 and stored at -20 °C.

### 2.4.4 Purification of insoluble inclusion bodies

The cell pellets were thawed on ice and were passed through a cell disrupter (20 PSI) twice at 4 °C to release their contents. To purify the inclusion bodies, the disrupted cells were centrifuged at 15,500  $xg$  for 20 min at 4 °C and the pellets were re-suspended in 30 ml 25 mM Tris, 1% Triton-X, pH 7.5. This was repeated five more times but after the last centrifugation, the pellet was re-suspended in 5 ml 20 mM Tris, 6 M guanidinium hydrochloride, pH 7.5 and left rotating overnight

at 4 °C to solubilise the protein. The solution was spun at 36,000 *xg* for 1 hour to remove the insoluble contaminants. The supernatant containing the solubilised derCD23 was stored at -20 °C.

### **2.4.5 Protein refolding**

Dithiothreitol (DTT) was added to thawed solubilised derCD23 to a final concentration of 1 mM and left to stand for 10 minutes at 4 °C. The protein solution was slowly diluted ten-fold into ice-cold refolding buffer, at 0.15 ml/min with rapid stirring and then left stirring at 4 °C overnight. NaCl was added from a 5 M stock solution to the solution to a final concentration of 50 mM and then left stirring at 4 °C for a further 2 hrs. The refolding solution was diafiltrated with a 10- fold excess of 25 mM Tris, pH 7.5 at 4 °C with a 5 kDa molecular weight cut-off (MWCO) membrane.

### **2.4.6 Heparin-sepharose chromatography**

A HiPrep Heparin 5 ml column (GE Healthcare) was pre-equilibrated with 10 column volumes (CVs) of 25 mM Tris, pH 7.5. The refolded derCD23 was filtered through a 0.45 µm filter (Sartorius) and loaded at 2 ml/min onto the column. The column was then washed with 10 CVs of 25 mM Tris, pH 7.5 at 5 ml/min to remove non-specifically bound protein. After achieving a stable absorbance at 280 nm, the flow rate was dropped to 0.75 ml/min. A gradient elution from 0 % to 40 % 25 mM Tris, 1 M NaCl, pH 7.5 was performed over 90 ml, collecting 3.5 ml fractions. Folded derCD23 was the dominant peak and eluted at around 20 % elution buffer. Following elution, the column was washed with 10 CVs of 25 mM Tris, 1 M NaCl, pH 7.5, 10 CVs of 25 mM Tris pH 7.5, and 10 CVs of 20 % ethanol.

### **2.4.7 Size exclusion chromatography**

A HiLoad 16/600 Superdex 75 PG column (GE Healthcare) was equilibrated with 200 ml 500 mM arginine, 25 mM Tris, 125 mM NaCl, 4 mM CaCl<sub>2</sub>, pH 7.5 at 0.75 ml/min. The selected fractions from the heparin column elution were concentrated to 5 ml using a 3 kDa MWCO centrifugal concentrator at 4 °C and 6,000 *xg*. The

derCD23 protein solution was loaded onto the column at 0.75 ml/min and eluted over 140 ml minutes at 0.75 ml/min. Fractions of monomeric derCD23 were pooled and concentrated using a 3 kDa MWCO Vivaspin<sup>TM</sup> centrifugal concentrator (Sartorius) at 4 °C and 6,000 *xg*. The purified derCD23 was then buffer exchanged into Tris buffered saline (TBS) pH 7.4 using a 3.5 kDa Slide-A-Lyzer<sup>TM</sup> cassette (Thermo Fisher Scientific) as per the manufacturer's instructions.

#### **2.4.8 Positive electrospray mass spectrometry**

Positive electrospray mass spectrometry (MS) was conducted on the purified derCD23 to ascertain the exact molecular mass of the protein. Protein sample, at 0.1 mg/ml, was dialysed into a solution of distilled and filtered water, 10 % acetonitrile and 0.1 % formic acid prior to MS analysis. The protein sample was injected at 40 µl/min directly into a Bruker MaXis ultrahigh-resolution electrospray ionisation quadrupole time-of-flight mass spectrometer. The multiple charge states were deconvoluted into the most probable single mass using the manufacturer's maximum entropy algorithm (Bruker Daltonics).

#### **2.4.9 One dimensional <sup>1</sup>H NMR spectroscopy**

One dimensional (1D) <sup>1</sup>H NMR spectroscopy was used to determine if the purified derCD23 was folded. The spectrum was recorded on 200 µM purified derCD23 in TBS with 5 % D<sub>2</sub>O at proton frequencies of 500 megahertz (MHz). 64 scans were taken at a temperature of 35 °C.

### **2.5 Anti-IgE antibody discovery**

UCB's core antibody discovery process was used to identify antibodies that bind to IgE-Fc and affect the IgE/CD23 interaction. The process is a single B cell process that involves:

- a) immunisation
- b) culturing of B cells from the immunised subject
- c) screening of B cell supernatants for 'hit' antibodies with desired characteristics

- d) isolation of the variable region genes of ‘hit’ antibodies from single B cells
- e) cloning of the variable region genes into suitable antibody/Fab constructs for expression
- f) expression and purification of antibody/Fab proteins

### **2.5.1 IgE-Fc immunisations**

Three New Zealand White rabbits were immunised subcutaneously with 500 µg of purified IgE-Fc (N265Q, N371Q). The IgE-Fc was emulsified in a 1:1 volume of complete Freund’s adjuvant (CFA). Booster injections were made at 21-day intervals using incomplete Freund’s adjuvant (IFA). Peripheral blood (10 % bleed) was taken from the ears of the rabbits 14 days after the second booster injection. Rabbit immunisations were performed in accordance with the provisions of the Animals (Scientific Procedures) Act 1986 and were approved by UCB’s ethical review process and conducted under project licence 30/2981. The blood was diluted in the same volume of sterile PBS and then layered onto 15 ml of Mammal Lympholyte (Cedarlane Laboratories Ltd., CL5120) in a 50 ml Falcon tube. The sample was centrifuged at 1500 *xg* for 15 minutes. The white lymphocyte layer was carefully transferred into a new 50 ml Falcon tube. The cells were washed in PBS using centrifugation at cells at 800 *xg* for 10 minutes. The cells were frozen in 10 % dimethyl sulfoxide (DMSO) in (fetal calf serum) FCS at -80 °C. (Work performed by Victoria O’ Dowd of UCB).

### **2.5.2 UCB’s core antibody discovery platform**

The automated system is composed of three linked class II safety cabinets. The B cell cultures were set up on the first safety cabinet using Thermo Combi Multidrop dispensers. The dispensers added the lymphocytes in growth medium to barcoded 96-well culture plates at 37 °C. The barcodes were registered and uploaded onto a tracking system. The plates were then placed into Liconic STX 500 incubators. Plates were moved within the cabinet by a Mitsubishi robotic arm.

The B cell culture plates were screened in the second safety cabinet. Each plate was sequentially moved into the second cabinet and its lid removed by another

Mitsubishi robotic arm. An Agilent Bravo liquid-handing robot then transferred 10  $\mu\text{l}$  of each cell culture supernatant to 384-well assay plates. Multidrop Combi dispensers were then used to add the assay reagents to the assay plates and were then incubated for 1 hour and run in the TTP Labtech Mirrorball plate reader. The Mitsubishi arm then transferred the cell culture plates to an STX 500 holding incubator where they were held until required for hit picking.

A text file of positive hits generated in the screen was supplied to a Beckman Biomek NX<sup>P</sup> in the third cabinet. The Biomek NX<sup>P</sup> picked off the positive supernatants from the B cell culture plates and put them into barcoded master plates. The masterplates were then returned to the incubator for collection.

The hardware and scheduling was controlled by Overload software via PAA's Harmony graphical interface.

### 2.5.3 B cell culture

The peripheral blood lymphocytes were slowly thawed and washed in PBS using centrifugation at 800 *xg*. The cells were then mixed with EL4 feeder cells (40,000 cells per well) and a T-cell conditioned media. The details of the T-cell conditioned media are protected by UCB but uses RPMI media as a basis (Gibco<sup>®</sup>, Life Technologies) containing 8.7 % FBS (Sigma-Aldrich), 1.7 % HEPES buffer, 1.7 % L-glutamine, 0.86 % penicillin/streptomycin solution, 0.17 % normacin and 0.09 %  $\beta$ -mercaptoethanol.

200  $\mu\text{l}$  of culture was dispensed into each well at density a of  $\sim$ 5,000 cell per well. At this empirically-derived lymphocyte density, the target-binding antibodies within a positive supernatant, will generally have come from a single B cell clone. The lymphocytes were incubated for seven days during which time the B cells expanded and secreted high enough antibody titres into the media for antigen-binding screening.

### **2.5.4 The primary fluorescence-based homogeneous screening assay**

The cell culture supernatants were screened for IgE-Fc binding using a homogeneous binding assay. 10  $\mu\text{m}$  superavidin polystyrene beads (Bangs Laboratories) were coated with biotinylated IgE-Fc. 0.5  $\mu\text{g}$  of biotinylated IgE-Fc was used to coat enough beads for the 384-well-plate and were left to incubate at room temperature for 1 hour. The coated beads were washed three times in PBS and 1 % BSA using centrifugation. Each well of each 384-well assay plate contained 10  $\mu\text{l}$  of beads coated in biotinylated IgE-Fc, 10  $\mu\text{l}$  of B cell supernatant and 10  $\mu\text{l}$  Alexa Fluor 488-conjugated goat anti-rabbit IgG Fc $\gamma$ -specific reagent (Jackson ImmunoResearch). The final dilution of the conjugated antibody was 1 in 5,000 and all dilutions were made in PBS and 1 % BSA. The plates were then left to incubate for 1 hour in the dark before fluorescence readings were taken on the Mirrorball cytometer.

### **2.5.5 Hit-picking**

The primary screening data from the homogeneous fluorescence-based assay were analyzed in Spotfire DecisionSite (TIBCO) and used to generate a list of positive wells. ‘Hits’ were identified as those supernatants that gave a fluorescence reading over 100. The supernatants from the top 800 readings were then transferred into 96-well masterplates, which were then used for secondary screening. The B cells cultures were then cryo-preserved and stored at -80 °C.

### **2.5.6 The secondary fluorescence-based screening assay**

The ‘hit’ cell culture supernatants were screened for modulation of CD23 binding to IgE-Fc using the homogeneous binding assay. Superavidin beads were coated with biotinylated IgE-Fc as previously described, except washes were performed in 10 mM HEPES , 1 % BSA and 5 mM CaCl<sub>2</sub> (Section 2.4). Each well of each 384-well assay plate contained 10  $\mu\text{l}$  of coated beads, 10  $\mu\text{l}$  of B cell diluted supernatant and 10  $\mu\text{l}$  of Alexa Fluor 488-labeled derCD23 at 1  $\mu\text{g}/\text{ml}$ . The B cell supernatants

were diluted 1 in 5 as assay design experiments showed some component of the culture media quenched fluorescence. All dilutions were made in 10 mM HEPES, 1 % BSA, 5 mM CaCl<sub>2</sub>. 32 'baseline' control wells were set up per a 384-well assay plate that contained the same components except that supernatant had not been identified as 'hits' in the primary screen. The 'baseline' supernatant came from a different rabbit immunisation and cell-culture. The plates were left to incubate in the dark for 1 hour and then the fluorescence readings were taken on the Mirrorball cytometer. As a negative control the same screens were carried out but without coating the beads with biotinylated IgE-Fc.

### 2.5.7 Foci-picking

The primary and secondary homogeneous assays identified the wells containing the B cells of interest. These wells contained both the B cells of interest and other B cells that were not IgE-Fc-specific. Foci picking is a novel technique that was used to identify and isolate the IgE-Fc-specific B cells. The B cell culture plates were removed from storage at -80 °C and gently thawed on ice. The B cell cultures of interest were washed using centrifugation in cell culture media (Gibco<sup>®</sup>, Life Technologies) containing 8.7 % FBS, 1.7 % HEPES buffer, 1.7 % L-glutamine, 0.86 % penicillin/streptomycin solution, 0.17 % normacin and 0.09 % β-mercaptoethanol. The B cells were re-suspended at a final density of 1.6 x 10<sup>6</sup> cells/ ml in cell culture media.

For each culture well, 15 µl of 3.99 µm superavidin magnetic beads (New England Biolabs) were coated with 0.5 µg biotinylated IgE-Fc and incubated for 1 hour at room temperature. The coated-beads were washed three times in 120 µl culture media using a magnetic rack.

Goat F(ab)<sub>2</sub> anti-rabbit Fcγ fragment-specific fluorescein isothiocyanate (FITC) conjugate (Jackson ImmunoResearch) was diluted 1:300 in cell culture media and was mixed with the washed B cells and the IgE-Fc coated beads in a 1:1:2 ratio respectively. The mixture was then spotted onto walled-glass slides coated with Sigmacote (Sigma-Aldrich) and then covered in mineral oil to prevent evaporation. The slides were then incubated at 37 °C for 1 hour. Following incubation the slides

were inspected for the formation of fluorescent foci using an Olympus IX70 microscope. Using an Eppendorf NK TransferMan micromanipulator, IgE-Fc-specific antibody-expressing single B cells were isolated and individual B cells were placed into 0.2 ml PCR tubes and put on dry ice immediately and stored at -80 °C. 6-12 IgE-Fc-specific B cells were picked from each well and placed in individual PCR tubes to try and guarantee the correct antibody was isolated.

### **2.5.8 Reverse transcription PCR (RT-PCR)**

RT-PCR was used to recover and amplify the cognate antibody genes from the isolated B cells. RT-PCR was performed on three foci for each ‘hit’ B cell culture to increase the chances of successful recovery of the variable region genes. The reverse transcription reactions were performed in a sterile environment using a class II safety cabinet. Superscript III reverse transcriptase (Invitrogen) primed with oligo (dT) was added to the PCR tubes containing the individual B cells. The B cells were kept on dry ice and moved onto a cold block to add the RT-PCR constituents to prevent non-buffered thawing and subsequent RNA degradation. The tubes were then placed in a PCR block and were incubated for 1 hour at 50 °C, and then 10 minutes at 70 °C to inactivate the Superscript enzyme.

### **2.5.9 Transcriptionally active PCR (TAP)**

A series of PCRs were performed to clone the variable region genes into a suitable construct for transient mammalian expression. PCR reactions, one for the  $V_H$  genes and one for the  $V_K$  genes were performed separately. The PCR primers were designed by UCB and their sequences cannot be disclosed. KOD DNA polymerase (EMD Millipore) was used for all reactions.

Both  $V_H$  and  $V_K$  primary PCR reactions were performed using two 5’ primers that annealed to the end of the leader sequence and two 3’ primers that annealed to the CH1 region ( $V_H$ ) or the  $C_K$  ( $V_K$ ). The cDNA from the RT reactions was used as the DNA template in both cases.

The secondary  $V_K$  PCR reactions were performed using a single 5’ primer that annealed to a small ‘tail’ at the 5’ end of the primary PCR product, and a set



of two reverse primers that annealed to J the region. The secondary  $V_{\kappa}$  PCR reactions were performed using the same 5' 'tail' primer and a set of three reverse primers that annealed to the J region of the primary PCR product. The secondary PCR reactions introduced restriction sites to facilitate later cloning steps and also introduced at the 5' end a region of  $\sim 25$  base pairs that overlap with a human cytomegalovirus (HCMV) promoter fragment. The secondary PCRs also added a small heavy/kappa chain constant region fragment overlap to the 3' end.

The tertiary PCRs combined the variable region DNA with a HCMV promoter fragment and constant region fragment containing a poly-adenylation sequence. This was then amplified to produce linear transcriptionally active PCR (TAP) products - one for the  $V_H$  genes and for the  $V_{\kappa}$  genes.

### **2.5.10 Cloning of variable region genes**

The secondary PCR products were run on a 1 % agarose gel and then isolated using the QIAquick Gel Extraction Kit (Qiagen). The isolated  $V_H$  PCR products were then digested with HindIII/Xho I restriction enzymes, and the isolated  $V_{\kappa}$  PCR products were digested with HindIII/BsiW restriction enzymes. The digested DNA was then gel purified and ligated, using T4 ligase (Promega), into a UCB in-house expression vector with a HCMV promoter, rabbit Fab constant region cassette and poly-adenylation sequence. XL1-Blue chemically competent *E. coli* (Agilent) were transformed with the ligated DNA using heatshock and plated onto LB agar plates supplemented with kanamycin (25  $\mu\text{g}/\text{ml}$ ). 5 ml over-night cultures were then set up from single kanamycin-resistant colonies in 2xYT broth supplemented with kanamycin (25  $\mu\text{g}/\text{ml}$ ). DNA from the cultures was extracted using the QIAprep Spin Miniprep Kit (Qiagen) and then sequenced using forward and reverse primers.

### **2.5.11 Small scale transient expression of anti-IgE antibodies and Fabs Expi293<sup>TM</sup> expression system**

The Expi293<sup>TM</sup> expression system (Gibco<sup>®</sup>, LifeTechnologies) is a transient mammalian expression system that uses lipofectamine to deliver exogenous DNA across the cell membrane of Expi293F<sup>TM</sup> human embryonic kidney (HEK) cells. The cell

density of Exp293F<sup>TM</sup> cell cultures were measured using a haemocytometer and trypan blue dye exclusion. Transfections were performed according to the manufactures instructions. 3 ml cultures were set up for each V<sub>H</sub> and V<sub>κ</sub> cognate pairing of tertiary full-length antibody TAP products (5 μl of each TAP product). 12 ml cultures were set up for each V<sub>H</sub> and V<sub>κ</sub> cognate pairing of μl aεFab plasmid DNA (3 μg of each DNA).

### **2.5.12 Large-scale transient expression of anti-IgE Fabs using the electroporation**

#### **Cell cultivation**

CHOSXE cells [150] were pre-adapted to CD-CHO media (Thermo Fisher Scientific) supplemented with 2 mM GlutaMAX<sup>TM</sup> (Thermo Fisher Scientific) according to manufacturers instructions. The cells were maintained in logarithmic growth phase agitated at 140 rpm on a shaking incubator (Kuhner AG) and cultured at 37 ° C supplemented with 8 % CO<sub>2</sub>.

#### **Electroporation transfection**

Prior to transfection, the cell numbers and viability were determined using a CEDEX cell counter (Innovatis). The cells were then spun at 1,400 rpm in a centrifuge for 10 minutes. The pelleted cells were re-suspended in sterile Earles Balance Salt Solution and spun for a further 10 minutes at 1,400 rpm. The pelleted cells were re-suspended to the desired cell density of 2 x 10<sup>8</sup> cells/ml. For each transfection the Fab vector DNA (1:1 ratio kappa:heavy) was added at final concentration of 400 μg per 2 x 10<sup>8</sup> cells/ml. The cells were transfected in 12 aliquots of 800 μl using the in-house electroporation system. The transfected cells were then transferred directly into 3 L Erlenmyer flasks containing 1L of ProCHO 5 (Lonza) media enriched with GlutaMAX<sup>TM</sup> (Thermo Fisher Scientific) and a 1 in 500 dilution of an antimetabolic (100x). The cells were cultured in a Kuhner shaker at 140 rpm, 37 °C and supplemented with 8 % CO<sub>2</sub>. After four days 3 mM sodium butyrate (n-butyric acid sodium salt, Sigma B-5887) was added to the culture. 14 days post-transfection the cultures were spun in a centrifuge at 4,000 rpm for 30

minutes to harvest the supernatant. The supernatant was filtered through a sterile 0.22  $\mu\text{m}$  filter followed by 0.22  $\mu\text{m}$  gamma gold filter and stored at 4  $^{\circ}\text{C}$ .

### **Protein G High Performance Liquid Chromatography (HPLC)**

The final Fab expression levels were determined by protein G HPLC. A HiTrap Protein G HP 1ml column (GE Healthcare) was equilibrated with 20 mM sodium phosphate 50 mM sodium chloride buffer pH 7.4. As a control, 100, 80, 64, 48, 32, 16, 8, 4 and 2  $\mu\text{l}$  of 1 mg/ml solution of Certolizumab Fab were separately injected onto the column at a flow rate of 2 ml/min, and eluted in 50 mM glycine-HCl pH 2.7 with column equilibration steps before each injection of control Fab. The peak areas were plotted as a function of the amount of control Fab. Once the column had been equilibrated again in 20 mM sodium phosphate, 50 mM sodium chloride, pH 7.4, 100  $\mu\text{l}$  of Fab expression supernatant was injected onto the protein G column at 2 ml/min and then eluted with 50 mM glycine-HCl pH 2.7. The resulting peak area was plotted onto the standard graph generated from the control injections to determine the amount of Fab present in 100  $\mu\text{l}$  of supernatant and accordingly to estimate the total amount of Fab expressed.

### **2.5.13 $\alpha\epsilon$ Fab purification**

#### **Supernatant concentration**

The supernatants were concentrated using a tangential flow ultrafiltration system with a 10 kDa membrane to an estimated Fab concentration of greater than 350 mg/L. A concentration greater than 350 mg/L was required for binding to the Protein G column.

#### **Protein G purification**

The  $\alpha\epsilon$ Fabs were purified by Protein G affinity chromatography.  $\alpha\epsilon$ Fab was bound to a 100 ml Protein G sepharose column (GE Healthcare) ( $\sim$  400 mg total Fab capacity) in PBS pH 7.4 and eluted in 100 mM glycine-HCl, pH 2.7. 20 ml fractions were collected and the peak fractions were pooled and neutralized with 1/25th fraction volume of 2 M Tris-HCl, pH 8.5. The pooled and neutralized fractions

collected from the Protein G column were concentrated to volumes between 10-18 ml using Amicon Ultra-15 centrifugal filter units (Millipore).

### **aεFab size exclusion**

Each aεFab was further purified by size exclusion chromatography (SEC) on a Superdex 26/60 S200 column (GE Healthcare) in PBS pH 7.4. The monomeric peak fractions were pooled and concentrated using Amicon Ultra-15 centrifugal filter units (Millipore).

### **aεFab analytical size exclusion**

30 µg of the pooled monomeric aεFab SEC peak fractions were run down a TSKgel G3000SWxl (Tosoh) analytical size exclusion column in 0.05 M Na<sub>2</sub>HPO<sub>4</sub>, 0.05 M NaH<sub>2</sub>PO<sub>4</sub>, 0.15 M NaCl, pH 6.8, at a rate of 1 ml/min. The area under the elution peaks was calculated using the manual integration function in the Clarity chromatography software (DataApex).

### **aεFab mass spectrometry**

Positive electrospray mass spectrometry was conducted on the aεFabs to ascertain their exact molecular masses. Protein samples, at 0.1 mg/ml, were dialysed into a solution of distilled and filtered water, 1 % acetic acid prior to MS analysis. Each protein sample was injected at 40 µl/min directly into a Bruker MaXis ultrahigh-resolution electrospray ionisation quadrupole time-of-flight mass spectrometer. The multiple charge states were deconvoluted into the most probable single mass using the manufacturer's maximum entropy algorithm (Bruker Daltonics).

## **2.6 Surface plasmon resonance**

Surface plasmon resonance (SPR) is a label-free technique that measures binding events in real-time and enables the determination of equilibrium and kinetic constants of biomolecular interactions. In SPR experiments, one of the binding partners is immobilised onto a matrix of non-cross-linked carboxymethylated dextran that is deposited on a metal surface (usually a thin layer of gold), and the other

is flowed over the immobilised partner. Binding between the immobilised partner (the ligand) and the partner in the medium (the analyte) is monitored through changes in the internal reflection of light at the metal-medium interface. SPR was used extensively in this project to identify anti-IgE Fabs, to characterise the kinetics of the interactions between IgE-Fc and different aεFabs, and to determine the affinity of the interactions. SPR was also used to characterise the binding of receptors to IgE-Fc in the presence of different anti-IgE Fabs in order to ascertain their effects on CD23 and FcεRI binding.

### 2.6.1 The SPR phenomenon

SPR is a phenomenon whereby incident light stimulates the oscillation of electrons in plasma of metals at a surface interface. The basic principle of SPR is schematically represented in Figure 2.1. SPR experiments are performed on sensor chips that have a thin layer of a metal, usually gold, on top. Conducting metals, like gold, contain free electrons that can oscillate. These oscillations are known as plasma waves. The sensor chip is placed on top of a prism and polarised light is shone through the prism onto the gold surface. Some of the light that hits the interface is reflected and this light has a measurable intensity. At a certain incident angle, the photons of the polarised light have a momentum that equals that of plasma waves; some of the energy of the incident light is transferred to the electrons in the gold film, generating plasma waves at the surface. At this so called ‘resonance angle’ the intensity of the reflected light is at a minimum because some of the incident photons have been converted to plasmons [151].

As analyte begins to flow over the sensing layer and binds to ligand, the angle of reflectivity that satisfies the resonance condition will change accordingly.

The resonance angle at which this minimum occurs is sensitive to changes in the composition of the material close to the gold film (within 300 nm), because these changes alter the momentum of the plasma waves and therefore SPR no longer occurs at the same resonance angle. The shift in resonance angle is directly proportional to the change of mass at the surface and can therefore be used to monitor binding occurring at the surface, such as protein binding to an immobilised

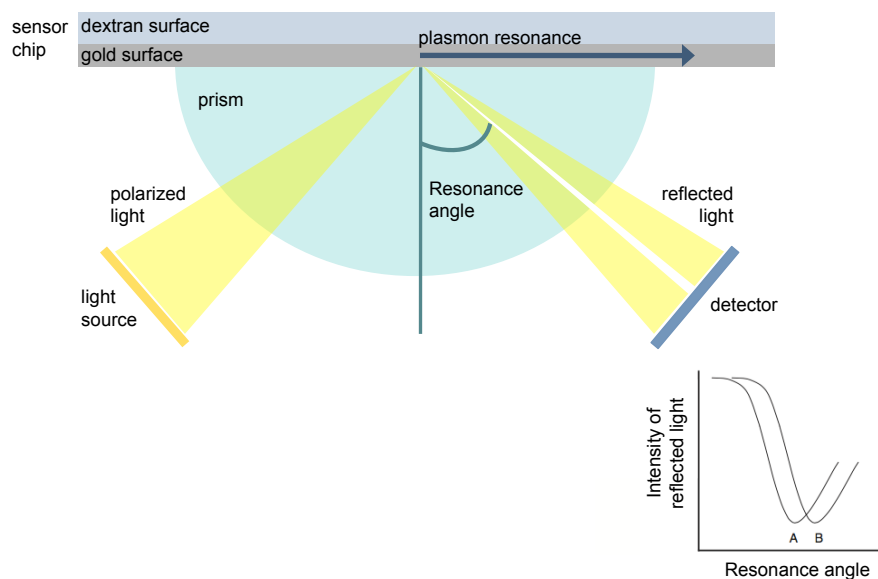


Figure 2.1: **A schematic representation of the principles of SPR.** At a certain incidence, light reflected from a prism excites plasmons in the gold surface of an SPR chip. The light is reflected out of the prism and a detector records the angle at which the plasmon resonance was satisfied, known as the resonance angle. The intensity of the reflected light is at a minimum at this angle because some of the incident photons were converted to plasmons. Changes at the surface of the SPR chip, such as an increase on mass upon ligand binding, alter the conditions required for plasmon resonance, and as such the resonance angle. In SPR experiments the change in resonance angle is called the SPR response and is used to measure the association and dissociation of complexes on the SPR surface.

ligand [151].

## 2.6.2 The SPR experiment

A typical SPR experiment involves four main steps.

Step 1: generating the ligand and control surfaces

Step 2: establishing a basal SPR angle observed as a stable response baseline

Step 3: injecting analytes and control analytes over the sensor surfaces

Step 4: regenerating the surfaces.

### Step 1: generating the ligand and control surfaces

In any SPR experiment the ligands of interest and control ligands must be immobilised to the binding flow-cell surface and the control flow-cell surface, respectively. Ligands may be directly or indirectly immobilised using a variety of methods, and

should be done in such a way as to limit any disruption to ligand activity.

It is very important when preparing SPR surfaces to consider the required or appropriate immobilisation density as this can affect various aspects of the experiment. The immobilisation density should be high enough to achieve a sufficient signal-to-noise ratio, but not so high that steric overcrowding, avidity effects and mass-transport effects significantly affect the data.

Steric overcrowding occurs when the initial binding of analyte to ligand physically occludes other analyte binding sites within the matrix, consequently reducing association. Reducing ligand density increases the distance between analyte binding sites on different ligand molecules, reducing potential steric overcrowding.

The intrinsic affinity of an interaction is the affinity between two sites that bind to each other monovalently. The functional affinity, or avidity, is the total binding strength resulting from all binding interactions of the interacting molecules. Ligand density may affect to what extent an SPR experiment measures intrinsic or functional affinity. At high enough ligand densities it is possible that a multivalent analyte may simultaneously bind two or more ligands. If the kinetics of the interaction sites are the same and independent of one another, the first interaction will depend on the intrinsic affinity of the site. The association of the subsequent sites is favoured because of the high local concentration of analyte. In general the dissociation rate will decrease because the dissociation of individual binding sites will not result in the the dissociation of the whole molecule, and consequently the possibility of rebinding increases. In cases where the multimeric interaction sites do not have identical kinetics and/or are dependent, the SPR data may also reflect the multiple different binding events and will be less reflective of the intrinsic affinity. Accordingly, if an experimenter wishes to proceed with an experiment at a 1:1 ligand:analyte stoichiometry, it is necessary to work at ligand densities low enough to prevent simultaneous engagement of one or more ligand molecules by analyte. One way to determine a suitable ligand density for investigating monovalent interactions is to perform initial experiments with a range of ligand densities to identify the densities at which the dissociation rate constant is independent of ligand density.

In SPR experiments, an analyte binds to a ligand on a sensor chip in a two-

step process. Initially an analyte is transferred from the bulk solution towards the matrix, and then the analyte-ligand interaction occurs. The first step is known as mass transfer and is the result of convection and diffusion [152]. Mass transport limitation occurs when the diffusion of analyte from the bulk solution is slower than the intrinsic rate of analyte-ligand binding. Mass transport limitation results in a depletion of analyte at the interaction surface and consequently the kinetic constants are more reflective of the mass transfer rate than the binding kinetics. In addition, if the transfer of analyte from the surface to the bulk solution is slower than the intrinsic rate of analyte-ligand binding, analyte that has dissociated from ligand is likely to rebind to ligand.

Limiting the amount of ligand at the interaction surface will help to prevent mass-transport effects as it reduces analyte consumption at the surface and reduces the number of sites available for re-binding. In addition, high flow rates can be used to minimize the diffusion distance from the bulk solution to the surface. Mass transport limitations can be tested by analysing the association and dissociation rate constants under different buffer flow rates; if the kinetic constants are independent of flow rate it is an indication that there is no mass transfer limitation [153]. Our group has performed experiments (data not shown) in which IgE-Fc was injected at different rates over SPR surfaces upon which aεFab1 had been immobilised at different densities. The kinetics of the interaction became dependent on injection rate at immobilisation densities above 10,000 RU of aεFab1, indicating mass-transport effects occurred at densities above 10,000 RU. It is possible to account for diffusion limited effects in surface plasmon resonance data using a fitting model that includes descriptors for mass transport kinetics, however it is always best to try and design the experiment in such a way that mass transport limitation is minimized [153].

Control surfaces are necessary to measure any non-specific binding and any background response. The control surface should be made in as similar a way to the ligand-surface as possible, and should have similar immobilisation densities [151].

Most pure proteins can be immobilised using a direct covalent immobilisation method that employs the free carboxymethyl groups on the sensor chip surface.



Direct coupling techniques include amine, thiol and aldehyde coupling that utilise lysine, cysteine and carbohydrate groups on glycoproteins, respectively. Direct coupling, however, has several associated problems including heterogeneity in ligand coupling, reduced ligand activity and difficult regeneration [154].

For the purposes of this project immobilisation was achieved by direct amine coupling to carboxymethylated sensor chips (CM5 chips, GE Healthcare). The carboxymethylated dextran surface of each CM5 chip was activated by a 420 s injection of 0.1 M N-hydroxysuccinimide (NHS) and 0.4 M 1-ethyl-3-(3-dimethylaminopropyl)-carbodiimide (EDC) at a 1:1 ratio in deionised water. The NHS/EDC solution reacts with free carboxyl-groups present on the chip and results in the generation of reactive succinimide esters that can react with surface exposed lysine residues of proteins, immobilising them on the surface. To immobilise the proteins, they were injected over the NHS/EDC activated surface at a concentration of 10  $\mu\text{g}/\text{ml}$  in 10 mM sodium acetate pH 5.0 in 60-300 s pulses, until the desired level of immobilisation was achieved. Any remaining active carboxymethylated groups were blocked by 1 M ethanolamine, pH 8.5, which was injected over the chip for 600 s. Reference cells were prepared using the same procedure, except that buffer was injected over the surface in place of protein. All immobilisations were performed at 25 °C with a flow rate of 20  $\mu\text{l}/\text{min}$ .

Ligands were also immobilised indirectly via capture of a covalently-coupled molecule, and details are reported in the relevant results sections. This approach requires that the covalently-coupled molecule recognises an epitope or tag on the ligand and binding does not significantly affect the ligand activity of interest. This approach avoids ligand heterogeneity since each molecule is bound to the covalently-immobilised molecule in the same way. Furthermore, regeneration is usually possible; using appropriate buffers the captured ligand or ligand/analyte complex can be selectively dissociated, leaving the covalently-bound ligand immobilised on the surface.

**Step 2 and 3: establishing a basal SPR angle and injecting analytes and control analytes over the sensor surfaces**

During an SPR experiment, changes in resonance angle as a result of changes at the surface of the gold surface are plotted in real-time as a change in response versus time in a sensorgram (Figure 2.2). At the start of an SPR experiment the running buffer is injected over the surface of the sensor chip until a stable baseline response in all flow cells is observed. The baseline response corresponds to the starting SPR angle. The analyte is subsequently injected in SPR sample buffer over ligand and control flow-cells at a continuous rate. The SPR phenomenon is sensitive to changes in mass at the surface and binding of the analyte to the immobilised ligand increases the mass at the surface and is reflected by an increase in SPR signal as explained above. The amount of complex present is directly related to the SPR response. The maximum response ( $B_{\max}$ ) is the maximum binding capacity of the ligand (L) for analyte (A), and occurs when all available analyte binding sites have been saturated.  $B_{\max}$  therefore depends on both the ligand density, determined from its immobilisation response, the relative masses of the ligand and analyte, and the stoichiometry of the interaction, according to Equation 2.3. Equation 2.3 can be used to derive the theoretical  $B_{\max}$  but the actual  $B_{\max}$  can be determined experimentally. Differences between the theoretical and experimental  $B_{\max}$  values may indicate that only a fraction of the binding sites are actually available [155].

$$B_{max} = \frac{MW_A}{MW_L} R_L V_L \quad (2.3)$$

Where  $B_{max}$  is the maximum capacity of the ligand,  $MW_A$  is the molecular weight of the analyte,  $MW_L$  is the molecular weight of the ligand,  $R_L$  is the immobilisation response of the ligand, and  $V_L$  is the stoichiometry of the ligand to analyte.

As analyte begins to flow over the sensing layer and binds to substrate, the angle of reflectivity that satisfies the resonance condition will change accordingly until it reaches saturation and all the binding sites have been occupied. The dissociation of analyte from the substrate causes the angle of the detector to return back to baseline once all the analyte has been completely removed. Changes in background

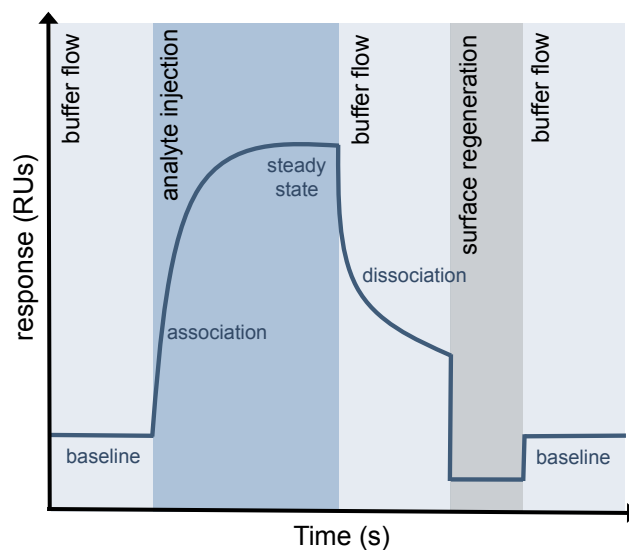


Figure 2.2: **A schematic representation of an SPR sensorgram.** During a typical SPR experiment, SPR running buffer is injected over immobilised ligand on the sensor surface to establish a robust baseline initial SPR angle and thereby a baseline ‘response’. During the analyte injection, the analyte binds to immobilised ligand, and the change in mass causes the angle of incidence that satisfies the resonance condition to change, and is plotted as a change in response. The angle continues to change until there is no net change in the formation of complex, and during this steady-state the response does not alter. Buffer is injected over the surface when the analyte injection stops, and the analyte dissociates from the ligand. The dissociation of analyte causes the resonance angle to return back towards the initial resonance angle, and consequently the SPR response returns back towards baseline. Sometimes the natural dissociation of the analyte from the ligand may take a long time and it is necessary to treat the surface with regeneration solutions that remove the analyte from the ligand and return the response to baseline.

response will also occur if there is a difference in the refractive indices of the running and sample buffers. The background response is therefore measured by injecting the analyte over a reference flow cell, which is treated identically as the sample surface, but without the immobilised ligand. The reference response is then subtracted from the response recorded on the ligand flow-cell, in order to obtain the actual binding response. One resonance unit (RU) represents the binding of approximately  $1 \text{ pg protein/mm}^2$  [154].

If the injection of analyte is long enough, the system will reach a steady state, during which time there is no net change in the amount of complex that is formed, and accordingly the response does not alter. During the dissociation phase the

analyte injection stops and instead SPR running buffer is injected over the sensor surface. Consequently, the analyte concentration is reduced to nothing and the complexes will dissociate. The resulting complex decay is observed as a decrease in SPR signal with time [154].

For the purposes of this project, all samples were prepared in filtered SPR running buffer (10 mM HEPES , 150 mM NaCl pH 7.4, 0.005 % surfactant P20, 4 mM CaCl<sub>2</sub>). In order to establish a steady baseline, each experiment began with three initial start-up cycles consisting of buffer injections only. Negative control samples (containing buffer only) and positive controls (containing molecules known to bind to the ligand with a certain profile) were also injected in cycles before and after the test sample cycles. Unless otherwise stated, serially-diluted analyte samples were injected over the ligand and experiments were run in duplicate. All injections were performed between 10 - 20  $\mu$ l/min, depending on the availability of sample, and all experiments were run in SPR buffer at 25 °. The concentrations of analyte injections, the length of analyte injections and the dissociation times varied between experiments, and are detailed separately in each respective section.

#### **Step 4: regenerating the surfaces**

To reuse the sensor chip before each new injection of analyte, the analyte from the previous injection must be completely removed but the ligand must stay in-tact on the surface. The intrinsic dissociation rate of the interaction may be slow and as such it may take a long time before the ligand is free, in such cases it is necessary to interrupt the interaction to regenerate the surface. The conditions required for regeneration are dependent upon the nature of the interaction between the ligand and the analyte, and need to be such that the analyte is effectively removed but that the ligand is not irreversibly damaged. In many cases, low pH buffers, such as 10 mM glycine pH 1.5 - 2.5, successfully regenerate SPR surfaces. At low pH most proteins partly unfold and become positively charged, and consequently it is thought that regeneration is achieved at low pH because the ligand and analyte repel each other. It is important, however, to only use the minimum acidic conditions required for regeneration so as to prevent irreversible ligand damage [155]. The regeneration conditions varied between experiments and are detailed in the

corresponding results sections.

### 2.6.3 Performing kinetic experiments using SPR

SPR can be used to determine the affinity of an interaction using either steady-state experiments or kinetic experiments. A steady-state experiment generates an equilibrium dissociation constant ( $K_D$ ) by determining the extent of a reaction as a function of the concentration of one of the reactants [151]. A kinetic experiment, however, measures the rates of the forward and reverse reactions as a function of the concentration of one of the reactants, which can be used to derive the forward and reverse rate constants ( $k_{on}$  and  $k_{off}$ ) [151], the ratio of which gives the equilibrium constant (Equation 2.4).

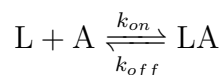
$$K_D = \frac{k_{off}}{k_{on}} \quad (2.4)$$

Where  $K_D$  is the dissociation constant with molar units (M), and describes the apparent affinity of the interaction.  $k_{off}$  is the dissociation rate constant with units  $s^{-1}$ , and describes the stability of the complex in terms of the fraction of complexes that dissociate per second.  $k_{on}$  is the association rate constant of the interaction with units  $M^{-1}s^{-1}$ , and describes the rate of complex formation.

#### First order kinetic experiments

Because SPR measurements are in real-time, the shape of the curve during association and dissociation can be used to determine the association and dissociation rate constants,  $k_{on}$  and  $k_{off}$ , respectively.

Consider the interaction between an immobilised ligand (L) and an analyte (A), assuming first order kinetics:



The rate at which the ligand and analyte associate to form complex is given by:

$$[L] \times [A] \times k_{on}$$

Once the complex has formed, it will dissociate at a rate equal to:

$$[LA] \times k_{off}$$

During the association phase of an SPR experiment the analyte is injected over the ligand, the analyte binds to the ligand and then dissociates from the ligand. The rate of the increase of the concentration of complex ( $[LA]$ ) is therefore given by both association and dissociation components, and is described by the following differential rate equation:

$$\frac{d[LA]}{dt} = ([L][A]k_{on}) - ([LA]k_{off}) \quad (2.5)$$

The concentration of ligand at any time ( $[L]_t$ ) is described by

$$[L]_t = [L]_{t=0} - [LA]_t \quad (2.6)$$

Therefore, equation 2.5 can be re-written:

$$\frac{d[LA]}{dt} = (([L]_{t=0} - [LA]_t)[A]k_{on}) - ([LA]k_{off}) \quad (2.7)$$

In SPR, complex formation is measured in real time as the response ( $R$ ) and because analyte is added in large excess to ligand, the change in concentration of free analyte upon association with ligand is assumed to be negligible. The concentration of the free ligand is equivalent to the maximum binding response ( $B_{max}$ ) minus the response at that time ( $R_t$ ). This can be substituted into the above equation, and rearranged to give the Equation 2.8.

$$\frac{dR}{dt} = ((B_{max} - R_t)[A]k_{on}) - (R_t k_{off}) \quad (2.8)$$

The one-to-one differential rate equation (Equation 2.8) cannot be used to fit the association curve for a one-to-one interaction. Instead the integral of this equation provides an integrated rate equation that can be used to fit the non-linear association phases of SPR sensorgrams for first order kinetics. First order interactions were fit in Origin software (OriginLab) using the integrated rate equation below:

$$R = \frac{(B_{max}k_{on}[A])(1 - e^{-(k_{on}[A]+k_{off}t)})}{k_{on}[A] + k_{off}} + R_0 \quad (2.9)$$

Where  $R_0$  is the response at  $t = 0$ .

During the dissociation phase of an SPR experiment the analyte dissociates from the ligand-analyte complex. The rate of dissociation is given by Equation 2.10

$$\frac{d[LA]}{dt} = -k_{off}[LA] \quad (2.10)$$

And since the concentration of complex is measured in SPR as the response signal ( $R$ ), this can be re-written as:

$$\frac{dR}{dt} = -k_{off}R \quad (2.11)$$

As with the association, it is easier to fit the experimental dissociation phase with an integrated rate equation. For the purposes of this project the dissociation phase was fitted using the following first order integrated rate equation:

$$R = R_0e^{-k_{off}(t-t_0)} + R_{t \rightarrow \infty} \quad (2.12)$$

Where  $R_0$  is the response at  $t = 0$  and represents the amount of bound complex to be dissociated over time ( $t$ ), and  $R_{t \rightarrow \infty}$  represents the response after infinite time.

### Higher order kinetic experiments

Not all data fit first order reaction kinetics and there are alternative kinetic models that can be applied to the measured data. First order reactions give sensorgrams with simple single exponential association and dissociation curves. In some cases, however, the sensorgrams may have biphasic character: that is they may have two components, a faster and a slower component. Biphasic character may be an indication of mass transport limitation, which occurs when the binding rate of an analyte is faster than its diffusion rate to the SPR surface. To avoid mass transport limitation effects the kinetic SPR experiments performed in this project used low ligand densities (<500 RU) and relatively fast flow rates (15 - 20  $\mu\text{l}/\text{min}$ ). Biphasic character can also indicate that an interaction has two components, for example a ligand may have two non-equivalent analyte binding sites, or the binding

of analyte to ligand may have fast and a slow component. For the purposes of this project, biphasic curves were fit using a double exponential integrated dissociation rate equation (Equation 2.13) and a double exponential integrated association rate equation (Equation 2.14) in Origin software (OriginLab).

$$R = (R1_0 e^{-k1_{off}(t-t_0)} + R1_{t \rightarrow \infty}) + (R2_0 e^{-k2_{off}(t-t_0)} + R2_{t \rightarrow \infty}) \quad (2.13)$$

Where 1 and 2 represent the two different components of the dissociation.

$$R = \left( \frac{(B1_{max} k1_{on}[A])(1 - e^{-(k1_{on}[A] + k1_{off})})}{k1_{on}[A] + k1_{off}} + R1_0 \right) + \left( \frac{(B2_{max} k2_{on}[A])(1 - e^{-(k2_{on}[A] + k2_{off})})}{k2_{on}[A] + k2_{off}} + R2_0 \right) \quad (2.14)$$

Where 1 and 2 represent the two different components of the interaction.

In instances where a third component was observed in the binding curves, a triple exponential integrated dissociation rate equation was used to fit the data (Equation 2.15).

$$R = (R1_0 e^{-k1_{off}(t-t_0)} + R1_{t \rightarrow \infty}) + (R2_0 e^{-k2_{off}(t-t_0)} + R2_{t \rightarrow \infty}) + (R3_0 e^{-k3_{off}(t-t_0)} + R3_{t \rightarrow \infty}) \quad (2.15)$$

Where 1, 2 and 3 represent the three different components of the dissociation.

#### 2.6.4 Performing steady-state experiments using SPR

If the dissociation rate of an interaction is high, the association and dissociation phases may be difficult to fit and therefore it may not be possible to determine the



association and dissociation rate constants [151]. In such cases, steady-state experiments may provide an alternative way to determine the dissociation constant of an interaction. During the steady-state of a SPR experiment the response remains steady ( $R_{eq}$ ) because the net rate complex formation is zero. The dissociation constant can be determined by measuring the concentration of free interactants ( $[L]$  and  $[A]$ ) and complex ( $[LA]$ ) during equilibrium (Equation 2.16). It should be noted, however, that the steady-state is not strictly at equilibrium because analyte is constantly being added and removed by sample flow.

$$K_D = \frac{k_{off}}{k_{on}} = \frac{[L][A]}{[LA]} \quad (2.16)$$

Where  $K_D$  is the dissociation constant,  $k_{off}$  is the dissociation rate constant,  $k_{on}$  is the association rate constant of the interaction, and  $[L]$ ,  $[A]$  and  $[LA]$  are the concentrations of ligand, analyte and complex, respectively.

The steady-state response ( $R_{eq}$ ) is directly proportional to the concentration of complex at equilibrium, and if analyte is in large excess of ligand (as in the experiments performed in this study), the concentration of analyte is assumed to be the concentration of analyte injected [155]. The concentration of the free ligand is equivalent to the maximum binding response ( $B_{max}$ ) minus the equilibrium response ( $R_{eq}$ ). This can be substituted into Equation 2.16, and rearranged to give Equation 2.17. Equation 2.17 may be used to determine the  $B_{max}$  and  $K_D$  of the one-to-one interaction between ligand and analyte, by fitting the steady-state response as a function of analyte concentration. For the purposes of this project, monophasic steady-state binding data was fit using Equation 2.17 in Origin software (OriginLab).

$$R_{eq} = \frac{B_{max}[A]}{K_D + [A]} \quad (2.17)$$

Where  $R_{eq}$  is the steady state response, and is directly proportional to the concentration of complex.  $B_{max}$  is the maximum binding capacity, and is directly proportional to the maximum amount of complex that can form.  $[A]$  is the concentration of free analyte and  $K_D$  is the dissociation constant.

### 2.6.5 Using $K_D$ and $B_{max}$ to characterise interactions

Interactions can be characterised using  $K_D$  and  $B_{max}$  values, and one or both of these values change in the presence of a modulator. An inhibitor for example, may increase the  $K_D$  and/or decrease the  $B_{max}$  of an interaction. The dissociation constant ( $K_D$ ) of an interaction equals the concentration of free analyte (derCD23) at which half of the total ligand molecules (complexed IgE-Fc) are associated with analyte (derCD23). An increase in the  $K_D$  of the IgE-Fc/derCD23 interaction, when IgE-Fc is pre-bound to  $\alpha\epsilon$ Fab would, in these experiments, suggest that more derCD23 is required for half saturation because the apparent affinity of the interaction has been reduced. An  $\alpha\epsilon$ Fab may act allosterically or sterically to reduce the affinity of the interaction, either by inducing conformational changes that affect the CD23 binding site, or by sterically preventing optimal coordination of the binding site, respectively.

If there is no increase upon injection of derCD23 over  $\alpha\epsilon$ Fab-bound IgE-Fc it would indicate that none of CD23 binding sites are available. Again,  $\alpha\epsilon$ Fab may elicit this effect through either steric or allosteric means: the  $\alpha\epsilon$ Fab may bind to the CD23 binding sites of IgE-Fc or it may sterically occlude CD23 binding, alternatively it may bind to IgE-Fc and cause a conformational switch to IgE-Fc conformers that cannot bind derCD23, respectively. It is possible that the number of CD23 binding sites in the  $\alpha\epsilon$ Fab-bound IgE-Fc population may be reduced rather than completely depleted, and this would be manifested as a reduction in  $B_{max}$ . In 2:1  $\alpha\epsilon$ Fab:IgE-Fc SPR experiments, we assume 100 % of IgE-Fc present is bound by two  $\alpha\epsilon$ Fabs via specific Fab binding sites, and therefore a reduction in  $B_{max}$  must indicate that the  $\alpha\epsilon$ Fab is an allosteric inhibitor: it causes a shift towards, but not completely to, conformations of IgE-Fc that cannot bind derCD23, thereby reducing the available derCD23 binding sites in the IgE-Fc population.

## 2.7 Flow cytometry

### 2.7.1 An introduction to flow cytometry

Flow cytometry is a widely used method for the analysis of cell surface and intracellular molecules and works by measuring cell-associated fluorescence intensities. In the context of this project it was used to analyse the binding of fluorescently-labeled rIgE to membrane CD23 expressed on the surface of RPMI 8866 cells (Sigma) in the presence of different  $\alpha$ Fabs. In flow cytometry experiments single-cell suspensions are incubated with fluorophore-labeled proteins specific for a particular cellular target, and the single-cell suspensions are subsequently run through the cytometer that consists of three main systems: the fluidics, the optics, and the electronics (Figure 2.3). The fluidics system moves the cells in a stream past the lasers, which are part of the optics system. The lasers illuminate the cells and the resulting fluorescence is directed towards the appropriate detectors using optical filters. The electronics system then converts the light signals into electronic signals that are processed by a computer [156].

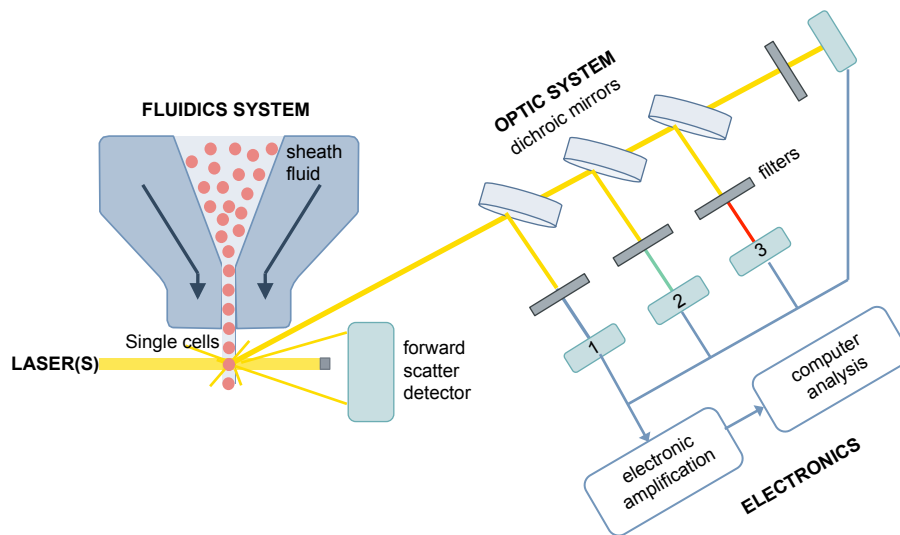


Figure 2.3: **A schematic representation of a flow cytometry experiment.** Sheath fluid focuses the single-cell suspension such that the cells pass through the beam of the laser one cell at a time. As the beam interrogates the cell the light is scattered in forward and side directions and fluorescence is emitted from the stained cells. A series of mirrors focus the fluorescent light onto filters so that each photomultiplier tube (1-3) detects a specific wavelength. The photomultiplier tubes then convert the photon energy into an electronic signal (a voltage) that is amplified and stored on a computer.

Initially in a flow cytometry experiment, the single-cell suspension is taken up and injected into a sheath fluid within a flow chamber. This forces the cells into a single-file stream and the cells pass by the laser light one at a time (Figure 2.3). When a cell intersects the light from the laser, some of the light is scattered (Figure 2.4.a). The extent of light scattering depends upon the physical properties of the cell, including its size, shape and granularity. Forward-scattered light (FSC) is proportional to the size of the cell and is measured by detectors just in front of the light beam. Whereas side-scattered light (SSC) correlates well with cell granularity and internal complexity, and is measured by detectors to the side of the incident beam. FSC and SSC measurement can therefore be used to differentiate cells from debris, single cells from doublets, and in some cases different cells types from one another. Additionally, because cells condense during apoptosis, FSC from dead cells is typically lower and populations of dead cells can usually be differentiated from live cells from FSC measurements (Figure 2.4.b) [156].

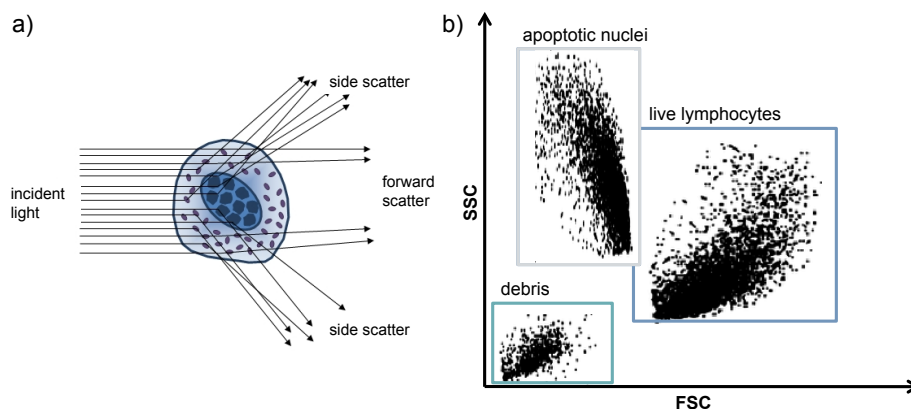


Figure 2.4: **Cells scatter light in forward and side directions.** (a) When the laser interrogates the cell, light scatters in forward (FSC) and side (SSC) directions and is measured by detectors in front of, or to the side of, the laser beam, respectively. The amount of forward scatter is dependent on the size of the cell, whereas the level of side scatter depends on its internal complexity. (b) A dot plot of the degree of forward and side scatter of each cell can be used to characterize the cells which pass through the flow cells and differentiate dead and live cells. (Figure adapted from [157]).

If a fluorescently-labeled protein is bound to the cell, when the cell enters the laser beam, electrons in the fluorophore are excited to higher energy levels and quickly decay to the ground state, emitting the excess energy as photons of light. Different fluorophores have characteristic absorption and emission spectra. The

optics of the BD FACSCanto™ II system, used for the purposes of this project, consists of an excitation source with blue, red and violet lasers. The fluorescent dyes, FITC and Alexa Fluor647, were used in this project and are excited by the blue and red lasers of the BC FACSCanto™ II system, respectively. The fluorescent signals are diverted to photomultiplier tubes (PMTs) via a system of mirrors and optical filters (Figure 2.3). Placing a particular filter in front of the PMT restricts the range of wavelengths that reach the detector and optimises detection of a specific fluorescent dye [158].

When the photons hit the PMT they are converted into a proportional, but greater, number of electrons. The electrical current then travels to an amplifier and is converted into a proportional voltage pulse, which is at a maximum when centre of the cell is at the centre of the laser beam. The measured voltage pulse area is directly proportional to the fluorescence intensity of that ‘event’. The mean fluorescence intensity (MFI) is the mean fluorescence intensity recorded for all selected ‘events’ [159]. The FSC, SSC and fluorescence data collected for every ‘event’ is stored on a computer. All flow cytometry data collected during this project were stored according to the flow cytometry standard (FCS) format [160] using FACSDiVa™ (BD Biosciences) and data analysis, was performed in FlowJo (FlowJo LLC).

### **2.7.2 Experimental details of cell-based assays using flow cytometry**

The RPMI 8866 cell line (Sigma) is a human B cell line that was established from the peripheral blood of a chronic myelogenous leukaemia patient, and expresses membrane CD23 [161]. RPMI 8866 cells were grown in RPMI 1640 media, supplemented with 10 % FBS, 2 mM L-glutamine, 50 µg/ml penicillin, 50 µg/ml streptomycin and 1 mM sodium pyruvate (Gibco®), Thermo Fisher Scientific). The cells were maintained under log phase growth at a cell density of  $3-9 \times 10^5$  cells/ml in a humidified incubator at 37 °C with 5 % CO<sub>2</sub>.

To remove soluble CD23 in the supernatant RPMI 8866 cells were washed twice by centrifugation at 1,000 g in cold supplemented RPMI 1640, and resuspended in

cold HBS supplemented with 0.1 % BSA and 2 mM  $\text{CaCl}_2$  at a cell density of  $2 \times 10^7$  cells/ml. Throughout the experiment the cells were kept on ice to prevent CD23 shedding.

The Fabs were serially diluted in HBS supplemented with  $\text{CaCl}_2$  to ten times their working concentrations. rIgE-A647 was diluted in HBS supplemented with 2 mM  $\text{CaCl}_2$  to 15 nM. 40  $\mu\text{l}$  rIgE-A647 was plated into a 96 well plate (Costar) with 5  $\mu\text{l}$  Fab, or for the unstained cell samples, 5  $\mu\text{l}$  HBS supplemented with 0.1 % BSA and 2 mM  $\text{CaCl}_2$ . 5  $\mu\text{l}$  Fab was also plated with 20  $\mu\text{l}$  A647-labeled control antibody and 20  $\mu\text{l}$  HBS supplemented with 0.1 % BSA and 2 mM  $\text{CaCl}_2$ . The plate was incubated at 37 °C in the dark for one hour. The plate was then placed on ice, and 5  $\mu\text{l}$  cells were added to each well. The samples were gently mixed and left to incubate on ice in the dark for one hour. Following incubation the cells were washed twice with 200  $\mu\text{l}$ /well of HBS supplemented with 0.1 % BSA and 2 mM  $\text{CaCl}_2$  and then resuspended in 200  $\mu\text{l}$ /well of the same buffer. The samples were then analysed in 14 ml FACS tubes (BD Bioscience) on a FACSCanto II (BD Biosciences) cytometer, with gating on live cells as determined by forward and side scatter. For each sample, measurements were collected from at least 5,000 single live cells.

## 2.8 Intramolecular fluorescence resonance energy transfer (FRET)

### 2.8.1 An introduction to FRET

#### Fluorescence

Fluorophores are chemical compounds that re-emit light upon their excitation to a higher energy level. Both the ground state and the excited state of a fluorophore have several vibrational energy levels. When a photon of energy ( $h\nu_{\text{ex}}$ ) is supplied to the fluorophore, for example by a laser, the fluorophore absorbs the energy and is excited from the ground state ( $S_0$ ) to the excited single state ( $S_1$ ). *i.e.* one of its electrons from the occupied orbital is excited to an unoccupied orbital. After a

finite time ( $\sim 10^{-15}$  s) the fluorophore relaxes to the lowest energy vibration level of the excited state ( $S_1$ ) by vibrational relaxation. Eventually the fluorophore returns to a ground state and the energy upon relaxation is dissipated either via radiative or non-radiative processes. The dissipation of energy through radiative processes results in fluorescent emission of a photon ( $h\nu_{em}$ ) (Figure 2.5) [162].

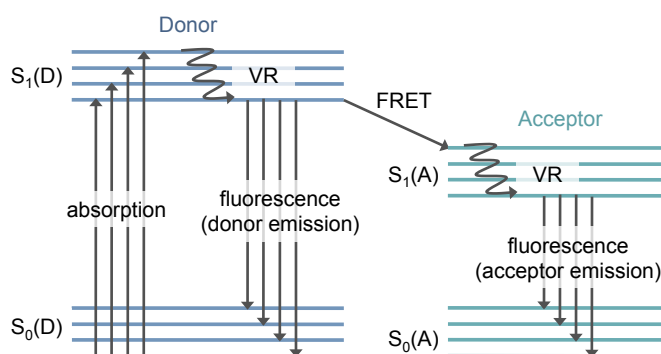


Figure 2.5: **A simplified Jablonski diagram illustrating the basic principles of FRET.** Electrons of a donor fluorophore that have been excited from the lowest vibrational level of the ground state ( $S_0$ ) to an excited state ( $S_1$ ) relax to the lowest vibrational level of the excited state by vibrational relaxation (VR). When the electron returns to the ground state, the energy can be dissipated as donor fluorescence, or the energy can be transferred non-radiatively from the excited state of the donor fluorophore to the excited state of the acceptor fluorophore. The acceptor fluorophore can then dissipate its energy, returning to the ground state to yield fluorescence emission of the acceptor.

## FRET

Fluorescence resonance energy transfer is the process through which the energy from the relaxation of an excited donor fluorophore is transferred non-radiatively to an acceptor molecule, which may or may not be fluorescent (Figure 2.5) [163]. As a result of FRET, the fluorescence intensity of the donor is reduced. FRET occurring between two chemically different molecules is called heterotransfer FRET, whereas FRET occurring between two chemically identical molecules is called homotransfer FRET. Homotransfer is only possible when the difference in the wavelength of the emission and absorption maxima (the Stokes shift) is small [164]. In order for FRET to occur the donor and acceptor pair must be close enough to one another (typically 10 – 100 Å), the dipole-dipole angles must not be at 90 degrees and the

emission spectrum of the donor must overlap with the excitation spectrum of the acceptor (Förster principle) (Figure 2.6) [165].

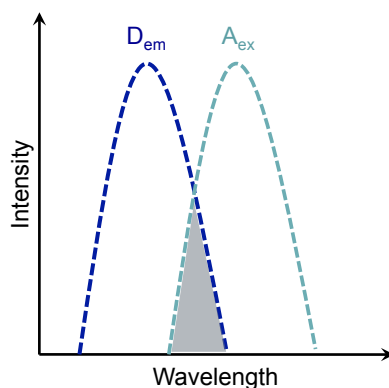


Figure 2.6: **A schematic illustration of the Förster principle.** For FRET to occur, the emission spectrum of the donor must overlap (grey) with the excitation spectrum of the acceptor.

The rate at which FRET occurs is calculated according to Equation 2.18 [164]. Because FRET is strongly dependent on the distance between the donor and acceptor pair, it is possible to use FRET to study the average distances between them. However, the FRET efficiency is dependent upon the Förster radius ( $R_0$ ), which is in turn dependent on the relative orientation of the donor-acceptor dipoles. Because the orientations of the dipoles cannot be measured exactly there is always some degree of error associated with distances determined by FRET (a maximum of  $\sim 35\%$ ) [164].

$$k_T = \frac{1}{\tau_D} \left( \frac{R_0}{r} \right)^6 \quad (2.18)$$

Where  $k_T$  is the rate of energy transfer,  $\tau_D$  is the decay time of the donor in absence of the acceptor, and  $r$  is the distance between the donor and the acceptor.

In FRET experiments the emission of a (donor/acceptor) fluorophore can be measured using two main methods: steady-state and time-resolved (TR) measurements. During steady-state experiments, the donor fluorophore is excited by a continuous beam of light, whereas in TR experiments, the donor is exposed to pulses of excitation light that are shorter than the time it takes for the excited donor to decay. There is a short wait after the excitation pulse and before measuring the emission, during which time possible background fluorescence of the



sample and auto-fluorescence of surrounding materials decreases. Accordingly, TR measurements of fluorophore emission are more specific than steady-state measurements [164]. All intramolecular FRET experiments performed in this project were performed using TR-FRET measurements of the emission of both the donor and acceptor upon donor excitation only. The TR-FRET value was determined as the ratio of the emission of the acceptor to the emission of the donor, with the donor emission acting as an internal standard.

TR-FRET measurements require that the lifetime of the fluorophore emission is sufficiently long to allow for the wait between donor excitation and emission measurement. Lanthanides are fluorescent metals that have very slow emission rates and decay times in aqueous solutions (0.5 – 3 ms) and consequently are very useful for TR-FRET experiments. In addition to their long decay times, the Stokes' shift of lanthanide chelates are large (>250 nm), which reduces interferences from excitation when measuring emission. Terbium chelate is a lanthanide and was used for the purposes of the intramolecular TR-FRET experiments performed during this project, and Alexa Fluor 488 was used as the acceptor fluorophore (Figure 2.7) [164].

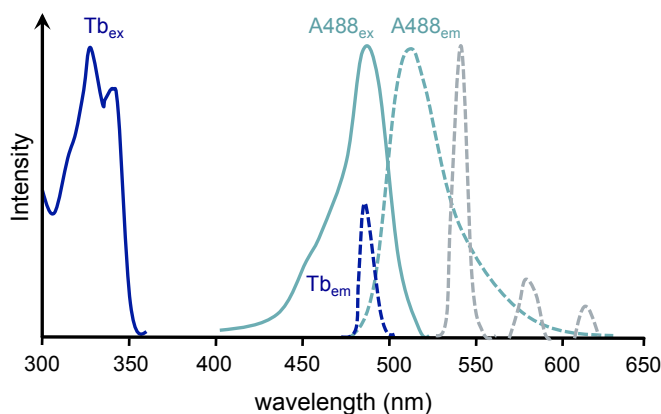


Figure 2.7: **An illustration of the terbium chelate and Alexa Fluor 488 emission and excitation spectra.** Terbium chelate (Tb) is maximally excited at around 340 nm, and its emission spectrum has four sharp peaks (blue and grey dotted line), with silent regions between each peak. The emission spectrum of Tb has multiple peaks because it has multiple ground states.

## 2.8.2 Experimental details of intramolecular FRET experiments

Intramolecular FRET experiments were used to determine the degree of ‘bendiness’ of IgE-Fc when bound to various  $\alpha$ Fabs. IgE-Fc(E289C)-biotinylated was fluorescently-labeled with the terbium-Alexa Fluor 488 donor-acceptor pair.

### Fluorophore labeling

Thiol-reactive terbium chelate was used to label the N-terminus IgE-Fc(E289C)-biotinylated via the introduced E298C mutation in the C $\epsilon$ 2 domains according to the manufactures instructions (LanthaScreen<sup>®</sup>, Thermo Fisher Scientific). The terbium to protein ratio was calculated using Equation 2.19 and Equation 2.20, and was determined to be 1.32:1.

$$[Tb\ chelate](M) = \frac{A_{343}}{12,570} \times dilution\ factor \quad (2.19)$$

Where  $[Tb\ chelate]$  is the concentration of terbium chelate,  $A_{343}$  is absorbance of the sample at 343 nm, and 12,570 is the extinction coefficient of the terbium chelate at 343 nm, in  $M^{-1}cm^{-1}$ .

$$[IgE-Fc](M) = \frac{A_{280} - (0.75 \times A_{343})}{48,830} \times dilution\ factor \quad (2.20)$$

Where  $[IgE-Fc]$  is the concentration of IgE-Fc,  $A^{280}$  is sample absorbance at 280 nm,  $0.75$  is the correction factor because when conjugated to a thiol the extinction coefficient of Tb chelate is 75 % of its value at 343 nm.  $A_{343}$  is sample absorbance at 343 nm and 48,830 is the extinction coefficient of IgE-Fc at 280 nm, in  $M^{-1}cm^{-1}$ .

The C-terminus of the terbium labeled IgE-Fc(E289C)-biotinylated was labeled with Alexa Fluor 488-streptavidin according to manufacturers instructions (Thermo Fisher Scientific). The Alexa Fluor 488 to protein ratio was calculated using Equation 2.21 and Equation 2.22, and was determined to be 2.39:1.

$$[A488](M) = \frac{A_{494}}{71,000} \times dilution\ factor \quad (2.21)$$

Where  $[A_{488}]$  is the concentration of Alexa Fluor 488,  $A_{494}$  is absorbance of the sample at 494 nm, and 71,000 is the extinction coefficient of the Alexa Fluor 488 at 494 nm, in  $M^{-1}cm^{-1}$ .

$$[IgE-Fc](M) = \frac{A_{280} - (0.11 \times A_{494})}{48,830} \times dilution\ factor \quad (2.22)$$

Where  $[IgE-Fc]$  is the concentration of IgE-Fc,  $A_{280}$  is sample absorbance at 280 nm, 0.11 is the correction factor to account for the absorption of the Alexa Fluor 488 dye at 280 nm.  $A_{494}$  is sample absorbance at 494 nm and 48,830 is the extinction coefficient of IgE-Fc at 280 nm, in  $M^{-1}cm^{-1}$ .

As a control for minimum FRET, the C-terminus of terbium-labeled IgE-Fc(E289C)-biotinylated was incubated with un-labeled streptavidin.

### Assay design

IgE-Fc is a homodimer and consequently contains two sites for each fluorophore. The intramolecular FRET signal could therefore arise from FRET occurring between an acceptor/donor pair on the same IgE-Fc chain or between an acceptor/donor pair on a different IgE-Fc chain [75]. In addition, there may be some homotransfer between two Alexa Fluor 488 labels on the two different chains of IgE-Fc since there is some overlap in their excitation/emission spectra [75]. Because of these inherent complexities, the intramolecular FRET data were not used to determine changes in intramolecular distances upon binding different  $\alpha$ Fabs, but rather the FRET signals were compared in relative terms to those for IgE-Fc alone (bent) and IgE-Fc bound to  $\alpha$ Fab1 (extended).

The doubly-labeled IgE-Fc was mixed with each  $\alpha$ Fab titrated to a final concentration of 1  $\mu$ M in 20 mM Tris, 150 mM NaCl, 0.002 % Tween 20, pH 7.2 in low volume black, non-binding 384-well plates (Corning). Terbium-only labeled IgE-Fc was also mixed with each of the  $\alpha$ Fabs titrated to 1  $\mu$ M in the same buffer. The final volume in each well was 25  $\mu$ l and the final concentration of IgE-Fc was 10 nM. The mixtures were left to incubate at room temperature in the dark with shaking for 120 minutes. The plates were read in time-resolved FRET mode on the EnVision Multilabel plate reader (PerkinElmer) with excitation at 330 nm

and emission read at 485 nm and 520 nm. The effect was expressed as % inhibition of the maximum signal generated in the assay (doubly-labeled IgE-Fc without  $\alpha$ εFab) after subtracting the minimum signal (terbium-labeled IgE-Fc with 1μM unlabelled streptavidin) from both. The FRET ratio  $((E_{520}/E_{485}) \times 10^4)$  was plotted as a function of  $\alpha$ εFab concentration and the data were fit to a four parameter logistic curve:

$$y = \frac{A_1 - A_2}{1 + (x/x_0)^p} + A_2 \quad (2.23)$$

Where  $x_0$  is the centre of the sigmoidal curve,  $p$  is the power,  $A_1$  is the initial y value,  $A_2$  is the final y value, and the y value at  $x_0$  is halfway between the two limiting values  $A_1$  and  $A_2$

### Statistical analysis

All statistical analysis was done using the nonparametric, unpaired Wilcoxon rank-sum test (or Mann-Whitney U test) [166]. The Wilcoxon rank-sum test, tests the null hypothesis - that it is equally likely that a randomly selected value from one sample will be less than or greater than a randomly selected value from a second sample. The tests were performed as such:

- All observations were ranked in increasing order of magnitude, ignoring the sample they are from. Observations with the same magnitude were given an average ranking.
- The ranks were summed in the smaller of the two samples, or either of the samples if they were matched in size.
- The two individual samples sizes were used to identify the appropriate critical values expressed in terms of a range in a predetermined table. If the sum of the ranks of the smaller sample lay inside the critical range then the null hypothesis was accepted, if the sum of the ranks of the smaller samples lay outside of the critical range then then null hypothesis was rejected.

# Chapter 3

## Allosteric modulation of the IgE-Fc/CD23 interaction by $\alpha\epsilon$ Fab1

### 3.1 Introduction

The interactions between immunoglobulin E (IgE) and its receptors (Fc $\epsilon$ RI and CD23) can be allosterically modulated (Section 1.3) [18, 89, 81, 108]. Previous studies have described two main types of rigid-body domain motions associated with the allosteric modulation of IgE-Fc-receptor interactions; an opening and closing of the C $\epsilon$ 3 domains [18, 81] and the extension of C $\epsilon$ 2 domains from a bent conformation [81]. Allosteric modulation through opening and closing of the C $\epsilon$ 3 domains was first described in terms of the mutual inhibition of IgE-receptor binding [18, 89] and it has since been associated with the inhibition of the interaction between Fc $\epsilon$ RI and  $\alpha\epsilon$ Fab1-bound IgE-Fc [81].

$\alpha\epsilon$ Fab1, a fragment antigen binding (Fab) molecule, binds to IgE-Fc with a 2:1 stoichiometry ( $K_{D1} \sim 80$  nM,  $K_{D2} \sim 1.5$   $\mu$ M) and inhibits the IgE-Fc/Fc $\epsilon$ RI interaction (Section 1.3.3) [81]. The extension of the C $\epsilon$ 2 domain pair in the  $\alpha\epsilon$ Fab1:IgE-Fc complex is striking, however, the C $\epsilon$ 3 domains of the structure are also in a very ‘open’ conformation [81]. Both of these features contribute to the allosteric inhibition of Fc $\epsilon$ RI by  $\alpha\epsilon$ Fab1, but the latter may also affect the binding of CD23 to IgE-Fc.

CD23 binds to ‘closed’ IgE-Fc with a 2:1 stoichiometry [18]; a single CD23 head domain binds to a single C $\epsilon$ 3 domain. The affinity of a single CD23 head domain

for IgE-Fc is relatively low ( $K_D \sim 1 \times 10^{-6}$  M), however on cell surfaces CD23 exists as trimer and the affinity of the interaction is increased through the avidity effect [88, 39, 167, 90].

Both aεFab1 and CD23 bind the Cε3 domain of IgE-Fc, but whether aεFab1 inhibits CD23 binding in addition to FcεRI binding has not been established. On the basis of evidence suggesting that CD23 binds a ‘closed’ conformation of IgE-Fc, and that aεFab1 stabilises an ‘open’ conformation, it was hypothesised that aεFab1 could inhibit CD23 binding. The following study was performed to test this hypothesis; it aimed to establish whether aεFab1 inhibits CD23 binding and whether this is a result of allosteric communication between the two sites, potentially involving the ‘opening’ and ‘closing’ of Cε3 domains.

## 3.2 Results

### 3.2.1 Production and purification of derCD23

derCD23 is a construct of CD23 composed of single CD23 lectin head domain (Section 2.4.1) [20]. derCD23 was produced recombinantly and purified in order to investigate the effect of aεFab1 on the CD23/IgE-Fc interaction.

#### Expression of derCD23

BL21 (DE3) *E. coli* were transformed with a pET5a vector containing an insert for derCD23. derCD23 expression was induced by addition of IPTG to the cell cultures (Section 2.4.2) (Figure 3.1).

derCD23 was intra-cellularly over-expressed into insoluble inclusion bodies (Figure 3.2). The inclusion bodies were separated from soluble cellular proteins and were washed, solubilised and denatured to yield relatively pure but unfolded derCD23. Approximately 20 mg of derCD23 was extracted from inclusion bodies produced from 1 L Luria broth (LB) cultures (Sections 2.4.3 and 2.4.4).

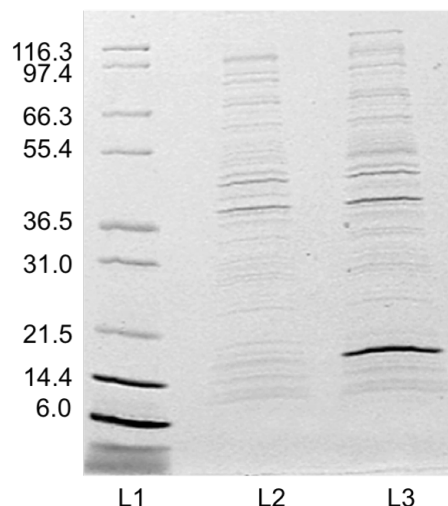


Figure 3.1: **Induced expression of derCD23 in *E. coli* BL21 (DE3) cells.** A 15 % SDS-PAGE analysis of solubilised cell pellets before (L2) and four hours after (L3) IPTG induction. A significant increase in derCD23 (16 kDa) expression was observed post IPTG induction. Protein makers (L1) are labelled with their respective molecular weights (kDa).

### Purification of derCD23

The solubilised and denatured derCD23 was refolded by drop-wise addition to refolding buffer. Refolded derCD23 was purified using a two-step purification protocol (Section 2.4.5).

Cation-exchange chromatography with a heparin column was used to purify correctly folded derCD23 from misfolded derCD23 (Section 2.4.6). After loading the column, an increasing salt gradient was applied to elute derCD23. Misfolded derCD23 eluted at a lower salt concentration, and hence a lower elution volume, than folded derCD23 owing to its lower affinity for the negatively charged matrix (Figure 3.3). The peak fractions of correctly folded derCD23 were pooled and SDS-PAGE analysis revealed the presence of contaminants with higher molecular weights than derCD23 (Figure 3.2). These contaminants were most likely small multimers of correctly folded derCD23 and were probably responsible for the small tail in the cation exchange elution peak (Figure 3.3).

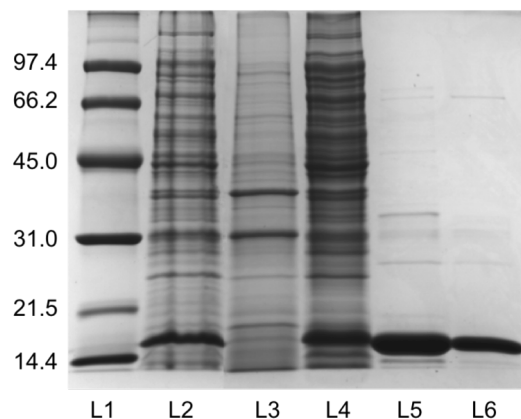


Figure 3.2: **derCD23 over-expression into insoluble inclusion bodies and purification.** 15 % SDS-PAGE gel analysis of culture fractions from derCD23 expression in *E. coli* and derCD23 samples post chromatographic purification. derCD23 (16 kDa) was expressed intracellularly post IPTG-induction (L2). derCD23 was not over-expressed in the soluble fraction (L3) but was over-expressed in the insoluble fraction (L4). Purification of monomeric derCD23 was improved through heparin chromatography (L5) and further still by size exclusion chromatography (L6). Protein makers (L1) are labelled with their respective molecular weights (kDa).

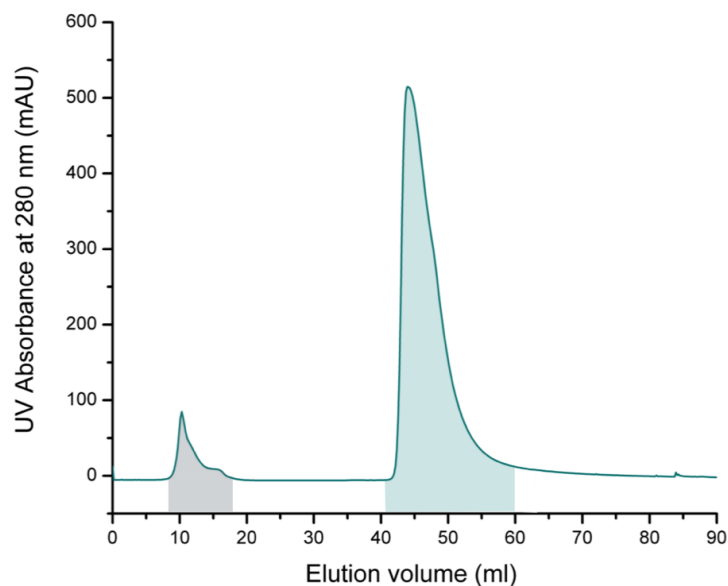


Figure 3.3: **Chromatogram of derCD23 purified by heparin-sepharose chromatography.** Folded derCD23 eluted during a gradient from 25 mM Tris, pH 7.5 to 40 % 25 mM Tris, 1 M NaCl, pH 7.5. Folded derCD23 (green) eluted at higher salt concentrations than misfolded derCD23 (grey).

The pooled fractions were subjected to size exclusion chromatography (SEC) in order to isolate the desired monomeric derCD23 from the multimeric forms (Section



2.4.7) (Figure 3.4).

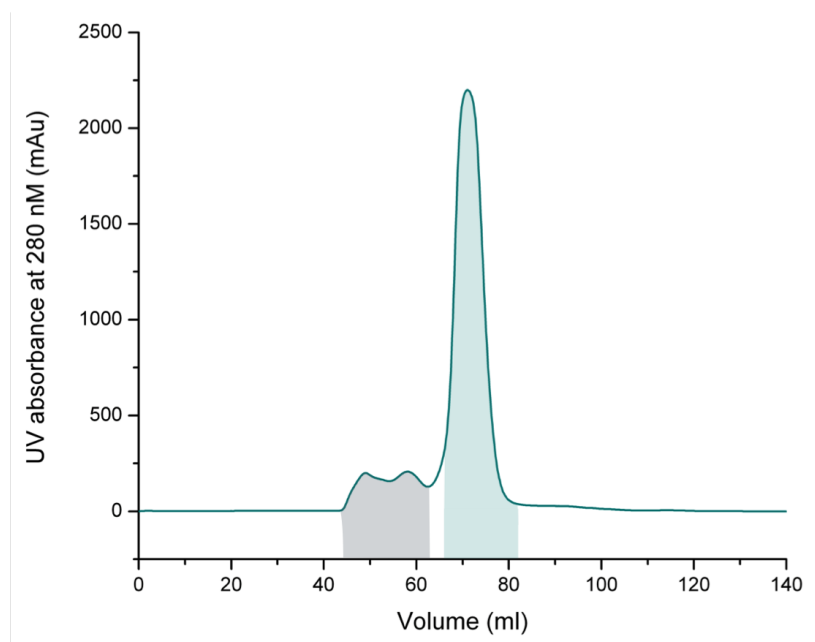


Figure 3.4: **Chromatogram of derCD23 purified by size exclusion.** Monomeric derCD23 was separated from aggregates based upon differences in hydrodynamic volume using a Superdex 75 column (GE Healthcare). The larger molecular weight aggregates eluted first (grey), followed by monomeric derCD23 (green).

The multimers were eluted at lower volumes during SEC, and appeared as ‘shoulders’ to the left of the main monomeric derCD23 elution peak. SEC fractions were pooled to avoid contamination with the multimeric forms and contained pure derCD23 (Figure 3.2).

### Mass spectrometry of derCD23

Positive ion electrospray mass spectrometry was used to corroborate the exact molecular weight of the purified derCD23 protein sample (Section 2.4.8). The mass spectrum consisted of a single peak at 16,137 Da, which corresponds to the mass of derCD23 with four disulphide bonds (Figure 3.5).

### 1D $^1\text{H}$ NMR spectroscopy of derCD23

1D  $^1\text{H}$  NMR spectroscopy was used to determine if the purified derCD23 was folded (Section 2.4.9). Several features of the  $^1\text{H}$  NMR spectra indicate that the purified

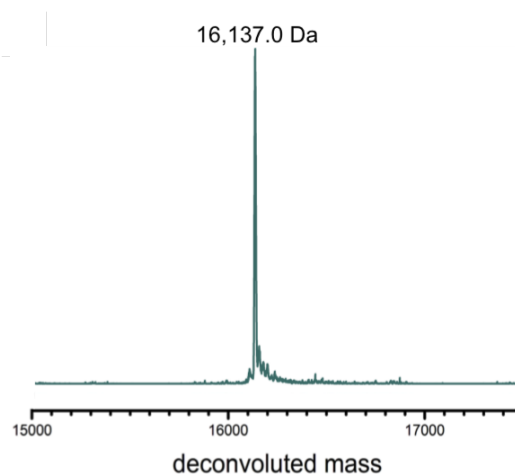


Figure 3.5: **Positive ion electrospray mass spectrometry of purified derCD23.** A single peak at 16,139 Da was observed, corresponding to the molecular mass of folded derCD23.

derCD23 was folded (Figure 3.6). The presence of signal dispersion at chemical shifts between 8.5-11 parts per million (ppm) demonstrate that the protein amides of the sample were in different chemical environments, which is indicative of a well-folded protein [168]. The signal dispersion in the aliphatic region of the 1D  $^1\text{H}$  NMR spectrum of the spectrum (between -1 and 1 ppm) also suggests that the sample was folded [168]. In addition to these general characteristics for folded proteins, the spectrum also displays four characteristic methyl peaks up-field of 0 ppm from residues 221, 223 and 227, which indicate that derCD23 is well folded [39].

### 3.2.2 Production of His-tagged IgE-Fc

His-tagged IgE-Fc was required as a control for surface plasmon resonance (SPR) investigations into the effect of  $\alpha\epsilon$ Fab1 on the interaction between IgE-Fc and derCD23.

#### Cloning and expression of His-tagged IgE-Fc

DNA of IgE-Fc(N265Q,N371Q) with a 6x N-terminal His-tag was synthesised and cloned into UCB's pNAFH vector by The GeneArt<sup>TM</sup> Gene Synthesis service (Thermo Fisher Scientific). The pNAFH vector is a mammalian expression vector under the control of the human cytomegalovirus promoter, it also has a

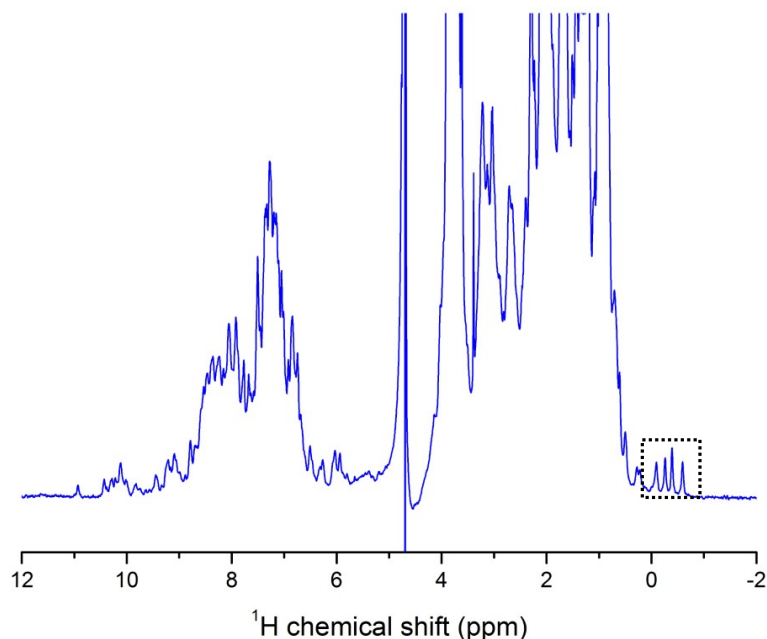


Figure 3.6: **1D  $^1\text{H}$  NMR spectroscopy of purified derCD23.** A 1D  $^1\text{H}$  NMR spectrum for purified derCD23 was recorded at 500 MHz at 35 °C. Signal dispersion from -1 to 1 and from 8.5 to 11 ppm, and four characteristic up-field shifted methyl peaks (in black dotted box) indicate that the protein was well-folded.

pUC origin of replication and encodes kanamycin resistance. BL21 *E. coli* were transformed with the pNAFH vector containing the His-tagged IgE-Fc construct, and the expanded plasmid DNA was isolated from LB cultures.

Human Embryonic Kidney 293 (HEK293) cells were transiently transfected with the pNAFH vector containing the His-tagged IgE-Fc insert using the 293fectin<sup>TM</sup> reagent (Thermo Fisher Scientific). The supernatant was harvested by centrifugation after six days of incubation.

### Verification of His-tagged IgE-Fc expression using SPR

SPR was used to determine if His-tagged IgE-Fc had been expressed into the supernatants and if it had native-like function. SPR is a label-free technique used to follow biomolecular interactions in real-time (Section 2.6). Changes in response can provide a measure of the change in the amount of binding of analyte in solution to a ligand immobilised on a sensor surface. Alpha-gamma [88] (the alpha subunit of Fc $\epsilon$ RI fused to IgG<sub>4</sub> constant domains) was immobilised on the surface of a sensor chip using amine-coupling (Section 2.6.2) at a moderate density ( $\sim 500$

RUs). IgE-Fc was injected for 180 s over the surface at various concentrations as a control. The His-tagged IgE-Fc supernatant was injected for 180 s over the surface at various dilutions. A 350 s dissociation phase followed each sample injection and the surface was regenerated by two 60 s pulses of 10 mM glycine-HCl pH 2.2. The SPR sensorgrams for the binding of IgE-Fc and His-tagged IgE-Fc to the alpha-gamma surface were comparable, indicating that His-tagged IgE-Fc was present in the supernatant and was functional (Figure 3.7).

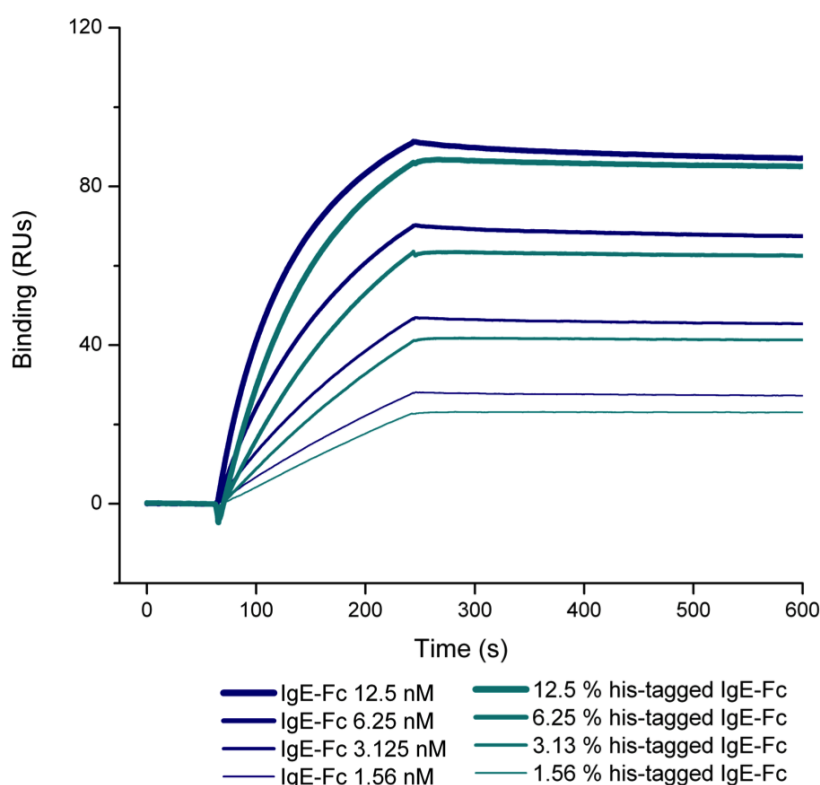


Figure 3.7: The SPR sensorgrams profiles for the binding of un-purified His-tagged IgE-Fc to immobilised alpha-gamma (an  $Fc\epsilon RI\alpha$  construct) are very similar to the binding of non-His-tagged IgE-Fc to the same surface.

### 3.2.3 SPR studies of the effect of $\alpha\epsilon$ Fab1 on the interaction between IgE-Fc and CD23

SPR was used to study the effect of  $\alpha\epsilon$ Fab1 on the interaction between IgE-Fc and derCD23. Steady-state analysis of SPR data can be used to determine the equilibrium constant ( $K_D$ ) and binding capacity ( $B_{max}$ ) of an interaction from a

plot of the steady-state response versus the analyte concentration (Section 2.6.4) [151]. Steady-state analysis is only appropriate if the interaction reaches steady-state during the course of analyte injection. The interaction between IgE-Fc and derCD23 reaches steady-state relatively fast, largely as a result of its rapid off-rate [39] and is therefore suitable for steady-state analysis. SPR experiments were performed to determine how aεFab1 affects the interaction between IgE-Fc and derCD23 and steady-state analysis was employed to quantify these effects in terms of  $K_D$  and  $B_{\max}$ .

An anti-His-tag antibody (THE<sup>TM</sup> His-Tag Antibody, mAb, Mouse, Genscript) CM5 sensor surface and an aεFab1 CM5 sensor surface were prepared using amine-coupling techniques (Section 2.6.2). A mock amine-coupled surface was used as a reference-subtraction surface. A 1 in 4 dilution of supernatant containing His-tagged IgE-Fc was injected over the surface for 180 s and was captured by the anti-His-tag antibody. Various concentrations of derCD23 were then injected for 120 s over the captured His-IgE-Fc in order to characterise the interaction between IgE-Fc and derCD23 in the absence of aεFab1 (Figure 3.8.a). Separately, IgE-Fc was injected for 180 s over the aεFab1 surface to generate an immobilised aεFab1:IgE-Fc (1:1) complex. IgE-Fc was captured at a higher density on the aεFab1 surface than on the anti-His antibody surface because the later surface had a lower immobilisation density. Nevertheless, the capture levels of IgE-Fc in each case were low enough to ensure that binding between IgE-Fc and immobilised antibody was monomeric and would not give density dependent phenomena (Section 2.6.2). derCD23 was then injected for 120 s over the aεFab1:IgE-Fc (1:1) complex using the same range of concentrations (Figure 3.8.b). 8 μM derCD23 was also injected for 120 s over both the anti-His-tag surface and the aεFab1 surface directly and no binding was observed (data not shown). A dissociation phase lasting 180 s followed all sample injections and the surfaces were fully regenerated by applying two 60 s pulses of 10 mM glycine-HCl pH 2.2. All experiments were run in duplicate and gave highly replicable results.

### **Comparisons of IgE-Fc/derCD23 binding profiles in the presence and absence of $\alpha\epsilon$ Fab1**

The double reference-subtracted sensorgram of derCD23 binding to the His-tag captured IgE-Fc (Figure 3.8.a) was very similar to previously reported IgE-Fc/derCD23 SPR binding profiles; association and dissociation were rapid and the interaction reached steady-state within seconds of the derCD23 injection [39, 89]. The binding profile for derCD23 to  $\alpha\epsilon$ Fab1-bound IgE-Fc (1:1) was markedly different. The association was still rapid, however a steady-state was only achieved at lower derCD23 concentrations. The affinity of the higher-affinity site of derCD23 has been estimated to be around 1  $\mu$ M [88], at concentrations above 1  $\mu$ M the response fell during the derCD23 injection (Figure 3.8.b). The drop indicates a loss of mass at the sensor surface, which can be explained by derCD23-mediated accelerated dissociation of IgE-Fc from  $\alpha\epsilon$ Fab1. The result is indicative of negative cooperativity: that binding of a second derCD23 molecule to the tertiary IgE-Fc complex (one  $\alpha\epsilon$ Fab1 molecule and one derCD23 molecule) weakens the  $\alpha\epsilon$ Fab1/IgE-Fc interaction.

There are many published examples of ligand-induced accelerated dissociation [169, 170, 171, 172, 109], in which the binding of increasing concentrations of a ligand to a complex, increases the rate of complex dissociation. Ligand-induced accelerated dissociation of IgE-Fc complexes is possible (Section 1.3.5); a ligand (DARPin E2.79) was found to increase the rate of an IgE-Fc-receptor complex (IgE-Fc:Fc $\epsilon$ RI $\alpha$ ) [109]. DARPin E2.79-induced accelerated dissociation of IgE-Fc:Fc $\epsilon$ RI $\alpha$  was attributed to competition for subsite attachment points within a ligand-binding site [109]. It is possible, however, that ligand-induced accelerated dissociation can occur as a result of allosteric communication (Section 1.3.5).

### **Steady-state analysis of IgE-Fc/derCD23 binding profiles in the presence and absence of $\alpha\epsilon$ Fab1**

The steady-state responses of derCD23 binding to anti-His-tag-bound IgE-Fc and to  $\alpha\epsilon$ Fab1-bound IgE-Fc were plotted against derCD23 concentration. The data were fit using a one-to-one binding model (Section 2.6.4, Equation 2.17) (Figure

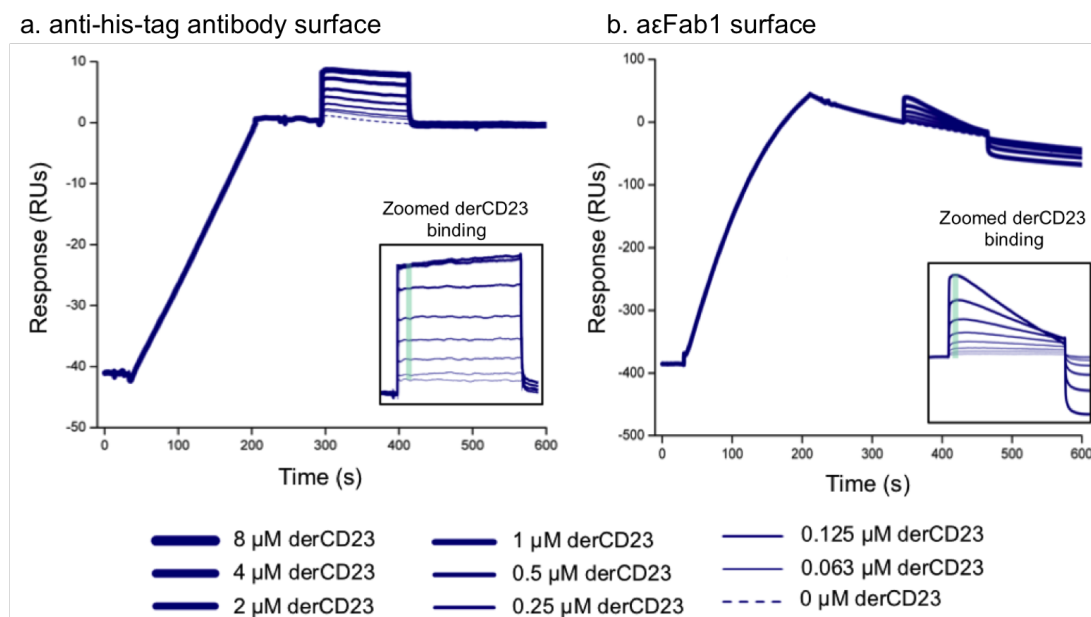


Figure 3.8: SPR sensorgrams of derCD23 binding to (a) His-tagged IgE-Fc and (b)  $\alpha$ εFab1-bound IgE-Fc. A steady-state of binding CD23 to His-tagged IgE-Fc and  $\alpha$ εFab1-bound IgE-Fc at low derCD23 concentrations was achieved. At higher derCD23 concentrations derCD23 caused accelerated dissociation of IgE-Fc from  $\alpha$ εFab1. The boxes show double reference-subtracted data for derCD23 binding in each case. The green indicates the 5 s interval at which steady-state response values were averaged in the equilibrium analysis.

3.9).

Steady-state analysis of the anti-His-bound-IgE-Fc/derCD23 interaction gave an estimated  $K_D$  of  $4.5 \pm 0.5 \mu\text{M}$ . At derCD23 concentrations below 1-2  $\mu\text{M}$  the occupancy of the lower-affinity binding site is low and therefore its overall contributions to the  $K_D$  are less significant. Consequently, it was more appropriate to apply a one-to-one fit to the data from 0-2  $\mu\text{M}$ . The fit to the data was improved (Figure 3.9.b) and the resultant  $K_D$  was  $0.88 \pm 0.1 \mu\text{M}$ , and provided an estimation of the binding of derCD23 to the higher affinity site on IgE-Fc.

In addition to the above considerations, it was also appropriate to perform steady-state analysis on the data collected from the binding of derCD23 to  $\alpha$ εFab1-bound IgE-Fc at lower derCD23 concentrations because at these concentrations there was little or no accelerated dissociation. The data fitted well to a one-to-one binding model, indicating only one derCD23-binding site was occupied (Figure 3.9.b). There was a notable reduction in the steady-state response for the inter-

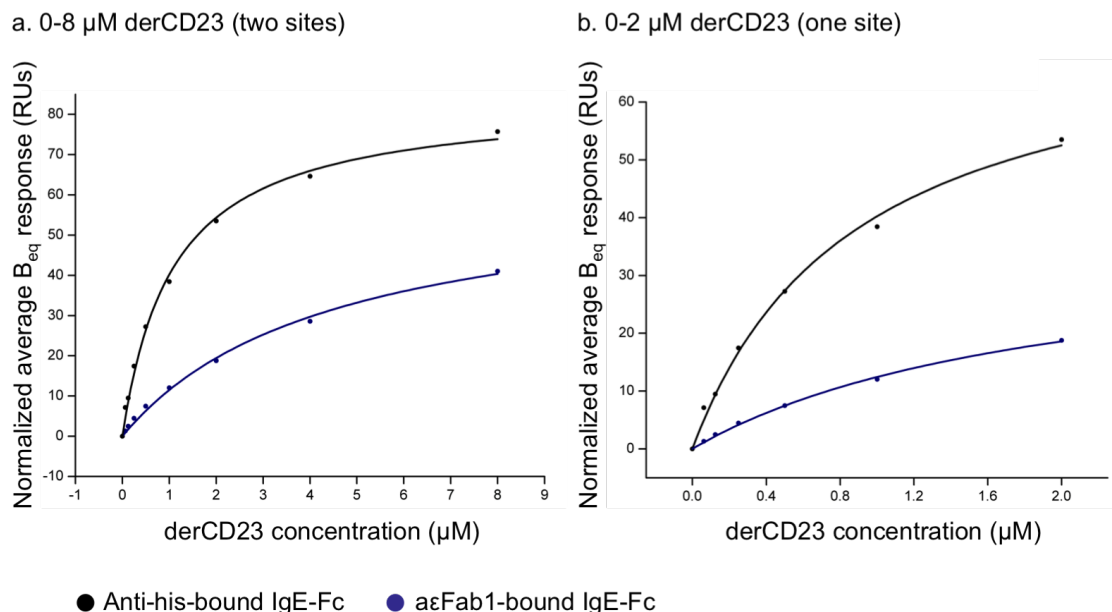


Figure 3.9: **IgE-Fc bound to  $\alpha\epsilon$ Fab1 has a lower capacity and affinity for derCD23.** Steady-state analysis was performed on derCD23/IgE-Fc steady-state binding responses from SPR experiments where IgE-Fc was either pre-bound to an anti-His-tag antibody surface or an  $\alpha\epsilon$ Fab1 surface. A one-site binding model was used to fit data over a range of (a) 0 - 8  $\mu\text{M}$  derCD23 and (b) 0 - 2  $\mu\text{M}$  derCD23. Each fit has been normalised according to the IgE-Fc-capture response.

action between IgE-Fc and derCD23 when IgE-Fc was pre-bound to  $\alpha\epsilon$ Fab1 and when it was not; the normalised  $B_{max}$  values were  $36.9 \pm 2.1$  RUs and  $75.7 \pm 4.1$  RUs respectively. The reduction in  $B_{max}$  indicates that pre-formed  $\alpha\epsilon$ Fab1:IgE-Fc has fewer available derCD23 binding sites. The  $K_D$  of the IgE-Fc/derCD23 interaction was higher when IgE-Fc was bound to  $\alpha\epsilon$ Fab1 compared to when it was not; the  $K_D$  values were  $2.0 \pm 0.2$   $\mu\text{M}$  and  $0.88 \pm 0.1$   $\mu\text{M}$  respectively. These results suggest that the interaction between one  $\alpha\epsilon$ Fab1 molecule and IgE-Fc reduces both the capacity and affinity of IgE-Fc's higher-affinity CD23 binding site.

### 3.2.4 Inhibition studies on the surface of B cells

Cell-based assays were performed in order to investigate how the IgE/CD23 interaction is affected by  $\alpha\epsilon$ Fab1 under homogeneous equilibrium conditions. The cell-based assays that were performed were homogeneous, essentially at equilibrium, and looked at the effect of  $\alpha\epsilon$ Fab1 on the binding of a full length IgE antibody (rIgE, [173]) to the more biologically relevant membrane-bound trimeric



CD23 (mCD23) expressed on the surface of RPMI 8866 cells.

Flow cytometry is a technique that can be used to measure the fluorescence intensity of a single-cell suspension when a fluorescently-labeled antibody binds a specific cell-associated molecule, or a ligand that detects a specific cell-associated molecule (Section 2.7.1). A readout of mean fluorescence intensity (MFI) at 660 nm by flow cytometry was used to investigate the effect of increasing concentrations of  $\alpha\epsilon$ Fab1 on the amount of binding of an Alexa Fluor 647-labeled rIgE (rIgE-A647) to mCD23. Prior to all biological replicates, mCD23 expression on the surface of the cells was confirmed using a FITC-labelled anti-human CD23 (MHM6-FITC, clone F7062, Dako) (data not shown).

### **Dose-dependent inhibition studies**

Preliminary experiments were performed in which a constant number of RPMI 8866 cells were incubated with increasing concentrations of rIgE-A647. Dose-dependent curves, a plot of the mean A647 fluorescence intensity as a function of rIgE-A647 concentration, estimated the  $K_D$  of the interaction between rIgE-A647 and mCD23 to be  $\sim 10$ -20 nM. The inhibition experiments were performed with 12 nM rIgE-A647, because at this concentration the rIgE-A647/mCD23 interaction will be sensitive to the effects of addition of the  $\alpha\epsilon$ Fabs.

12 nM of rIgE-A647 was incubated with a constant number of RPMI 8866 cells in the presence of increasing concentrations of anti-IgE-Fc control Fabs (Xolair Fab mutant 3 and  $\alpha\epsilon$ Fab3) or  $\alpha\epsilon$ Fab1 (Section 2.7.2). The MFI readings of the single-cell suspensions were measured at 660 nm using flow cytometry. 0 % inhibition was defined as the MFI when neither control Fab nor  $\alpha\epsilon$ Fab1 were present. 100 % inhibition was defined as the mean fluorescence intensity when rIgE-A647 was replaced with an A647-labelled antibody with no mCD23 binding activity. The experiments were performed in duplicate and gave good agreement (Figure 3.10).

$\alpha\epsilon$ Fab3 is a monoclonal Fab that binds to IgE-Fc and has no dose-dependent effect on the rIgE/mCD23 interaction in cell-binding assays. Xolair Fab mutant 3 ( $\alpha\epsilon$ FabXol3) also binds to IgE-Fc but it is known to inhibit the IgE/CD23 interaction in a dose-dependent manner (Section 1.3.4) [82]. For both biological replicates,  $\alpha\epsilon$ Fab3 had no dose-dependent effect on the rIgE/mCD23 interaction and

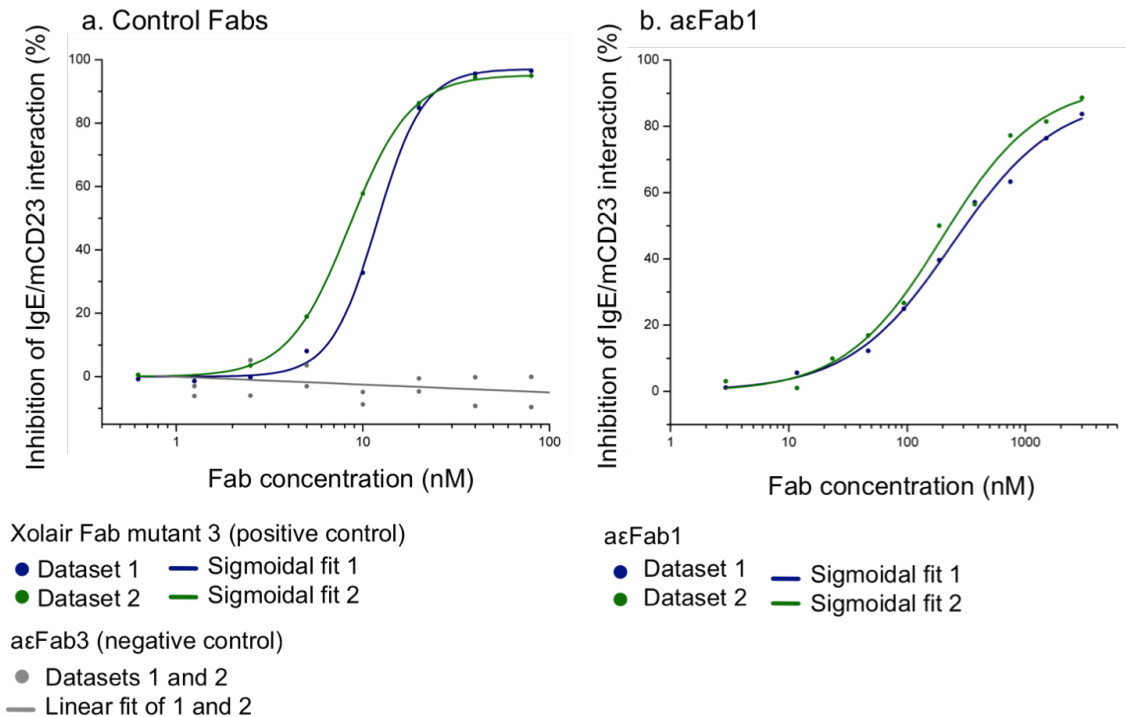


Figure 3.10:  $\alpha\epsilon$ Fab1 caused dose-dependent inhibition of the IgE/CD23 interaction on the surface of B cells. RPMI 8866 cells, constitutively expressing CD23 on their surface were incubated with fluorescently-labeled rIgE (rIgE-A647) and increasing concentrations of (a) control Fabs or (b)  $\alpha\epsilon$ Fab1. The mean fluorescent intensity (MFI) of the single-cell suspensions was measured by flow cytometry. Inhibition of the IgE/CD23 interaction was assumed to be equivalent to the reduction in MFI. The experiments were run in duplicate on different days.

$\alpha\epsilon$ FabXol3 inhibited the interaction in a dose-dependent manner (Figure 3.10.a).

In both biological replicates,  $\alpha\epsilon$ Fab1 inhibited the rIgE/mCD23 interaction in a dose-dependent manner (Figure 3.10.b). The Xolair Fab mutant 3 data and the  $\alpha\epsilon$ Fab1 data fitted well to sigmoidal models and indicate a maximal level of inhibition of around 98 % and 95 % by Xolair Fab mutant 3 and  $\alpha\epsilon$ Fab1, respectively. The concentration of  $\alpha\epsilon$ Fab1 that was required to reach maximum inhibition is above the  $K_D$  of both the higher and lower affinity  $\alpha\epsilon$ Fab1 binding sites on IgE ( $K_{D1} = 95 \pm 6$  nM  $K_{D2} = 1,400 \pm 100$  nM). Since  $\alpha\epsilon$ Fab1 is in molar excess of rIgE-A647 at both 95 and 1,400 nM, the data indicate that both  $\alpha\epsilon$ Fab1 sites must be occupied for maximal inhibition of the rIgE/mCD23 interaction, assuming that the IgE-Fc/ $\alpha\epsilon$ Fab1  $K_D$  values are not significantly altered in this system.

Multiple replicates were performed for the lowest and the highest tested concentrations of  $\alpha\epsilon$ FabXol3 and  $\alpha\epsilon$ Fab1. The lowest concentrations of  $\alpha\epsilon$ FabXol3 and

aεFab1 were 0.125 nM and 0.02 μM, respectively, and both resulted in approximately 0 % inhibition of the rIgE/mCD23 interaction. The highest concentrations for Xolair Fab mutant 3 and aεFab1 were 80 nM and 3 μM, respectively, and resulted in around 95 % and 85 % inhibition, respectively. The mean values of the replicated data agreed with the previous data, and Wilcoxon sum-rank tests [166] suggested that that the 85 % increase in inhibition of the rIgE/mCD23 interaction observed by the addition of 3 μM compared to 0.02 μM is statistically significant ( $p < 0.025$ ) (Figure 3.11). Similarly, Wilcoxon sum rank tests confirmed that the observed 95 % increase in inhibition of the rIgE/mCD23 interaction was statistically significant ( $p < 0.01$ ).

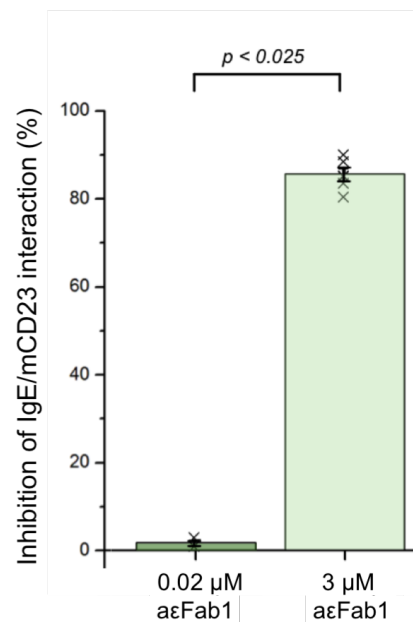


Figure 3.11: **The aεFab1 dose-dependent inhibition of the IgE/CD23 interaction on the surface of (RPMI 8866) B cells is statistically significant.** Wilcoxon sum-rank tests on replicate MFI readings indicate that the ~ 85 % inhibition of the rIgE-A647/mCD23 interaction observed upon incubation with 3 μM of aεFab1 statistically different from the ~ 0 % inhibition of MFI signal observed when only 0.02 μM aεFab1 is incubated with CD23-expressing cells and rIgE-A647. The crosses indicate the individual measurements for each of the replicates, the green bars show the mean averages of the readings, and the error bars show the standard error of the mean.

### 3.2.5 Structural comparisons of derCD23-bound IgE-Fc and $\alpha$ εFab1-bound IgE-Fc

The crystal structures of  $\alpha$ εFab1-bound IgE-Fc [81] and derCD23-bound IgE-Fc [18] were compared to try and understand the basis for  $\alpha$ εFab1 inhibition of derCD23 and derCD23-induced accelerated dissociation of the  $\alpha$ εFab1:IgE-Fc complex. In these comparisons, the structures, or different regions of the structures, were superposed on one another in Pymol using the ‘align’ function. This function performs a sequence alignment of the two structures, or regions of the structures, and then minimises the root mean square deviation (RMSD) between the aligned residues (Equation 3.1).

$$RMSD = \sqrt{(\sum dii^2)/N} \quad (3.1)$$

Where  $dii$  is the distance between the  $i$ th atom of structure 1 and the  $i$ th atom of structure 2 and  $N$  is the number of atoms matched in each structure.

Superpositions may show conformational differences between two states of macromolecule, such as between two ligand-bound states of a protein. However proteins are dynamic and care must be taken to not over interpret these static image comparisons.

#### Binding-site analysis

Both derCD23 and  $\alpha$ εFab1 bind the Cε3 domain of IgE-Fc [39]. Superposition of the derCD23:IgE-Fc(3-4) complex [18] and the  $\alpha$ εFab1:IgE-Fc complex [81] upon the Cε4 domain pairs (Section A.1) revealed that the derCD23 and  $\alpha$ εFab1 binding sites are non-overlapping (Figure 3.12). Additionally, the derCD23 and  $\alpha$ εFab1 molecules occupy distinct space, which suggests that  $\alpha$ εFab1 inhibition of derCD23-binding to IgE-Fc, and derCD23-mediated accelerated dissociation of  $\alpha$ εFab1 from IgE-Fc are allosterically driven.

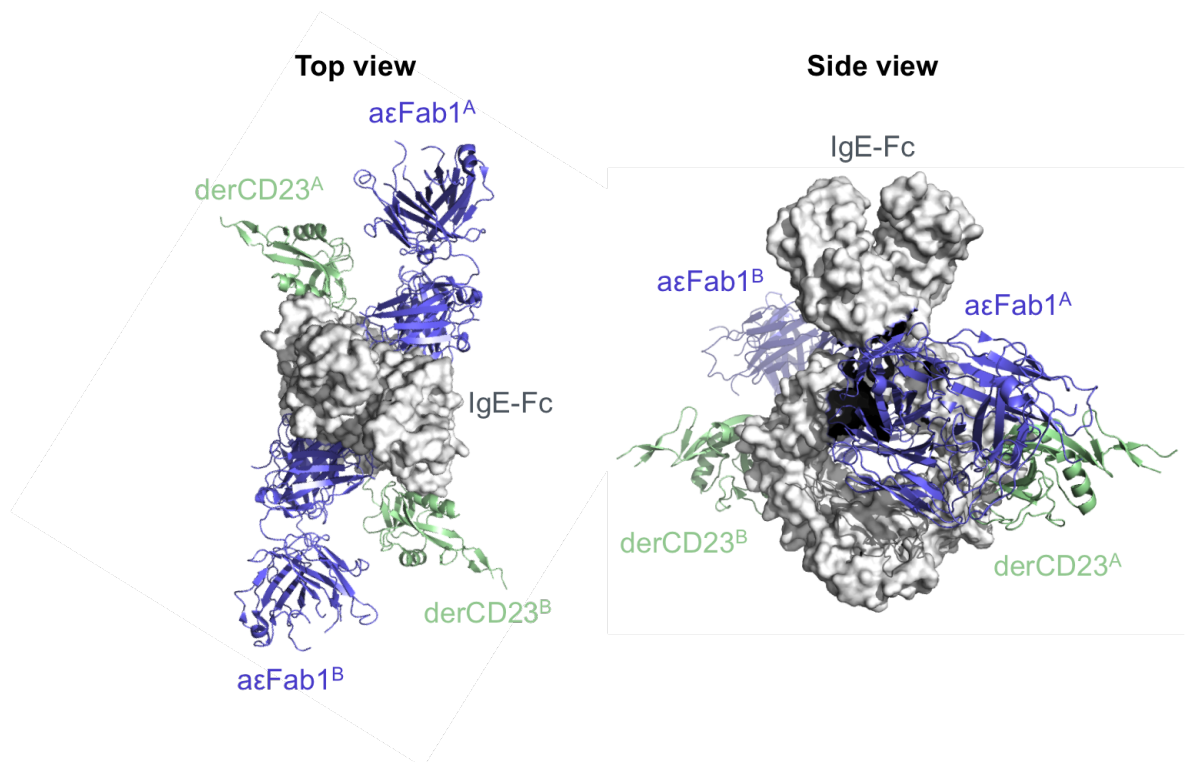


Figure 3.12: **Superposition of derCD23-bound IgE-Fc onto  $\alpha$ εFab1-bound IgE-Fc upon the C $\epsilon$ 4 domains suggests that the CD23 and  $\alpha$ εFab1 binding sites are spatially distinct and non-overlapping.** Superposition was performed in Pymol using the ‘align’ function.  $\alpha$ εFab1-bound IgE-Fc structure PDB ID: 4J4P, derCD23-bound IgE-Fc (3-4) structure PDB ID: 4EZM

### Inter-domain angle comparison

The movement of C $\epsilon$ 3 domains upon the C $\epsilon$ 4 domain pair is thought to contribute to the reciprocal allosteric inhibition of CD23 and Fc $\epsilon$ RI-binding to IgE-Fc (Section 1.3.1) [18, 89]. The crystal structure of IgE-Fc (3-4) bound to two derCD23 molecules represents the most ‘closed’ conformation of IgE-Fc (3-4) described [18], in which both C $\epsilon$ 3-C $\epsilon$ 4 inter-domain angles are acute. The crystal structure of IgE-Fc bound to two  $\alpha$ εFab1 molecules, however, is the most ‘open’ IgE-Fc conformation that has been published to date (Figure 3.13) [81].

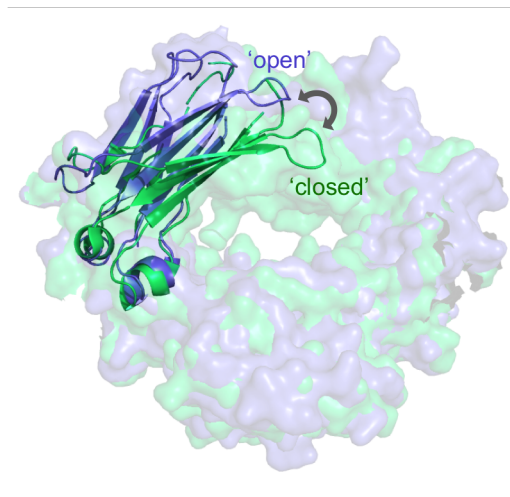


Figure 3.13: **Superposition of the derCD23 bound IgE-Fc (3-4) and  $\alpha$ Fab1-bound IgE-Fc (3-4) shows that the C $\epsilon$ 3 domains differ in the extent of their openness.** IgE-Fc (3-4) of the derCD23-bound crystal structure (green) was superposed onto the IgE-Fc (3-4) of the  $\alpha$ Fab1-bound crystal structure (blue) upon the C $\epsilon$ 4 domain pair. One C $\epsilon$ 3 domain from each symmetrical complex is depicted in cartoon representation. IgE-Fc is shown in surface representation.  $\alpha$ Fab1-bound IgE-Fc structure PDB ID: 4J4P, derCD23-bound IgE-Fc (3-4) structure PDB ID: 4EZM.

Superpositions of the ‘closed’ derCD23-bound IgE-Fc (3-4) crystal structure and the ‘open’  $\alpha$ Fab1-bound IgE-Fc crystal structure upon one or the other C $\epsilon$ 3 domains were performed *i.e.* each chain of  $\alpha$ Fab1-bound IgE-Fc was superposed onto the derCD23-bound IgE-Fc structure by alignment of each C $\epsilon$ 3 domain (Section A.1) and *visa versa*. The comparisons show that steric clashes could potentially prevent optimal binding of both ligands at the same time. The ‘Show Bumps’ Pymol script [174] was used to determine the steric clashes (default settings). The superposition shows both derCD23 molecules clash with the open C $\epsilon$ 3 domains and the C $\epsilon$ 4 domains of the IgE-Fc chain to which they would bind (Figure 3.14.a). Similarly, in the closed derCD23-bound conformation, the images indicate each  $\alpha$ Fab1 molecule could clash with the C $\epsilon$ 3 domain of the opposite chain to which it is bound (Figure 3.14.b).

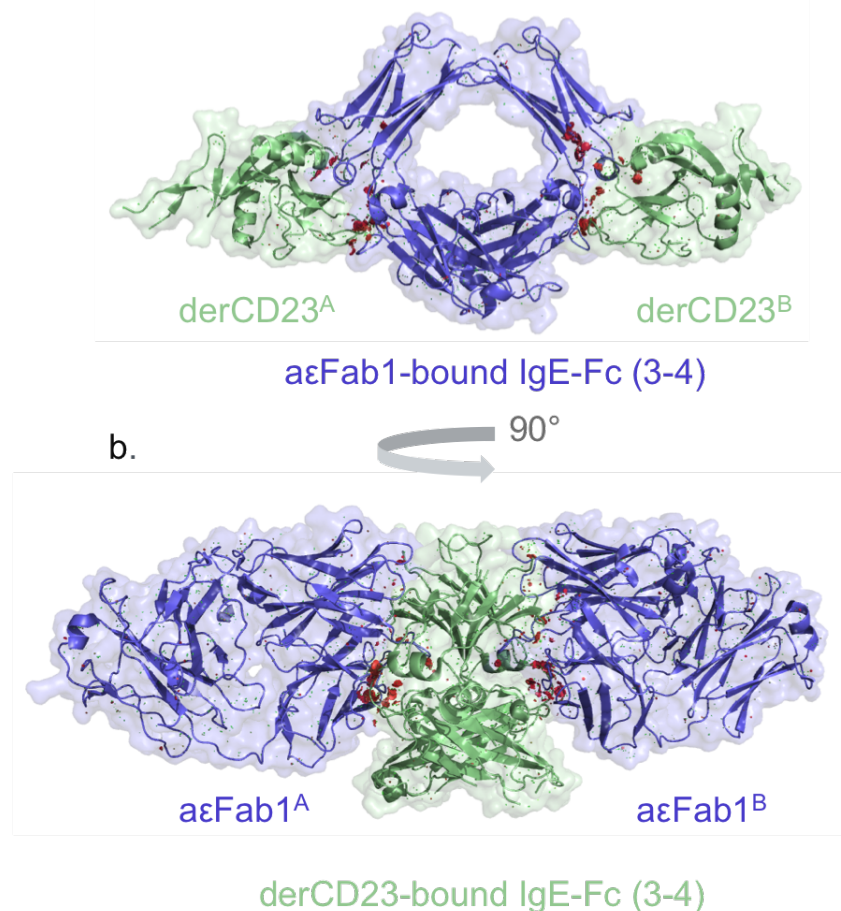


Figure 3.14: **Superposition images of the derCD23 (green) and  $\alpha\epsilon$ Fab1 (blue) complexes with IgE-Fc(3-4) show mutual incompatibility of optimal binding.** The complexes were superposed on their C $\epsilon$ 4 domain pairs. (a) Steric clashes between derCD23 and C $\epsilon$ 3-4 of the  $\alpha\epsilon$ Fab1:IgE-Fc (3-4) complex are shown in red. (b) Steric clashes between  $\alpha\epsilon$ Fab1 and C $\epsilon$ 3-4 of the derCD23:IgE-Fc (3-4) complex are shown in red. The steric clashes were determined using the pymol script ‘show bumps’ [174].  $\alpha\epsilon$ Fab1-bound IgE-Fc structure PDB ID: 4J4P, derCD23-bound IgE-Fc (3-4) structure PDB ID: 4EZM. There is a 90 degree rotation of IgE-Fc between (a) and (b).

### C $\epsilon$ 3 domain comparison

The C $\epsilon$ 3 domain, to which both  $\alpha\epsilon$ Fab1 and CD23 bind, is highly dynamic [78]. Different ligands may bind to/induce different C $\epsilon$ 3 conformations, which could have an impact on the degree of C $\epsilon$ 3 opening and closing, as well as on the coordination of residues at various ligand binding sites within the domain. The C $\epsilon$ 3 domains (Section A.1) of the derCD23/IgE-Fc(3-4) complex and the  $\alpha\epsilon$ Fab1/IgE-Fc complex were superposed with a RMSD of matched atoms of 0.7 Å (Figure 3.15). C $\epsilon$ 3 has two cysteine residues that form an intra-domain disulphide bond,

in the superposition the difference in the distance between the two C $\alpha$  atoms of these cysteine residues for the  $\alpha\epsilon$ Fab1-bound C $\epsilon$ 3 and the derCD23-bound C $\epsilon$ 3 was 0.2 Å. The difference in the distance between C $\alpha$  atoms of E412 and R440, two residues important in CD23 binding [18], was 1.6 Å; greater than the RMSD. A large change in coordination of derCD23-binding residues, as described in the superposed  $\alpha\epsilon$ Fab1-bound structure, could negatively affect CD23 binding. The superposition also showed shifts of 1.3-2.2 Å in the C $\alpha$  atoms of residues involved in  $\alpha\epsilon$ Fab1 binding in the derCD23-bound structure. The observed change in position of the  $\alpha\epsilon$ Fab1-binding residues in the CD23-bound structure may disrupt  $\alpha\epsilon$ Fab1 binding.

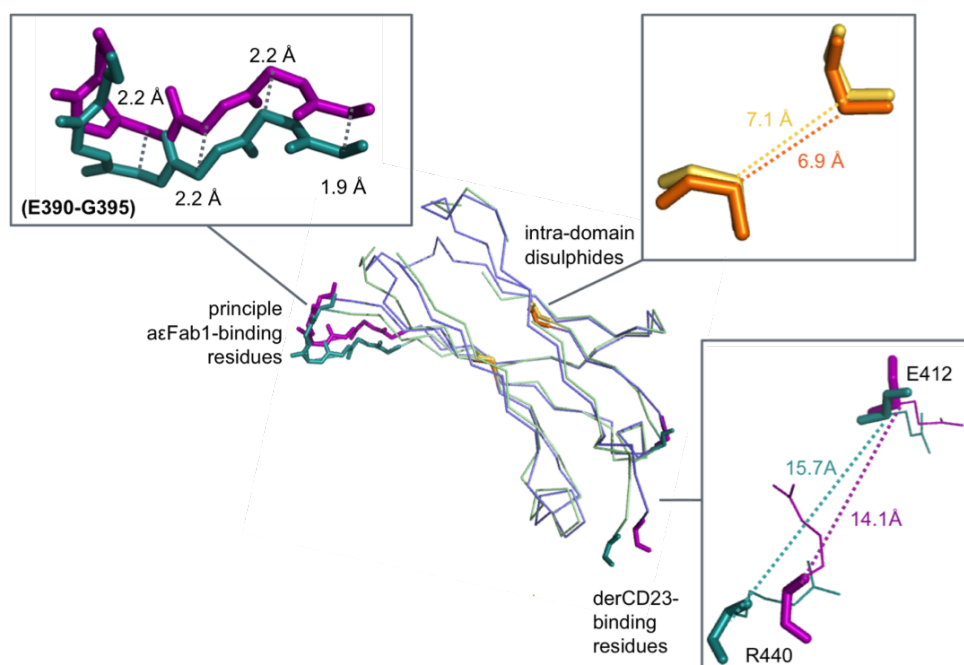


Figure 3.15: **Superposition images of the C $\epsilon$ 3 of derCD23-bound IgE-Fc (3-4) (green) and  $\alpha\epsilon$ Fab1-bound (blue) IgE-Fc shows mutual incompatibility of optimally coordinated binding sites.** The C $\epsilon$ 3 domains were superposed upon one another in Pymol with an RMSD of 0.7 Å. Shifts in key residues of the  $\alpha\epsilon$ Fab1 binding site and the derCD23 binding site were greater than the overall RMSD. These shifts could prevent optimal coordination of both molecules simultaneously. The C $\epsilon$ 3 domains used in this superposition were from the  $\alpha\epsilon$ Fab1-bound IgE-Fc structure, PDB ID: 4J4P, and the derCD23-bound IgE-Fc (3-4) structure, PDB ID: 4EZM.



### 3.2.6 The effect of Cε3 rigidification on allosteric communication between $\alpha$ εFab1 and CD23 binding sites

In the SPR experiments described in Section 3.2.3, derCD23 was found to cause accelerated dissociation of IgE-Fc from immobilised  $\alpha$ εFab1. Further SPR experiments were performed by Dr Seema Mayank to determine if reducing the conformational flexibility of the Cε3 domain has an effect on the accelerated dissociation. Disulphide-stabilised IgE-Fc (dssIgE-Fc) is a mutant form of IgE-Fc in which each Cε3 domain has been rigidified through the introduction of an additional intra-domain disulphide bond. L340 and R341 of the Cε3 domain of IgE-Fc were mutated to cysteine residues and their close proximity allowed for disulphide bond formation (Figure 3.16). Isolated Cε3 exists as a molten globule [78], 1-anilino-8-naphthalene sulphonate (ANS) binding studies showed the disulphide-stabilised Cε3 domain to be less molten globule-like than wildtype Cε3. Moreover,  $\{^1\text{H}\}$ ,  $^{15}\text{N}$ -heteronuclear nuclear Overhauser effect studies indicated that the extra disulphide bond reduced Cε3 backbone dynamics (unpublished data).

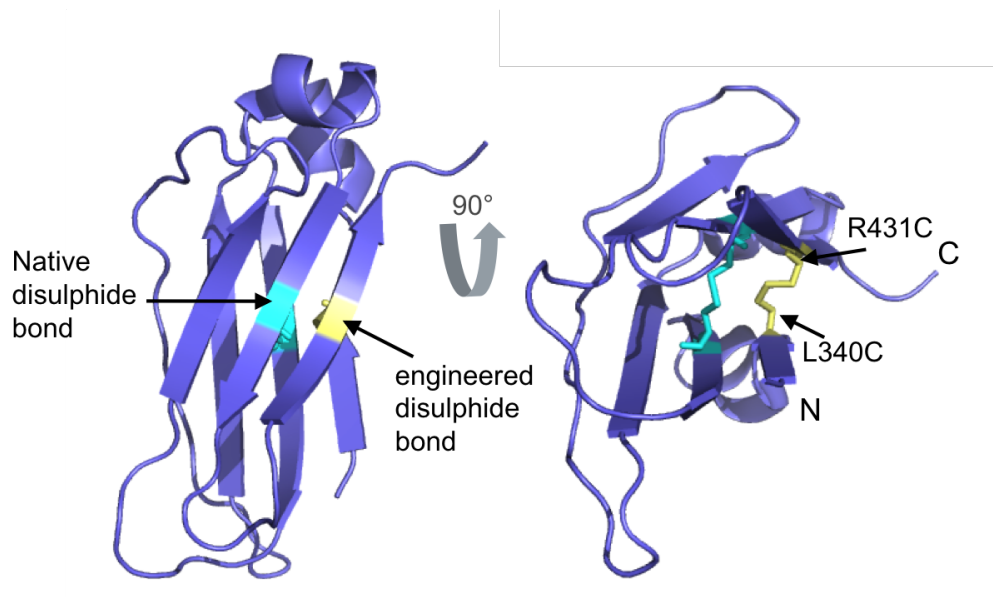


Figure 3.16: **Model of the Cε3 disulphide-stabilised IgE-Fc (dssIgE-Fc)**. In native IgE-Fc a disulphide forms between C358 and C418 of Cε3 (aqua). dssIgE-Fc was engineered, by Dr Seema Mayank, to contain an additional disulphide bond in the Cε3 domain (yellow), through the introduction of L340C and R431C mutations. The Cε3 domain was taken from the IgE-Fc structure 1O0V, and the mutations were made in Pymol. The image shows the dssCε3 model from two perspectives that are rotated 90 degrees from one another.

IgE-Fc or dssIgE-Fc were captured by  $\alpha$ Fab1 immobilised on the surface of a sensor chip and His-tagged IgE-Fc was captured by an anti-His-tag surface to be used as a control for unperturbed derCD23 binding. derCD23 was injected at various concentrations over the two surfaces. As previously observed, the signal decreased when derCD23 bound  $\alpha$ Fab1-captured IgE-Fc but not when it bound anti-His-captured His-IgE-Fc (Figure 3.17). The signal also decreased when derCD23 bound  $\alpha$ Fab1-captured dssIgE-Fc, but at a slower rate to  $\alpha$ Fab1-captured IgE-Fc. A decrease in signal may result from loss of mass at the surface but also from performing a reference subtraction with the sensorgram from a surface that non-specifically bound higher amounts of analyte than the experimental surface. If IgE-Fc and dssIgE-Fc bound non-specifically and variably to the reference surface, this may have given rise to the difference in the rate of signal decrease on derCD23 injection. Inspection of the reference surface sensorgrams showed neither IgE-Fc or dssIgE-Fc bound to the reference surface non-specifically, and therefore the effect is not a result of differential non-specific binding. Instead, we suggest that the difference in the rate of signal decrease may be due to a differential rate of loss of IgE-Fc/dssIgE-Fc from  $\alpha$ Fab1 and that derCD23-induced accelerated dissociation of  $\alpha$ Fab1 from IgE-Fc is dependent on the flexibility of the C $\epsilon$ 3 domain (Figure 3.18).

The sensorgrams for the binding of 5  $\mu$ M derCD23 to  $\alpha$ Fab1-captured IgE-Fc and dssIgE-Fc both show an apparent increase in response during the dissociation phase following the derCD23 injection, once the respective control sensorgrams (0  $\mu$ M derCD23) have been subtracted (Figure 3.18). However, this phenomenon is *not* due to molecules associating to the  $\alpha$ Fab1/IgE-Fc complex during the dissociation phase, it is due to the subtractions of the control surface (routinely used in SPR to control for bulk refractive indices from injected buffers). The upward trend in the dissociation phase is a result of slower dissociation of IgE-Fc from  $\alpha$ Fab1 occurring after derCD23-mediated accelerated dissociation compared to the dissociation of IgE-Fc from  $\alpha$ Fab1 in the absence of accelerated dissociation; this is clearly seen in Figure 3.17.b. The upward trend in the dissociation phase is an inevitable consequence of an accelerated dissociation event. The most extreme version of this phenomenon would be seen if accelerated dissociation stripped away *all*

of the bound IgE-Fc; in that case the amount of apparent association occurring in the dissociation phase would be equal to the amount of dissociating material from the control surface.

In the case of derCD23-mediated acceleration of the  $\alpha\epsilon$ Fab1/IgE-Fc complex, the observed effects during the dissociation phase are somewhat more complicated due to the heterogeneity of the system. The population of IgE-Fc molecules that remain bound to  $\alpha\epsilon$ Fab1 after accelerated dissociation is more stably bound than the overall (unperturbed) population of IgE-Fc molecules bound to  $\alpha\epsilon$ Fab1. This indicates that IgE-Fc/ $\alpha\epsilon$ Fab1 complexes cannot be structurally homogeneous. The simplest explanation for this heterogeneity would be the two different  $\alpha\epsilon$ Fab1 binding sites present on the IgE-Fc homodimer, each with distinct affinities [81] If derCD23-mediated accelerated dissociation was more effective at dissociating IgE-Fc from the weaker  $\alpha\epsilon$ Fab1 binding site than the stronger  $\alpha\epsilon$ Fab1 binding site, then the remaining population of bound IgE-Fc after accelerated dissociation would be expected to show slower dissociation than the overall heterogeneous population. The conformational heterogeneity of IgE-Fc and its implications on receptor binding are discussed further in Chapter 6.

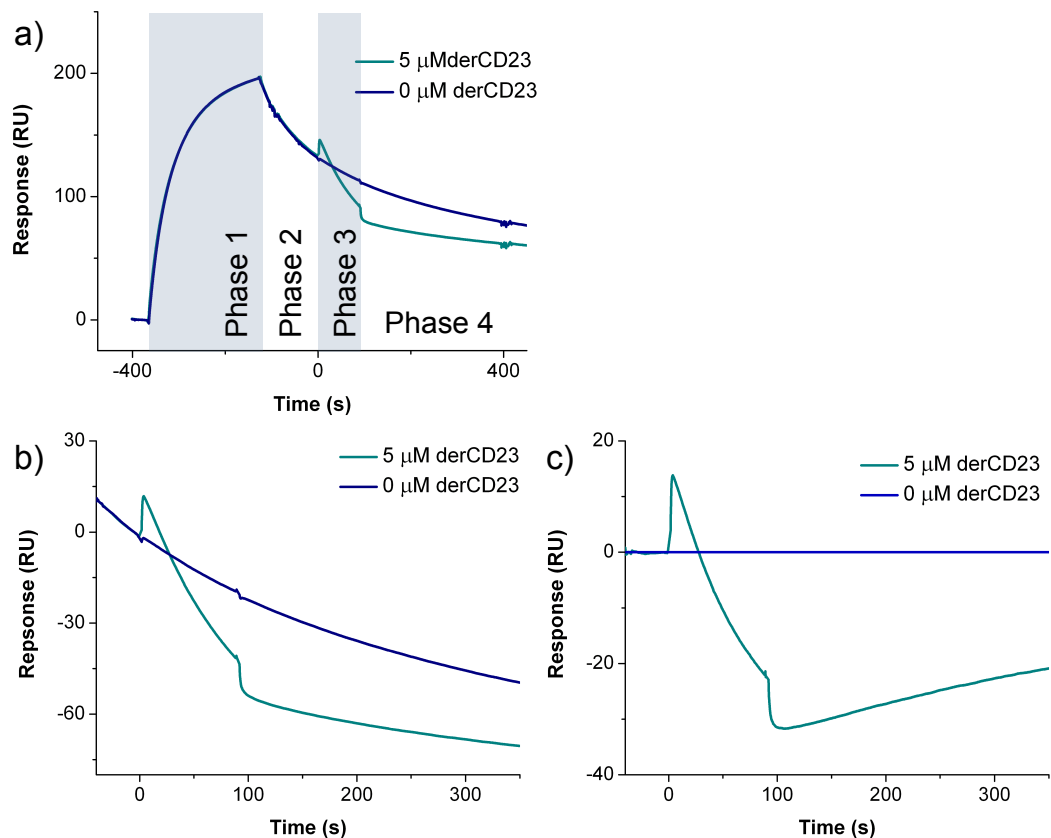


Figure 3.17: **SPR sensorgrams showing derCD23-mediated accelerated dissociation of wildtype IgE-Fc from  $\alpha$ εFab1.** (a) IgE-Fc was injected over the  $\alpha$ εFab1 surface (phase 1) and then buffer was injected over the surface during a short dissociation phase (phase 2). 5  $\mu$ M derCD23 or 0  $\mu$ M derCD23 was then injected over the  $\alpha$ εFab1:IgE-Fc (1:1) complex (phase 3), followed by a dissociation phase (phase 3) in which only buffer was injected over the surface. The derCD23 injection and dissociation phases are enlarged in (b) and show that when 0  $\mu$ M derCD23 was injected over the  $\alpha$ εFab1-captured IgE-Fc there was no change increase in response. Subtracting the 0  $\mu$ M derCD23 sensorgram from the 5  $\mu$ M derCD23 sensorgram removes changes in response that occurred as a result of the inherent dissociation of IgE-Fc from the  $\alpha$ εFab1 surface (c). When 5  $\mu$ M derCD23 was injected over the  $\alpha$ εFab1-captured IgE-Fc there was an initial increase in response that was quickly followed by a decrease in response, indicating binding followed by the accelerated dissociation of IgE-Fc from  $\alpha$ εFab1.

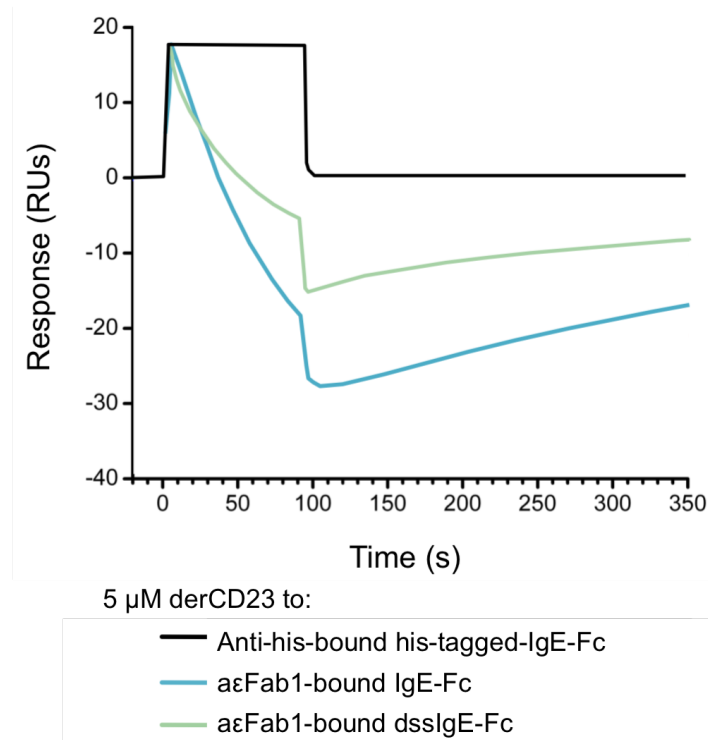


Figure 3.18: **Rigidifying the C $\epsilon$ 3 domain of IgE-Fc reduces the effect of derCD23-mediated accelerated dissociation from  $\alpha\epsilon$ Fab1.** SPR sensorgrams of the effect of binding 5  $\mu$ M derCD23 to  $\alpha\epsilon$ Fab1-bound IgE-Fc, with a wildtype or rigidified (dssIgE-Fc) C $\epsilon$ 3 domain. derCD23 does not induce accelerated dissociation of IgE-Fc from an anti-His-tag antibody.

### 3.3 Discussion

The mutual inhibition of receptor binding to IgE-Fc is associated with the movement of the C $\epsilon$ 3 domains upon the C $\epsilon$ 4 domain pair [18]. Crystal structure comparisons suggest that derCD23 binds a closed form of IgE-Fc that cannot bind Fc $\epsilon$ RI, and Fc $\epsilon$ RI binds an open form of IgE-Fc that cannot bind CD23 (Section 1.3.1) [18]. This study provides another example in which opening and closing of the C $\epsilon$ 3 domain could act as a means of allosteric communication between two sites within IgE. Furthermore, the study alludes to an additional or alternative mechanism of allosteric communication in IgE-Fc that involves rearrangements within the intrinsically flexible C $\epsilon$ 3 domains, and which affect the positioning of key CD23 and  $\alpha\epsilon$ Fab1 binding residues.

The results of the SPR and cell-based binding studies show that  $\alpha\epsilon$ Fab1:IgE-Fc (1:1) complexes have a reduced affinity (negative cooperatively with respect to

CD23) and capacity for CD23 binding, and increasing concentrations of  $\alpha$ εFab1 inhibit the interaction of IgE and CD23 on the surface of cells, respectively. The data indicate that saturation of the first  $\alpha$ εFab1 binding site on IgE-Fc has an inhibitory effect on the interaction between IgE-Fc and CD23, but that the binding of two  $\alpha$ εFabs to IgE-Fc is required for maximal inhibition. To have greater confidence in the effect of  $\alpha$ εFab1 stoichiometry on CD23 inhibition one could perform the cell-binding assays with IgE in molar excess of  $\alpha$ εFab1, ensuring only a one-to-one  $\alpha$ εFab1:IgE-Fc stoichiometry. However, this is hard to do in practice since this would require working at  $\mu$ M concentrations of IgE, and therefore at IgE/mCD23 saturating conditions.

Comparisons of the  $\alpha$ εFab1:IgE-Fc X-ray structure [81] and the derCD23:IgE-Fc (3-4) X-ray structure [18] show that derCD23 and  $\alpha$ εFab1 binding sites are non-overlapping and that their binding is spatially distinct, thereby supporting the hypothesis that  $\alpha$ εFab1 works allosterically to inhibit the CD23/IgE interaction. Cε3 domain opening and closing could be involved in allosterically inhibiting the interaction. Potential steric clashes with IgE-Fc(3-4) would prevent CD23 binding optimally to an open  $\alpha$ εFab1:IgE-Fc complex, or  $\alpha$ εFab1 binding optimally to a closed CD23:IgE-Fc complex (Section 3.2.5). Molecular dynamic simulations that take thermal fluctuations into account would help to validate the clashes [175].

Additional data are required to test the hypothesis that allosteric-communication between the  $\alpha$ εFab1 and CD23 binding sites in IgE is mediated by Cε3 domain opening and closing. SPR binding studies of  $\alpha$ εFab1 and derCD23 to mutant IgE constructs that are locked in either ‘open’ or ‘closed’ states could help interrogate the hypothesis. However, ‘open’ and ‘closed’ states of IgE-Fc can be subtly different [77] and molecular dynamics indicate the energy landscape of IgE-Fc is complex [81]. There is a danger in thinking of ‘open’ and ‘closed’ states as being binary; for example IgE-Fc ‘closed’ and ‘open’ mutants may not be representative of the ‘closed’ derCD23-bound IgE-Fc state or the  $\alpha$ εFab1-bound state, in terms of exact conformation or thermodynamic profile, both of which could affect their ability to bind ligands. NMR spectroscopy could be used to compare differences in IgE-Fc dynamics upon titration of  $\alpha$ εFab1 and derCD23. Such titration experiments would provide a wealth of knowledge about the conformational and dynamic changes as-

sociated with allosteric communication between the  $\alpha\epsilon$ Fab1 and derCD23 binding sites. However, IgE-Fc is a challenging NMR target and as of yet no NMR studies of IgE-Fc have been published.

Additional structural comparisons investigating C $\epsilon$ 3 domain conformations in isolation indicate that allosteric communication between the CD23- and  $\alpha\epsilon$ Fab1-binding sites may additionally, or alternatively, involve intra-domain rearrangements (Section 3.2.5). C $\epsilon$ 3 superposition reveals significant conformational shifts in key residues involved in the either  $\alpha\epsilon$ Fab1 or CD23 binding sites, when one or the other site is occupied. The C $\epsilon$ 3 domain exhibits a high degree of conformational flexibility that would facilitate such intra-domain motions [78]. The fact that it is possible to limit CD23-mediated accelerated dissociation of  $\alpha\epsilon$ Fab1 from IgE-Fc by rigidifying the C $\epsilon$ 3 domain supports the notion that conformational changes within the C $\epsilon$ 3 domain itself could contribute to this mechanism of allosteric communication (Section 3.2.6). The current literature largely explains allostery in IgE-Fc in terms of rigid-body motions and this study highlights that intra-domain movements may also contribute to allostery in IgE and should be explored in the future.

The SPR studies showed that not only can  $\alpha\epsilon$ Fab1 inhibit the interaction between IgE-Fc and derCD23, but derCD23 can negatively affect the kinetics of the IgE-Fc/ $\alpha\epsilon$ Fab1 interaction (Section 3.2.3). The IgE receptors themselves reciprocally inhibit the binding of the other to IgE-Fc allosterically [18, 89], which prevents soluble CD23 from cross-linking Fc $\epsilon$ RI-bound IgE-Fc on the surface of mast cells and basophils, which would otherwise result in anaphylaxis (Section 1.1.1). Here, however, we describe a form of mutual inhibition in IgE-Fc in which simultaneous binding of inhibitors can occur. The SPR experiments performed in this study showed that derCD23 bound the  $\alpha\epsilon$ Fab1:IgE-Fc complex and induced accelerated IgE-Fc dissociation from  $\alpha\epsilon$ Fab1 (Section 3.2.3). Both allostery and facilitated dissociation can describe ligand-induced accelerated dissociation (Section 1.3.5) [172, 109]. Facilitated dissociation, in which the ligand competes for a subset of ligand attachment points that become exposed during partial complex dissociation, was used to describe how the protein DARPin E2.79 accelerates the dissociation of IgE-Fc from its Fc $\epsilon$ RI receptor [109]. Here we show that ligand-induced accelerated dissociation of IgE-Fc complexes can occur via an allosteric mechanism.

Therapeutics with the ability to destabilise pre-formed IgE-Fc:receptor complexes could potentially have increased efficacy (Section 1.3.5) and so the fact that it is possible to induce accelerated dissociation of IgE-Fc complexes via allosteric means is particularly interesting.



# Chapter 4

## Anti-IgE antibody discovery

### 4.1 Introduction

By gaining a comprehensive understanding of allostery in IgE-Fc it may be possible to start to harness it therapeutically in the design of drugs for allergy and asthma. Characterising antibodies that modulate IgE-Fc structure and function has been validated as a method to identify mechanisms of allostery in IgE-Fc [81] (Section 1.3.3). Generating allosteric modulators with varied effects on IgE-Fc structure and function will provide a deeper comprehension of its allosteric nature. Projects to screen for antibodies that affect the IgE-Fc/FcεRI interaction were already in progress in an ongoing collaboration between KCL and UCB. Finding and characterising antibodies that affect the IgE-Fc/CD23 interaction could potentially contribute to our understanding of allostery in IgE-Fc (Section 1.5). Using UCB's Core Antibody Discovery Process, a number of antibodies were generated that bind IgE-Fc and modulate the interaction between IgE-Fc and CD23. The panel of antibodies were again tested for their ability to bind IgE-Fc and modulate the IgE-Fc/CD23 interaction using surface plasmon resonance (SPR). The aim was to identify antibodies that bind IgE-Fc with a high affinity and have a range of effects on the IgE-Fc/CD23 interaction. 15 anti-IgE antibodies (αAbs) were selected for their expression as αFabs and for further selection on the basis of biophysical analysis.

Antibodies are composed of a constant Fc region that binds to receptors and a Fab region that is responsible for antigen binding activity (Figure 4.1). The Fab region is composed of heavy and light chains (which can be of two types, kappa or

lambda), each chain has a single constant and a single variable domain. The variable domains contain the antigen binding site, and are comprised of a set of three complementary determining regions (CDRs) which have highly variable sequences and are critical for antigen specificity. The immense repertoire of antigen binding sites is largely generated by the combinatorial assembly of germline-encoded variable domain gene segments. This process, known as V(D)J recombination, occurs in developing B cells and generates a diverse set of naive B cells that can then express functioning antibodies on their surface. The third complementarity region (CDR3) is composed of V, (D) and J sections and is the most diverse of the three CDRs. Specific binding of antigen to antibodies expressed on the surface of naive B cells triggers somatic hypermutation in the V region genes, and mutations that increase the affinity of the antibody for the antigen are selected for [1].

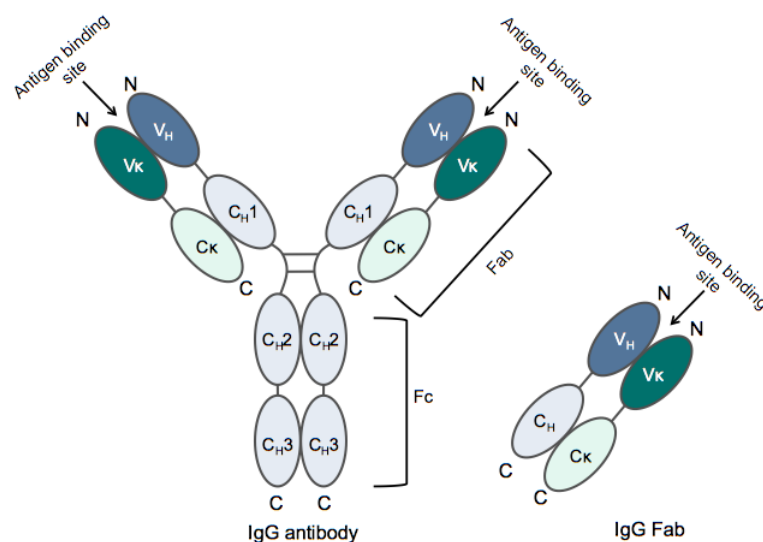


Figure 4.1: **Schematic representation of a full-length IgG antibody and an IgG Fab.** IgG antibodies and IgG Fabs are composed of heavy and light chains. IgG antibodies have three regions, an Fc region and two Fab regions. The Fc region is composed of two constant domains from two heavy chains. The Fab region is composed of heavy chain domains and a light chain. There are two types of light chain; kappa and lambda light chains. The heavy chain of a Fab is composed of a constant domain ( $C_H1$ ) and a variable domain ( $V_H$ ). The light chain, which is a kappa light chain in this example, is also composed of a constant domain ( $C_K$ ) and a variable domain ( $V_K$ ). Antigen binds to the variable domains, whose high sequence diversity is crucial for antigen affinity and specificity.

Because of their incredible diversity and high specificity monoclonal antibodies are powerful tools in research and the diagnosis and treatment of diseases [176].

Hybridoma technology has traditionally been instrumental in the discovery of mAbs with desired specificities [177, 178]. Antibody-producing B cells, generally from subjects exposed to the antigen of interest, are fused with myeloma cells to generate hybridomas, which can still produce antibodies but have an extended lifetime and greater reproductive ability than B cells in culture. The hybridomas are then screened for the production of antibodies with the desired characteristics [177]. Hybridoma technology, however, is restricted by the poor efficiency of the fusion process [179], which in turn narrows the B cell repertoire that can be screened.

Phage display technology is an alternative to hybridoma technology, in which recombinant libraries of antibodies or antibody fragments are displayed on the surface of bacteriophage. This technique allows rapid antibody selection through methods such as enzyme-linked immunosorbent assays (ELISAs) and provides a direct link between phenotype and genotype [180]. The libraries can be made from a range of different sources and do not require immunisation. The libraries can be displayed on a range of platforms other than phage, including; yeast, mammalian cells and ribosomes [181]. Phage display technologies can screen vast numbers of antibody genes and circumnavigate the hybridoma process, however the natural cognate heavy and light chain pairings are usually lost, which can result in the generation of lower affinity antibodies and antibodies with undesirable physical properties [180, 147].

To navigate the issues associated with hybridoma and display technologies a number of single B cell approaches have been developed [176]. Single B cell approaches involve screening B cells for the production of antibodies of interest, isolation of B cells expressing the antibodies of interest, isolating the complementary DNA (cDNA) for those antibodies, then cloning and expressing the antibodies *in vitro*. UCB's Core Antibody Discovery Process achieves this by linking a B cell culture method to homogeneous assay screening [146], positive B cell picking and a sensitive PCR process [147], to ultimately isolate cognate antibody variable regions of interest [146] (Figure 4.2).

UCB's Core Antibody Discovery Process is highly automated and allows screening in excess of 1 billion different immune B cells for the production of antibodies with desired binding specificities. The high-throughput nature of the process per-

mits a very wide, and highly efficient, screen of the immune B cell repertoire, in which only a very small percentage of relevant and suitable heavy and light chain pairings may reside [148].

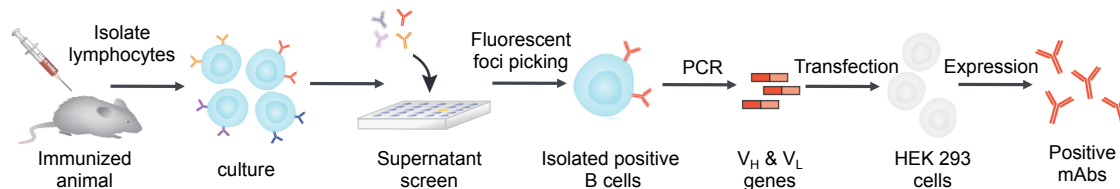


Figure 4.2: **Schematic representation of the workflow for UCB’s Core Antibody Discovery Process.** Lymphocytes from three New Zealand White rabbits, immunised against IgE-Fc, were seeded into 150 96-well culture plates (50 per animal) at a density of  $\sim 5,000$  cells per well ( $\sim 7.2 \times 10^7$  lymphocytes in total).

## 4.2 Results

### 4.2.1 Primary fluorescence-based homogeneous screening

Three New Zealand White rabbits (*Oryctolagus cuniculus*) were immunised subcutaneously with IgE-Fc in order to elicit an immune response against IgE-Fc (Section 2.5.1). Using UCB’s Core Antibody Discovery Process, the peripheral blood from these animals was used to set up B cell cultures in 96-well culture plates (Section 2.5.2) [148]. The B cells were cultured for one week to allow enough time for clonal expansion, antibody expression and secretion (Section 2.5.3) [147]. The immunisations and sample preparation were performed by Victoria O’ Dowd of UCB. Using a fluorescence-based homogeneous assay, the B cell supernatants were screened for containing antibodies that bind IgE-Fc (Section 2.5.4).

The primary homogeneous assay consisted of three components: biotinylated IgE-Fc bound to streptavidin-coated beads, B cell supernatant (containing expressed antibodies), and a fluorescently-labeled antibody that binds rabbit IgG-Fc (Goat Anti-Rabbit IgG, Fc fragment specific F(ab’)<sub>2</sub>, Alexa Fluor 488-conjugated, Jackson ImmunoResearch, 111-546-046). The components were incubated for an hour in the dark and the fluorescence intensity around the beads was measured using the TTP Labtech Mirrorball<sup>®</sup> fluorescence cytometer. The Mirrorball<sup>®</sup> fluorescence cytometer detects beads and measures the fluorescence intensity around

those beads. Bead-localised fluorescence was used as an indication of the presence of an anti-IgE-Fc antibody in the supernatant (Figure 4.3).

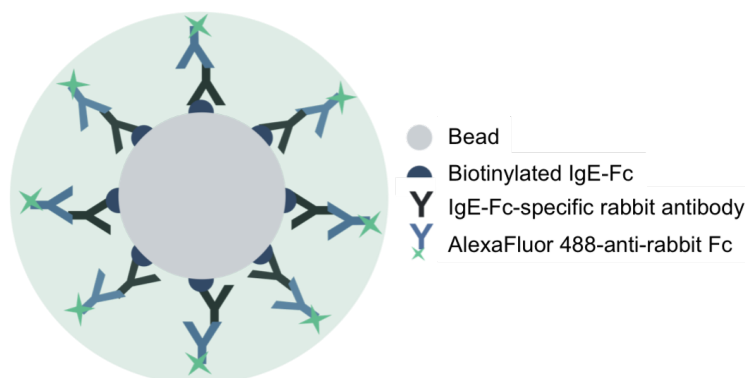


Figure 4.3: **Schematic representation of the primary fluorescence-based homogeneous assay.** Beads were coated with IgE-Fc and incubated with supernatants from the rabbit B cell cultures as well as a AlexaFluor488-labeled rabbit IgG-Fc specific F(ab')<sub>2</sub> (Jackson ImmunoResearch, 111-546-046) (AlexaFluor 488-anti-rabbit Fc). Localised fluorescence around the bead, measured by a TTP Labtech Mirrorball<sup>®</sup> fluorescence cytometer, indicated the presence of an anti-IgE antibody in the supernatant, and the supernatant was listed as a 'hit'.

The primary screening data were analysed in Spotfire DecisionSite<sup>®</sup> (TIBCO), which rapidly produces visual reports of data. 14,400 supernatants were screened and 1,702 'hit' supernatants were identified, which gave a fluorescence reading over the background level (100 AFUs), suggesting they contained an antibody that bound to IgE-Fc. The Spotfire software then generated a top 'hit list' of 796 'hit' B cell culture wells (Section 2.5.5). The supernatants that produced the highest bead-localised mean fluorescence intensity came from these wells. The supernatants from these 'hit' wells were then plated into 96-well masterplates and taken on for further screening for IgE-Fc/CD23 modulating activity. The B cell cultures were frozen and stored at -80 °C.

#### 4.2.2 Secondary fluorescence-based homogeneous screening

A secondary fluorescence-based homogeneous assay was developed to screen the 800 top IgE-Fc binding supernatants for antibodies that modify the interaction between IgE-Fc and CD23 (Section 2.5.6). The secondary assay was based upon

the same homogeneous fluorescence-based method as the primary screen, however fluorescently-labeled derCD23 (derCD23-A488) was added instead of the fluorescently-labeled anti-rabbit-Fc antibody. The intensity of bead-localised fluorescence was used as a measure of derCD23-A488 binding to biotinylated IgE-Fc on the surface of the bead (Figure 4.4).

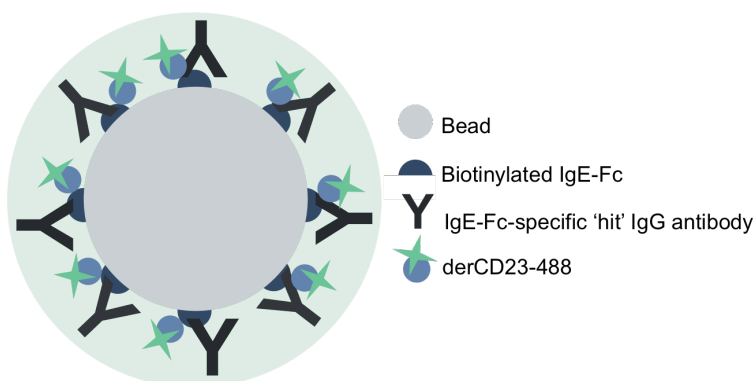


Figure 4.4: **Schematic representation of the secondary fluorescence-based homogeneous assay.** Beads were coated with IgE-Fc and incubated with 'hit' B cell supernatants identified from the primary screen, as well as fluorescently-labeled derCD23 (derCD23-A488). Localised fluorescence around the bead, measured by a Mirrorball<sup>®</sup> fluorescence cytometer, was used as a measure of the binding of derCD23-A488 to IgE-Fc on the surface of the beads.

### Development of the secondary screen

Prior to the secondary screen, preliminary experiments were performed to find the optimal conditions for screening. Different concentrations of biotinylated IgE-Fc were tested for coating the superavidin beads, alongside a titration of fluorescently-labeled derCD23 in order to establish the best fluorescent signal-to-noise ratio. Initially optimisations were performed in HEPES buffer with 4 mM calcium in place of what would be 'hit' B cell supernatant. An increase in fluorescence intensity was observed upon addition of increasing concentrations of derCD23-A488 when the beads were coated with 1 and 0.75  $\mu\text{g}/\text{plate}$  of biotinylated IgE-Fc (Figure 4.5.a).

When the beads were coated with biotinylated IgE-Fc at concentrations lower than 0.75  $\mu\text{g}/\text{plate}$  the fluorescent signal was relatively low and there was no obvious dose-dependent response (Figure 4.5.a). A linear dependence between

derCD23-A488 concentration and bead fluorescence intensity was observed between 0.3 - 1  $\mu\text{g}/\text{ml}$  derCD23-A488 in the dose-response curve for 1.0  $\mu\text{g}$  IgE-Fc/plate (Figure 4.5.b). At 3.2  $\mu\text{g}/\text{ml}$  derCD23-A488 the bead fluorescence intensity dropped and at 10  $\mu\text{g}/\text{ml}$  the signal fell to around 0 AFUs, which could be the result of high background levels of fluorescence.

When binding experiments are performed with both reactants at concentrations above the  $K_D$  of the interaction, binding becomes limited by the ratio of the reactants - all of the analyte will bind the ligand, up until the point where the ligand becomes saturated, and past that point excess analyte will exist in solution. In this assay, bead-based fluorescence was the result of crosslinking of immobilised IgE-Fc molecules by trimeric derCD23-A48 ( $K_D \sim 1\text{-}10$  nM). At concentrations above 1  $\mu\text{g}/\text{ml}$  derCD23-A488 ( $\sim 20$  nM trimeric derCD23-A488) the drop in fluorescence may have occurred because both reactants were at concentrations above the  $K_D$  of the interaction, and IgE-Fc was saturated. Any excess derCD23-A488 would have resulted in an increase in Alexa Fluor 488 background fluorescence. Any bead-localised fluorescence within two standard deviations of the background fluorescence of the well was not acquired by the cytometer, and therefore an increase in background fluorescence would have increased the threshold for acquisition of bead-localised measurements [182]. Accordingly, the drop in average bead-localised fluorescence to 0 AU at 10  $\mu\text{g}/\text{ml}$  derCD23-A488 could be because the excess derCD23-A488 resulted in a level of background fluorescence so great that even when IgE-Fc was saturated, none of the beads had localised fluorescence two-standard deviations above the background level. Similar ‘hook effects’ are commonly observed in other Mirrorball assays and alternative ‘mix and read’ immunoassays when excessive primary antibody saturates the assay, preventing the true readout of bound fluorescence from the detection antibody [183].

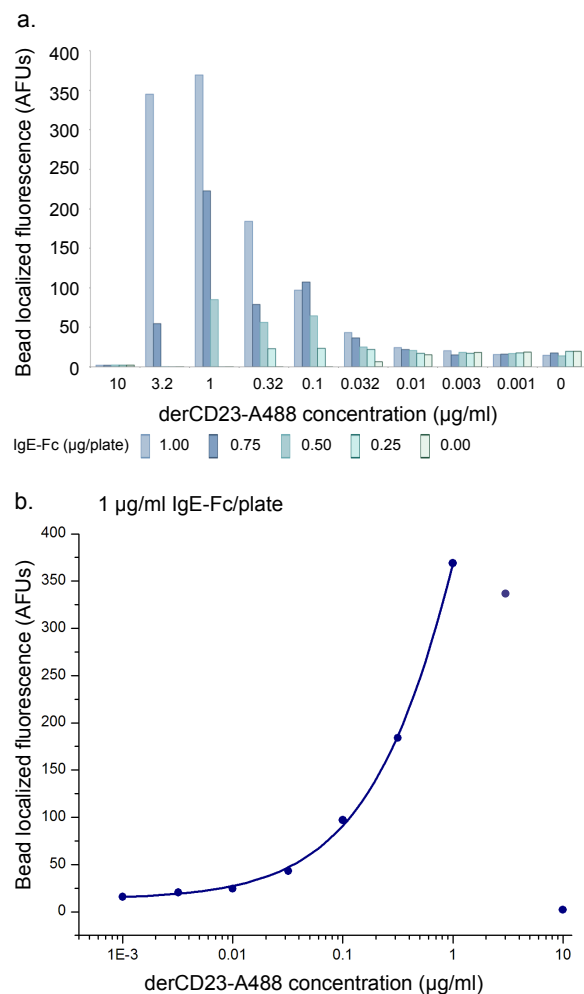


Figure 4.5: **Secondary screen development in HEPES buffer.** (a) Beads coated with varying concentrations of biotinylated IgE-Fc were incubated with increasing concentrations of derCD23-A488 in HEPES buffer with 4 mM calcium. Bead-localised fluorescence was used as a measure for binding of derCD23-A488 to IgE-Fc on the surface of the beads. Readings for experiments performed with 1 and 0.75 µg IgE-Fc/plate showed a general dose-dependent response to increasing derCD23-A488 until 3.16 µg/ml derCD23-A488. (b) The bead-localised fluorescence recorded when increasing concentrations of derCD23-A488 was incubated with superavidin beads coated in 1 µg/plate biotinylated IgE-Fc. A linear dependence between derCD23-A488 concentration and bead fluorescence intensity was observed between 0.3 - 1 µg/ml derCD23-A488.

When the same development assays were performed in a non ‘hit’ B cell culture (from a different rabbit immunisation and B cell culture) there was no fluorescent signal, suggesting that something in the culture-media quenched the fluorescence. UCB has also observed this effect in other systems (data not shown). It was therefore necessary to establish an appropriate level of supernatant dilution in order to optimise the fluorescent signal. Using 1 µg of biotinylated IgE-Fc per plate gave



the most robust fluorescent signal in the initial development screen (Figure 4.5.a) and accordingly this concentration of IgE-Fc was used to coat the beads that were then incubated with increasing concentrations of derCD23-A488 and at different negative B cell supernatant dilutions. It was decided that for the secondary screens the supernatant should be diluted to 20 % in HEPES buffer with 4 mM calcium chloride, as this still gave a robust signal in the linear range of the binding curve (Figure 4.6).

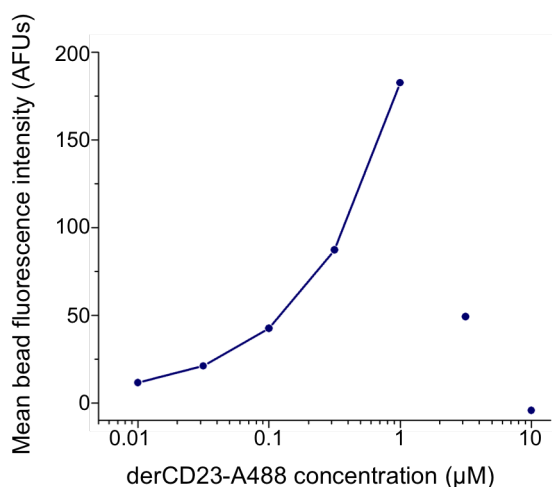


Figure 4.6: **Secondary screen development in non-‘hit’ B cell supernatant.** The bead-localised fluorescence recorded when increasing concentrations of derCD23-A488 were incubated with 20 % non-‘hit’ supernatant and superavidin beads coated in 1 µg/plate biotinylated IgE-Fc. A linear dependence between derCD23-A488 concentration and bead fluorescence intensity was observed between 0.5 - 1 µg/ml derCD23-A488.

### The secondary screen

Each of the supernatants was diluted to 20 % and the supernatant solution was incubated for an hour in the dark with IgE-Fc-coated beads (constant density, coated at 1 µg/plate) and derCD23-A488 (1 µg/ml). The bead-localised fluorescence was read in 384-well plates. Supernatant from another B cell culture, without IgE-Fc binding activity, was also sampled in order to determine a baseline level of fluorescence indicative of an ‘average’ interaction between IgE-Fc and derCD23 under this system (Section 2.5.6).

The average bead-localised fluorescence reading for the ‘baseline’ supernatants

was higher than the average for the ‘hit’ supernatants (Figure 4.7). A majority of the supernatants gave fluorescent readings below the ‘baseline’ suggesting that a majority of the antibodies had a negative effect on the interaction. This interpretation, however must be treated with caution since the ‘baseline’ supernatants originated from a rabbit immunisation and B cell culture set-up different to the origin of the ‘hit’ supernatants. In the absence of a robust control baseline level of fluorescence intensity, selection of ‘secondary hit’ supernatants was based on an internal comparison.

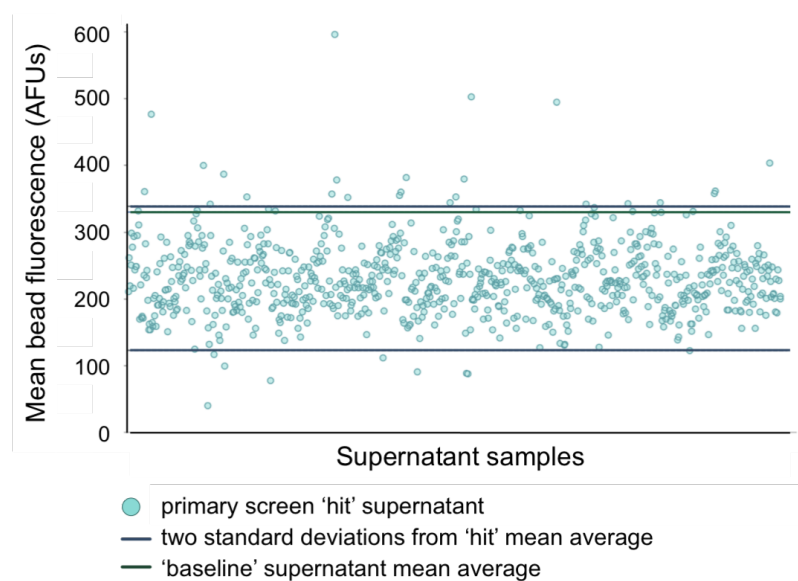


Figure 4.7: **Secondary homogeneous fluorescence-based assay results.** Bead-localised fluorescence intensity was used as a guide to how the ‘hit’ supernatants, containing IgE-Fc-specific antibodies, affected the interaction between IgE-Fc and derCD23-A488. Each green circle represents the result from a single B cell supernatant. An average of the results from the ‘baseline’ supernatant (no IgE-Fc-specific antibody) suggests a ‘baseline’ level of fluorescence and hence a ‘baseline’ level of interaction between derCD23-A488 and IgE-Fc on the surface of the beads. Two standard deviations from the mean of the plate ‘hit’ results were used as a guide to select a range of supernatants to take on for further analysis.

Several ‘hit’ supernatants gave readings above or below two standard deviations from the mean. The internal comparison unfortunately could not indicate whether the effects of the supernatants on the IgE-Fc/derCD23 interaction were actually positive or negative, respectively. Even if a robust baseline had been established it would have been difficult to determine this since the concentration of the antibodies in the supernatant was unknown. A strong inhibitor present at very low

concentrations could appear to be neutral in its effect on the interaction.

IgE-Fc - free screens were performed in parallel to the actual secondary screens. These ‘negative’ screens were the same in all respects except that the super-avidin beads had not been coated with biotinylated IgE-Fc. The results from the negative screens showed no bead-localised fluorescence, indicating that in each case the fluorescently-labeled derCD23 did not stick to the beads and any localised fluorescence in the actual screens was the result of the interaction between IgE-Fc and derCD23. Those supernatants above and below two standard deviations from the mean were selected as ‘secondary hits’, as were random supernatants within two standard deviations from the mean.

### **4.2.3 Cloning of variable region genes and DNA sequencing**

UCB’s proprietary fluorescent foci picking method was used to isolate 6-12 individual IgE-Fc-specific B cells from the selected ‘secondary hit’ B cell cultures (Section 2.5.6) [147]. The ‘secondary hit’ B cell cultures containing the ‘secondary hit’ B cells were incubated with superavidin beads coated in biotinylated IgE-Fc in addition to a fluorescently-labeled (AlexaFluor 488) anti-rabbit IgG-Fc F(ab’)<sub>2</sub> (Jackson ImmunoResearch, 111-546-046), used for detection. A fluorescent microscope was used to visualise the B cells of interest, which were surrounded by a ‘halo’ of fluorescence due to localised binding of their secreted antibodies to proximal IgE-Fc-coated beads. A micromanipulator was used to pick these individual ‘hit’ B cells, alternatively named fluorescent foci. 44 different B cell cultures were selected based on the results of the secondary homogeneous fluorescence-based assay (named F89-132) and foci were successfully isolated from 43 of these (Table 4.1).

Foci ID	1° screen (AFUs)	2° screen (AFUs)	V <sub>H</sub> CDR3 family	V <sub>K</sub> CDR3 family	SPR: CD23 occupancy (% thB <sub>eq</sub> )	azFab
F118	4515	40.2	A	Z	LOW CAP	
F102	4963	78	B	Y	LOW FC	
F128	2226	88.3	B	X	65	17
F127	2528	89	B	X	68	15
F123	4686	90.8	N/A	N/A	LOW CAP	
F119	4634	100	B	X	42	13
F90	4288	101	B	Z	56	2
F111	3914	134	B	Z	53	
F103	4337	138	B	Z	49	
F89	5803	214	C	Z	34	19
F115	1629	224	B	Y	45	
F130	6558	232	C	Z	48	18
F93	1430	279	A	Y	54	
F91	2162	285	B	Y	44	3
F117	2165	306	A	Y	48	
F107	2293	314	B	X	71	
F109	3215	325	B	Y	LOW FC	
F94	2400	332	B	X	47	5
F101	2038	335	B	X	69	9
F114	2010	337	N/A	Z	LOW CAP	
F92	3369	342	A	X	53	4
F112	4594	342	C	N/A	28	10
F116	4386	343	C	X	87	12
F125	4633	344	B	N/A	LOW FC	
F131	6939	344	C	Y	LOW CAP	
F132	6250	344	N/A	Y	LOW CAP	
F105	4407	352	N/A	X	LOW CAP	
F108	2787	352	C	X	LOW FC	
F100	1408	353	B	Z	83	7
F122	5075	355	B	Z	53	14
F120	1564	357	A	Y	LOW CAP	
F95	1790	361	B	Z	52	
F121	3460	378	B	Z	LOW CAP	
F126	4996	380	B	Z	50	
F106	2051	382	A	Z	LOW CAP	
F99	4596	387	B	Z	60	
F98	2920	400	C	Y	52	6
F96	2056	477	B	X	56	
F110	3145	495	B	Z	LOW CAP	
F104	4328	596	N/A	Y	LOW CAP	

Table 4.1: **An overview of the screening and sequencing data from the different ‘secondary hit’ antibodies that were successfully cloned and transiently expressed.** The antibodies are named according to the foci number from which they were derived, and are listed in terms of their secondary screen result, from lowest to highest arbitrary units AFUs. The primary screen identified IgE-Fc binding activity of B cell supernatants, with higher values indicative of greater binding. The secondary screen measured the effect on the interaction between derCD23 and IgE-Fc, with higher values indicative of greater binding between IgE-Fc and CD23. The SPR screen investigated the effect on derCD23 binding to IgE-Fc pre-bound to antibody. The occupancy of derCD23 binding sites on IgE-Fc during the steady-state was expressed as a percentage of the theoretical steady-state occupancy (thB<sub>eq</sub>). LOW CAP indicates the antibody capture level was too low for analysis. LOW FC indicates the antibody did not bind IgE-Fc. The families were based on nodal analysis of the phylogenetic trees outputted from the CDR3 sequence alignments. For antibodies assumed to be clones, only the data for one clone is shown. 15 antibodies were selected to be expressed as Fabs based on this screening.

Single B cell reverse transcription PCR (RT-PCR) was performed on three of the 6-12 foci picked in each of the 43 cultures (Section 2.5.8). The RT-PCR produced cDNA for the antibody produced by that particular B cell clone. The cDNA for each antibody was used to amplify the heavy and the light variable domain genes and clone them into transcriptionally active DNA fragments [184] using several rounds of transcriptionally active PCR (TAP) (Section 2.5.9) (Figure 4.8) [147].

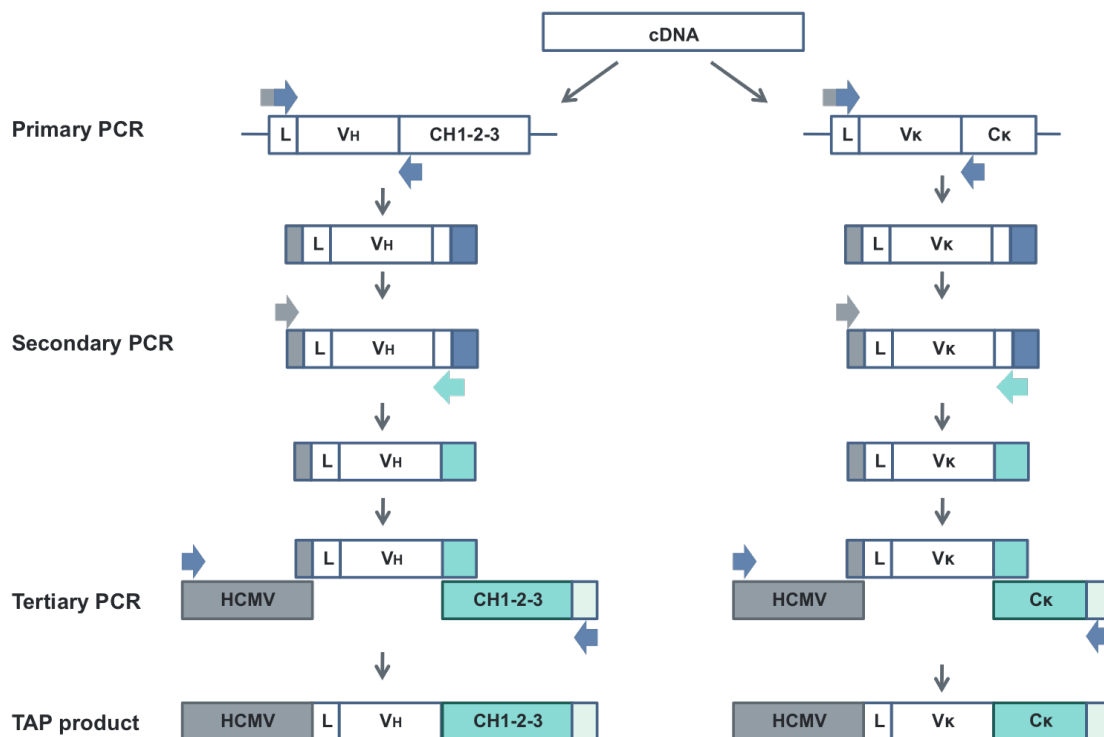
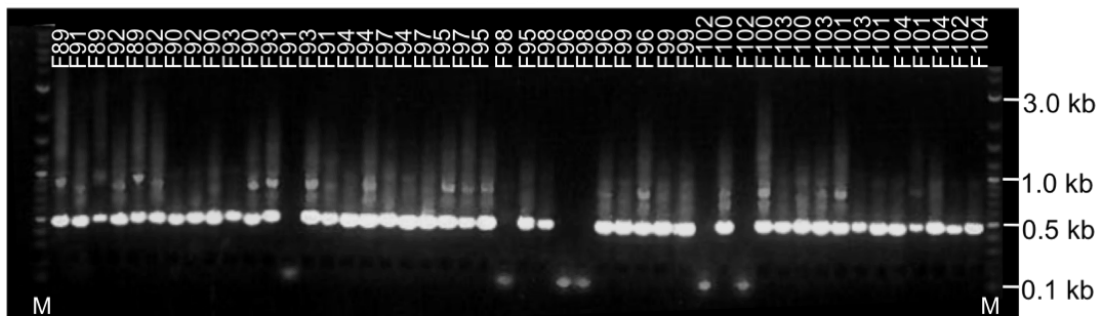


Figure 4.8: **Workflow for transcriptionally active PCR (TAP) of variable region genes.** Three rounds of PCR were used to amplify cognate pairs of variable region genes and to anneal them into transcriptionally active DNA fragments. Primary PCRs were performed using the cDNA from isolated B cells to amplify the variable region genes. The secondary PCRs added small sequences at each end of the variable regions that overlap with the human cytomegalovirus (HCMV) promoter (grey) and the heavy or kappa chain constant regions (teal) containing a polyadenylation sequence (light green). In the tertiary PCRs the HCMV, variable regions and constant regions were annealed to give a transcriptionally active product.

The heavy and light variable domain DNAs from the secondary TAP reactions were gel purified. At least one of the three isolated B cells from each of the 43 B cell cultures gave secondary TAP products that ran at the expected size on a 1% agarose gel (Figure 4.9). Following purification, the DNA encoding the heavy and light variable domains were cloned into UCB in-house ‘rabbit-Fab vectors’

containing the DNA encoding for the heavy  $C_H1$  and  $C_k$  domains, respectively. The plasmid also contained an HMCV promoter, a polyadenylation sequence, a pUC origin of replication and encoding kanamycin resistance. The secondary TAP reactions introduced restriction sites at the 5' and 3' ends of the variable domain sequences, so that the variable domains could be cloned into the plasmid using restriction enzymes (Section 2.5.10) (Figure 4.10).

### a. Kappa chain



### b. Heavy chain

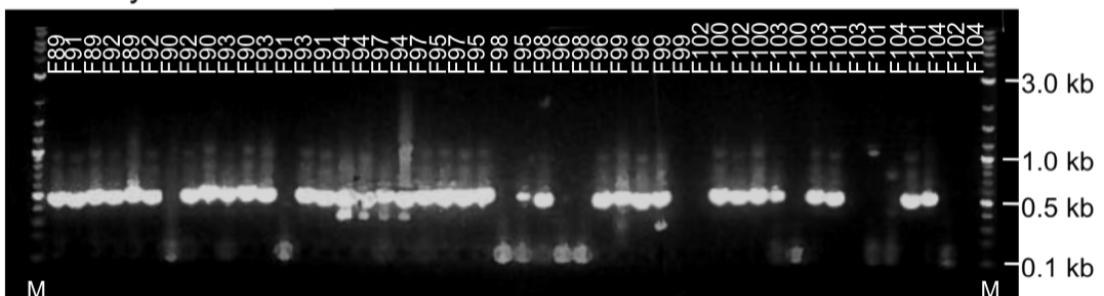


Figure 4.9: 1 % agarose gel of secondary TAP products. (a) kappa chain variable regions (b) heavy chain variable regions. The first and last lane of both gels contained 2 log DNA ladder (New England Biolabs). The intermediate lanes contained the PCR products from the secondary PCRs from three different foci for 16 of the 43 different 'secondary hit' B cells cultures (F89-F104). The variable region DNA runs at 0.5 kb.

The plasmid DNA was used to transform XL1-Blue *E. coli* (Stratagene) using heat shock (Section 2.2.3). The expanded plasmid DNA was purified from overnight cultures and sequenced in both forward and reverse directions. A sequence comparison of the third complementary determining region (CDR3) (Section 4.1) of the heavy and the kappa chains was performed using the MUSCLE multiple sequence alignment tool [185] (Figure 4.11). Some of the antibodies were found to have the same heavy and kappa CDR3 sequences, which for the purpose of selection were

assumed to be clones. It was promising to see that the supernatants containing the presumed clones had similar secondary screening results (Table 4.2).

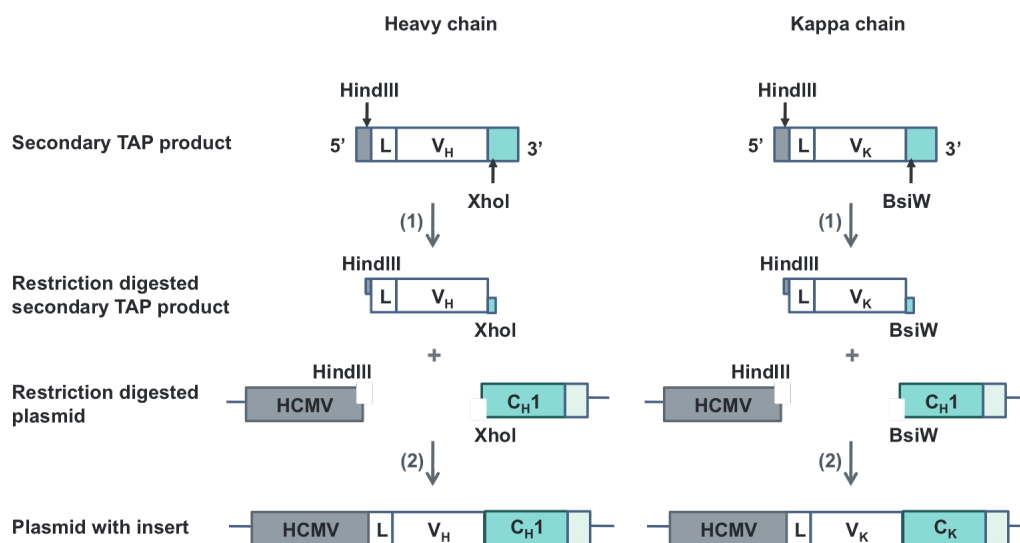


Figure 4.10: **Heavy and light chain variable domains were cloned into UCB in-house plasmids using restriction enzymes.** The variable domains were excised from the secondary TAP products using restriction enzymes and introduced into a UCB in-house plasmid cut with the same enzymes. The heavy variable domain was cloned into a ‘heavy chain Fab vector’ containing a downstream  $C_H1$  domain and the light chain variable domain was cloned into a ‘light chain Fab vector’ containing a downstream  $C_K$  domain.

	Presumed clones	2° screen (AFUs)
A	F97	125
	F119	100
B	F100	352
	F126	380
C	F109	328
	F113	325
D	F116	343
	F129	504

Table 4.2: **There is good agreement between the secondary screen measurements of the supernatants of presumed clones.** Sequence alignment of heavy and kappa CDR3s indicated that some antibodies were clones, shown here as A, B, C and D. The secondary screen results were in relatively close agreement for the different supernatants from which these clones were identified.

The phylogenetic trees that were output from the alignments of the heavy and kappa chain CDR3s were used to assign the antibodies to families based on their sequence similarities (Figure 4.12). The phylogenetic trees show the inferred evolu-

tionary relationship between the CDR3 sequences. The lengths of the branches indicate the closeness of the evolutionary relationships between the different CDR3s. The branches split off from nodes, which suggest a common ‘ancestor’. The first set of nodes in both phylogenetic trees were used to class heavy CDR3s into A, B and C families, and kappa CDR3s into X, Y and Z families. There appears to be no obvious or immediate correlation between the different CDR3 families and effect on the derCD23/IgE-Fc interaction as determined by the secondary screens. The two antibodies with C and Z heavy and kappa CDR3s, respectively, were both associated with lower derCD23/IgE-Fc binding, but due to the small numbers of sequences it is inappropriate to assign any significance to this.

#### **4.2.4 Investigating the effect of the full-length antibodies on the interaction between IgE-Fc and derCD23 using SPR**

ExpiF293<sup>TM</sup> HEK cells (Thermo Fisher Scientific) were transfected with cognate tertiary TAP products and cultured for transient expression of full-length rabbit IgG antibodies (Section 2.5.11). The 43 supernatants were harvested and subjected to SPR analysis to ascertain the effect of the antibody/IgE-Fc interaction on the binding of derCD23 to IgE-Fc.

An IgG-Fc-specific goat anti-rabbit F(ab')<sub>2</sub> fragment (Jackson ImmunoResearch, 111-006-046) was immobilised on the surface of the sensor chip using amine-coupling techniques (Section 2.6.2) at a density of ~1,200 RUs. A mock amine-coupled surface was used as a reference-subtraction surface (Section 2.6.2). The supernatants were diluted 1 in 4 in SPR running buffer and were injected over the surfaces for 120 s. The antibodies in the supernatants were separately captured on the sensor chip surface by the anti-rabbit-Fc surface at low density (<200 RUs). IgE-Fc was injected for 120 s over the captured rabbit antibodies and the reference surface. IgE-Fc/antibody binding was measured in response units (RUs). Following the IgE-Fc injection, derCD23 was injected over the surfaces for 120 s at 10 µM and the derCD23/IgE-Fc response on binding was measured (Figure 4.13). A 100 s dissociation phase followed each derCD23 injection, and the surface was regenerated



each time by two 60 s pulses of 10 mM glycine-HCl pH 1.7, and one 30 s pulse of 5 mM NaOH.

## a. Heavy chains

```

H100 MYYCVRNAGSGY----VADAFDPWGPGLV
H126 MYYCVRNAGSGY----VADAFDPWGPGLV
H128 TYFCAEGPSYVRAGTYYPYLN LWGPGLV
H101 TYFCARDCYDTS-----SWQYSMWGPGLV
H130 AHFCARGSEIYG-----SGYALWGPGLV
H102 TYFCARPYASSS-NYYWEYF TLWQGGLV
H97 TYFCARDSYGAY---VGFAYAT LWGPGLV
H119 TYFCARDSYGAY---VGFAYAT LWGPGLV
H131 TTYCASRYPAYG--TGPYDGM DLWGPGLV
H107 TYFCARDYGGSA-----YYVFD FWGPGLV
H127 TYFCARDYGGSA-----YYVFD FWGPGLV
H108 -YLCARGWPNYG-----YFFDLWGPGLV
H116 TYLCARGWPNYG-----YFFDLWGPGLV
H129 TYLCARGWPNYG-----YFFDLWGPGLV
H91 VYFCARRYSAA-----FDPWGPGLV
H89 TYFCARPA YGAG---GALNGM DLWGPGLV
H95 TYFCARTYIWSSGGYTYASYFN LWGPGLV
H98 TYFCARLGLAGN-----MGVWQGLV
H109 TYFCVRRYAGSG-----WDLWQGLV
H113 TYFCVRRYAGSG-----WDLWQGLV
H115 TYFCVRRYAGSG-----WDLWQGLV
H106 TYFCARGSTYDW-----LDLWQGLV
H117 TYFCARGSTYDW-----LDLWQGLV
H120 TYFCARGSTYDW-----LDLWQGLV
H92 TYFCVRDSDSG-----YDLWQGLV
H93 TYFCVRDSDSG-----YDLWQGLV
H118 TYFCARDADYAA----SGYIFDLWQGLV
H96 TYFCAREASGWG-----DALDPWGPGLV
H112 TYFCARANDDYG----EDGLHLWQGLV
H99 TYFCARDLGDGD--VDYGYGFNLWGPGLV
H103 TYFCARGALYGTRSGYYPYFN LWGPGLV
H111 TYFCARGALYGTRSGYYPAYFN LWGPGLV
H125 TYFCAREAGNSD-----YYTLWGPGLV
H90 TYFCARANIYGISGVYYPNYFN LWGPGLV
H121 TYFCARDRNGDD-----LNLWGPGLV
H110 TYFCARDLPDTS-----SAFNLWGPGLV
H122 TYFCARGSHVGV-----RFFNLWGPGLV
H94 TYFCAREAGDSN-----NLWQGLV

```

## b. Kappa chains

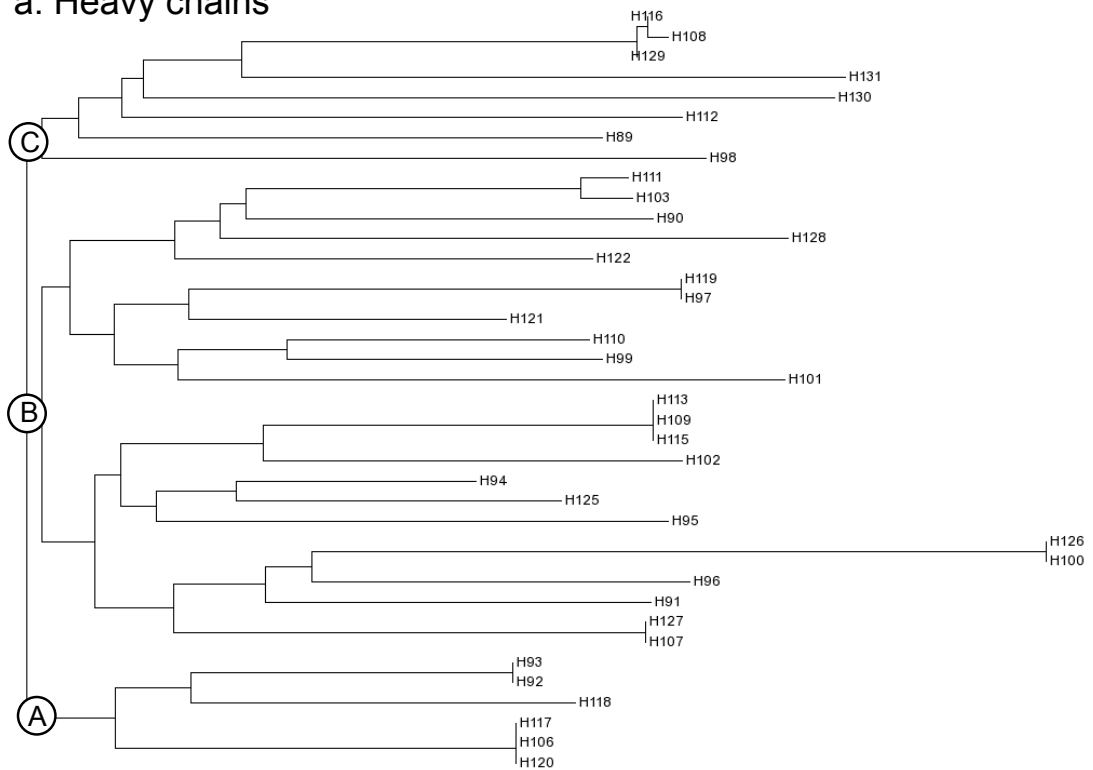
```

K102 YYCAGYKTYNND-----NAFGG
K92 YYCQQDAAVNTY-----NSFGG
K101 YCCQQGASVSNVD-----NSFGG
K127 YYCQGGGTISGVD-----NTFGG
K128 YYCQGGGTISGVD-----NTFGG
K107 YYCQGGGTISNVD-----NTFGG
K94 YYCQQTAAASINVE----YAFGG
K96 YYCQQTAAVININ----NAFGG
K117 YYCLGGYSGSSE-----NGFGG
K120 YYCLGGYSGSSE-----NGFGG
K90 YYC-SYYPSS-----VAFGG
K106 YYCGDYGGGN-----VAFGG
K104 YYCAGRFDDV-----YVFG-
K109 YYCAGGYSGNV-----FTFGG
K113 YYCAGGYSGNV-----FTFGG
K115 YYCAGGYSGNVFT----FCFGG
K91 YYCAGGYIDNI-----FVFGG
K98 YYCAGGYDCRSADC---ITFGG
K105 YYCQAFYVGYI-----WTFGG
K108 YYCQAFYVGYI-----WTFGG
K116 YYCQAFYVGYI-----WTFGG
K129 YYCQAFYVGYI-----WTFGG
K118 YYCQGTLYSSGWY----IAFGG
K97 YYCQSATYDSTTD----TTFGG
K119 YYCQSATYDSTTD----TTFGG
K99 YYCQCTDYGSSYV---NAFGG
K110 YYCQSCDYSSSSS----YAFGG
K130 YYCQSYYSRSSRSVG--FAFGG
K95 YYCQ-TYGGIGRSGY-GNAFGG
K89 YYCQ-TYGSSSSTSYF--FAFGG
K100 YYCQCIYGSSSSTSY-GNAFGG
K126 YYCQCIYGSSSSTSY-GNAFGG
K131 YYCQCTYGTSSSTSY-GNAFGG
K121 YYCQCTYGSSSSTSY-GNAFGG
K114 YYCQCTYGSSASSSY-GNAFGG
K122 YYCQCTYGSVVSSTY-GNAFGG
K93 YYCQCTYGSTVSSTY-GNAFGG
K103 YYCQSYYSISSNMYV--GAFGG
K111 YYCQSYYSISSNMYV--GAFGG
K132 YYCQSYYSDSGSRTYAVPNAFGG

```

Figure 4.11: Protein sequence alignment of the (a) heavy and (b) kappa CDR3s of ‘secondary hit’ antibodies. The sequence alignment was performed using the online MUSCLE sequence alignment tool [185]. Identical amino acids are coloured dark blue, similar amino acids are coloured light blue. For shading, 50 % of the sequences must agree with the identity or similarity.

a. Heavy chains



b. Kappa chains

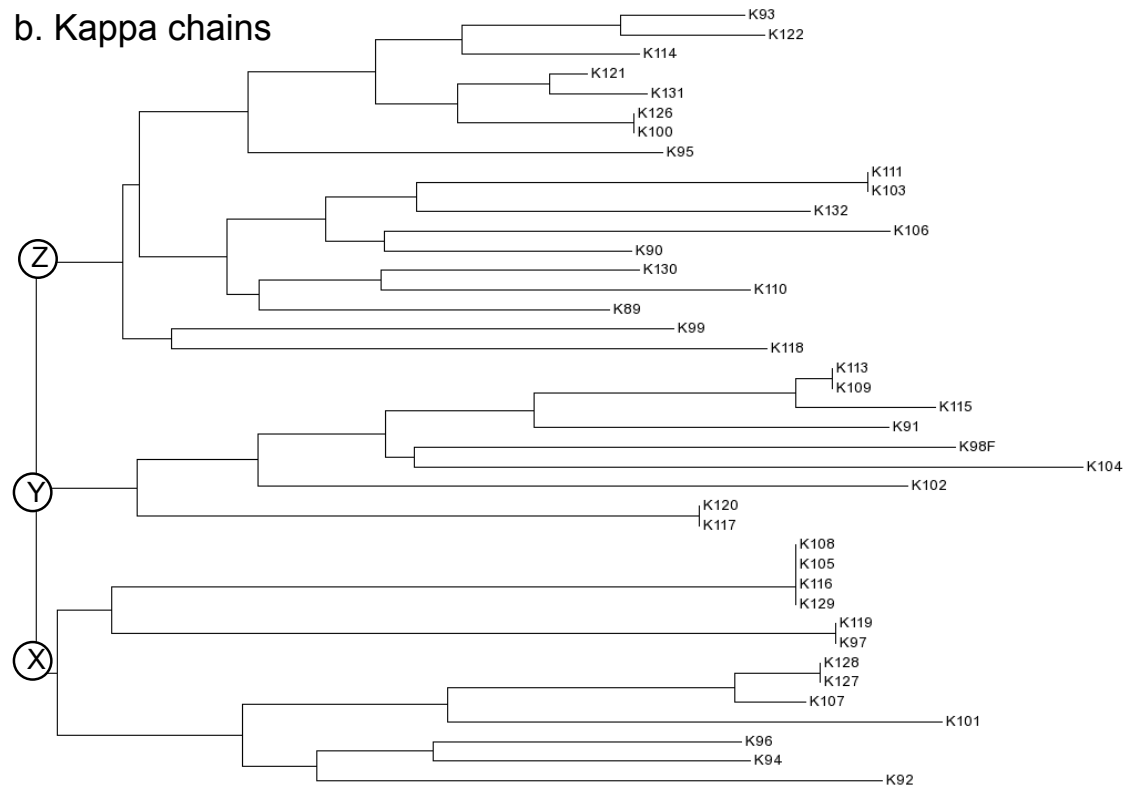


Figure 4.12: **Protein sequence alignment and phylogenetic analysis of the CDR3s of ‘secondary hit’ antibodies using the online MUSCLE tool.** (a) Heavy CDR3 phylogenetic tree with the main families and assigned from the first three nodes. (b) Kappa CDR3 phylogenetic tree with the main families assigned from the first three nodes.

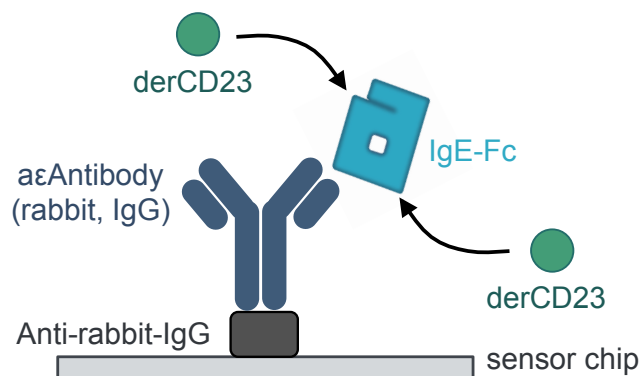


Figure 4.13: **A schematic representation of SPR experiments performed to ascertain the effect of the antibody/IgE-Fc interaction on the binding of derCD23 to IgE-Fc.** Antibody, in supernatant, was captured by an immobilised anti-rabbit-IgG F(ab')<sub>2</sub> fragment (Jackson ImmunoResearch, 111-006-046). IgE-Fc bound to the captured rabbit antibody, and derCD23 binding to the complex was measured as an increase in SPR response. Two molecules of derCD23 bind to native IgE-Fc.

Unfortunately, at this time there was no antibody available that was known to have no effect on the interaction between IgE-Fc and CD23 and therefore there was no control for IgE-Fc/CD23 binding. As such, the recorded values were expressed as a percentage of a theoretical steady-state response. The SPR response is directly related to mass (Section 2.6.4) and IgE-Fc (75 kDa) can potentially bind two molecules of derCD23 (2 x 16 kDa, 32 kDa). Theoretically if all the derCD23 sites on the captured IgE-Fc were saturated, the binding response of derCD23 to IgE-Fc during the steady-state ( $B_{eq}$ ) would be 0.43 (32/75) times the response recorded during IgE-Fc binding. The percentage of the theoretical steady-state response gives an approximation of the derCD23 occupancy of IgE-Fc, which was used for comparisons between different antibodies (Table 4.1).

Eleven of the supernatants did not cause an increase in response when injected over the anti-rabbit-Fc surface indicating that no antibody bound to the surface. This may be a result of very low expression levels or incorrectly folded protein. As a result, analysis of how these antibodies affected the interaction between IgE-Fc and derCD23 was not possible using this method. Four of the antibodies bound to the anti-rabbit-Fc surface but did not bind IgE-Fc. It is possible that these antibodies were classified as 'hits' in the primary screens because they bound non-specifically to the bead or they recognised superavidin/ biotin rather than IgE-Fc.

The remaining  $\alpha\epsilon$ Abs captured IgE-Fc capable of binding derCD23. The estimated occupation of derCD23 binding sites on IgE-Fc ranged from 28 % to 87 % depending on the  $\alpha\epsilon$ Ab used to capture IgE-Fc on the SPR surface. 100 % occupancy of derCD23 binding sites on IgE-Fc was not achieved when IgE-Fc was pre-bound to any of the  $\alpha\epsilon$ Abs, which could suggest that all of the antibodies had some inhibitory effect on the interaction between IgE-Fc and derCD23. In the absence of a rigorous control, however, we cannot be certain of such an interpretation. It is also possible that under these experimental conditions theoretical saturation of the derCD23 binding sites was not possible.

### 4.3 Discussion

Using UCB's Core Antibody Discovery Process, 25 different monoclonal IgG rabbit antibodies, which bound specifically to IgE-Fc and appeared to differentially modulate the IgE-Fc/CD23 interaction, were successfully isolated and recombinantly expressed. The secondary homogeneous fluorescence-based assay was designed to screen supernatants for their effect on the IgE-Fc/CD23 interaction. The secondary screen could be performed in high-throughput; it required small volumes of supernatant and could be performed in 384-well formats. Unfortunately, the presence of something in the cell-culture media that quenched the derCD23-A488 fluorescence meant that it was necessary to test diluted supernatant, thereby reducing the signal-to-noise ratio. Performing the screens repeatedly would have provided greater confidence in the observed values, especially in the absence of a robust control for a 'baseline' level of IgE-Fc/derCD23-A488 binding. To avoid the problem of fluorescence quenching one could look at the effect of the supernatants on the IgE-Fc/CD23 interaction using a label-free technique, such as SPR or BioLayer Interferometry (BLI) [186].

Sequence comparisons of the heavy and light chain CDR3s suggested that the selected antibodies were relatively diverse and consequently more likely to bind and affect IgE-Fc in different ways. A by-eye analysis suggested there were no obvious correlations between the CDR3 sequence and effect on IgE-Fc/CD23 binding as ascertained by the secondary screen. Regions other than the CDR3 contribute

towards antibody specificity including CDR1 and CDR2. These regions were not sequenced, and a sequence alignment of the whole variable domain would provide a better basis for drawing correlations between genealogical lineage and modulation of the IgE-Fc/CD23 interaction. A computational comparison may also reveal subtle links missed in this analysis. Although potentially interesting, investigating the evolution of the immune response to IgE-Fc was tangential to the antibody discovery process and so it was not pursued further.

SPR was successfully used to eliminate poorly expressing and non-IgE-Fc-specific antibodies from further selection. It was also employed as a means of further probing the effect of the antibodies on the interaction between IgE-Fc and derCD23. The experiment investigated how much derCD23 could bind IgE-Fc pre-bound to one  $\alpha\epsilon$ Ab. Unfortunately, without an experimental control it was only possible to compare the relative effects of pre-binding IgE-Fc with  $\alpha\epsilon$ Ab.

In some cases there was agreement between the results of the effect of  $\alpha\epsilon$ Ab on the IgE-Fc/CD23 interaction from the SPR and secondary screening assays. For example F119 was identified in both assays as having had a particularly negative effect on the IgE-Fc/derCD23 interaction relative to the other  $\alpha\epsilon$ Ab. Similarly, F116 was identified in both assays as having had a particularly positive effect on the IgE-Fc/derCD23 interaction relative to the other  $\alpha\epsilon$ Ab. In other cases the results from the two assays were quite contrasting; the secondary screen reading for F98 suggested it had a positive effect on IgE-Fc/CD23 binding but in the SPR experiments gave a slightly below average CD23 occupancy measurement (Table 4.1). These differences in results are perhaps to be expected given that the two assays are fundamentally different in their approach to investigating the effect of  $\alpha\epsilon$ Ab on the IgE-Fc/CD23 interaction. The secondary assay is performed at equilibrium with unknown concentrations of  $\alpha\epsilon$ Ab, whereas the SPR experiments are non-homogeneous and not at equilibrium. By pre-forming  $\alpha\epsilon$ Fab complexes the SPR experiments bias the interpretation of the effect of  $\alpha\epsilon$ Ab on the IgE-Fc/CD23 interaction in favour of the  $\alpha\epsilon$ Ab. The SPR experiments, however, do allow for the normalisation of signal with respect to antibody concentration.

Despite its imperfections the SPR analysis provided a basis for the selection of antibodies to take on to the next stage of the process. The eleven supernatants

that did not elicit a response when injected onto the anti-rabbit-Fc surface were not selected to be expressed as Fabs. Similarly, four other antibodies that bound IgE-Fc poorly in the SPR assay were also not selected, since antibodies with low affinity for IgE-Fc may make some biophysical characterisations more difficult. Positive selections were made to try to cover the range of results from the SPR analysis, with a preference for those antibodies that gave most robust responses. We are more likely to be interested in the aεAbs at either end of the occupancy spectrum, irrespective of the nature of the effect, since we hope to select antibodies that have different effects on the IgE-Fc/CD23 interaction. More aεAbs were selected that gave the highest or lowest derCD23 occupancy levels (Table 4.1). In the next stage of the process, the chosen heavy and light chains pairings will be expressed as aεFabs and further scrutinised for their effect on receptor binding with the hope of ultimately identifying and characterising novel allosteric IgE-Fc/CD23 modulators.

# Chapter 5

## Anti-IgE Fab selection and generation

### 5.1 Introduction

The previous chapter described how we used UCB's Core Antibody Discovery Process [148, 147] to find monoclonal rabbit antibodies that bind IgE-Fc and modulate its binding to the IgE-receptor, CD23. The screening resulted in the selection of 15 anti-epsilon antibodies (aεAbs) to take on to the next stage of the process, in which the cognate heavy and light variable regions of each antibody are expressed as a fragment antigen-binding (Fab) protein (Table 4.1). Due to its lower mass and monovalent antigen-binding capacity, the Fab format is often favoured over full-length antibodies for biophysical and structural studies.

In this chapter we describe how surface plasmon resonance (SPR) was used to investigate the binding properties of 13 of the 15 cognate pairs of heavy and light variable regions, each expressed as Fabs. We characterise how well the 13 aεFabs bind IgE-Fc, how differently they affect receptor binding (CD23 and FcεRI) and how they affect the binding of one another to IgE-Fc. The aim was to identify five or six aεFabs that bind IgE-Fc with high affinity and have a diverse range of allosterically mediated effects on IgE-Fc receptor. These selected aεFabs were expressed on a larger scale and purified. The next chapters will describe how further biophysical examination of the purified aεFabs has expanded our knowledge of allosteric processes in IgE.

Here we used SPR to investigate the binding characteristics of the 13 aεFabs.

This versatile technique can be used to determine the dissociation constant ( $K_D$ ) and binding capacity ( $B_{\max}$ ) of an interaction using steady-state binding responses (Section 2.6.4). Steady-state analysis of SPR data is particularly useful for characterising interactions with fast-on and fast-off rates, whose kinetics cannot be easily analysed. Providing the kinetics of an interaction are not too fast, or too slow, to accurately fit the association and dissociation rates, SPR can be used to analyse the binding kinetics and thermodynamic properties of an interaction (Section 2.6.3). By fitting the association and dissociation phases of an SPR sensorgram it is possible to determine the association and dissociation rate constants (Section 2.6.3). The rate constants can be used not only to characterise the kinetics of an interaction but also to derive the  $K_D$  of an interaction (Equation 2.4). We used both kinetic and steady-state analysis of SPR data to describe how the different  $\alpha$ Fabs interact with IgE-Fc, and to compare the different ways they affect receptor binding using derCD23 and sFc $\epsilon$ RI $\alpha$  constructs.

## 5.2 Results

### 5.2.1 Investigating binding of IgE-Fc to $\alpha$ Fabs using SPR

A laboratory clean-out unfortunately resulted in the misplacement of the plasmid DNA for  $\alpha$ Fab10 and  $\alpha$ Fab15. It would have been possible to perform the tertiary TAP experiments again, but since there were 13 other  $\alpha$ Fabs to select from it was decided, in the interest of time, to proceed without making  $\alpha$ Fab10 and  $\alpha$ Fab15. Plasmids for the cognate pairs of rabbit IgG heavy and kappa chain Fab fragments were used to transiently co-transfect HEK293 cells using 293fectin<sup>TM</sup> (Thermo Fisher Scientific) (Section 2.5.11) [187]. The Fabs, in transient transfection supernatant, were tested for their ability to bind IgE-Fc using SPR.

A Fab-specific goat anti-rabbit F(ab')<sub>2</sub> fragment (Jackson ImmunoResearch, 111-046-047) was immobilised on the surface of a sensor chip using amine-coupling techniques (Section 2.6.2). A mock amine-coupled surface was used as a reference-subtraction surface (Section 2.6.2). The supernatants were diluted 1 in 4 in SPR running buffer and were injected over the sensor surfaces for 240 s. The  $\alpha$ Fabs



were captured on the goat anti-rabbit-Fab surface at low densities (<200 RUs). IgE-Fc was injected for 210 s over the surface at various concentrations and the binding between the  $\alpha$ Fab and IgE-Fc was measured as a change in SPR response (Figure 5.1 and Appendix A.2). A dissociation phase lasting 700 s followed each  $\alpha$ Fab injection and the surfaces were completely regenerated with two 60 s pulses of 10 mM glycine-HCl pH 1.7 and one pulse of 5 mM NaOH. Experiments were performed in duplicate and gave highly replicable results.

There was no increase in response when  $\alpha$ Fab19 was injected over the anti-rabbit surface.  $\alpha$ Fab6 and  $\alpha$ Fab14 bound to the anti-rabbit surface but bound IgE-Fc very weakly (Figure 2). The remaining  $\alpha$ Fabs were successfully captured by the anti-rabbit Fab surface and bound IgE-Fc.

The interactions between IgE-Fc and the different  $\alpha$ Fabs showed varied kinetic profiles. The interaction between IgE-Fc and  $\alpha$ Fab2, for example, had a very slow off-rate, whereas the off-rate between the same concentration of IgE-Fc and  $\alpha$ Fab3 was comparatively fast (Figure 5.2.a). The interaction between IgE-Fc and  $\alpha$ Fab9, and the interaction between IgE-Fc and  $\alpha$ Fab17, had very similar off-rates, however there were clear differences in their association rates at the same IgE-Fc concentration (Figure 5.2.b).

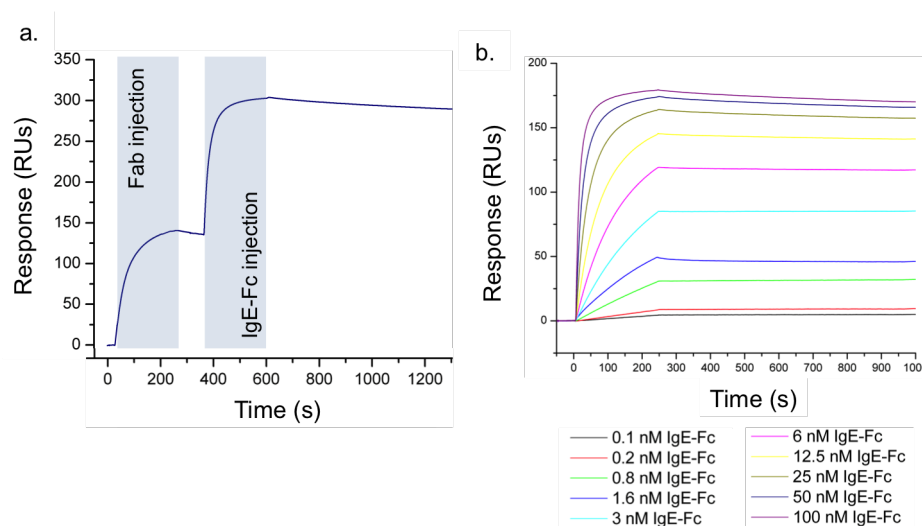


Figure 5.1: **Example sensorgrams from SPR experiments to investigate the binding of IgE-Fc to  $\alpha\epsilon$ Fabs in transient transfection supernatant.** (a) Transient supernatants containing  $\alpha\epsilon$ Fab ( $\alpha\epsilon$ Fab2 here) were injected over a Fab-specific goat anti-rabbit F(ab')<sub>2</sub>. IgE-Fc was injected over the captured  $\alpha\epsilon$ Fab, and binding was observed as change in SPR response. (b) The response when 0 nM IgE-Fc was injected over the captured  $\alpha\epsilon$ Fab and was subtracted from the response measured when IgE-Fc was injected over the  $\alpha\epsilon$ Fab at increasing concentrations in order to eliminate changes in response as a result of dissociation of  $\alpha\epsilon$ Fab from the anti-rabbit-Fab surface.

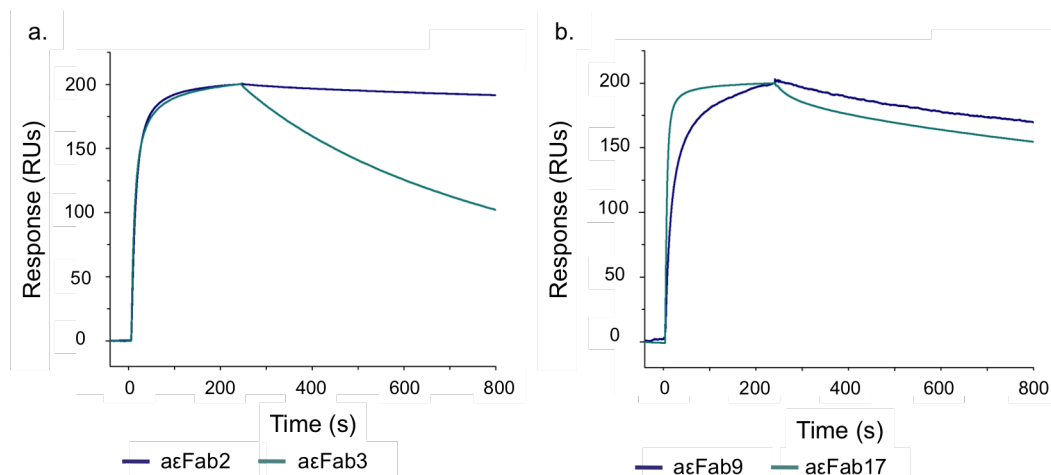


Figure 5.2: **The binding of IgE-Fc to the different  $\alpha\epsilon$ Fabs show varied kinetics as determined by SPR.** A comparison of the binding kinetics of IgE-Fc binding to captured (a)  $\alpha\epsilon$ Fab2 and  $\alpha\epsilon$ Fab3, (b)  $\alpha\epsilon$ Fab9 and  $\alpha\epsilon$ Fab17. The  $\alpha\epsilon$ Fabs were captured by Fab-specific goat-anti-rabbit F(ab')<sub>2</sub> (Jackson ImmunoResearch) immobilised on a sensor surface. For clarity, binding of only a single concentration of IgE-Fc is shown (100 nM). Each sensorgram has been normalised to give a maximal response of 200 RUs.

The dissociation and association rates for the interactions between each of the

aεFabs and IgE-Fc were fit in order to determine the dissociation and association rate constants ( $k_{\text{off}}$  and  $k_{\text{on}}$ , respectively) for each of the aεFab-IgE-Fc interactions. The data were fit using single  $k_{\text{off}}$  and  $k_{\text{on}}$  models (Section 2.6.3) (Figure 5.3 and Appendix A.2) and were used to determine the  $K_D$  of each aεFab/IgE-Fc interaction using Equation 2.4. Some binding curves, particularly at higher IgE-Fc concentrations, were obviously biphasic, for example the curve for binding of 100 nM IgE-Fc to aεFab17 (Figure 5.2). The simplest interpretation of this biphasicity is that there are two aεFab binding sites on IgE-Fc that have different affinities. Single  $k_{\text{off}}$  and  $k_{\text{on}}$  models do not accurately fit biphasic data but may still provide a simplified understanding of the kinetic data. The data from the 6 nM IgE-Fc injections were fit because at these concentrations of IgE-Fc the binding was mostly monophasic. Although fitting the data in this way did not provide a full account of the kinetics of the interactions, it did allow for an estimation of the overall affinity of the interaction. The aεFabs (excluding 6, 14 and 19, which did not bind the anti-rabbit surface/IgE-Fc) bound IgE-Fc with sub-nanomolar binding affinities (Table 5.1). Only these aεFabs were used in further SPR experiments to determine which aεFabs to express on a large-scale and purify for a more in-depth biophysical characterisation.

### **5.2.2 Investigating the effect of one aεFab molecule on the IgE-Fc/derCD23 interaction using SPR.**

aεFabs 2, 3, 4, 5, 7, 9, 12, 13, 17 and 18 were shown to bind IgE-Fc in SPR experiments (Section 5.2.1). SPR experiments with the supernatants containing these aεFabs were performed to determine which of the aεFabs have the most diverse effects on IgE-Fc's apparent affinity and binding capacity for derCD23. A Fab-specific goat anti-rabbit F(ab')<sub>2</sub> fragment (Jackson ImmunoResearch, 111-046-047) was immobilised on the surface of a CM5 sensor chip using amine coupling techniques (Section 2.6.2). A mock amine-coupled surface was used as a reference-subtraction surface (Section 2.6.2). The Fabs, in supernatant, were diluted 1 in 4 in SPR running buffer and were injected for 240 s over the sensor surfaces. The Fabs were captured on the goat anti-rabbit-Fab surface at a low density (<200

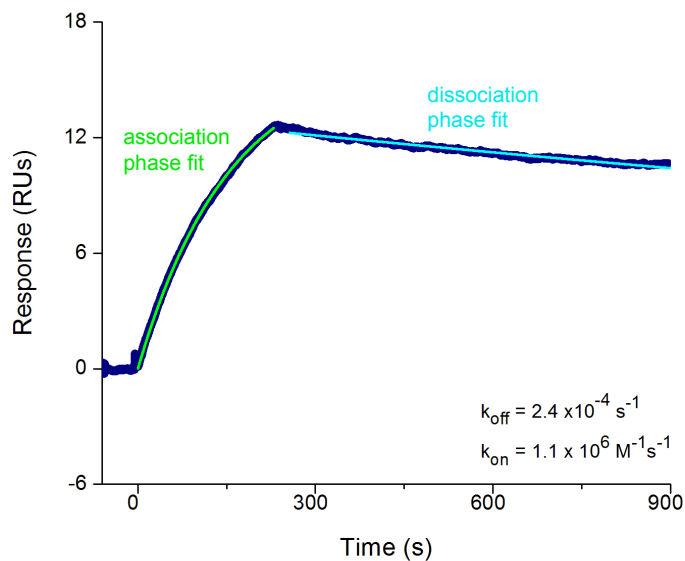


Figure 5.3: **Example of fitting kinetic data for the  $\alpha\epsilon$ Fab/IgE-Fc interaction as determined by SPR.** Single  $k_{\text{off}}$  and  $k_{\text{on}}$  models were used to fit SPR data for IgE-Fc binding to captured  $\alpha\epsilon$ Fab. This example shows the kinetic fits (light green and light blue) of the data (dark blue) for the interaction between  $\alpha\epsilon$ Fab9 and 6 nM IgE-Fc.

RUs). 100 nM IgE-Fc was injected over the sensor surface for 210 s and bound the captured  $\alpha\epsilon$ Fab, forming an  $\alpha\epsilon$ Fab:IgE-Fc (1:1) complex. derCD23 was injected for 120 s over the captured complex at various concentrations, and binding to the  $\alpha\epsilon$ Fab:IgE-Fc (1:1) complex was measured as a change in the SPR response (Figure 5.4). A dissociation phase of 300 s followed each derCD23 injection and the surface was regenerated by two 60 s pulses of 10 mM glycine-HCl pH 1.7 and one 30 s pulse of 5 mM NaOH.

The  $\alpha\epsilon$ Fab:IgE-Fc (1:1) complexes bound derCD23, and reached a steady-state during the time-course of the injection (Section 2.6). Steady-state analysis of the steady-state response was performed and the binding curves were fit using a one-to-one binding model (Section 2.6.4, Equation 2.17) (Figure 5.5 and Appendix A.3). The  $K_D$  values of the different  $\alpha\epsilon$ Fab1:IgE-Fc (1:1)/derCD23 interactions ranged from  $0.6 \times 10^{-6}$  M -  $4.9 \times 10^{-6}$  M (Table 5.2). The interaction between IgE-Fc and derCD23 is reported to have a  $K_D$  of  $1 \times 10^{-6}$  M [89, 88]. There is an 8-fold difference between the highest and lowest  $K_D$  values, which suggests that the  $\alpha\epsilon$ Fab:IgE-Fc complexes have a range of cooperative effects on the IgE-Fc/derCD23 interaction.

At these working concentrations of derCD23 only the higher-affinity CD23-

	<b>Fab/IgE-Fc interaction</b>		
	<b><math>k_{\text{on}}</math> <math>\text{M}^{-1} \text{s}^{-1}</math></b>	<b><math>k_{\text{off}}</math> <math>\text{s}^{-1}</math></b>	<b><math>K_{\text{D}}</math> (M)</b>
<b>aεFab17</b>	$2.7 \times 10^6$	$2.4 \times 10^{-4}$	$0.9 \times 10^{-10}$
<b>aεFab2</b>	$6.9 \times 10^5$	$7.0 \times 10^{-5}$	$1.0 \times 10^{-10}$
<b>aεFab12</b>	$2.3 \times 10^6$	$2.4 \times 10^{-4}$	$1.0 \times 10^{-10}$
<b>aεFab7</b>	$2.0 \times 10^6$	$2.7 \times 10^{-4}$	$1.4 \times 10^{-10}$
<b>aεFab4</b>	$1.1 \times 10^6$	$1.7 \times 10^{-4}$	$1.5 \times 10^{-10}$
<b>aεFab9</b>	$1.1 \times 10^6$	$2.4 \times 10^{-4}$	$2.2 \times 10^{-10}$
<b>aεFab5</b>	$1.6 \times 10^6$	$4.9 \times 10^{-4}$	$3.1 \times 10^{-10}$
<b>aεFab18</b>	$1.7 \times 10^6$	$6.3 \times 10^{-4}$	$3.6 \times 10^{-10}$
<b>aεFab3</b>	$1.4 \times 10^6$	$9.9 \times 10^{-4}$	$7.1 \times 10^{-10}$
<b>aεFab13</b>	$8.4 \times 10^5$	$6.4 \times 10^{-4}$	$7.6 \times 10^{-10}$
<b>aεFab6</b>	N/A	N/A	N/A
<b>aεFab14</b>	N/A	N/A	N/A
<b>aεFab19</b>	N/A	N/A	N/A

Table 5.1: **Summary of the association and dissociation rate constants, and the dissociation constants for IgE-Fc binding to aεFabs as determined by SPR and using transiently transfected aεFab supernatants.** The data for the binding of 6 nM IgE-Fc to the aεFabs were fit using single  $k_{\text{off}}$  and  $k_{\text{on}}$  models (Section 2.6.3). aεFab was captured by injection of transiently transfected supernatant, containing aεFab, over an immobilised surface of Fab-specific goat-anti-rabbit F(ab')<sub>2</sub> (Jackson ImmunoResearch).

binding site on native IgE-Fc ( $K_{\text{D}} \sim 1 \mu\text{M}$ ) would be significantly occupied (Section 1.2.3). The normalised  $B_{\text{max}}$  values were therefore reported in terms of a theoretical  $B_{\text{max}}$  (th $B_{\text{max}}$ ) for the binding of one molecule of derCD23 to IgE-Fc (Section 2.6.2). Except for aεFab17, the  $B_{\text{max}}$  values were all in excess of 100 %, which indicated that the lower-affinity derCD23 binding site was partially occupied. The binding of two derCD23 molecules to aεFab-bound IgE-Fc indicates that the aεFabs did not sterically occlude binding of derCD23. It is therefore likely, but not certain, that any inhibitory effects the aεFabs (excluding aεFab17 and potentiall aεFab12, which had a  $B_{\text{max}}$  value that was 105 % of the theoretical  $B_{\text{max}}$ ) had on the IgE-Fc/derCD23 interaction were allosteric in nature. This will be discussed further in Chapter 7. The  $B_{\text{max}}$  values, given as a percentage of the theoretical  $B_{\text{max}}$ , ranged

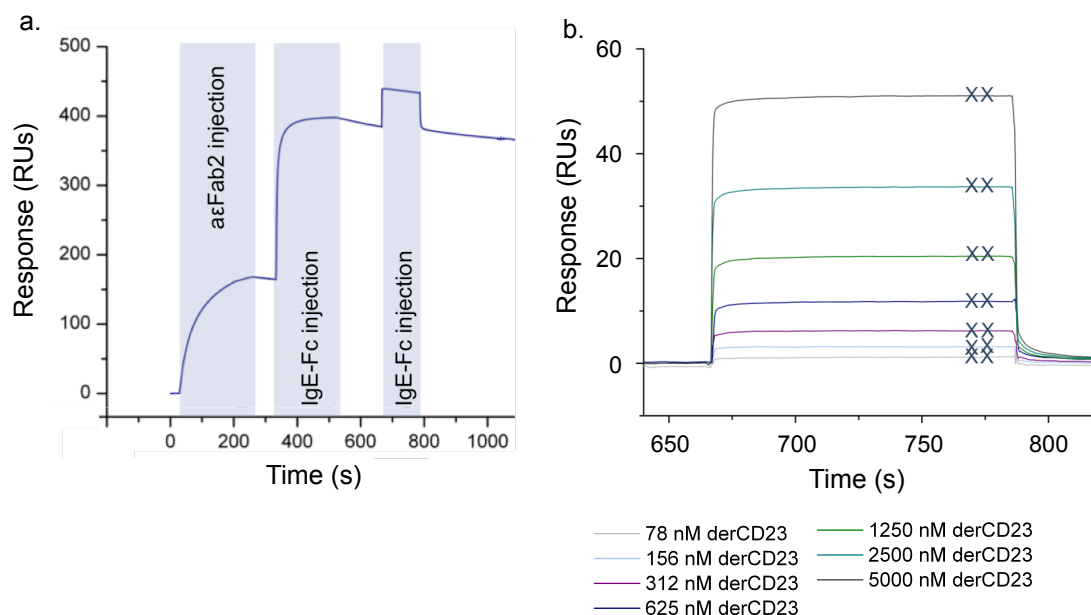


Figure 5.4: **Example sensorgrams from SPR experiments to investigate the binding of derCD23 to  $\alpha\epsilon$ Fab-bound IgE-Fc in transient transfection supernatant.** (a) Transient transfection supernatant, containing  $\alpha\epsilon$ Fab ( $\alpha\epsilon$ Fab2 here), was injected over a Fab-specific goat anti-rabbit F(ab')<sub>2</sub>. IgE-Fc bound the captured  $\alpha\epsilon$ Fab and derCD23 was injected over the  $\alpha\epsilon$ Fab:IgE-Fc (1:1) complex. Binding was observed as change in SPR response. (b) The response when 0 nM derCD23 was injected over the captured  $\alpha\epsilon$ Fab:IgE-Fc (1:1) complex, at increasing concentrations, in order to eliminate changes in response as a result of dissociation of  $\alpha\epsilon$ Fab from the anti-rabbit-Fab surface and IgE-Fc from the  $\alpha\epsilon$ Fab. The crosses indicate the 5 s interval during the steady-state response for which the response was averaged for steady-state analysis.

from 90 - 163 %, which implies that the different  $\alpha\epsilon$ Fab:IgE-Fc complexes have differing binding capacities for derCD23.

The binding of derCD23 to  $\alpha\epsilon$ Fab13-bound IgE-Fc was distinct in that it appears to have accelerated the dissociation of IgE-Fc from  $\alpha\epsilon$ Fab13 (Figure 5.6). There was an increase in response upon the injection of derCD23 to  $\alpha\epsilon$ Fab13-bound IgE-Fc, which indicated that derCD23 bound the  $\alpha\epsilon$ Fab13:IgE-Fc (1:1) complex and formed a tertiary ( $\alpha\epsilon$ Fab13:IgE-Fc:derCD23) complex, but instead of reaching a steady-state, the SPR signal began to decrease during the association phase. This decrease in response indicates negative cooperativity: that the binding of derCD23 increased the rate of IgE-Fc dissociation from  $\alpha\epsilon$ Fab13. Accelerated dissociation of the IgE-Fc/sFc $\epsilon$ RI $\alpha$  complex by DARPin E2-79 has been proposed to be due

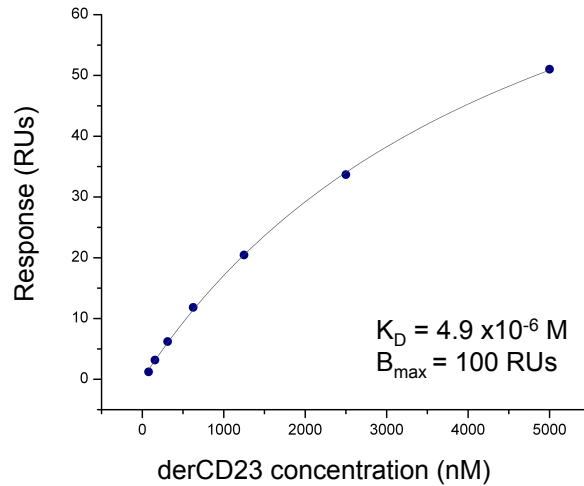


Figure 5.5: **The binding curve for the interaction between derCD23 and aεFab2-bound IgE-Fc.** The data were generated from SPR experiments in which derCD23 binding to a captured aεFab2:IgE-Fc (1:1) complex was measured as a change in response. The steady-state response was averaged from 5 s of steady-state binding data (blue circles) and was fit (black line) using a one-to-one binding model (Section 2.6.4).

to the partial overlap of ligand binding [109], however in Chapter 3 we proposed that it is possible that the binding of a ligand to a pre-bound IgE-Fc complex can affect the rate of dissociation of that complex via allosteric means (Section 3.2.3). Perhaps derCD23-mediated accelerated dissociation of aεFab13 from IgE-Fc is also allosteric in nature.

Fab-bound IgE-Fc/derCD23 interaction					
	$K_D$ ( $\mu$ M)	$B_{\max}$ (% of th $B_{\max}$ )		$K_D$ ( $\mu$ M)	$B_{\max}$ (% of th $B_{\max}$ )
aεFab12	0.6	105	aεFab9	1.9	163
aεFab17	1.0	97	aεFab7	1.9	133
aεFab4	1.1	138	aεFab13*	1.9	133
aεFab3	1.4	130	aεFab18	2.4	156
aεFab5	1.5	118	aεFab2	4.9	156

Table 5.2: **Summary of the dissociation constants and  $B_{\max}$  values for derCD23 binding to aεFab-bound IgE-Fc as determined by SPR using transiently transfected aεFab supernatants.** The steady-state response of derCD23 binding to aεFab-bound IgE-Fc was plotted as a function of derCD23 concentration. The data were fit using a one-to-one binding model (Section 2.6.4). The  $B_{\max}$  values are expressed as a percentage of the theoretical  $B_{\max}$  (Section 2.6.2). The asterisk indicates derCD23-mediated aεFab:IgE-Fc accelerated dissociation.

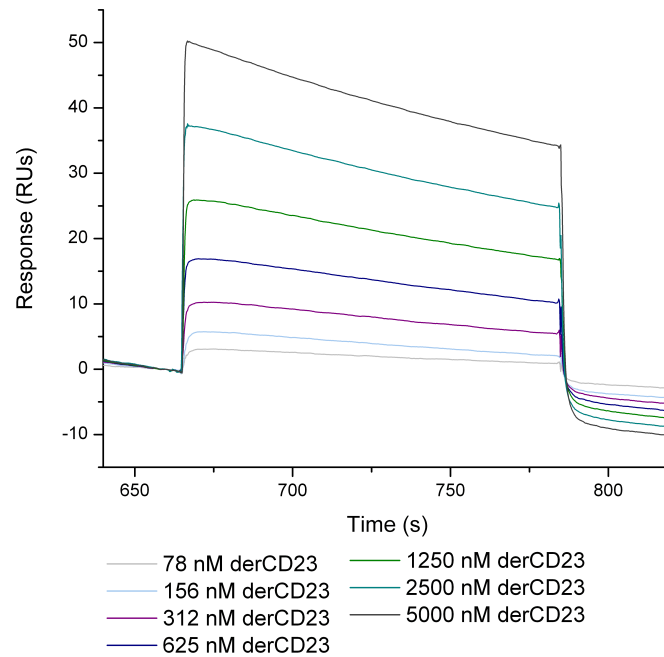


Figure 5.6: **derCD23 accelerates the dissociation of IgE-Fc from aεFab13 as shown by SPR experiments using aεFab transient transfected supernatants.** A double-reference subtracted SPR sensorgram of derCD23 binding to captured aεFab13:IgE-Fc.

### 5.2.3 Investigating the effect of one aεFab molecule on the IgE-Fc/sFcεRIα interaction using SPR.

SPR experiments with supernatants containing the aεFabs were performed to determine what effects the aεFabs have on the binding of sFcεRIα to IgE-Fc. A Fab-specific goat anti-rabbit F(ab')<sub>2</sub> fragment (Jackson ImmunoResearch, 111-046-047) was immobilised on the surface of the sensor chip using amine-coupling techniques (Section 2.6.2). A mock amine-coupled surface was used as a reference-subtraction surface (Section 2.6.2). The supernatants, containing the aεFab, were diluted 1 in 4 in SPR running buffer and injected for 210 s over the sensor surfaces. The Fabs were captured on the goat anti-rabbit-Fab surface at low densities (<200 RUs). 100 nM IgE-Fc was then injected for 150 s over the sensor surfaces and bound the captured aεFab to form an aεFab:IgE-Fc (1:1) complex. sFcεRIα was injected for 120 s over the captured complex at various concentrations and binding to the aεFab:IgE-Fc (1:1) complex was measured as a change in the SPR response (Figure 5.7). A dissociation phase of 300 s followed each sFcεRIα injection and the goat



anti-rabbit-Fab surface was regenerated by two 60 s pulses of 10 mM glycine pH 1.7 and one 30 s pulse of 5 mM NaOH.

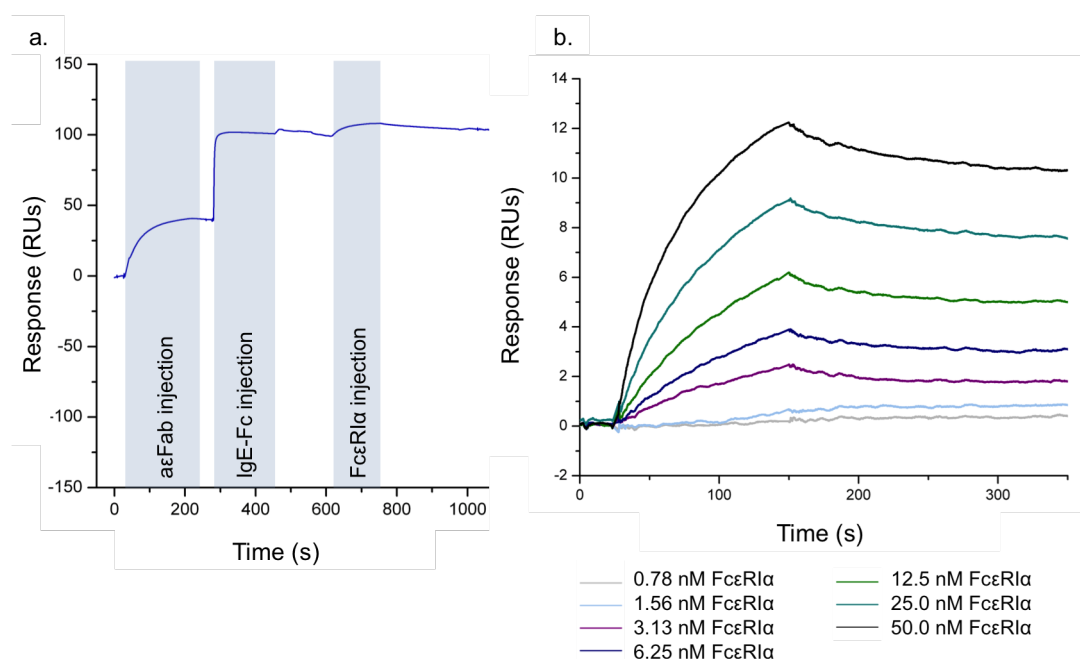


Figure 5.7: **Example sensorgrams from SPR experiments to investigate the binding of sFcεR1α to αεFab-bound IgE-Fc in transient transfection supernatant.** (a) transient supernatant containing αεFab (αεFab2 here) was injected over a Fab-specific goat anti-rabbit F(ab')<sub>2</sub>. IgE-Fc bound the captured αεFab, sFcεR1α was injected over the αεFab:IgE-Fc (1:1) complex. Binding was observed as change in SPR response. (b) The response when 0 nM sFcεR1α was injected over the captured αεFab:IgE-Fc (1:1) complex was subtracted from the response measured when sFcεR1α was injected over the αεFab:IgE-Fc (1:1) complex at increasing concentrations, in order to eliminate changes in response as a result of dissociation of αεFab from the anti-rabbit-Fab surface and IgE-Fc from the αεFab.

There was an increase in SPR response upon injection of sFcεR1α onto all of the αεFab-IgE-Fc complexes indicating that the different αεFab-IgE-Fc complexes were all capable of binding sFcεR1α (Appendix A.4). From looking at the sensorgrams, the binding of FcεR1α to IgE-Fc bound to the different αεFabs broadly fell into three classes: those with slower off-rates (αεFab2, 12 and 17), those with faster off-rates (αεFab3, 7, 13 and 18) and those more difficult to interpret because the signal was significantly limited by the capture level (αεFab4, 5 and 9). The data for the first two groups were fit using single  $k_{\text{off}}$  and  $k_{\text{on}}$  models (Section 2.6.3) (Figure 5.8) and were used to determine the  $K_D$  of each αεFab-IgE-Fc interaction using

Equation 2.4. Because of the low signal, the data for  $\alpha\epsilon 4$ ,  $\alpha\epsilon 5$  and  $\alpha\epsilon\text{Fab9}$  were not suitable for fitting. The rest of the  $\alpha\epsilon\text{Fab}:\text{IgE-Fc}$  complexes bound  $\text{sFc}\epsilon\text{RI}\alpha$  with nanomolar binding affinities (Table 5.3).

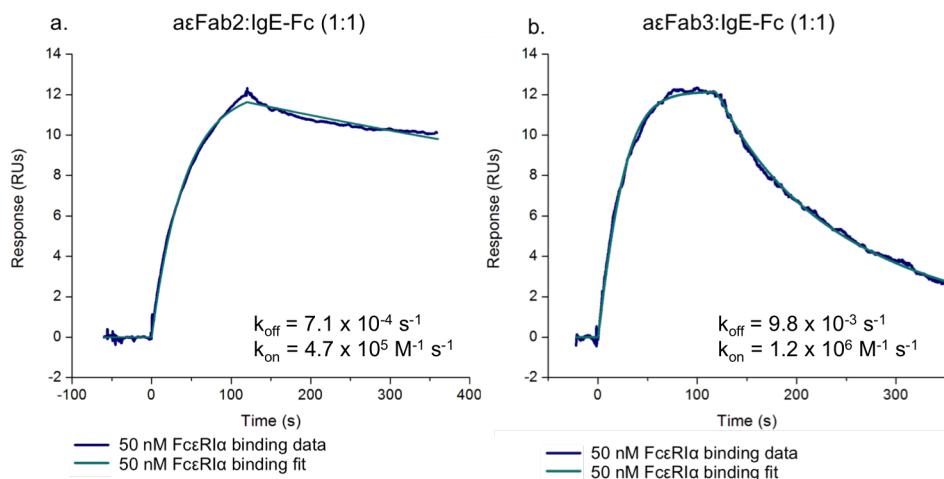


Figure 5.8: **Different  $\alpha\epsilon\text{Fab}:\text{IgE-Fc}$  (1:1) complexes bind  $\text{sFc}\epsilon\text{RI}\alpha$  with different kinetics.** A comparison of the kinetics of binding by SPR of (a)  $\alpha\epsilon\text{Fab2}:\text{IgE-Fc}$  (1:1) and (b)  $\alpha\epsilon\text{Fab3}:\text{IgE-Fc}$  (1:1) to 50 nM  $\text{sFc}\epsilon\text{RI}\alpha$ . The data has been normalised to give a maximal response of 12 RUs. The data were fit in the Biacore Evaluation software (GE Healthcare) using their single  $k_{\text{off}}$  and  $k_{\text{on}}$  model.

The  $K_{\text{D}}$  values were around one order of magnitude greater than the published values for the interaction between  $\text{sFc}\epsilon\text{RI}\alpha$  [83]. The published  $k_{\text{on}}$  and  $k_{\text{off}}$  values for the  $\text{IgE-Fc}/\text{sFc}\epsilon\text{RI}\alpha$  interaction are about  $3 \times 10^5 \text{M}^{-1} \text{s}^{-1}$  and  $1.9 \times 10^{-4} \text{s}^{-1}$  respectively [83]. The  $k_{\text{on}}$  values determined from the  $\alpha\epsilon\text{Fab}$  experiments were also in the  $10^5 \text{M}^{-1} \text{s}^{-1}$  range. The  $k_{\text{off}}$  values were generally in the range of  $10^{-4} \text{s}^{-1}$ . This relatively small discrepancy could be accounted for by differences in experimental set-up and does not necessarily mean that the presence of the  $\alpha\epsilon\text{Fabs}$  had a negative effect on the  $\text{IgE-Fc}/\text{sFc}\epsilon\text{RI}\alpha$  in each case.

These experiments were performed in the absence of a control for the  $\text{sFc}\epsilon\text{RI}\alpha:\text{IgE-Fc}$  interaction as we did not have a previously characterised  $\alpha\epsilon\text{Fab}$  that was known not to effect the interaction, therefore the comparisons were made in relation to the published values [83]. Assuming  $k_{\text{on}}$  values closer to  $10^5 \text{M}^{-1} \text{s}^{-1}$  and  $k_{\text{off}}$  closer to  $10^{-4} \text{s}^{-1}$  represent more ‘native-like’  $\text{IgE-Fc}/\text{sFc}\epsilon\text{RI}\alpha$  binding, the binding of  $\text{sFc}\epsilon\text{RI}\alpha$  to  $\text{IgE-Fc}$  clearly appears to have been affected by pre-complexing  $\text{IgE-Fc}$  with  $\alpha\epsilon\text{Fab3}$ . Both the association and dissociation rate constants of the interac-

tion are different from the most ‘native-like’ values, for example those of aεFab2 (Figure 5.8). The dissociation rate constant is nearly 14 times faster than that of the aεFab2:IgE-Fc/sFcεRIα interaction. Although less marked, aεFab7, aεFab13 and aεFab18-IgE-Fc complexes also exhibited more rapid sFcεRIα dissociation. The observed increase in IgE-Fc/sFcεRIα off-rate suggests that these aεFabs do not completely block the FcεRI binding site but do make the IgE-Fc/sFcεRIα complex less stable.

<b>Fab-bound IgE-Fc/FcεRIα interaction</b>			
	$k_{\text{on}} \text{ M}^{-1} \text{ s}^{-1}$	$k_{\text{off}} \text{ s}^{-1}$	$K_{\text{D}} (\times 10^{-9} \text{ M})$
<b>aεFab12</b>	$5.9 \times 10^5$	$6.9 \times 10^{-4}$	1.2
<b>aεFab2</b>	$4.7 \times 10^5$	$7.1 \times 10^{-4}$	1.5
<b>aεFab17</b>	$5.4 \times 10^5$	$9.9 \times 10^{-4}$	1.8
<b>aεFab7</b>	$6.8 \times 10^5$	$3.5 \times 10^{-3}$	5.2
<b>aεFab18</b>	$7.4 \times 10^5$	$4.8 \times 10^{-3}$	6.5
<b>aεFab13</b>	$8.3 \times 10^5$	$5.7 \times 10^{-3}$	6.9
<b>aεFab3</b>	$1.2 \times 10^6$	$9.8 \times 10^{-3}$	8.2

Table 5.3: **Summary of the association and dissociation rate constants and the dissociation constants for sFcεRIα binding to aεFab-bound IgE-Fc as determined by SPR.** The data for binding 50 nM (or 25 nM for aεFab18) of sFcεRIα were fit in the Biacore Evaluation software (GE Healthcare) using their single  $k_{\text{off}}$  and  $k_{\text{on}}$  model.

#### 5.2.4 aεFab competition experiments using SPR.

Surface plasmon resonance experiments were performed in an effort to determine if the different aεFabs share overlapping binding epitopes on IgE-Fc. To do this we investigated the binding of each of the aεFabs to different captured aεAb:IgE-Fc:aεFab complexes. The complexes were made by sequential injections of aεAb, IgE-Fc and then the respective aεFab. In these experiments full length aεAbs (Section 4.2.4) were captured by an anti-IgG-Fc surface rather than aεFabs by an anti-Fab surface in order to prevent the binding of aεFabs to the SPR surface in subsequent injections.

An SPR sensor surface was generated onto which a goat anti-rabbit IgG-Fc-

specific F(ab')<sub>2</sub> fragment (Jackson ImmunoResearch) was immobilised using amine-coupling techniques (Section 2.6.2). A mock amine-coupled surface was used as a reference-subtraction surface (Section 2.6.2). The aεAbs, in supernatant, were diluted 1 in 4 in SPR running buffer and were injected over the sensor surfaces for 150 s. The aεAbs were captured on the IgG-Fc-specific goat-anti-rabbit surface at a low density (<250 RUs). 100 nM IgE-Fc was injected for 150 s over the surfaces and bound to form aεAb:IgE-Fc (1:1) complexes. The equivalent aεFab in supernatant (diluted 1 in 4 in SPR running buffer) was then injected over the surfaces for 150 s to determine if the aεFabs/Abs bind IgE-Fc with a 2:1 stoichiometry, and if so, to ensure that a majority of the sites were occupied. Finally, each of the other aεFabs, in supernatant (diluted 1 in 4 in SPR running buffer) were injected over the surfaces for 150 s, and any binding was observed as an increase in SPR response (Figure 5.9 and Appendix A.5). A dissociation phase of 300 s was followed by two 60 s injections of 10 mM glycine-HCl pH 1.7 and one 30 s injection of 5 mM NaOH to regenerate the surface for the next cycle.

All of the aεFabs bound to their corresponding aεAb:IgE-Fc complexes, indicating that they all bind IgE-Fc with a 2:1 stoichiometry (aεFab:IgE-Fc). There were several instances where the injection of an aεFab did not result in an increase in response when injected over a different aεAb:IgE-Fc:aεFab complex and *visa versa* (Figure 5.10). For example, aεFab4 did not bind to the aεAb5:IgE-Fc:aεFab5 complex and aεFab5 did not bind to the aεAb4:IgE-Fc:aεFab4 complex. Pairs of aεFabs that mutually inhibited one another may share overlapping binding epitopes on IgE-Fc or sterically occlude one another's binding, however the observed inhibition could also be allosteric in nature. Interestingly, aεFab2 and aεFab3 mutually inhibited one another as did aεFab2 and aεFab18, however aεFab3 bound aεAb18:IgE-Fc:aεFab18 complex and aεFab18 bound aεAb3:IgE-Fc:aεFab3. Perhaps aεFab18 and aεFab3 IgE-Fc binding sites do not overlap but the aεFab2 binding site partially overlaps both. Alternatively, aεFab2 may communicate allosterically with either or both aεFab3 and aεFab18. The aεAb12:IgE-Fc:aεFab12 complex did not prevent binding of any of the other aεFabs, which suggests that it binds distinct sites on IgE-Fc.

In some cases aεFab inhibition was not reciprocal. For example, aεFab9 did not

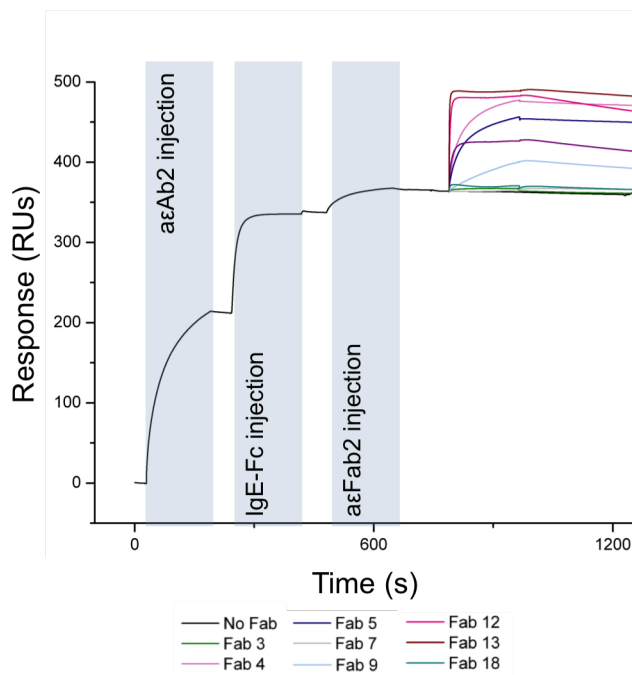


Figure 5.9: **An example sensorgram from SPR experiments to investigate aεFab competition.** This is the data for the binding of aεFabs in transiently transfected supernatant to a captured aεAb2:IgE-Fc:aεFab2 (1:1:1) complex. aεAb (aεAb2, here), in transiently transfected supernatant, was captured by immobilised IgG-Fc-specific goat-anti-rabbit F(ab')<sub>2</sub> (Jackson ImmunoResearch). IgE-Fc was injected over the captured aεAb to generate an aεAb:IgE-Fc complex. The corresponding aεFab (aεFab2, here), in transiently transfected supernatant, was injected in over the surface and bound to give an aεAb:IgE-Fc:aεFab (1:1:1) complex. Other aεFabs, in transiently transfected supernatant, were then injected over the complex and binding was measured as a change in SPR response.

bind the aεAb:IgE-Fc:aεFab 3, 7, 13 and 18 complexes, but aεFabs 3, 7, 13 and 18 did bind the aεAb13:IgE-Fc:aεFab9 complex. This observation could be explained by a situation in which the binding of aεFab9 to IgE-Fc does not significantly affect the conformational ensemble of IgE-Fc, and therefore the binding of other aεFabs is still viable. Whereas the other aεFabs may bind and stabilise conformations of IgE-Fc where aεFab9 binding is not permissible.

Another interesting observation was that aεFab18 caused accelerated dissociation of the aεAb13:IgE-Fc:aεFab13 complex (Figure 5.6). With this experimental setup, it is not possible to deduce whether aεFab18 caused accelerated dissociation of aεFab13 from IgE-Fc or aεFab13:IgE-Fc from aεAb13. Although accelerated dissociation is not necessarily an allosteric phenomenon, in Chapter 3 we showed that accelerated dissociation can occur as a result of allosteric communication (Section

3.3).

Initially the aim of these experiments was to try to identify  $\alpha$ Fabs that may bind to very similar sites, and thereby prevent the selection of similar  $\alpha$ Fabs. The results, however, also provided insights into possible allosteric communication between different  $\alpha$ Fab binding sites, which together with the results from the receptor-binding assays, helped in the selection of which  $\alpha$ Fabs to express on a larger-scale. It should be noted that these experiments were performed with a single unknown concentration of  $\alpha$ Fab, which limits the certainty of the observed results. Once the selected  $\alpha$ Fabs have been purified and their concentration ascertained, we plan to perform these experiments again at a range of different  $\alpha$ Fab concentrations in order to determine the extent of competition between the different antibodies.

### 5.2.5 Selection of six $\alpha$ Fabs

The ultimate aim of the project is to find, express and characterise Fabs that bind to IgE-Fc and allosterically modulate binding of IgE to its ‘low affinity receptor’, CD23. The previous chapter described how the immune repertoires of rabbits, immunised against IgE-Fc, were screened to discover antibodies that bind IgE-Fc and have an effect on derCD23 binding. This chapter describes how those antibodies were expressed as Fabs and characterised in greater detail for their ability to bind IgE-Fc and modulate derCD23 binding using SPR. We wanted to select about six antibodies that have diverse effects on derCD23 binding, therefore we also analysed their effect on the interactions between IgE-Fc and the ‘high-affinity receptor’, Fc $\epsilon$ RI, and IgE-Fc and the other Fabs. Two Fabs, for example, may appear to have the same effect on CD23 binding as each other, but by investigating these additional binding characteristics we can perhaps see if the way they interact with IgE-Fc is actually distinct. Importantly, we also wanted to select for those  $\alpha$ Fabs that appear to modulate receptor binding by allosteric processes. Of the 13 Fabs tested in this chapter, six were selected for large-scale expression:  $\alpha$ Fab2,  $\alpha$ Fab3,  $\alpha$ Fab9,  $\alpha$ Fab12,  $\alpha$ Fab13 and  $\alpha$ Fab18.


$\alpha$ Fab2 and  $\alpha$ Fab12 were selected because of their apparent effects on derCD23 binding: the  $\alpha$ Fab2:IgE-Fc complex had the lowest apparent affinity for derCD23


( $K_D = 4.9 \times 10^{-6}$  M), whereas  $\alpha\epsilon\text{Fab12:IgE-Fc}$  had the highest apparent affinity for derCD23 ( $K_D = 0.6 \times 10^{-6}$  M). In the absence of a control for derCD23 binding to captured IgE-Fc we are unable, at this point, to describe the  $\alpha\epsilon\text{Fabs}$  as ‘inhibitors’ or ‘enhancers’, however given the difference in  $K_D$  values of the various  $\alpha\epsilon\text{Fab:IgE-Fc/derCD23}$  interactions, it is probable that at least one of the  $\alpha\epsilon\text{Fab:IgE-Fc}$  complexes has a significant cooperative effect on derCD23 binding.

The  $B_{\max}$  value for derCD23 binding to the  $\alpha\epsilon\text{Fab2:IgE-Fc}$  complex was 156 % of the theoretical  $B_{\max}$  value calculated for the binding of one derCD23 molecule to IgE-Fc, indicating partial occupancy of the second, lower-affinity, derCD23 binding site. This suggests that saturation of the first  $\alpha\epsilon\text{Fab2}$  binding site does not completely prevent binding of derCD23 to either of the two CD23 binding sites on IgE-Fc and instead its effect on the CD23/IgE-Fc interaction may be allosteric. The  $B_{\max}$  value for the  $\alpha\epsilon\text{Fab12:IgE-Fc}$  complex was estimated to be around 100 % of the theoretical  $B_{\max}$  value calculated for the binding of a single derCD23 molecule to IgE-Fc.  $\alpha\epsilon\text{Fab12}$  may have blocked the lower-affinity derCD23 binding site so that IgE-Fc could only bind derCD23 with a 1:1 stoichiometry.

The relatively high  $K_D$  of the interaction between  $\alpha\epsilon\text{Fab2:IgE-Fc}$  and derCD23 could suggest that  $\alpha\epsilon\text{Fab2}$  reduces the affinity of the IgE-Fc/derCD23 interaction. Whereas the relatively low  $K_D$  of the interaction between  $\alpha\epsilon\text{Fab12:IgE-Fc}$  and derCD23 may suggest that  $\alpha\epsilon\text{Fab12}$  increases the affinity of the IgE-Fc/derCD23 interaction. However, as described, the  $B_{\max}$  values of the two interactions (expressed as a percentage of the theoretical  $B_{\max}$  of IgE-Fc binding one molecule of derCD23) are also markedly different and suggest that the  $K_D$  values for the  $\alpha\epsilon\text{Fab2:IgE-Fc/derCD23}$  interaction and the  $\alpha\epsilon\text{Fab12:IgE-Fc/derCD23}$  interaction may reflect contributions from both, and just one, of CD23 binding sites, respectively. Because the two CD23 binding sites have two different affinities and because these appear differentially occupied in the the  $\alpha\epsilon\text{Fab2}$  and  $\alpha\epsilon\text{Fab12}$  experiments, the  $K_D$  values cannot be directly used to compare the effects of these two  $\alpha\epsilon\text{Fabs}$  on the affinity of the IgE/CD23 interaction. Nevertheless, the marked differences in both the  $K_D$  and  $B_{\max}$  values for these two  $\alpha\epsilon\text{Fab:IgE-Fc}$  complexes indicates the effects that they have on the IgE-Fc/derCD23 interaction are probably very different.

	aεFab2	aεFab3	aεFab4	aεFab5	aεFab7	aεFab9	aεFab12	aεFab13	aεFab18
aεAb2:IgE-Fc:aεFab2									
aεAb3:IgE-Fc:aεFab3									
aεAb4:IgE-Fc:aεFab4									
aεAb5:IgE-Fc:aεFab5									
aεAb7:IgE-Fc:aεFab7									
aεAb9:IgE-Fc:aεFab9									
aεAb12:IgE-Fc:aεFab12									
aεAb13:IgE-Fc:aεFab13									
aεAb18:IgE-Fc:aεFab18									

 No binding

 binding


 Not tested

Figure 5.10: **An overview of the results from the aεFab SPR competition experiments.** Tertiary IgE-Fc complexes were formed in which IgE-Fc was bound to an aεAb and its corresponding aεFab. Other aεFabs, in transiently transfected supernatant, were injected over the captured tertiary complex to determine if binding could occur - *i.e.* to see if a quaternary complex could form. Blue indicates that the quaternary complex did not form, white indicates a quaternary complex did form, and AD indicates that binding of the aεFab triggered accelerated dissociation of the tertiary complex.

Like the aεFab2:IgE-Fc/derCD23 interaction, the aεFab13:IgE-Fc/derCD23 interaction had a  $B_{\max}$  value in excess of 100 % of the theoretical  $B_{\max}$  for the binding



of a single molecule of derCD23 (133 % of the theoretical  $B_{\max}$ ). The  $\alpha\epsilon$ Fab13:IgE-Fc complexes therefore appears to be able to bind two molecules of derCD23, indicating that the  $\alpha\epsilon$ Fab13 binding sites do not overlap with the CD23 binding sites on IgE-Fc. The interaction between derCD23 and the  $\alpha\epsilon$ Fab13:IgE-Fc complex had a  $K_D$  value about half the value of the  $K_D$  for the  $\alpha\epsilon$ Fab2:IgE-Fc complex, indicating  $\alpha\epsilon$ Fab2 and  $\alpha\epsilon$ Fab13 may affect the affinity of the IgE-Fc/CD23 interaction differently.  $\alpha\epsilon$ Fab13 is also interesting because the binding of derCD23 to  $\alpha\epsilon$ Fab13:IgE-Fc induced accelerated dissociation of IgE-Fc from  $\alpha\epsilon$ Fab13. Similarly,  $\alpha\epsilon$ Fab18 induced accelerated dissociation of the  $\alpha\epsilon$ Ab13:IgE-Fc: $\alpha\epsilon$ Fab13 complex. We showed in Chapter 3 that derCD23 can accelerate the dissociation of IgE-Fc complexes via allosteric means. Accelerated dissociation is an interesting phenomenon, and an understanding of its mechanisms could allow the design of drugs that can accelerate the dissociation of pre-formed IgE:receptor complexes (Section 5.2.4).

The  $\alpha\epsilon$ Fab3:IgE-Fc complex appeared to have little effect on derCD23 binding when compared to the other  $\alpha\epsilon$ Fab:IgE-Fc complexes and also appeared to be able to bind two derCD23 molecules. However,  $\alpha\epsilon$ Fab3 appeared to have a cooperative effect on the interaction between IgE-Fc and sFc $\epsilon$ RI $\alpha$ .  $\alpha\epsilon$ Fab3-bound IgE-Fc had both the largest association rate constant and the largest dissociation rate constant. The off-rate for the interaction between sFc $\epsilon$ RI $\alpha$  and  $\alpha\epsilon$ Fab3:IgE-Fc was seven times faster than that of the slowest off-rate. The competition experiments showed that  $\alpha\epsilon$ Ab2:IgE-Fc: $\alpha\epsilon$ Fab2 could not bind  $\alpha\epsilon$ Fab3 and  $\alpha\epsilon$ Ab3:IgE-Fc: $\alpha\epsilon$ Fab3 could not bind  $\alpha\epsilon$ Fab2, indicating that these  $\alpha\epsilon$ Fabs are inhibitors of one another, but further experiments using a range of known  $\alpha\epsilon$ Fab2 and  $\alpha\epsilon$ Fab3 concentrations are necessary to confirm this. This result is particularly interesting as  $\alpha\epsilon$ Fab3 appears to affect sFc $\epsilon$ RI $\alpha$  binding but not derCD23 binding, and  $\alpha\epsilon$ Fab2 appears to affect derCD23 binding but not sFc $\epsilon$ RI $\alpha$ .  $\alpha\epsilon$ Fab2 and  $\alpha\epsilon$ Fab3 could be allosteric or orthosteric inhibitors of one another; either way it is interesting that they each appear to affect the binding of only one of the IgE receptors, both of which allosterically inhibit one another [18, 89].

The competition experiments revealed potential asymmetry in binding of the different  $\alpha\epsilon$ Fabs to IgE-Fc.  $\alpha\epsilon$ Ab9:IgE-Fc: $\alpha\epsilon$ Fab9 was able to bind all of the  $\alpha\epsilon$ Fabs except 4 and 5, yet  $\alpha\epsilon$ Fab9 was unable to bind the  $\alpha\epsilon$ Ab:IgE-Fc: $\alpha\epsilon$ Fab complexes

except for aεFab2 and aεFab12. This suggests that the binding of aεFab9 may cause a smaller shift in the IgE-Fc conformational ensemble than the other aεFabs, however, repeating these experiments with known concentrations of aεFab would be necessary to confirm this observation. Furthermore, the  $K_D$  and  $B_{max}$  values determined for the SPR analysis of the binding of derCD23 to aεFab9-bound IgE-Fc were not the highest or lowest compared to the other aεFab:IgE-Fc complexes (Tables 5.2, perhaps suggesting that aεFab9 could act as a control aεFab in future studies of the IgE-Fc/CD23 interaction. Low signal levels made determining the effect of aεFab9 on the interaction between IgE-Fc and FcεRIα difficult, and we plan to perform these experiments again in the future with purified material.

### 5.2.6 Expression of the selected aεFabs in CHOSXE cells

Previously, the DNA for the heavy and light variable domains of the aεFabs had been separately cloned into UCB mammalian expression vectors (Section 2.5.10 and 5.2.1). Heavy variable domain DNA was inserted into a plasmid containing a downstream rabbit IgG CH1 domain, whereas the kappa variable domain DNA was inserted into a plasmid containing a downstream rabbit IgG C<sub>κ</sub> domain. Both plasmids were under the control of a HMCV promoter, encoded kanamycin resistance, and contained a pUC origin of replication in addition to a SV40 5' polyadenylation sequence.

Greater quantities of each of the plasmids were required for large-scale transfections of a mammalian cell culture. Therefore, XL1-Blue chemically competent *E. coli* (Stragene) were transformed, using heat shock, with the heavy and light chain plasmid DNA for each of the selected aεFabs (Section 2.2.3). The transformed XL1-Blue cells were grown in 1.5 L overnight cultures of LB and the expanded plasmid DNA was purified using Qiagen's GigaPrep Kit according to manufacturer's instructions. For each of the six selected aεFabs, the Fab heavy chain plasmid DNA (encoding the V<sub>H</sub>1 and C<sub>H</sub>1 domains) and the Fab kappa chain plasmid DNA (encoding the V<sub>κ</sub>1 and C<sub>κ</sub> domains) were sequenced. The online tool, ExPasy Translate [188], was used to translate the DNA sequences into protein sequences (Figure 5.11). The CDR3 protein sequences were compared with the

CDR3 sequences of the DNA used for transformation, which had been previously sequenced (Section 4.2.3). For both the heavy and light chains of the six selected  $\alpha$ Fabs there was 100 % agreement between the CDR3 sequences of the DNA used for transformation and the CDR3 sequences of the GigaPrep-derived DNA.

CHOSXE cells [150] were co-transfected with 1:1 ratios of heavy:kappa  $\alpha$ Fab plasmid, using electroporation (Section 2.5.12). The cells were cultured at 37 °C, with shaking at 140 rpm and supplemented with 8 % CO<sub>2</sub>. After 14 days of incubation, the cell cultures were centrifuged to harvest the supernatants. The supernatants were sterile filtered and small aliquots were run on a protein G HPLC column to determine the approximate  $\alpha$ Fab concentration in the supernatants (Section 2.5.12). Protein G is a bacterial cell wall protein from group B *streptococci*. It binds to the Fc region of most mammalian antibodies, however protein G can also bind the C<sub>H</sub>1 domain of heavy chains bound to C<sub>κ</sub> light chains, albeit with a lower affinity [189]. Protein G HPLC analysis of the supernatants indicated that five of the six selected  $\alpha$ Fabs had been expressed: Fab was not detected in the  $\alpha$ Fab9 supernatant (Table 5.4). The transfections and the protein G HPLC analysis were kindly performed by Hanna Hailu of UCB.

<b>Transfection supernatant</b>	<b>Fab concentration (mg/L)</b>	<b>Supernatant volume (L)</b>	<b>Total Fab amount (mg)</b>
<b>aεFab2</b>	539.4	0.9	485.5
<b>aεFab3</b>	490.0	0.9	441.0
<b>aεFab9</b>	1.0	0.9	0.9
<b>aεFab12</b>	284.3	0.9	255.8
<b>aεFab13</b>	325.7	0.9	293.2
<b>aεFab18</b>	135.2	0.9	121.7

Table 5.4: **Protein G HPLC analysis of aεFab transfection supernatants.** CHOSXE cells [150] were transfected with a 1:1 ratio of heavy:kappa chain aεFab plasmid DNA. The supernatants were harvested after a 14 day culture and 100  $\mu$ l was run on a 1 ml protein G HPLC column (GE Healthcare). The concentration of aεFab in each supernatant was determined by comparing the area of the aεFab elution peak to the elution peaks of a standard (Certolizumab Fab) at known concentrations.

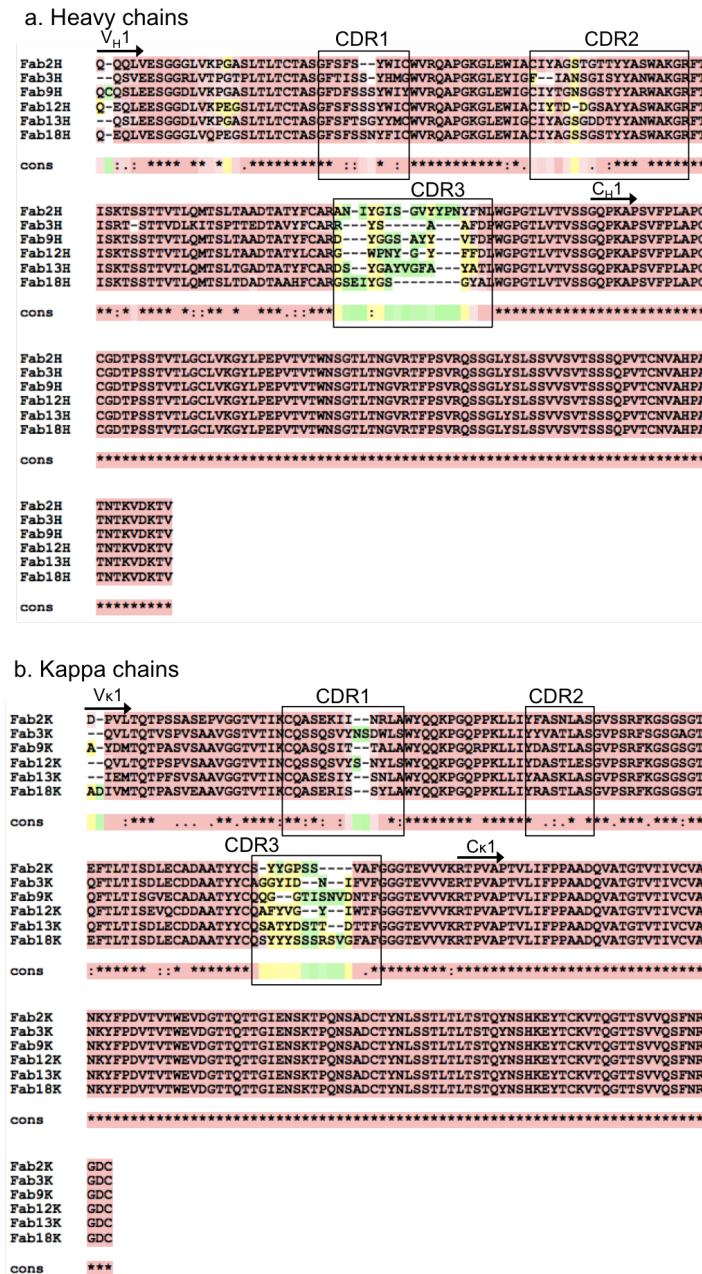


Figure 5.11: **Sequence alignment of the six  $\alpha$ Fabs selected for large scale expression and purification.** The DNA encoding the (a) heavy and (b) kappa chains of the  $\alpha$ Fabs were in a UCB in-house mammalian expression vector containing containing an HMCV promoter, a polyadenylation sequence, a pUC origin of replication and encoding kanamycin resistance. The DNA for the heavy and kappa chains were sequenced using a forward primer complementary to the region of the plasmid immediately upstream of the  $\alpha$ Fab leader sequence (not shown) by the Eurofins Genomics sequencing service. The sequence alignment was performed using Tcoffee [190] version 11.00.d625267, which produces alignments based on analysis of results from a variety of different methods. The default multiple sequence alignment methods were analysed in this alignment.

### 5.2.7 Purification of the $\alpha\epsilon$ Fabs

Protein G affinity chromatography was used to purify the five  $\alpha\epsilon$ Fabs, but because of the relatively low affinity of the Protein G/Fab interaction, the  $\alpha\epsilon$ Fab supernatants were first concentrated to at least 350 mg/L using a tangential flow ultrafiltration system with a 10 kDa membrane (Section 2.5.13). The concentrated  $\alpha\epsilon$ Fab supernatants were run down a 100 ml column packed with protein G sepharose (GE Healthcare) and the  $\alpha\epsilon$ Fabs were eluted from the column using acid elution (Section 2.5.13) (Figure 5.12).

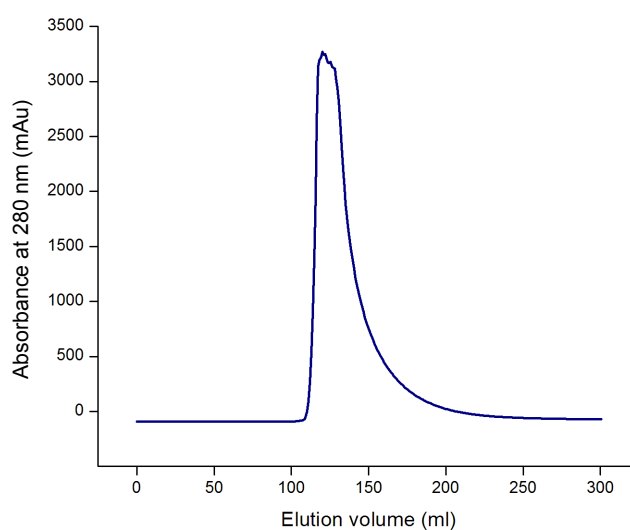


Figure 5.12:  $\alpha\epsilon$ Fab12 purification using protein G affinity chromatography. Supernatant, containing  $\alpha\epsilon$ Fab12, was run down a 100 ml column packed with protein G-sepharose (GE Healthcare) in PBS pH 7.4. Bound  $\alpha\epsilon$ Fab12 was eluted in 100 mM glycine-HCl, pH 2.7 and immediately neutralized.

The  $\alpha\epsilon$ Fab peak fractions were pooled, neutralised and concentrated using centrifugal filter units (Millipore) and subsequently run on a size exclusion column (HiLoad 26/600 Superdex 200 pg, GE Healthcare) to isolate monomeric  $\alpha\epsilon$ Fab (Section 2.5.13) (Figure 5.13). The chromatograms consisted of a small peak, assumed to be  $\alpha\epsilon$ Fab aggregates, followed by a major peak containing eluted monomeric  $\alpha\epsilon$ Fab. The aggregated  $\alpha\epsilon$ Fab could account for the tailing seen in the Protein G affinity purification chromatograms (Figure 5.12) as the aggregates may have had a longer retention time than the monomers. The monomeric  $\alpha\epsilon$ Fab peak fractions from the preparative SEC were pooled and concentrated using centrifugal filter units (Millipore).

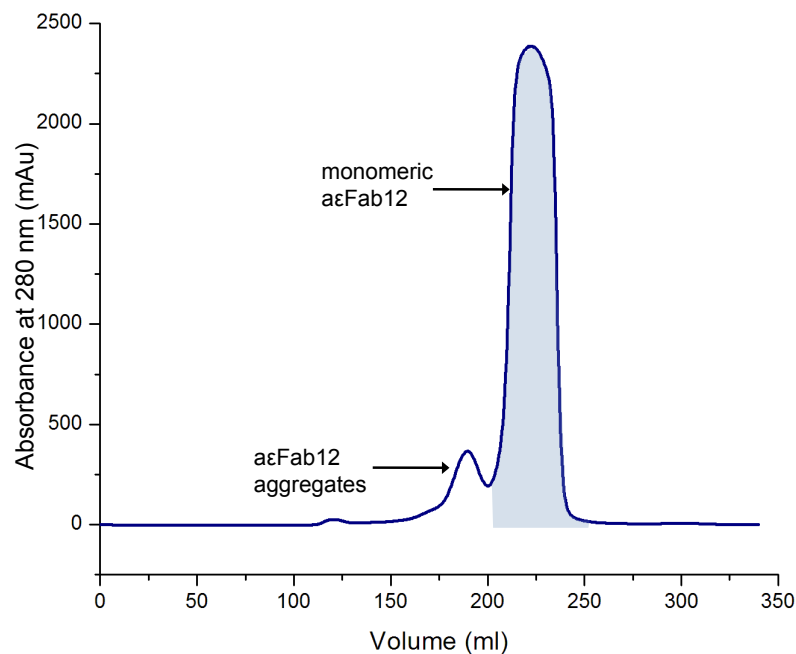


Figure 5.13: **Purification of αεFabs by size exclusion chromatography (SEC).** Protein G-purified αεFab (αεFab12 here) was further purified using SEC. Monomeric αεFab12 was separated from αεFab12 aggregates based upon differences in hydrodynamic volume using a Superdex 26/60 S200 column (GE Healthcare). The larger molecular weight aggregates eluted in a lower volume of PBS pH 7.4 than monomeric αεFab12. The blue shading indicates the pooled eluate.

30 μg of each of the purified αεFabs was run down a SEC HPLC column (G3000 SWXL, Tosoh) (Section 2.5.13). The analytical HPLC of the pooled fractions resolved aggregated and monomeric αεFab (Figure 5.14). The area under the respective elution peak gave an estimation of the percentage of contamination from αεFab aggregates; each αεFab sample contained less than 1.9 % αεFab aggregate (Table 5.5).

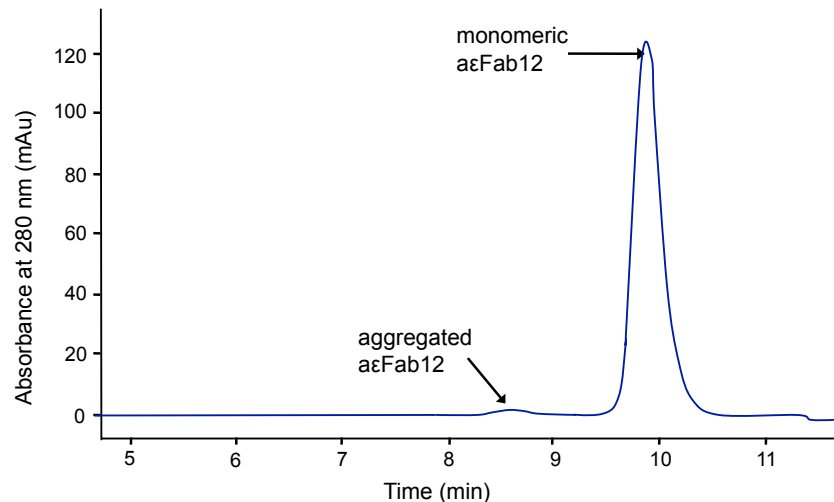


Figure 5.14: **An HPLC SEC chromatogram for purified  $\alpha\epsilon$ Fab12.** 30  $\mu\text{g}$  of purified  $\alpha\epsilon$ Fab12 was run down a G3000SWxl HPLC SEC (Tosoh) in in 0.05 M  $\text{Na}_2\text{HPO}_4$ , 0.05 M  $\text{NaH}_2\text{PO}_4$ , 0.15 M  $\text{NaCl}$ , pH 6.8 to assess the purity of the sample. Aggregated and monomeric  $\alpha\epsilon$ Fab were resolved in separate elution peaks. The areas under the elution peaks were calculated using the manual integration function of the Clarity chromatography software (DataApex) and the proportional peak areas were used to estimate the percentage of aggregated  $\alpha\epsilon$ Fab in each sample.

	<b>Fab aggregate (%)</b>
<b><math>\alpha\epsilon</math>Fab2</b>	0.47
<b><math>\alpha\epsilon</math>Fab3</b>	0.97
<b><math>\alpha\epsilon</math>Fab12</b>	1.87
<b><math>\alpha\epsilon</math>Fab13</b>	1.11
<b><math>\alpha\epsilon</math>Fab18</b>	0.52

Table 5.5: **The estimated level of aggregated  $\alpha\epsilon$ Fab contaminants in each of the the purified  $\alpha\epsilon$ Fab samples as determined by HPLC SEC.** 30  $\mu\text{g}$  of each purified  $\alpha\epsilon$ Fab sample was run down a G3000SWxl HPLC SEC (Tosoh) in 0.05 M  $\text{Na}_2\text{HPO}_4$ , 0.05 M  $\text{NaH}_2\text{PO}_4$ , 0.15 M  $\text{NaCl}$ , pH 6.8. For each  $\alpha\epsilon$ Fab, the chromatogram showed a minor peak preceding the major peak, in which it was assumed  $\alpha\epsilon$ Fab aggregate and monomeric  $\alpha\epsilon$ Fab eluted, respectively. The area under the peaks were calculated using the manual integration function of the Clarity chromatography software (DataApex), and the proportional peak areas were used to estimate the percentage of  $\alpha\epsilon$ Fab aggregate in each sample.



### 5.2.8 $\alpha$ Fab mass determination mass spectrometry

Positive ion electrospray mass spectrometry (ES-MS) (Section 2.5.13) of the purified  $\alpha$ Fabs was performed to determine the mass of the five different  $\alpha$ Fabs, in order to corroborate that they were composed of the correct cognate heavy and light chains. The heavy and kappa chains of rabbit IgG Fabs each have two intra-chain disulphide bonds and they also form an inter-chain disulphide bond. In order to break the inter-chain disulphide bond and thereby separate the chains, each of the  $\alpha$ Fabs was incubated overnight at room temperature with a molar excess of the reducing agent TCEP (Thermo Fisher Scientific). The samples were subsequently dialysed into 1 % acetic acid before being run on the mass spectrometer. The mass spectra for  $\alpha$ Fab2 (Figure 5.15.a),  $\alpha$ Fab13 and  $\alpha$ Fab18 showed two distinct peaks corresponding to the masses of the heavy and light chains. The mass spectra for  $\alpha$ Fab3 and  $\alpha$ Fab12 (Figure 5.15. b), however, were composed of two distinct peaks corresponding to the masses of the heavy chains and the entire Fabs.

The presence of a peak corresponding to the mass of whole Fab indicates that either the samples were not fully reduced and as such the chains did not completely separate, or that upon dialysis, and hence removal of the reducing agent, an inter-chain disulphide (re)formed. The masses of the single chain MS peaks were lower than the values of the single chains estimated from the protein sequence using the online tool ExPASy ProtParam [191]. The ProtParam program estimates the molecular weight of a protein based upon the protein sequence and does not take into account disulphide bond formation or post-translational modifications. The differences can be accounted for by:

a) The presence of intra-chain disulphide bonds. The formation of a disulphide bond is accompanied by the loss of two protons and therefore the loss of 2 Da.

b) The conversion of N-terminal glutamine residues (Gln) to pyroglutamate (pGlu). Cyclization of N-terminal Gln to pGlu (Figure 5.16) is a common post-translational modification of monoclonal antibodies [192, 193, 194] and is accompanied by the loss of  $\text{NH}_3$  (17.03 Da).

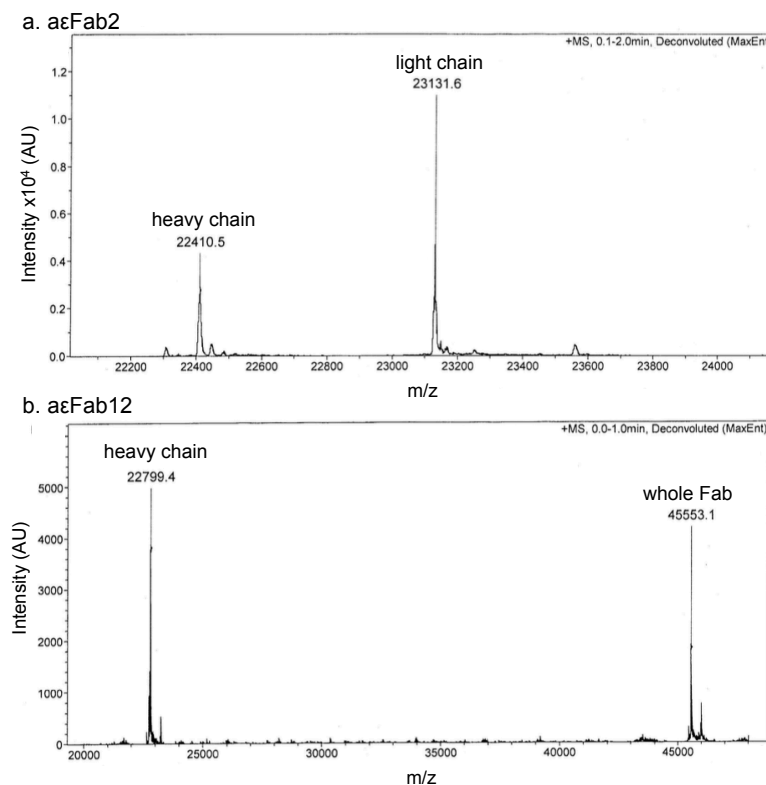


Figure 5.15: **The ES-MS mass spectra of (a)  $\alpha\epsilon$ Fab2 and (b)  $\alpha\epsilon$ Fab12.** Prior to molecular weight determination via ES-MS, purified  $\alpha\epsilon$ Fabs were incubated with a molar excess of the reducing agent TCEP (Thermo Fisher Scientific) overnight and dialyzed into 1 % acetic acid. The disulphide bond between the heavy and kappa chain of  $\alpha\epsilon$ Fab2 was reduced, resulting in two distinct peaks for the two chains. The mass spectrum of  $\alpha\epsilon$ Fab12 also shows two distinct peaks, however, these correspond to the mass of the whole  $\alpha\epsilon$ Fab (45553.1 Da) and the single heavy chain (22799.4 Da), suggesting that reduction was insufficient separate the chains.

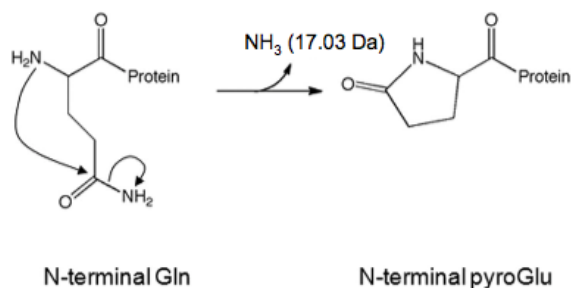


Figure 5.16: **The mechanism of N-terminal glutamine conversion to N-terminal pyroglutamate.** Adapted from from Liu *et al.* [193].

The single-chain mass-spectra peaks were found to agree with the correct predicted masses having taken into account the formation of intra-chain disulphide

bonds and N-terminal Gln to pyGlu conversion (Table 5.6).

The masses of the whole aεFab MS peaks were around 45 Da lower than the values estimated from the protein sequences using the online tool ExPASy ProtParam [191]. Each aεFab has four intra-chain disulphide bonds and one inter-chain disulphide bond, which accounts for a difference of 10 Da. Moreover, both the heavy and kappa chains of aεFab3 and aεFab12 have N-terminal Gln, and so N-terminal Gln to pGlu conversion accounts for a difference of 34.06 Da (Table 5.7).

aεFab chain	General Fab information	MS peak mass (Da)	ProtPram mass (Da)	MS peak mass – ProtPram mass (Da)	Suggested state of species in responsible for the MS peak	N-Gln to pGlu	MS mass – suggested mass (Da)	
	Number of Cys	N-terminal residue			Disulphide bonds formed			
aεFab2H	8	Gln	23154.2	23131.6	22.6	3	1	0.39
aεFab2κ	7	Asp	22417.0	22410.5	6.5	3	0	-0.98
aεFab3H	6	Gln	21892.7	21871.3	21.4	2	1	-0.36
aεFab12H	8	Gln	22822.7	22799.4	23.2	3	1	-0.22
aεFab13H	8	Gln	22782.6	22759.4	23.2	3	1	-0.17
aεFab13κ	7	Ile	22647.1	22642.2	4.9	2	0	-0.93
aεFab18H	8	Gln	22483.3	22458.8	24.5	3	1	-1.43
aεFab18κ	7	Ala	23151.9	23146.6	5.3	2	0	-1.25

Table 5.6: **Reconciling the differences between the ES-MS-determined aεFab single chain masses and the ProtPram-predicted aεFab single chain masses.** Prior to molecular weight determination via ES-MS, purified aεFabs were incubated with the reducing agent, TCEP (Thermo Fisher Scientific) overnight and dialyzed into 1 % acetic acid. ES-MS mass peaks for single chains indicated that the inter-chain disulphide of the aεFabs had been reduced, however the difference in the ES-MS-determined and ProtPram-predicted masses suggest that presence of native and non-native intra-chain disulphide bonds. Additionally, several of the aεFab chains have an N-terminal glutamine (N-Gln) that appear to have undergone cyclization to pyroglutamate (pGlu). The N-Gln to pGlu transition results in the loss of ammonia (17 Da), whereas the formation of a disulphide bond results in the loss of two protons (2 Da).

	MS peak mass (Da)	ProtPram mass (Da)	ProtPram mass- MS peak mass (Da)
<b>aεFab3</b>	44560.9	44605.9	45.0
<b>aεFab12</b>	45553.1	45598.0	44.9

Table 5.7: **The differences between the ES-MS-determined whole aεFab masses and the ProtPram-predicted whole aεFab masses.** ProtPram [191] estimates the molecular weights of proteins based upon their primary amino acid sequence, and does not account for post-translation modifications of disulphide bond formation. The difference between the ES-MS-derived masses and the ProtPram-predicted masses for aεFab3 and aεFab12 can be accounted for by the formation of 5 native disulphide bonds (5 x -2 Da), and the conversion of N-terminal glutamine residues to pyroglutamate in both Fab chains (2 x -17 Da).

Together the formation of 5 disulphide bonds and the conversion of 2 Gln residues to 2 pGlu residues per Fab accounts for a difference of 44.06 Da between the MS-derived mass and the ProtPram-derived mass. In the case of both aεFabs, this gives a final difference between the MS-derived mass and the theoretical mass of less than 1 Da. After accounting for disulphide bond formation and N-terminal Gln to pGlu conversion, the differences between the MS-determined and predicted masses of the five purified aεFab and aεFab chains were less than 1.5 Da. This indicated that the aεFabs were composed of the expected cognate heavy and light chain pairings. Moreover, all the peaks in the spectra corresponded to the expected masses of either the heavy and light aεFab chains or to the whole aεFab, which confirmed the samples were pure from non-aεFab protein contaminants.

### 5.3 Discussion

Five aεFabs, selected for their high affinity for IgE-Fc and their apparent ability to differentially modulate the binding of IgE-Fc receptors, were successfully expressed and purified. SPR analysis of IgE-receptor binding provided a way to quantitatively compare the effects of pre-binding IgE-Fc with the 13 different aεFabs. Although aεFab selection was primarily based on their relative effects on the  $K_D$  of the interaction between IgE-Fc and derCD23, their effects on the  $K_D$  and kinetics of the interaction between IgE-Fc and sFcεRIα were also assessed, as well as how

they modulate one-another's binding to IgE-Fc. These additional selection criteria provided information to help pick a diverse set of aεFabs that appear to elicit their effects on derCD23 binding in different ways (Table 5.8). The lack of a suitable control for derCD23 binding to captured-IgE-Fc means we cannot unambiguously describe any of the aεFabs as 'inhibitors' or 'enhancers', however the range of different effects observed for the different aεFab:IgE-Fc complexes suggests that the panel of antibodies does contain inhibitors and/or enhancers. Moreover, it is important to note that whilst these experiments were performed in duplicate, experimental repeats were not performed. In the future it will be necessary to repeat these experiments and perform them in the presence of an experimental control in order to have greater confidence in the observed effects.

	<b>aεFab2</b>	<b>aεFab3</b>	<b>aεFab12</b>	<b>aεFab13</b>	<b>aεFab18</b>
<b>K<sub>D</sub> of aεFab/IgE-Fc</b> (x10 <sup>-10</sup> M)	1.0	7.1	1.0	7.6	3.6
<b>K<sub>D</sub> of aεFab:IgE-Fc)/</b> <b>derCD23 (x10<sup>-6</sup> M)</b>	4.9	1.4	0.6	1.9	2.4
<b>K<sub>D</sub> of aεFab:IgE-Fc /</b> <b>FcεRIα (x10<sup>-9</sup> M)</b>	1.5	8.2	1.2	6.9	6.5
<b>Inhibition of other aεFabs</b>	aεFab3 aεFab18	aεFab2	None	aεFab3	All
<b>Other notable</b> <b>characteristics</b>		aεFab3:IgE- Fc/ FcεRIα interaction has fast off- rate		derCD23 accelerates aεFab13: IgE-Fc dissociation	aεFab18 accelerates aεAb13:IgE- Fc:aεFab13 dissociation

Table 5.8: **A summary of the binding characteristics of the selected aεFabs as determined by SPR experiments of transient transfection supernatants.**

In addition to providing a route for quantitative analysis of receptor binding, the SPR experiments also revealed all receptor binding sites were still accessible in the aεFab:IgE-Fc complexes, indicating that the CD23 and aεFab binding sites do not overlap, and the aεFabs may elicit their effects allosterically. The experiments also indicated several cases of ligand-induced accelerated dissociation of aεFab:IgE-Fc complexes (Section 5.2.2 and Section 5.2.4). Without knowledge of the different aεFab binding sites we cannot be sure of the mechanism by which derCD23 induces

accelerated dissociation of the  $\alpha\epsilon$ Fab13:IgE-Fc complex or the mechanism by which  $\alpha\epsilon$ Fab18 induces the accelerated dissociation of the  $\alpha\epsilon$ Ab13:IgE-Fc: $\alpha\epsilon$ Fab13 complex. However, since it appears that an  $\alpha\epsilon$ Fab13:IgE-Fc:derCD23 (1:1:2) complex can form (Section 5.2.2) it could be that derCD23 induces accelerated dissociation of the  $\alpha\epsilon$ Fab13:IgE-Fc complex by allosteric means. In Chapter 3 it was posited that derCD23 can allosterically induce accelerated dissociation of  $\alpha\epsilon$ Fab1 from IgE-Fc through a mechanism involving a combination of intra- and inter-domain motions. It would be interesting to determine the mechanisms of these newly observed instances of accelerated dissociation, since understanding this process in IgE could provide insights for the development of novel therapeutics that work by disrupting IgE:receptor complexes.

The effect of  $\alpha\epsilon$ Fab on the IgE-Fc/CD23 interaction binding was examined in the context of an  $\alpha\epsilon$ Fab:IgE-Fc complex, which meant that the  $\alpha\epsilon$ Fabs did not have to be purified from their transient transfection supernatant. However, the experimental set-up was inherently biased towards the interaction between the  $\alpha\epsilon$ Fab:IgE-Fc complexes – we only observe binding events that were possible between the receptor and conformations of IgE-Fc when it was pre-bound to an  $\alpha\epsilon$ Fab. In the future, purified  $\alpha\epsilon$ Fabs could be used in homogeneous assays to determine their effect on receptor binding at equilibrium, when the conformational ensemble of IgE-Fc has not been biased by pre-binding to  $\alpha\epsilon$ Fab.

# Chapter 6

## Characterisation of the anti-IgE Fab/IgE interactions

### 6.1 Introduction

IgE-Fc is a homodimer of two chemically identical chains each composed of three domains: C $\epsilon$ 2, C $\epsilon$ 3 and C $\epsilon$ 4 (Figure 6.1). FRET experiments [73, 74, 75], X-ray solution scattering studies [76] and X-ray crystal structures of IgE-Fc [71, 72] together suggest that IgE-Fc exists predominantly in a compact bent conformation, in which the C $\epsilon$ 2 domain pair folds back onto the C $\epsilon$ 3 and C $\epsilon$ 4 domains (Figure 6.1). Different X-ray crystallographic structures of the C $\epsilon$ 3-C $\epsilon$ 4 subfragment of IgE-Fc (IgE-Fc(3-4)) suggest that the C $\epsilon$ 3 domains can move upon the C $\epsilon$ 3-4 hinge to adopt a range of ‘open’ and ‘closed’ conformations [77] (Section 1.2.1). This conformational flexibility partly explains why receptor-binding to IgE-Fc is mutually exclusive (Section 1.3.1) [18]. The Fc $\epsilon$ RI binding site is comprised of two subsites that are composed of residues from the different C $\epsilon$ 3 domains (Figure 6.1). To engage both subsites, both C $\epsilon$ 3 domains must adopt ‘open’ conformations [86, 72] (Figure 6.2). Two molecules of CD23 bind to IgE-Fc, one to each C $\epsilon$ 3 domain, and they bind at the opposite end of the C $\epsilon$ 3 domain to Fc $\epsilon$ RI (Figure 6.1). In contrast to Fc $\epsilon$ RI binding, CD23 binding requires both of the C $\epsilon$ 3 domains to adopt relatively ‘closed’ conformations (Figure 6.2), and this, in part, prevents simultaneous receptor engagement. Additionally, X-ray crystal structures of IgE-Fc bound to various engineered ligands (Figure 6.1) have provided evidence that IgE-Fc can adopt conformations in which the C $\epsilon$ 3 domains are even further apart than



in the sFcεRIα-bound structure (Figure 6.2) and that their relative dispositions contribute to inhibition of receptor binding [81, 82] (Section 3.2.5).

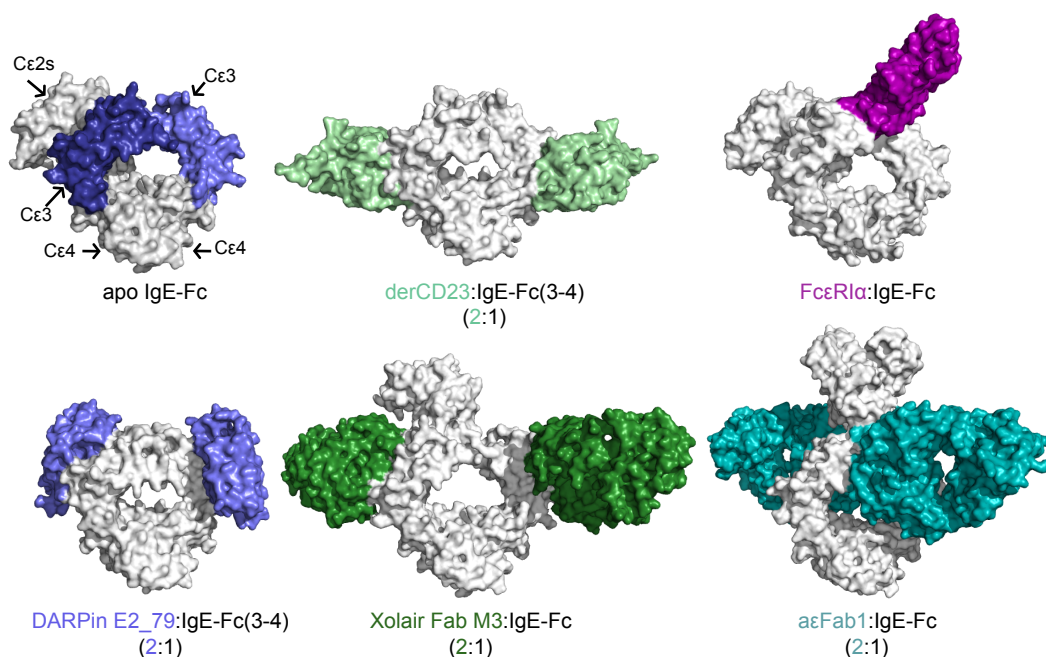


**Figure 6.1: X-ray crystal structures of IgE-Fc bound to the different anti-IgE-Fc ligands.** The crystal structures are shown in surface representations. IgE-Fc is shown in white, except for the Cε3 domains in the first image. The different anti-IgE receptors and ligands are coloured in accordance with the text. The binding sites of the engineered ligands are located in the Cε3 domains of IgE-Fc (coloured blue in the first image), to which the receptors (FcεRI and CD23) also bind. The engineered anti-IgE-Fc ligands bind to IgE-Fc with 2:1 stoichiometry. Apo IgE-Fc PDB: 2WQR [72], derCD23:IgE-Fc(3-4) (2:1) PDB: 2WQR [18], sFcεRIα:IgE-Fc PDB: 2Y7Q [72], DARPin E2\_79:IgE-Fc(3-4) (2:1) PDB: 4GRG [109], αεFab1:IgE-Fc (2:1) PDB: 4J4P [81], Xolair Fab mutant 3:IgE-Fc (2:1) PDB: in press.

The structures of αεFab1-bound and Xolair Fab mutant 3 bound-IgE-Fc also illustrate a more extreme form of IgE-Fc conformational flexibility. The Cε2 domains of the αεFab1:IgE-Fc (2:1) complex ‘unbend’ and IgE-Fc adopts an extended and almost symmetrical structure that is irreconcilable with FcεRI binding [81] (Figures 6.1 and 6.2). Similarly, the structure of IgE-Fc bound to two molecules of Xolair Fab mutant 3 is partially extended [82] (Figures 6.1 and 6.2). Molecular dynamic simulations suggest IgE-Fc has a complex energy landscape and when free in solution IgE-Fc may be able to unbend and the Cε2 domains might even ‘flip’ from one side of IgE-Fc (3-4) to the other [81] (Figure 6.3).

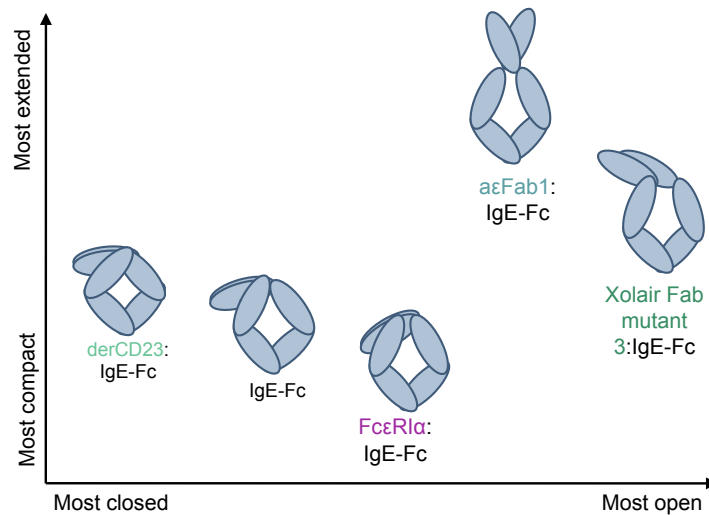


Figure 6.2: **Different IgE-Fc complexes show that IgE-Fc is flexible and can adopt a wide range of conformations.** A schematic representation of the different conformations that IgE-Fc adopts when bound to its receptors and to anti-IgE-Fc Fabs. The C $\epsilon$ 3 domains exist in a range of ‘open’ and ‘closed’ conformations: derCD23 binds the most closed conformation in which the C $\epsilon$ 3 domains make the closest approach to one another, the most open conformation known to date is that of the Xolair Fab mutant 3:IgE-Fc (2:1) complex [82], whereas the most closed is the derCD23:IgE-Fc (1:1) complex [95]). The C $\epsilon$ 2 domains of IgE-Fc also undergo considerable conformational changes: sFc $\epsilon$ RI $\alpha$  bound IgE-Fc adopts the most compact structure [71, 72], whereas a $\epsilon$ Fab1-bound IgE-Fc is fully extended [81].

The engineered anti-IgE-Fc ligands described in the literature (DARPin E2.79 [109], a $\epsilon$ Fab1 [81], Xolair [195]) elicit their effects on IgE-Fc conformation and IgE-Fc-receptor interactions by binding to the C $\epsilon$ 3 domains. Each anti-IgE ligand completely, or principally, binds one C $\epsilon$ 3 domain [106, 105, 109, 81, 108, 82] and consequently they can bind IgE-Fc with a 2:1 stoichiometry (Figure 6.1). Although IgE-Fc is a homodimer, for each of the anti-IgE-ligands, the affinities of their two binding sites are not identical [109, 81, 108, 82]. This is thought to be at least in part because in solution, free IgE-Fc exists predominantly in a bent asymmetric conformation.

The described engineered anti-IgE-Fc ligands were selected for their ability to inhibit the interaction between IgE-Fc and Fc $\epsilon$ RI [195, 109, 81]. Structures indicate that Xolair [108, 82] and DARPin E2.79 [109] also sterically inhibit the CD23/IgE-Fc interaction (Figure 6.1) and in Chapter 3 we showed that a $\epsilon$ Fab1 is

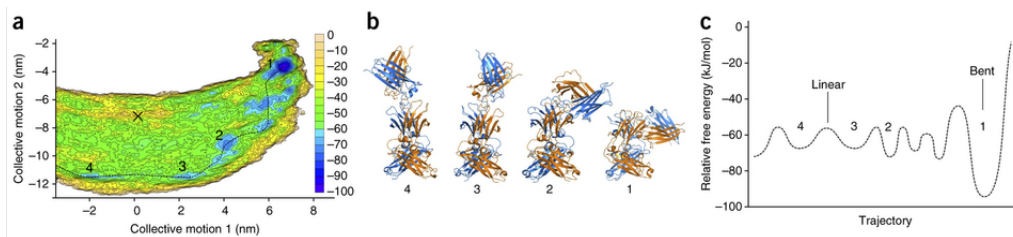


Figure 6.3: **Molecular dynamic simulations of IgE-Fc extension.** Figure taken from Drinkwater *et al.* [81]. (a) The free-energy surface diagram generated from a metadynamics simulation of IgE-Fc unbending suggests that IgE-Fc exists predominantly in the bent conformation but that it can escape this conformation and extend. A suggested pathway for IgE-Fc extension is shown by a dotted line between energy minima. Models for the conformations of IgE-Fc that exist in the minima are shown in (b) and a sketch of the suggested pathway is illustrated in (c).

an allosteric inhibitor of CD23. In the previous chapter, five  $\alpha\epsilon$ Fabs were selected for their ability to bind IgE-Fc with a high affinity, and for their different effects on the IgE-Fc/CD23 interaction. The  $\alpha\epsilon$ Fab/IgE-Fc interactions had sub-nanomolar binding affinities, as determined by SPR, and the binding curves appeared biphasic, which suggested that the  $\alpha\epsilon$ Fabs may bind IgE-Fc with a 2:1 stoichiometry (Section 5.2.1). The  $\alpha\epsilon$ Fabs were subsequently expressed on a larger scale and purified (Section 5.2.6).

In this chapter we describe  $\alpha\epsilon$ Fab/IgE-Fc binding experiments that were performed with the purified  $\alpha\epsilon$ Fabs, and examine the binding kinetics in greater detail. In doing so, we determined the stoichiometries and affinities of the interactions, and provided further evidence of IgE-Fc heterogeneity. Intramolecular IgE-Fc FRET assays indicated that the binding of  $\alpha\epsilon$ Fab2,  $\alpha\epsilon$ Fab12 and  $\alpha\epsilon$ Fab13 to IgE-Fc results in IgE-Fc unbending and suggests that at least these three  $\alpha\epsilon$ Fabs can cause significant shifts in the conformational ensemble of IgE-Fc. Furthermore, we describe how SPR was used to investigate the interactions between the  $\alpha\epsilon$ Fabs and different IgE-Fc subfragments. The results showed that these  $\alpha\epsilon$ Fabs, unlike any of the previously engineered anti-IgE-Fc ligands, bind principally to the C $\epsilon$ 2 domains of IgE-Fc.

## 6.2 Results

### 6.2.1 Determining the stoichiometry of the $\alpha\epsilon$ Fab/IgE-Fc interactions using SEC

Size exclusion chromatography experiments were performed to determine the stoichiometry of the different  $\alpha\epsilon$ Fab/IgE-Fc interactions. Four samples were incubated overnight at 4 °C for each of the  $\alpha\epsilon$ Fabs: 10  $\mu$ M purified IgE-Fc, 17  $\mu$ M purified  $\alpha\epsilon$ Fab, 12  $\mu$ M IgE-Fc with 5  $\mu$ M  $\alpha\epsilon$ Fab, and 5  $\mu$ M IgE-Fc with 12  $\mu$ M  $\alpha\epsilon$ Fab. The samples were then separately run down a Superdex S200 10x30 GL SEC column (GE Healthcare) in PBS pH 7.4.

The chromatogram for IgE-Fc,  $\alpha\epsilon$ Fab2 and  $\alpha\epsilon$ Fab2:IgE-Fc complexes is shown in Figure 6.4. Figure 6.4 is representative of the chromatograms for the other  $\alpha\epsilon$ Fabs and  $\alpha\epsilon$ Fab:IgE-Fc complexes as they shared a similar profile (Appendix A.6). Purified IgE-Fc eluted as a single peak on the chromatogram, as did purified  $\alpha\epsilon$ Fab, but at a slightly later retention time owing to its smaller size (IgE-Fc MW = 75 kDa,  $\alpha\epsilon$ Fab MWs  $\sim$  45-50 kDa). The sample with 12  $\mu$ M  $\alpha\epsilon$ Fab and 5  $\mu$ M IgE-Fc eluted as three different peaks: two peaks appeared at lower retention times than either IgE-Fc or  $\alpha\epsilon$ Fab, indicating the formation of two distinct  $\alpha\epsilon$ Fab:IgE-Fc complexes, the third peak had the same retention time as IgE-Fc, indicating that not all of the IgE-Fc was in complex (as expected since IgE-Fc was in molar excess). The sample with 12  $\mu$ M  $\alpha\epsilon$ Fab and 5  $\mu$ M IgE-Fc eluted as two different peaks: one major peak at the same retention time as the larger complex peak in the previous sample, and one minor peak at the same retention time as purified  $\alpha\epsilon$ Fab.

Given that the  $K_D$  of the different  $\alpha\epsilon$ Fab/IgE-Fc interactions are thought to be in the sub-nanomolar range (Section 5.2.1), at 5  $\mu$ M or 12  $\mu$ M IgE-Fc the stoichiometry of complex formation was dictated by the molar ratios of IgE-Fc and  $\alpha\epsilon$ Fab. The presence of two complex peaks when the  $\alpha\epsilon$ Fab was in slight molar excess of IgE-Fc suggests that the peaks correspond to a 1:1  $\alpha\epsilon$ Fab:IgE-Fc complex (later retention time) and a 2:1  $\alpha\epsilon$ Fab:IgE-Fc complex (earlier retention time). This is further supported by the fact that only one complex peak, corresponding to the

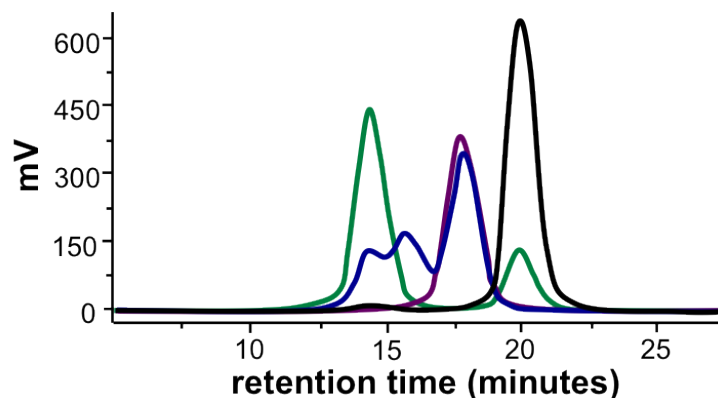


Figure 6.4: **A representative size exclusion chromatogram for aεFab, IgE-Fc and aεFab:IgE-Fc complexes.** Purified aεFab (aεFab2 here) was incubated with purified IgE-Fc overnight at 4 °C at 1:2.4 (blue) and 2.4:1 molar ratios (green). The mixture samples, aεFab alone (black), and purified IgE-Fc (purple), were run down a Superdex S200 10x30 GL SEC column (GE Healthcare) in PBS, pH 7.4. The results suggest the formation of 1:1 and 2:1 aεFab:IgE-Fc complexes.

2:1 complex was observed when aεFab was mixed with IgE-Fc at concentrations in excess of a 2:1 molar ratio.

### 6.2.2 Determining the equilibrium dissociation constants of the aεFab/IgE-Fc interactions using SPR

SEC indicated that a single IgE-Fc can bind two molecules of each of the selected aεFabs. SPR was used to determine the  $K_D$  values of the different aεFab binding sites. Each aεFab was immobilised on to a different CM5 SPR sensor chip surface (GE Healthcare) using amine-coupling (Section 2.6.2). aεFab was immobilised at a low density (<400 RUs) that ensures that nearly all of the IgE-Fc that binds is bound to only one aεFab molecule (Section 2.6.2). A titration of IgE-Fc was injected for 180 s over the different aεFab surfaces as well as a mock amine-coupled surface. The change in SPR response on the immobilised aεFab surfaces after subtracting the response from the mock amine-coupled surface was used to measure the specific binding of IgE-Fc to aεFab. Following each injection of IgE-Fc there was a 780 s dissociation phase and the anti-rabbit-Fab surface was then regenerated by two 60 s pulses of 10 mM glycine pH 1.7 and one pulse of 5 mM NaOH. The experiments were performed in duplicate and the results were highly replicable.

The double reference-subtracted SPR sensorgrams indicated that the different

$\alpha$ Fab/IgE-Fc interactions had varied binding kinetics (Figure 6.5), as was previously observed in Chapter 5 (Section 5.2.1). At low IgE-Fc concentrations the binding of IgE-Fc to the  $\alpha$ Fabs is monophasic: the data fit well to a monophasic kinetic model as represented here by the fit of data for  $\alpha$ Fab2 (Figure 6.6).

At higher IgE-Fc concentrations, binding had increasing biphasic character: the binding curves did not fit well to a monophasic model (Figure 6.7.a) and were better described by a biphasic model (Section 2.6.3), represented here by the example of IgE-Fc binding to  $\alpha$ Fab2 (Figure 6.7.b). Given that the  $\alpha$ Fab:IgE-Fc complexes can bind with a 2:1 stoichiometry and that the experiments were performed at low immobilisation densities to encourage monomeric binding, the biphasicity of the binding curves is likely to be because the two  $\alpha$ Fab binding sites on IgE-Fc have non-identical intrinsic affinities, as also observed for both  $\alpha$ Fab1 [81] and Xolair Fab Mutant 3 [82]. Accordingly, monophasic binding, which was observed at low IgE-Fc concentrations, was the result of the binding of IgE-Fc to captured  $\alpha$ Fab via its higher-affinity  $\alpha$ Fab binding site, whereas the biphasic binding observed at higher IgE-Fc concentrations describes the interactions that occurred between  $\alpha$ Fab and both the higher-affinity and the lower-affinity  $\alpha$ Fab binding sites.

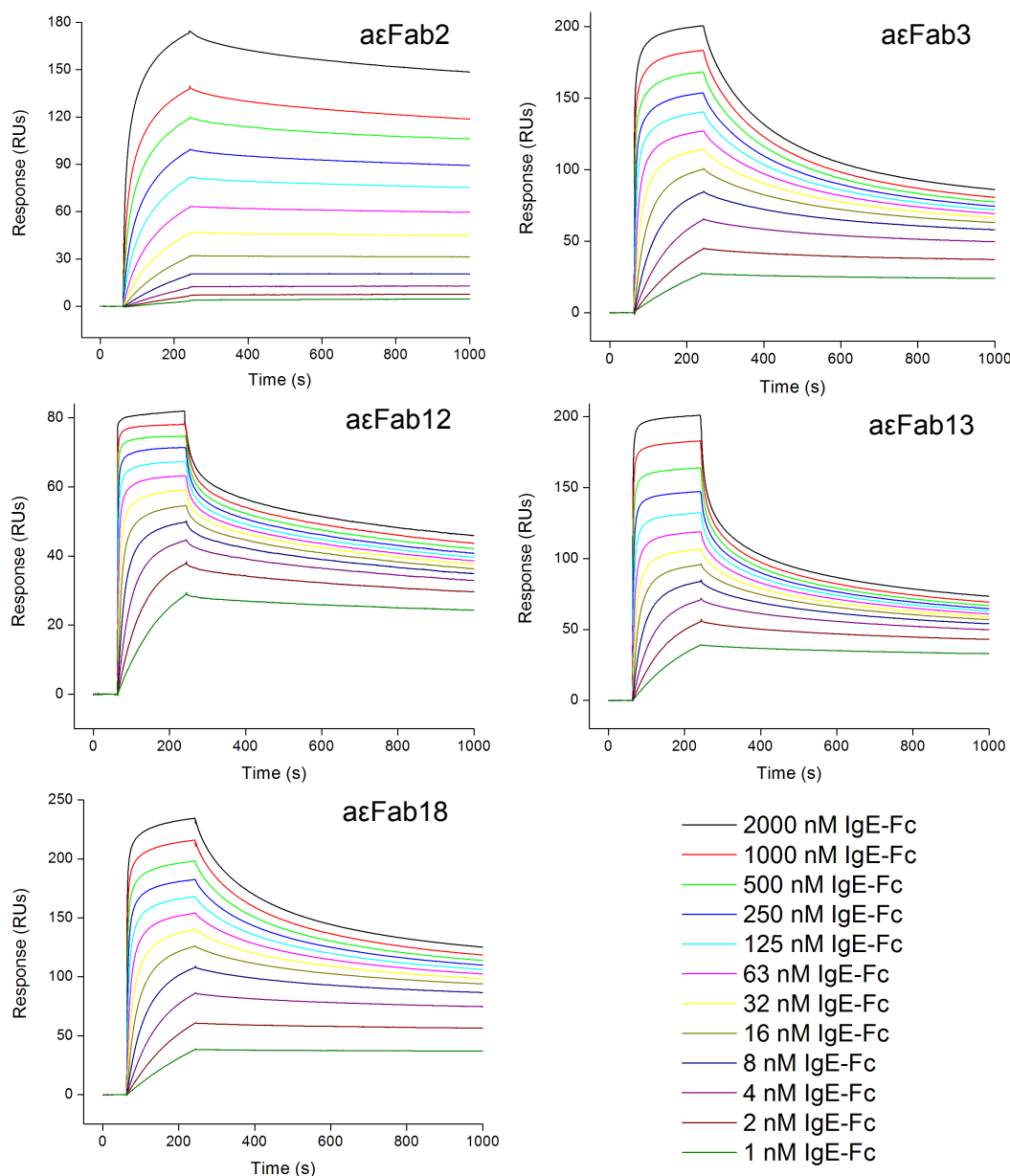


Figure 6.5: **SPR sensorgrams for the binding of IgE-Fc to the different immobilised  $\alpha$ E Fabs.** IgE-Fc was injected over  $\alpha$ E Fabs immobilised to an SPR sensor surface at a low density ( $< 400$  RUs) using amine-coupling.

The association rate constant ( $k_{\text{on}}$ ) and dissociation rate constant ( $k_{\text{off}}$ ) were determined from fitting the data using either monophasic or biphasic models where appropriate (Section 2.6.3). The equilibrium dissociation constants ( $K_D$ ) were determined from the dissociation and association phases using Equation 6.1. Fitting both the monophasic (not shown) and the biphasic data indicated that the higher-affinity  $\alpha$ E Fab/IgE-Fc interactions have  $K_D$  values in the high picomolar range (Table 6.1 and Appendix A.7). Fitting the biphasic data indicated that the lower-

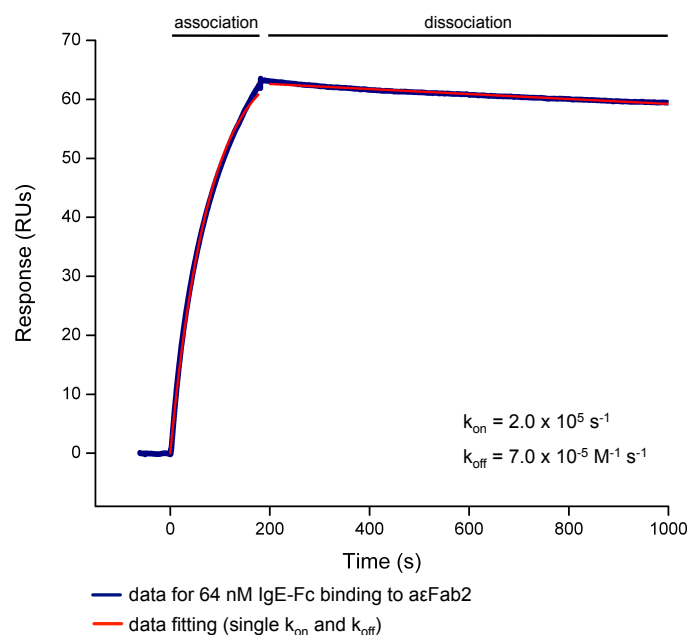


Figure 6.6: **The binding of 64 nM IgE-Fc to immobilised aεFab2 is well described by single  $k_{on}$  and  $k_{off}$  kinetic models.** 64 nM IgE-Fc was injected over aεFab2 immobilised to an SPR sensor surface at a low density ( $< 400$  RUs) using amine-coupling. The association and dissociation phases were fit using single  $k_{on}$  and  $k_{off}$  models kinetic models (Section 2.6.3) and were used to derive the dissociation and association rate constants of the interaction ( $k_{off}$  and  $k_{on}$ , respectively).

affinity aεFab/IgE-Fc interactions have  $K_D$  values in the high nanomolar range (Table 6.1.b and Appendix A.7).

$$K_D = \left( \frac{k_{off}}{k_{on}} \right) \quad (6.1)$$

Where  $K_D$  is the equilibrium dissociation constant,  $k_{off}$  is the dissociation rate constant and  $k_{on}$  is the association rate constant.

The association and dissociation curves for the binding of 0 - 2  $\mu\text{M}$  IgE-Fc to aεFab2, 3, and 18 could be fit using monophasic (at lower concentrations) or biphasic (at higher concentrations) models. A biphasic model, however did not accurately describe the interaction between IgE-Fc and aεFab12 or IgE-Fc and aεFab13 at IgE-Fc concentrations above 8 nM (Figure 6.8.a). The dissociation phase of the interaction between 2  $\mu\text{M}$  IgE-Fc and aεFab12, and the dissociation phase of the interaction between 2  $\mu\text{M}$  IgE-Fc and aεFab13, fit to triphasic models (Section 2.6.3) (Figure 6.8.b and Appendix A.7). Based on our previous experience of characterising IgE-Fc binding interactions, we think that it is likely that the



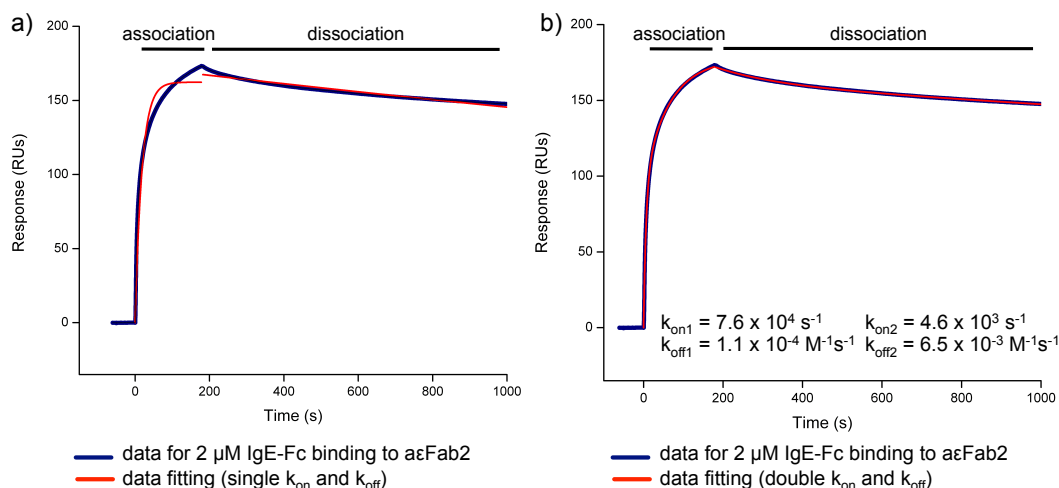


Figure 6.7: **The binding of 2  $\mu\text{M}$  IgE-Fc to immobilised  $\alpha\epsilon\text{Fab2}$  is well described by biphasic kinetic models.** 2  $\mu\text{M}$  IgE-Fc was injected over a  $\alpha\epsilon\text{Fab2}$  immobilised to an SPR sensor surface at a low density ( $<400$  RUs) using amine-coupling. The association and dissociation phases were not accurately described using (a) monophasic kinetic models and were described better using (b) biphasic kinetic models. The biphasic fits were used to derive the dissociation and association rate constants of the interaction ( $k_{\text{off}}$  and  $k_{\text{on}}$ , respectively).

observed triphasic binding kinetics are a result of IgE-Fc conformational heterogeneity. In our laboratory we have observed similar complexities in the interaction between IgE-Fc and  $\text{sFc}\epsilon\text{RI}\alpha$  that are not the result of SPR artifacts and that we propose are the due to IgE-Fc heterogeneity.

### 6.2.3 IgE-Fc heterogeneity

#### An introduction to IgE-Fc heterogeneity and the IgE/Fc $\epsilon$ RI interaction

As discussed in the chapter introduction (Section 6.1), X-ray structures and molecular dynamic simulations suggest that IgE-Fc is highly dynamic and can exist in a range of different conformations. The C $\epsilon$ 3 domains of IgE-Fc can move upon the C $\epsilon$ 3-C $\epsilon$ 4 hinges to adopt a range of ‘open’ and ‘closed’ states that have differential receptor-binding capabilities [77, 18, 86, 72]. Moreover, IgE-Fc can exist in an extended conformation and the C $\epsilon$ 2 domains may even flip from one side of the molecule to the other [81]. Our laboratory has demonstrated that conformational heterogeneity is reflected in the binding kinetics of the interaction between IgE-Fc and Fc $\epsilon$ RI.

a)	$k_{\text{off1}}$ ( $\times 10^{-4} \text{ s}^{-1}$ )	$k_{\text{on1}}$ ( $\times 10^5 \text{ M}^{-1} \text{ s}^{-1}$ )	$K_{\text{D1}}$ ( $\times 10^{-10} \text{ M}$ )
<b>aεFab2</b>	0.80	0.88	9.0
<b>aεFab3</b>	3.7	4.8	7.7
<b>aεFab12</b>	1.5	6.9	2.2
<b>aεFab13</b>	2.8	22	1.3
<b>aεFab18</b>	3.0	4.6	6.5

b)	$k_{\text{off2}}$ ( $\times 10^{-3} \text{ s}^{-1}$ )	$k_{\text{on2}}$ ( $\times 10^4 \text{ M}^{-1} \text{ s}^{-1}$ )	$K_{\text{D2}}$ ( $\times 10^{-7} \text{ M}$ )
<b>aεFab2</b>	4.4	0.67	6.6
<b>aεFab3</b>	7.6	1.9	4.0
<b>aεFab12</b>	6.5	0.82	7.9
<b>aεFab13</b>	7.9	0.47	19
<b>aεFab18</b>	8.2	1.0	8.2

Table 6.1: **The equilibrium dissociation constants of the (a) higher- and (b) lower-affinity aεFab/IgE-Fc interactions as derived from kinetic binding experiments.** The dissociation and association phases for the binding of IgE-Fc to aεFabs immobilised to separate SPR sensor surfaces at a low density ( $< 400$  RUs) using amine-coupling were fit using biphasic kinetic models (Section 2.6.3). The resulting dissociation and association rate constants ( $k_{\text{off}}$  and  $k_{\text{on}}$ , respectively) were used to derive the equilibrium dissociation constants ( $K_{\text{D}}$ ) of the interactions using Equation 6.1. The fittings were performed on the data for the binding of  $2 \mu\text{M}$  IgE-Fc to immobilised aεFab2, aεFab3 and aεFab18, and the data for the binding of  $8 \text{ nM}$  IgE-Fc to immobilised aεFab12 and aεFab13. The fits were performed in Origin (OriginLab). The fitting errors of  $k_{\text{on1}}$ ,  $k_{\text{off1}}$  and  $k_{\text{off2}}$  were all less than 1 %. The fitting errors for  $k_{\text{on2}}$  were less than 10 %.

FcεRI is expressed on mast cells, basophils and a range of other immunological cells as a tetrameric complex of  $\alpha\beta\gamma_2$  chains. Cross-linking of IgE-bound FcεRI on the surface of mast cells and basophils by allergen results in cell degranulation and the release of a range of inflammatory-mediators that cause the immediate hypersensitivity reactions associated with allergic disease [14]. The interaction between IgE and FcεRI has a very high affinity ( $K_{\text{D}} \approx 1 \times 10^{-10} - 1 \times 10^{-9} \text{ M}$ ) [4] owing to a very slow off rate ( $k_{\text{off}} \approx 10^{-5} \text{ s}^{-1}$ ) [196, 197]. As a result of the slow off-rate of the IgE/FcεRI interaction, the binding of IgE to FcεRI on the surface of mast cells and basophils can cause long-term sensitization, allowing for an instantaneous inflammatory response upon allergen encounter.

The IgE-Fc binding activity of FcεRI is located in the alpha chain of the protein. Crystal structures of the soluble domains of FcεRI (sFcεRIα) bound to IgE-Fc

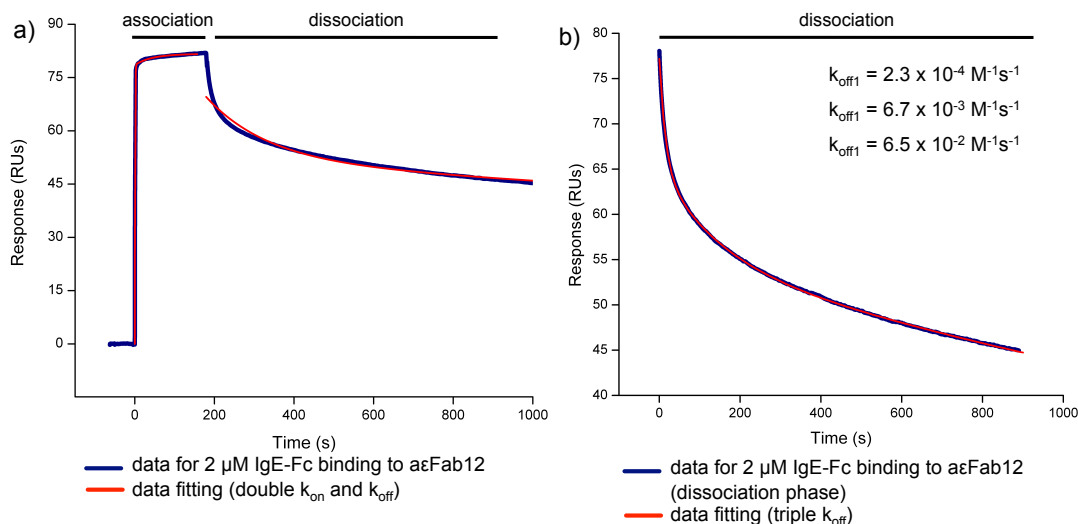


Figure 6.8: **The aεFab12/IgE-Fc interaction has multiphasic binding kinetics at high IgE-Fc concentrations.** (a) The binding kinetics of the interaction between 2 μM IgE-Fc and aεFab12 captured on the surface of an SPR sensor chip is not well described by a biphasic model. (b) The dissociation phase of the interaction is better described by a triphasic model with three distinct  $k_{\text{off}}$  values.

show that one molecule of sFcεRIα binds to one molecule of IgE-Fc [86, 72]. The binding interface is extensive, largely hydrophobic and is composed of two non-identical subsites located in the two different Cε3 domains of IgE-Fc (Figure 6.9). The crystal structures indicate that two salt-bridges and three hydrogen bonds in subsite 1, and packing interactions between a proline of IgE-Fc sandwiched between two sFcεRIα tryptophan residues in subsite 2 are important in stabilising the IgE-Fc:sFcεRIα complex [86, 72] (Figure 6.9).

The Cε2 domains of IgE-Fc are required to achieve the very slow off-rate between IgE-Fc and sFcεRIα [83], yet the crystal structure of the complex indicates that no specific contacts form between sFcεRIα and the Cε2 domains [72]. Instead, sFcεRIα binds to a more compact asymmetric IgE-Fc and the Cε2 domains make more extensive contacts with the Cε3 domains than in the apo-state structure [72]. The Cε2-Cε3 interactions are thought to stabilise the Cε3 domains, reducing their intrinsic flexibility and thereby reducing the entropic penalty that is incurred upon FcεRI binding [83, 72].

Despite sFcεRIα binding IgE-Fc with a 1:1 stoichiometry, the binding of IgE-Fc to SPR sensor chips with either sFcεRIα or IgG<sub>4</sub>-Fc-(sFcεRIα)<sub>2</sub> immobilised on the surface has biphasic binding kinetics and two distinct binding constants ( $K_{D1} \approx$

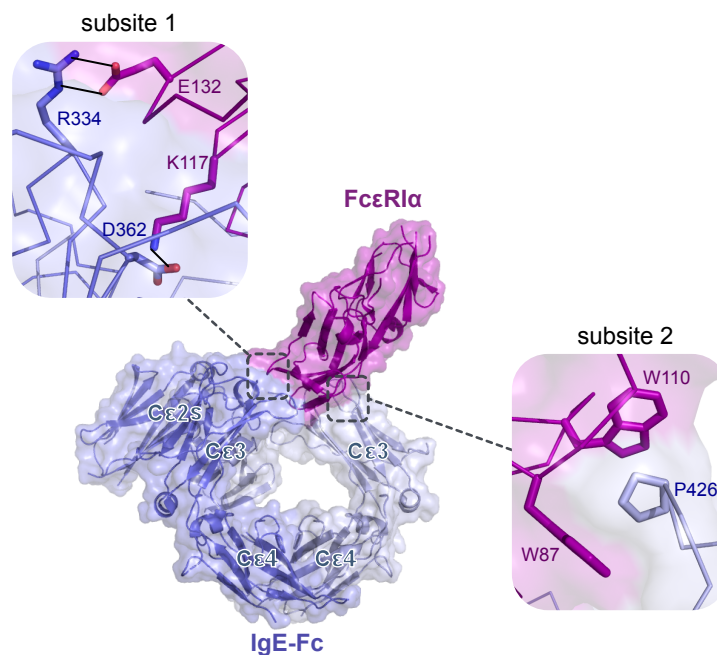


Figure 6.9: **The extensive and largely hydrophobic sFcεRIα:IgE-Fc binding interface involves specific interactions at two subsites that involve residues from the two different Cε3 domains of IgE-Fc.** The crystal structure of the sFcεRIα:IgE-Fc complex [72]. sFcεRIα (purple) binds IgE-Fc (blue) with a 1:1 stoichiometry. Salt bridges and hydrogen bonds form between sFcεRIα and Cε3 at subsite 1 of the binding interface. Stacking interactions between a IgE-Fc proline residue sandwiched between two sFcεRIα tryptophan side chains occurs at subsite 2.

0.1-1 nM,  $K_{D2} \approx 100$  nM) [196, 197]. The heterogeneity of the binding affinities is attributed to two different binding phases, the nature of which have not been fully resolved [196, 197].

Until recently, SPR experiments in our laboratory have largely focused on the binding of IgE-Fc (or subfragments of IgE-Fc) to immobilised sFcεRIα or IgG<sub>4</sub>-Fc-(sFcεRIα)<sub>2</sub> because immobilising IgE or IgE-Fc on a sensor surface has historically been problematic due to two established issues. Firstly, when immobilised through amine-coupling, the immobilised IgE-Fc appears to be ~90 % inactive, which is almost certainly because covalent coupling occurs within the Cε3 domain. Secondly, even when the (~10 %) immobilised material is active, regeneration conditions that are sufficient to dissociate IgE-Fc from sFcεRIα rapidly deactivate IgE-Fc, making repeating injections impossible. The most recent data from our laboratory makes use of a new way of capturing IgE-Fc for SPR studies, and are supported by

solution-based stopped-flow intrinsic fluorescence assays and stopped-flow FRET studies.

### Recent studies of IgE-Fc heterogeneity in relation to FcεRI binding performed in our laboratory

IgE-Fc with a 6x histidine tag at C-terminus was expressed in Expi293<sup>TM</sup> HEK cells (Thermo Fisher Scientific) (Section 3.2.2). Immobilisation of an anti-His-antibody (THE<sup>TM</sup> his-tag monoclonal antibody, mouse, Genscript) to an SPR sensor surface, via amine-coupling, allowed the capture of His-IgE-Fc. Capturing IgE-Fc via a His-tag eliminated the problems associated with covalent immobilisation of IgE-Fc and provided a system for the straightforward deconvolution of binding rates/affinities and  $B_{\max}$  values for IgE-Fc/analyte interactions (Figure 6.10).

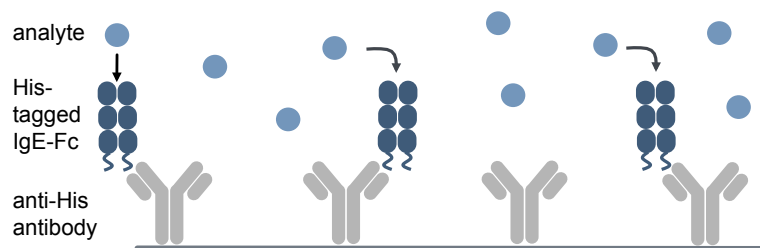


Figure 6.10: **Capturing His-IgE-Fc via its His-tag provides a straightforward way of deconvoluting the  $K_D$  and  $B_{\max}$  of IgE-Fc/analyte interactions.** THE<sup>TM</sup> anti-His mouse monoclonal antibody (Genscript) is immobilised to a CM5 SPR sensor chip surface using amine-coupling. His-tagged IgE-Fc, in transient transfection supernatant is injected over the surface and is captured by the anti-His antibody. Analyte is then injected over the anti-His:His-IgE-Fc complex and specific binding of analyte to IgE-Fc is observed as an increase in SPR response once reference subtractions have been performed.

Professor James McDonnell performed SPR experiments to determine the  $B_{\max}$  and  $K_D$  of the interaction between sFcεRIα and captured His-IgE-Fc using picomolar to low nanomolar concentrations of sFcεRIα. The expected steady-state response was estimated from fitting the association and dissociation phases. The estimated steady-state response was then plot as a function of sFcεRIα concentration and the data were fit using a one-to-one binding model (Section 2.6.4). The  $K_D$  of the His-IgE-Fc/sFcεRIα interaction was estimated to be  $\sim 100$  pM. The  $B_{\max}$ , however was estimated to be one-third the value of the theoretical  $B_{\max}$  value, which suggests that only about one-third of the IgE-Fc binds sFcεRIα with

the sub-nanomolar affinity that is often reported for the interaction. In contrast, the  $B_{\max}$  values for the interaction between derCD23 and the captured His-IgE-Fc indicated that  $\sim 100\%$  of the IgE-Fc molecules bound derCD23 with affinities of  $\sim 1\ \mu\text{M}$  and  $\sim 15\ \mu\text{M}$  (Figure 6.11).

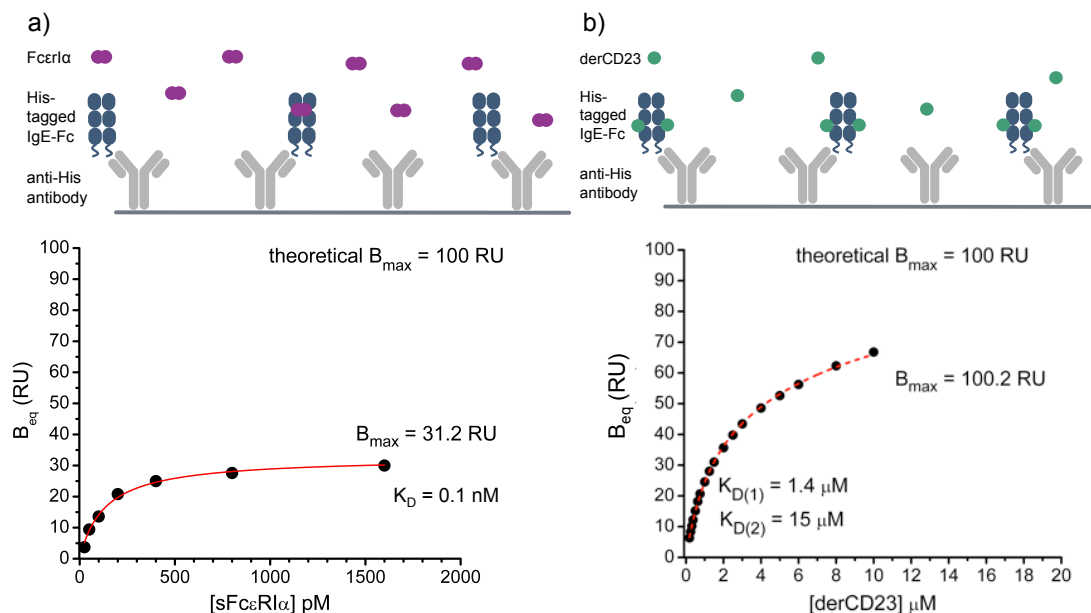


Figure 6.11: **Binding curves for (a) sFc $\epsilon$ RI $\alpha$  (b) derCD23 binding to His-tagged IgE-Fc.**  $B_{\text{eq}}$  is the steady-state response. The  $B_{\max}$  of the sub-nanomolar affinity interaction between His-IgE-Fc and sFc $\epsilon$ RI $\alpha$  is one third of the theoretical  $B_{\max}$  value, indicating that only one-third of IgE-Fc can bind Fc $\epsilon$ RI with a sub-nanomolar binding affinity.

A wide concentration range of sFc $\epsilon$ RI $\alpha$  was injected over the captured His-IgE-Fc in subsequent experiments. The resultant sensorgrams show a change in the character when only the high affinity sites are occupied (at 4 nM for example) compared to when the low affinity sites are also occupied (at 4  $\mu\text{M}$  for example) (Figure 6.12). At low concentrations, the binding kinetics for the interaction between sFc $\epsilon$ RI $\alpha$  and His-IgE-Fc fit a monovalent model. However, at very high sFc $\epsilon$ RI $\alpha$  concentrations three populations of binding affinities were observable, indicating a greater level of binding heterogeneity than suggested by previous SPR experiments of the IgE-Fc/sFc $\epsilon$ RI $\alpha$  interaction [196, 197]. These three binding affinities were estimated to be  $\sim 100\ \text{pM}$ ,  $\sim 20\ \text{nM}$  and  $\sim 1\ \mu\text{M}$ .

The multiphasic nature of the IgE-Fc/sFc $\epsilon$ RI $\alpha$  interaction does not appear to be an artifact of SPR and further evidence supporting multiphasic binding

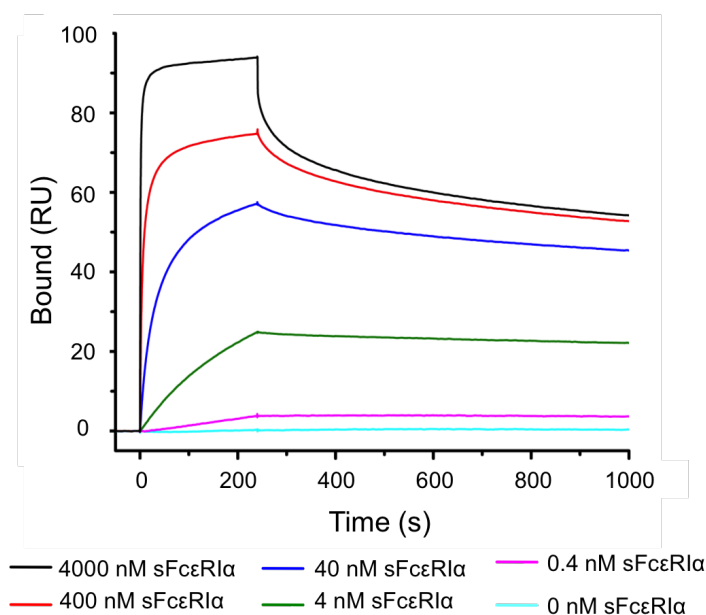


Figure 6.12: **SPR sensorgrams for the binding of sFcεRIα to His-tagged IgE-Fc.** Fitting the association and dissociation rate constants from this data suggested that IgE-Fc binds FcεRI with three different binding affinities:  $\sim 100$  pM,  $\sim 20$  nM and  $\sim 1$   $\mu$ M.

was provided in solution-state studies performed by Dr Anthony Keeble (Figure 6.13). Stopped-flow intrinsic fluorescence studies of the IgE-Fc/sFcεRIα interaction showed an immediate change in fluorescence as a result of the initial bimolecular interaction event. The stopped-flow derived  $K_D$  for this interaction was estimated to be  $\sim 1$   $\mu$ M, and thereby  $\sim 1000$  times weaker than the previously determined  $K_D$  values of the interaction. Following the initial binding event there was a further change in fluorescence, hypothesised to be the result of isomerisation events required for the formation of a sub-nanomolar affinity complex (Figure 6.13.a).

Similarly, a stopped-flow FRET dissociation experiment indicated the presence of multiple populations of IgE-Fc:sFcεRIα complexes.  $1$   $\mu$ M of a Alexa488-IgE-Fc:sFcεRIα-Alexa594 complex, equilibrated for 24 hours, was chased with  $10$   $\mu$ M of unlabeled sFcεRIα. The displacement of the labeled sFcεRIα by unlabeled sFcεRIα resulted in a decrease in FRET signal. Three dissociation rates were observed, consistent with the existence of at least three different populations of bound complexes with different affinities ( $\sim 1$   $\mu$ M,  $\sim 20$  nM,  $\sim 100$  pM as determined by SPR, Figure 6.13.b). Unlike for IgE-Fc, the literature does not suggest that

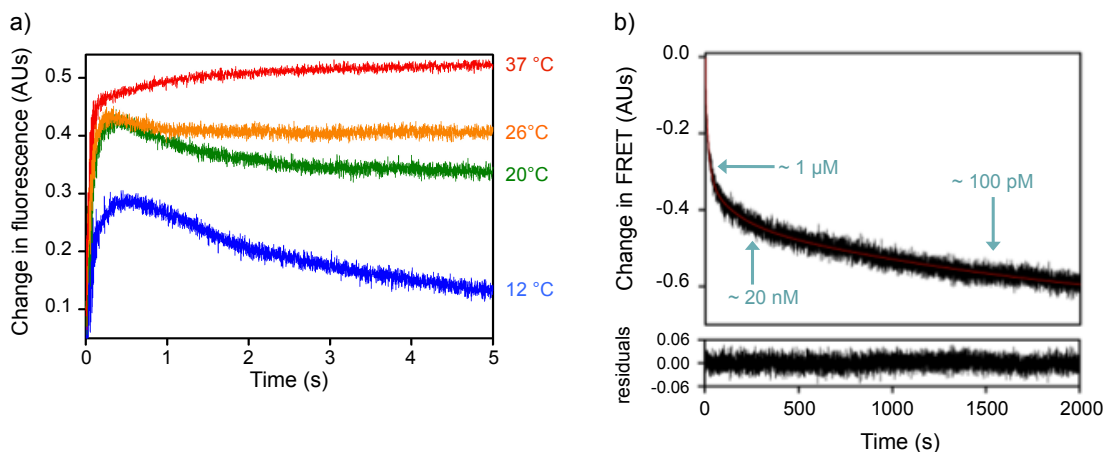


Figure 6.13: **Solution-based stopped-flow experiments show the IgE-Fc/sFc $\epsilon$ RI $\alpha$  has multiphasic binding characteristics.** (a) Stopped-flow intrinsic fluorescence experiments of IgE-Fc and sFc $\epsilon$ RI $\alpha$  showed an initial change in fluorescence as a result of the bimolecular collision, and a subsequent change in fluorescence as a result of isomerisation towards a higher affinity state. (b) Stopped-flow FRET experiments, in which 1  $\mu$ M Alexa488-IgE-Fc:sFc $\epsilon$ RI $\alpha$ -Alexa594 was chased with 10  $\mu$ M unlabeled sFc $\epsilon$ RI $\alpha$ , resulted in multiphasic changes in FRET, indicating the dissociation of three distinct populations of IgE-Fc:sFc $\epsilon$ RI $\alpha$  complexes with different affinities. The low affinity complexes seem to be overpopulated. Experiments performed by Dr Anthony Keeble, figures courtesy of Dr Anthony Keeble.

sFc $\epsilon$ RI $\alpha$  is conformationally diverse or particularly dynamic. The stopped-flow FRET data therefore indicate that even when IgE-Fc is bound to sFc $\epsilon$ RI $\alpha$  it can still exist in multiple conformations with different receptor-binding affinities.

The SPR and the stopped flow data demonstrate the heterogeneous nature of IgE-Fc and indicate that there are at least three different populations of sFc $\epsilon$ RI $\alpha$ -bound IgE-Fc with affinities of around 1  $\mu$ M, 20 nM, and 100 pM. The data also indicate that the weakly-bound IgE-Fc:sFc $\epsilon$ RI $\alpha$  complexes are highly populated. The Boltzmann equation (Equation 6.2) can be used to describe the frequency distribution of particles in the different states of a system at equilibrium. Using the experimentally determined  $K_D$  values of the highest and lowest affinity IgE-Fc/sFc $\epsilon$ RI $\alpha$  complexes to derive their Gibb's free energy ( $\Delta G$ ) (Equation 6.3), the Boltzmann equation (Equation 6.2) can be applied to determine the expected population distribution of the weakly-bound and strongly-bound complexes (Figure 6.14). A Boltzmann distribution suggests the ratio of the strongly-bound complex (the 100 pM complex) to the weakly-bound complex (the 1  $\mu$ M complex) should



be around 11,000:1. The experimental data indicate that the weakly-bound IgE-Fc:sFcεRIα complexes are much more populated than the calculated Boltzmann distribution: the lower-affinity IgE-Fc:sFcεRIα complexes are markedly overpopulated.

$$n_i : n_j = \exp\left(\frac{-\Delta E}{k_B T}\right) \quad (6.2)$$

Where  $n_i : n_j$  is the ratio of the number of molecules in state  $i$  compared to state  $j$ .  $\Delta E$  is the difference in the energy of states  $i$  and  $j$ .  $T$  is the temperature and  $k_B$  is the Boltzmann constant.

$$\Delta G = RT \ln K_D \quad (6.3)$$

Where  $\Delta G$  is the Gibb's free energy of an interaction,  $R$  is the ideal gas constant,  $T$  is the temperature and  $K_D$  is the dissociation constant of the interaction.

Since the Boltzmann distribution only applies to systems at equilibrium, one potential explanation for the observed the non-Boltzmann distribution is that the data were derived from essentially non-equilibrium measurements. If the Gibb's free energy of the two different sFcεRIα-bound states is very large ( $\Delta\Delta G$ ), the energy barrier between the different states may be so high that the states essentially never exchange and consequently experimental measurements cannot be recorded at equilibrium. However, this is unlikely to be the case, as evidence from re-binding SPR experiments showed that the species responsible for the multiphasic nature of the IgE-Fc/sFcεRIα interaction must interconvert [196]. Accordingly, an alternative explanation for the observed Boltzmann paradox is that the weaker binding IgE-Fc:sFcεRIα state is overpopulated because in fact *it is not a single state*, but instead represents many conformations (Figure 6.15).

Our current interpretation of the data suggests that there is heterogeneity within the sFcεRIα-binding population of IgE: IgE-Fc exists in conformations that can bind sFcεRIα with affinities of  $\sim 100$  pM,  $\sim 20$  nM and  $\sim 1$  μM. The lower affinity IgE-Fc is not represented by a single state, but by a large number of different low-affinity conformations. Upon sFcεRIα binding, the complexes undergo slow

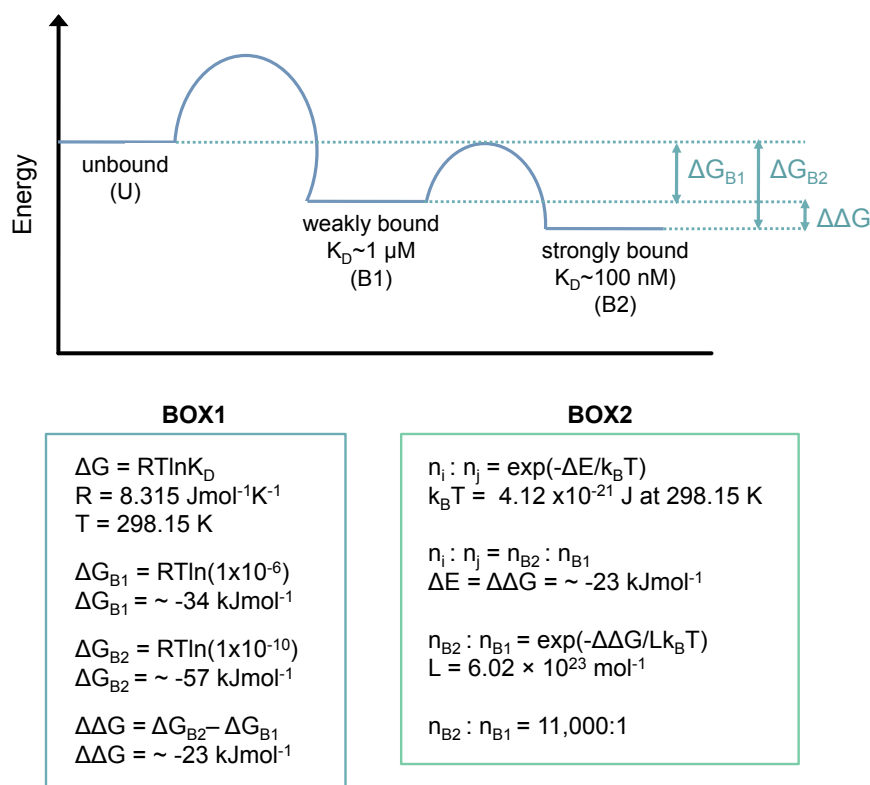


Figure 6.14: **The Boltzmann distribution suggests that for each weakly-bound IgE-Fc:sFcεRIα complex, there should be 11,000 strongly-bound Fc:sFcεRIα complexes.** Results from the SPR and stopped-flow fluorescence experiments suggest that at 298 K the IgE-Fc:sFcεRIα complexes can exist in either weakly-bound states or strongly-bound states. The experimentally determined  $K_D$  values for these two complexes can be used to derive the Gibb's free energy ( $\Delta G$ ) for each interaction using Equation 6.3, and thereby the energy difference between the two states ( $\Delta \Delta G$ ). By substituting  $\Delta \Delta G$  for  $\Delta E$  in the Boltzmann equation (Equation 6.2), the Boltzmann distribution of the weakly-bound and the strongly-bound states can be calculated.

isomerisation via induced-fit intermediates, resulting in an equilibrium mixture of high-, low- and intermediate-strength IgE-Fc:sFcεRIα complexes (Figure 6.16).

### **IgE-Fc heterogeneity within the αεFab12 and αεFab13 binding population**

It is possible that the multiphasic nature of the kinetics observed for the binding of IgE-Fc to αεFab12 and αεFab13 may also be a result of IgE-Fc conformational heterogeneity. Perhaps within the conformational ensemble of IgE-Fc there exist states that bind αεFab12 (or αεFab13) with higher- and lower-affinities. To ensure that the multiphasic nature of the interaction was not an artifact of the SPR

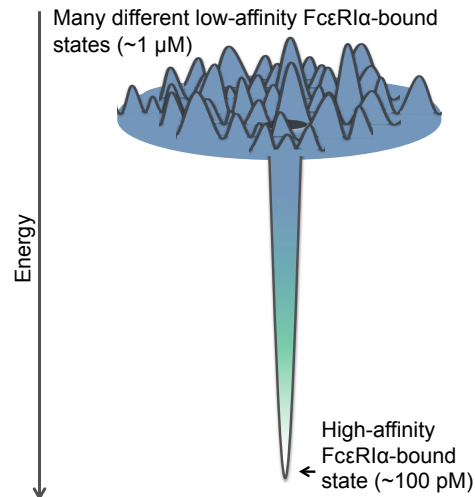


Figure 6.15: **A schematic representation of the proposed IgE-Fc:sFc $\epsilon$ RI $\alpha$  energy landscape.**

experiments performed and to see if different affinity states persist in the form of the  $\alpha\epsilon$ Fab:IgE-Fc complexes, SPR and stopped-flow FRET experiments like those described for the IgE-Fc/sFc $\epsilon$ RI $\alpha$  interaction, could be performed but with  $\alpha\epsilon$ Fab12 and  $\alpha\epsilon$ Fab13 instead of sFc $\epsilon$ RI $\alpha$ .

#### 6.2.4 Intramolecular FRET experiments

IgE-Fc's conformational flexibility is central to both the heterogeneity of IgE-Fc and its susceptibility to allosteric modulation. C $\epsilon$ 2 domain extension in IgE-Fc was predicted by molecular dynamic simulations [81] and is an extreme form of conformational flexibility. Crystal structures the  $\alpha\epsilon$ Fab1:IgE-Fc [81] and Xolair Fab mutant 3:IgE-Fc complexes [82], show IgE-Fc can exist in fully linearized and partly extended conformations. Intramolecular FRET data indicate that C $\epsilon$ 2 domain extension occurs in solution as a result of the interaction between IgE-Fc and these Fabs: an acceptor/donor fluorophore were attached to the C $\epsilon$ 2 and C $\epsilon$ 4 domains of IgE-Fc (Figure 6.17) and a reduction in FRET between the fluorophores was observed upon titration of  $\alpha\epsilon$ Fab1 or Xolair Fab mutant 3. The reduction in FRET signal was attributed to IgE-Fc unbending, which increases the C $\epsilon$ 2-C $\epsilon$ 4 domain distance [81, 82]. Evidence suggests that the extension of the C $\epsilon$ 2 domains that is associated with the binding of  $\alpha\epsilon$ Fab1 is partly responsible for the inhibition of the IgE-Fc/Fc $\epsilon$ RI interaction [81]. Intramolecular IgE-Fc FRET experiments

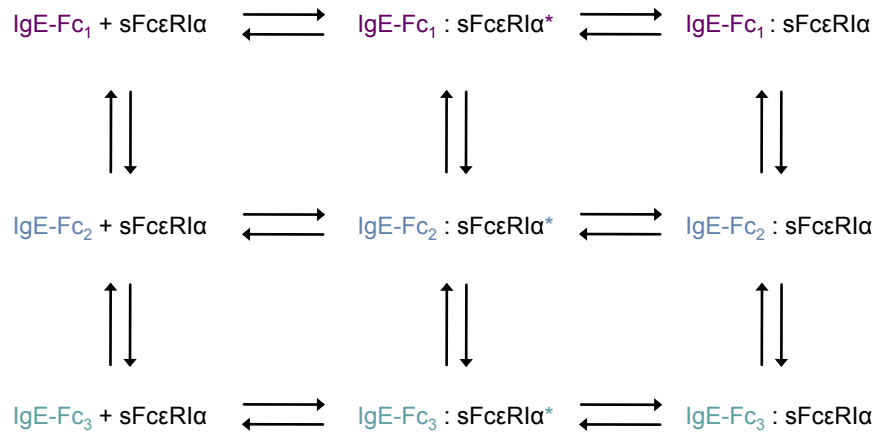


Figure 6.16: **Our current best description of the IgE-Fc/sFc $\epsilon$ RI $\alpha$  binding equation.** We propose that IgE-Fc is heterogeneous: it can bind sFc $\epsilon$ RI $\alpha$  with at least three different affinities (IgE-Fc<sub>1</sub>, IgE-Fc<sub>2</sub> and IgE-Fc<sub>3</sub>). When IgE-Fc binds sFc $\epsilon$ RI $\alpha$  it undergoes an induced-fit conformational change via an intermediate. Three different final complex states exist at equilibrium, which have different affinities ( $\sim 1 \mu\text{M}$ ,  $\sim 20 \text{ nM}$ ,  $\sim 100 \text{ pM}$ ). The weakly-bound complexes are not represented by a single conformation but by a large number of different conformations.

were performed to ascertain whether the binding of any of the five selected  $\alpha\epsilon$ Fabs to IgE-Fc is associated with the linearization of IgE-Fc.

### The experimental set up of the intramolecular FRET experiments

An IgE-Fc mutant (E289C), biotinylated at the C-terminus using a BirA tag, was labeled with donor and acceptor fluorophores in the C $\epsilon$ 2 domains and in the C $\epsilon$ 4 domains, respectively. The donor fluorophore, a thiol-reactive terbium chelate (Invitrogen), bound the C289 thiol in the C $\epsilon$ 2 domains, and a monovalent amine-reactive Alexa Fluor 488 (Invitrogen) labeled streptavidin bound the C-terminal BirA tags (Figure 6.17).  $\alpha\epsilon$ Fab1 (positive control for IgE-Fc linearization) and the different  $\alpha\epsilon$ Fabs were titrated into IgE-Fc in PBS to give a final concentration of 10 nM IgE-Fc and 1  $\mu\text{M}$   $\alpha\epsilon$ Fab, and then were incubated for 120 min at 25  $^\circ\text{C}$ . FRET was measured on an Analyst HT microplate reader (LJL Biosystems) with an excitation wavelength of 330 nm, and emission wavelengths of 485 and 520 nm. The FRET signal (The FRET ratio  $((E_{520}/E_{485}) \times 10^4)$  in the absence of any  $\alpha\epsilon$ Fab was defined as the maximum FRET signal (0 % inhibition). The FRET signal when the experiments were performed with unlabeled streptavidin was defined as the minimum FRET signal (100 % inhibition). The FRET measurements (in terms of

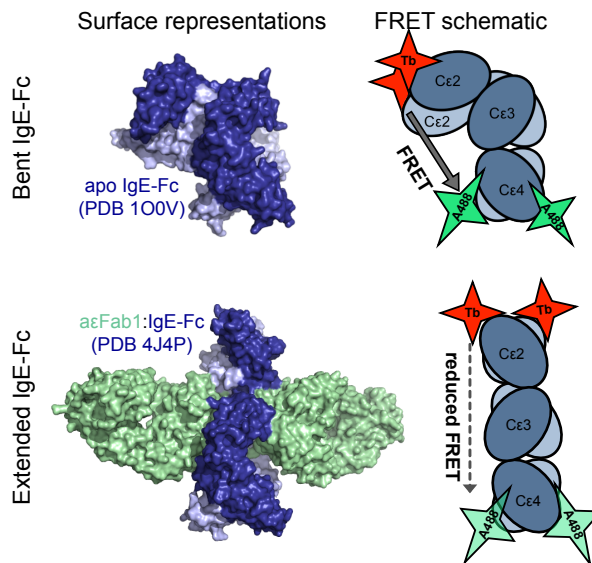


Figure 6.17: **A schematic representation of the experimental setup for the IgE-Fc intramolecular FRET assays.** IgE-Fc (E289C), with a C-terminal BirA tag, was labeled with thiol-reactive terbium (Invitrogen) via an interaction with C289 in the C $\epsilon$ 2 domains, according to manufacturers instructions. Monovalent Alexa Fluor 488 (Thermo Fisher Scientific) labeled streptavidin also bound to IgE-Fc(E289C) but via the C-terminal BirA tag. IgE-Fc in solution exists in an asymmetrically bent state. Excitation of the N-terminal terbium results in the excitation of the C-terminal A488 via FRET. The resulting fluorescence signal of the A488 fluorophore was measured and used to define the basal FRET efficiency between the donor/acceptor pair. When  $\alpha\epsilon$ Fab1 binds IgE-Fc, IgE-Fc adopts an extended conformation in which the distance between the C $\epsilon$ 2 and C $\epsilon$ 4 domains is increased. Since FRET is a distance sensitive phenomenon, the FRET efficiency between the donor/acceptor pair is reduced and accordingly so is excitement of A488. Consequently the measured A488-fluorescence levels are lower.

percentage of FRET inhibition) were plotted as a function of  $\alpha\epsilon$ Fab concentration and fit to a four parameter logistical equation (Equation 2.23) (Figure 6.18).

### Intramolecular FRET results.

The binding of  $\alpha\epsilon$ Fab1 to IgE-Fc results in a nearly fully extended IgE-Fc structure [81]; the  $\alpha\epsilon$ Fab1 titration here did not reach the concentrations required to saturate the  $\alpha\epsilon$ Fab1 binding sites on IgE-Fc, but fitting predicts that the maximal FRET inhibition achieved by  $\alpha\epsilon$ Fab1 would have been  $\sim 60\%$  (Figure 6.18).  $\alpha\epsilon$ Fab3 and  $\alpha\epsilon$ Fab18 did not affect the FRET signal at saturating concentrations, whereas  $\alpha\epsilon$ Fab2,  $\alpha\epsilon$ Fab12 and  $\alpha\epsilon$ Fab13 did inhibit the FRET signal ( $\sim 60\%$ ,  $\sim 20\%$ ,  $\sim 50\%$ , respectively) (Figure 6.18).

These results suggest that the  $\alpha\epsilon$ Fab2:IgE-Fc complex is nearly fully extended, the  $\alpha\epsilon$ Fab13:IgE-Fc complex is mostly extended, and the  $\alpha\epsilon$ Fab12:IgE-Fc complex is only partially unbent. The  $K_D$  values for the second (lower-affinity)  $\alpha\epsilon$ Fab binding sites on IgE-Fc were determined to be  $\sim 640$  nM,  $\sim 800$  nM and  $\sim 170$  nM for  $\alpha\epsilon$ Fab2,  $\alpha\epsilon$ Fab12 and  $\alpha\epsilon$ Fab13, respectively. Since the maximum FRET inhibition was achieved by the addition of  $\sim 20$ - $30$  nM of these  $\alpha\epsilon$ Fabs, the binding of the first  $\alpha\epsilon$ Fab was sufficient for maximal FRET inhibition, and hence the proposed C $\epsilon$ 2 domain extension. Neither  $\alpha\epsilon$ Fab3 nor  $\alpha\epsilon$ Fab18 markedly inhibited the intramolecular IgE-Fc FRET signal, indicating  $\alpha\epsilon$ Fab3:IgE-Fc (1:1) complexes and  $\alpha\epsilon$ Fab18:IgE-Fc (1:1) complexes are bent.

SPR studies described in the previous chapter indicated that  $\alpha\epsilon$ Fab2,  $\alpha\epsilon$ Fab12 and  $\alpha\epsilon$ Fab13 differentially affect receptor binding. The experiments were performed in the absence of robust controls for unmodulated IgE-Fc/receptor interactions, however  $\alpha\epsilon$ Fab2 and  $\alpha\epsilon$ Fab13 appeared to have an inhibitory effect on the IgE-Fc/derCD23 interaction, whereas  $\alpha\epsilon$ Fab12 appeared to enhance the interaction (Section 5.2.2). Furthermore,  $\alpha\epsilon$ Fab13 appeared to increase the off-rate of the IgE-Fc:sFc $\epsilon$ RI $\alpha$  interaction (Section 5.2.3). The results of the intramolecular FRET experiments performed here suggest that  $\alpha\epsilon$ Fab2,  $\alpha\epsilon$ Fab12 and  $\alpha\epsilon$ Fab13 are capable of shifting the conformational landscape of IgE-Fc, which is a prerequisite of allosteric modulation. However, whether the unbending of IgE-Fc by these  $\alpha\epsilon$ Fabs plays a role in their apparent effects on receptor binding has yet to be established.

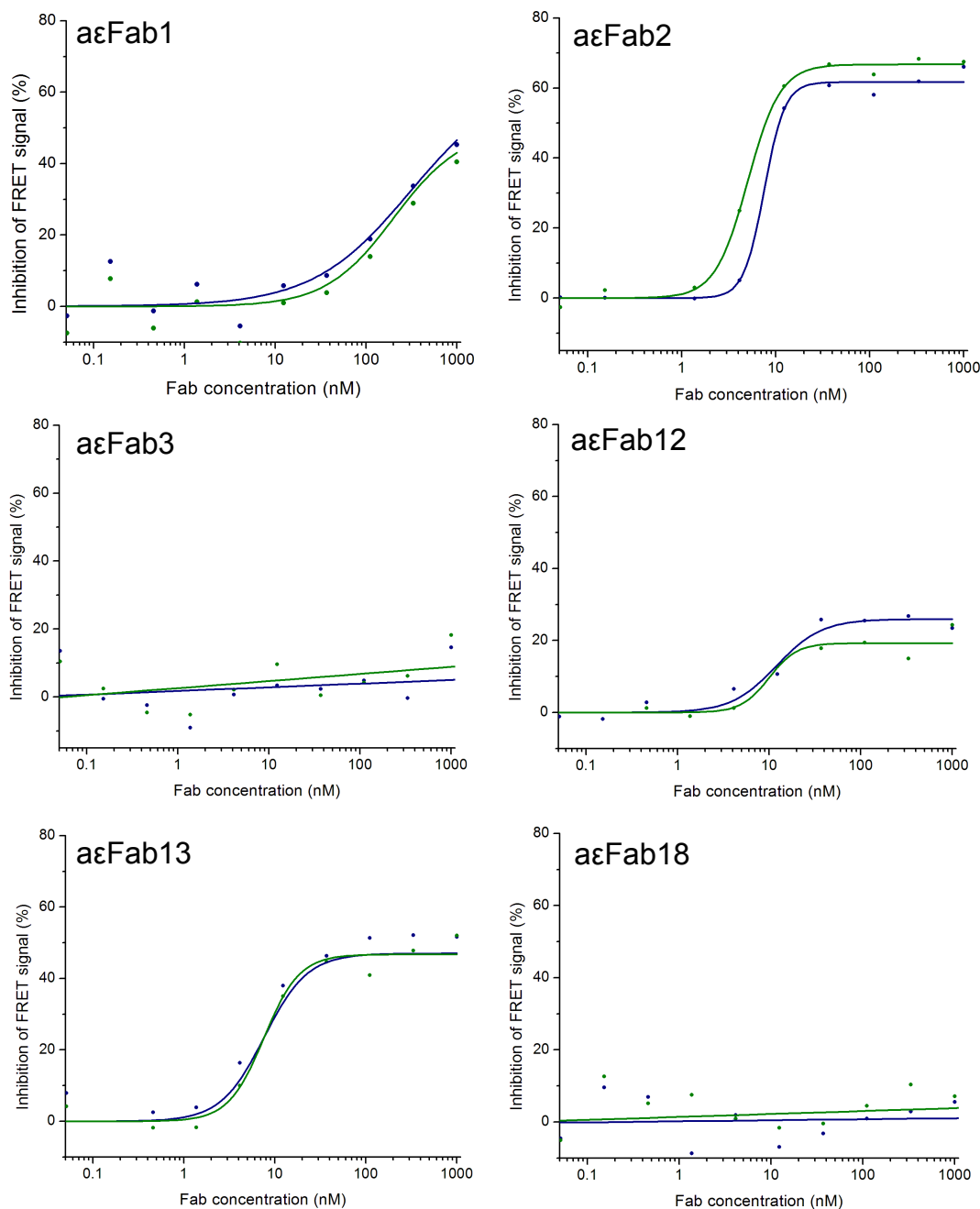


Figure 6.18: **IgE-Fc intramolecular FRET experiments suggest that binding of  $\alpha\epsilon$ Fab2,  $\alpha\epsilon$ Fab12 and  $\alpha\epsilon$ Fab13 to IgE-Fc is associated with a conformational change in IgE-Fc.** IgE-Fc was labeled with an N-terminal fluorophore donor (terbium) and a C-terminal fluorophore acceptor (Alexa Fluor 488), and incubated with increasing concentrations of each of the  $\alpha\epsilon$ Fabs. The terbium was excited by light at a wavelength of 330 nm and fluorescence emission was read at wavelengths of 485 nm and 520 nm. The FRET signal (the FRET ratio  $((E_{520}/E_{485}) \times 10^4)$  in the absence of any  $\alpha\epsilon$ Fab was defined as the maximum FRET signal (0 % inhibition). The FRET signal when the experiments were performed with unlabeled streptavidin was defined as the minimum FRET signal (100 % inhibition). The experiments were performed in duplicate and the data were fit to a four-parameter logistic curve.  $\alpha\epsilon$ Fab1 is known to bind to an almost completely extended IgE-Fc.

### 6.2.5 The binding of different IgE-Fc subfragments to the $\alpha\epsilon$ Fabs

Having established the stoichiometries and affinities for the  $\alpha\epsilon$ Fab/IgE-Fc interactions, further SPR experiments were performed to try to determine to which domains of IgE-Fc the different  $\alpha\epsilon$ Fabs bind. SPR experiments were performed in which the binding between different IgE-Fc subfragments and each of the selected  $\alpha\epsilon$ Fabs were measured. Each  $\alpha\epsilon$ Fab was immobilised at a low density ( $<400$  RUs) on a separate CM5 SPR sensor chip surface (GE Healthcare) using amine-coupling (Section 2.6.2). Full length IgE-Fc, IgE-Fc(3-4), C $\epsilon$ 2 dimer, and C $\epsilon$ 2 monomer protein constructs (Figure 6.19) were injected at different concentrations over the  $\alpha\epsilon$ Fab surfaces and over a mock amine-coupled surface. IgE-Fc and IgE-Fc(3-4) were injected at concentrations of 0 - 0.1  $\mu$ M and the C $\epsilon$ 2 dimer and monomer were injected at concentrations of 0 - 5  $\mu$ M. The changes in SPR response from the immobilised  $\alpha\epsilon$ Fab surfaces, subtracting the changes in response from the mock amine coupled surface upon the IgE-Fc subfragment injections, were used to measure the specific binding of IgE-Fc subfragments to the  $\alpha\epsilon$ Fabs. Scott Isherwood and Virginia Casblancas Antras performed these experiments in duplicate and the results were highly replicable.

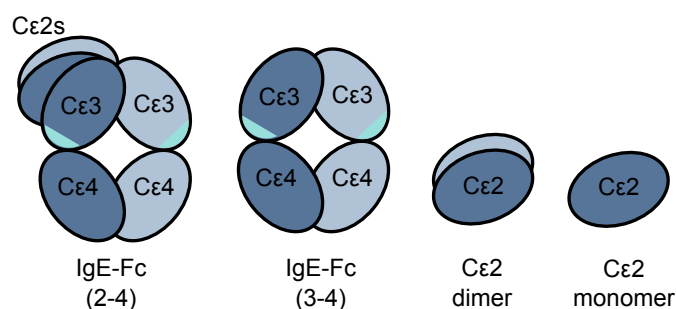


Figure 6.19: **Schematic representation IgE-Fc and different subfragments of IgE-Fc.** The binding of these different IgE-Fc subfragments to the five selected  $\alpha\epsilon$ Fabs was measured using SPR. The light green patches illustrate the approximate locations of the CD23 binding sites. IgE-Fc, IgE-Fc(3-4) and the C $\epsilon$ 2 monomer were recombinantly expressed and then purified. The C $\epsilon$ 2 dimer was a spontaneously proteolytically processed product of recombinantly expressed IgE-Fc, which was purified by SEC and its mass confirmed by mass spectrometry.



**IgE-Fc vs. IgE-Fc(3-4) vs. C $\epsilon$ 2 dimer**

All of the  $\alpha\epsilon$ Fabs bound to IgE-Fc as expected (Figure 6.20). With the exception of  $\alpha\epsilon$ Fab12, none of the  $\alpha\epsilon$ Fabs bound IgE-Fc(3-4) (Figure 6.20). A further SPR experiment was performed to confirm that  $\alpha\epsilon$ Fab12 does bind to IgE-Fc(3-4) (Appendix A.8). The double-subtracted SPR sensorgrams, showed that all of the  $\alpha\epsilon$ Fabs bound the C $\epsilon$ 2 dimer (Figure 6.20), indicating that the binding of each of the five selected  $\alpha\epsilon$ Fabs to IgE-Fc involves the C $\epsilon$ 2 domains.

For  $\alpha\epsilon$ Fab2,  $\alpha\epsilon$ Fab3 and  $\alpha\epsilon$ Fab13 the sensorgrams for the binding of IgE-Fc (0 - 100 nM) and the sensorgrams for the binding of the C $\epsilon$ 2 dimer (0 - 156 nM) have very similar profiles (Figure 6.20). It should be noted that the IgE-Fc and C $\epsilon$ 2 dimer have not been normalised for immobilisation density or for differences in the masses of IgE-Fc and C $\epsilon$ 2, and so RU values are not directly comparable). Fitting the low concentration data to monophasic models where appropriate (not shown), suggested that  $\alpha\epsilon$ Fab2,  $\alpha\epsilon$ Fab3 and  $\alpha\epsilon$ Fab13 bind the C $\epsilon$ 2 dimer with around 10-50 times lower affinity than IgE-Fc. Given that  $\alpha\epsilon$ Fab2,  $\alpha\epsilon$ Fab3 and  $\alpha\epsilon$ Fab13 did not bind IgE-Fc(3-4), the results suggest that the binding sites for these Fabs are primarily located in the C $\epsilon$ 2 domains but that only in the context of the full IgE-Fc molecule is native affinity binding achieved. The C $\epsilon$ 3-C $\epsilon$ 4 fragment may provide additional stabilising contacts or may contribute entropically to the interaction.

The sensorgrams for the binding of C $\epsilon$ 2 to  $\alpha\epsilon$ Fab18 are markedly different from that of the binding of IgE-Fc (Figure 6.20). The off-rate of the interaction is significantly faster for the binding of the C $\epsilon$ 2 dimer, and it was estimated, by steady-state analysis (data not shown), that the interaction had a micromolar binding affinity. Since  $\alpha\epsilon$ Fab18 did not bind IgE-Fc(3-4) and bound the C $\epsilon$ 2 dimer very weakly, we propose that the  $\alpha\epsilon$ Fab18 binding sites are located at the C $\epsilon$ 2-C $\epsilon$ 3 domain interface. C $\epsilon$ 2 domain residues probably provide the major surface contacts, but C $\epsilon$ 3 residues are also likely to have significant roles in stabilising the  $\alpha\epsilon$ Fab18/IgE-Fc interaction. The results of these experiments also suggest that  $\alpha\epsilon$ Fab12 binds to the C $\epsilon$ 2-C $\epsilon$ 3 interface. Unlike  $\alpha\epsilon$ Fab18, both the C $\epsilon$ 2 dimer and the IgE-Fc(3-4) bound at significant levels to  $\alpha\epsilon$ Fab12 (Figure 6.20). The interaction between  $\alpha\epsilon$ Fab12 and the C $\epsilon$ 2 dimer, and the interaction between  $\alpha\epsilon$ Fab12 and IgE-Fc(3-4)

had about 100 and 10 times lower affinities than the interaction between  $\alpha\epsilon$ Fab12 and IgE-Fc, respectively. This suggests that although  $\alpha\epsilon$ Fab12 is capable of binding both domains (further SPR experiments confirming this finding are shown in Appendix A.8 and Appendix A.9), both domains are required to achieve native-binding affinity. Furthermore, the C $\epsilon$ 3 domains appear to have a more significant role in binding of  $\alpha\epsilon$ Fab12 than in the binding of any of the other five selected  $\alpha\epsilon$ Fabs.

### **C $\epsilon$ 2 dimer vs. C $\epsilon$ 2 monomer**

Comparisons of sensorgrams for the interaction of each  $\alpha\epsilon$ Fab with the C $\epsilon$ 2 dimer and the C $\epsilon$ 2 monomer constructs (Figure 6.21) developed our understanding of the nature of the interactions between the  $\alpha\epsilon$ Fabs and the C $\epsilon$ 2 domains of IgE-Fc. Having accounted for the difference in molecular mass of the C $\epsilon$ 2 monomer and dimer, the sensorgrams for the interactions between  $\alpha\epsilon$ Fab2 and the C $\epsilon$ 2 monomer and C $\epsilon$ 2 dimer were very similar (Figure 6.21); the response for the binding of the monomer was half that of the response for the binding of the dimer, because the C $\epsilon$ 2 monomer has half the molecular mass. This suggests that one molecule of  $\alpha\epsilon$ Fab2 binds a single C $\epsilon$ 2 domain. Likewise, the sensorgram for the binding of the C $\epsilon$ 2 dimer to  $\alpha\epsilon$ Fab18 and the sensorgram for the binding of the C $\epsilon$ 2 monomer to  $\alpha\epsilon$ Fab18 (Figure 6.21) suggests that that one molecule of  $\alpha\epsilon$ Fab18 binds a single C $\epsilon$ 2 domain.

Despite being half the molecular mass, the binding of the C $\epsilon$ 2 monomer to  $\alpha\epsilon$ Fab3, and the binding of the C $\epsilon$ 2 monomer to  $\alpha\epsilon$ Fab13, gave the same SPR responses as the binding of the C $\epsilon$ 2 dimer to  $\alpha\epsilon$ Fab3 and  $\alpha\epsilon$ Fab13, respectively (Figure 6.21). This suggests that either a single molecule of  $\alpha\epsilon$ Fab3 (or  $\alpha\epsilon$ Fab13) can bind two molecules of C $\epsilon$ 2, perhaps by binding the C $\epsilon$ 2 dimer interface, and/or  $\alpha\epsilon$ Fab3 (or  $\alpha\epsilon$ Fab13) induces C $\epsilon$ 2 dimerisation.

$\alpha\epsilon$ Fab12 was the only  $\alpha\epsilon$ Fab that did not bind to the C $\epsilon$ 2 monomer, despite binding the C $\epsilon$ 2 dimer (Figure 6.21). This suggests that when binding to the C $\epsilon$ 2 domains, one molecule of  $\alpha\epsilon$ Fab12 engages both C $\epsilon$ 2 domains of IgE-Fc. The most plausible explanation is that  $\alpha\epsilon$ Fab12 binds at the C $\epsilon$ 2 dimerisation interface.

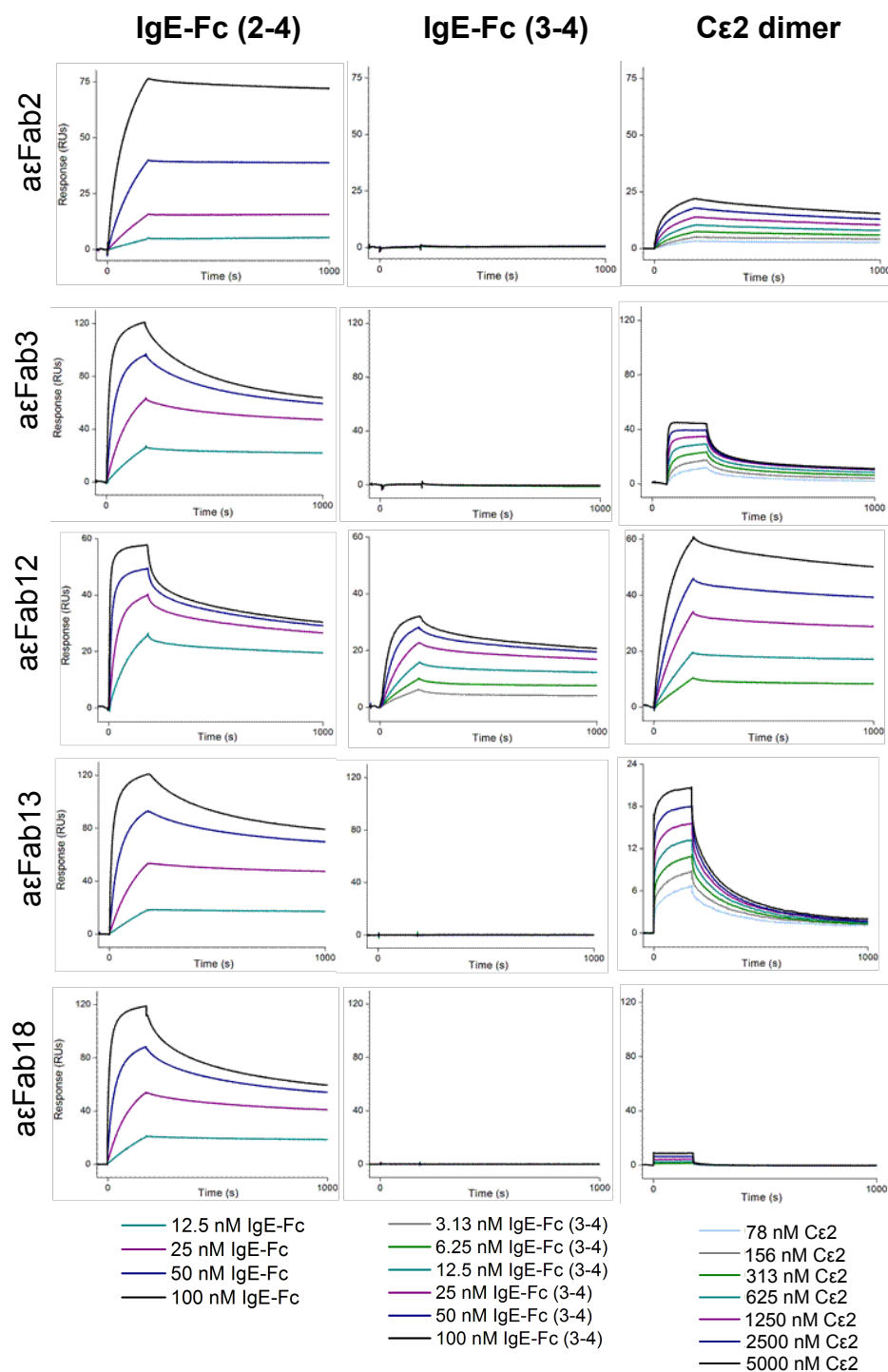


Figure 6.20: **The five selected  $\alpha\epsilon$ Fabs bind to the C $\epsilon$ 2 domains of IgE-Fc.** SPR sensorgrams for the binding of different fragments of IgE-Fc to the five selected  $\alpha\epsilon$ Fab surfaces. IgE-Fc, IgE-Fc(3-4) and C $\epsilon$ 2 dimer was injected over  $\alpha\epsilon$ Fab immobilised on individual SPR sensor surfaces at low densities ( $< 400$  RUs) using amine coupling. Whilst all  $\alpha\epsilon$ Fabs bound the C $\epsilon$ 2 dimer, as shown by an increase in SPR response upon injection of the dimer, only  $\alpha\epsilon$ Fab12 bound IgE-Fc(3-4). It should be noted that the sensorgrams have not been normalised for immobilisation density (which differ between the IgE-Fc/IgE-Fc (3-4) and C $\epsilon$ 2 experiments), or for differences in the masses of the analytes, and so RU values are not directly comparable.

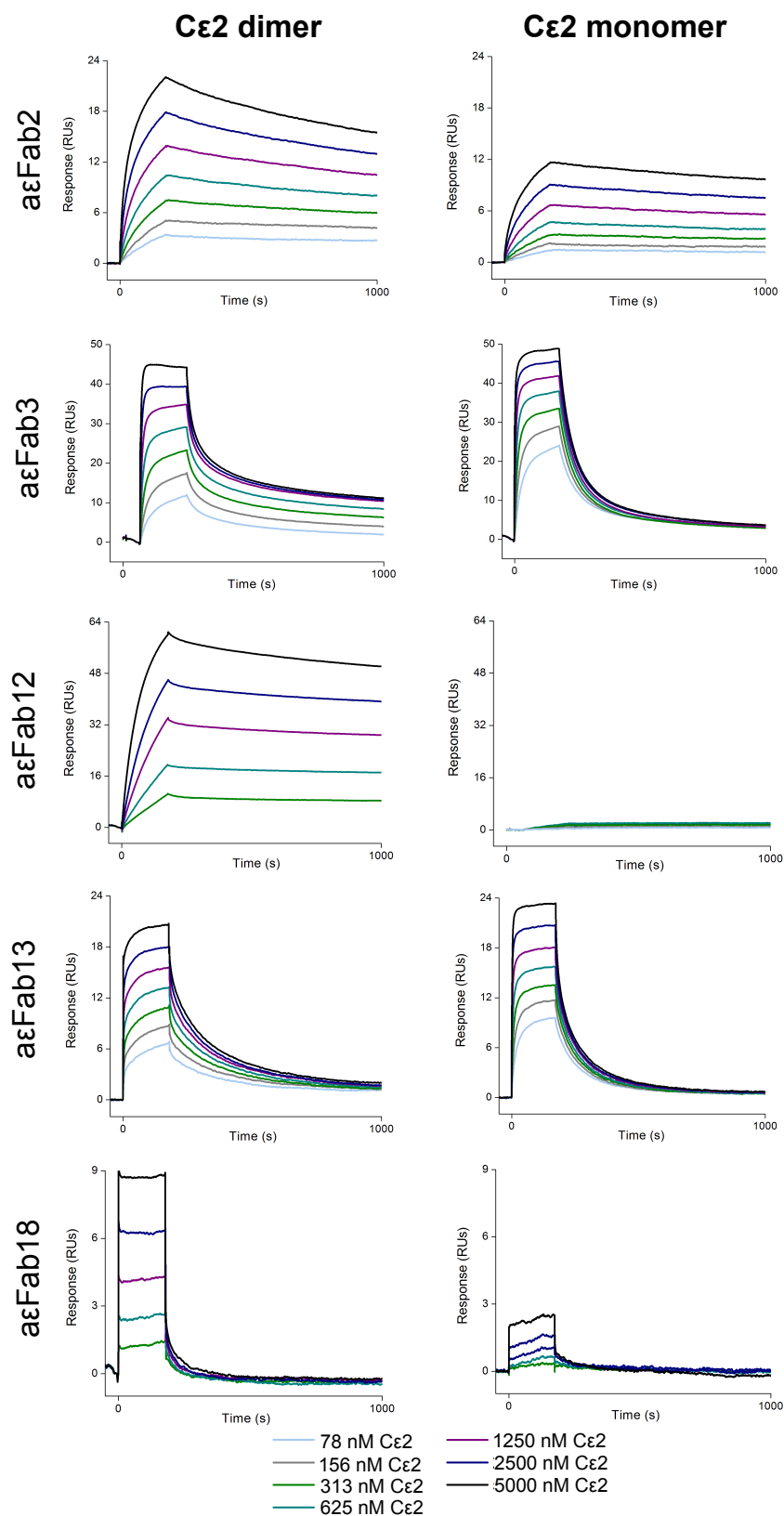


Figure 6.21: **SPR sensorgrams for the binding of Cε2 dimer and Cε2 monomer to the five selected αεFab surfaces.** Cε2 dimer and Cε2 monomer were injected over αεFab immobilised on individual SPR sensor surfaces at low densities (< 400 RUs) using amine-coupling. The Cε2 dimer data is replicated from Figure 6.20.

## 6.3 Discussion

Size exclusion chromatography and SPR binding experiments indicate that the five selected  $\alpha\epsilon$ Fabs bind to IgE-Fc with a 2:1 stoichiometry. IgE-Fc is a homodimer and ligands specific for IgE-Fc may bind to two symmetrically related epitopes, as has been observed for other IgE-Fc binding proteins (Figure 6.1) [18, 109, 81, 108, 82]. The SPR binding data further suggests that the  $\alpha\epsilon$ Fab binding sites have different binding affinities: in each case the higher-affinity binding site has a very low nanomolar, or even sub-nanomolar, binding affinity and the second binding site has a high nanomolar binding affinity. Data for the binding of other anti-IgE Fabs to IgE-Fc have also suggested that the symmetrically-related binding sites on IgE-Fc are non-equivalent (derCD23 [88, 18, 89],  $\alpha\epsilon$ Fab1 [81] and Xolair [108, 82]), and it is proposed that this is at least partly because IgE-Fc exists predominantly in an asymmetric bent conformation in solution (Section 6.1) [71, 72]. In these respects, the five selected  $\alpha\epsilon$ Fabs are similar to anti-IgE-ligands already described in the literature, however, the  $\alpha\epsilon$ Fabs that have been generated in this project are set-apart by the location of their binding sites on IgE-Fc.

SPR experiments showed that all of the five selected  $\alpha\epsilon$ Fabs bind exclusively, or principally, to the C $\epsilon$ 2 domains of IgE-Fc, whereas other previously described engineered anti-IgE-Fc ligands bind exclusively, or primarily, to the C $\epsilon$ 3 domains [109, 81, 108, 82] (Figure 6.1). Like these anti-IgE-Fc ligands, the selected  $\alpha\epsilon$ Fabs affect the binding of IgE-Fc receptors, but unlike the other anti-IgE-ligands, the  $\alpha\epsilon$ Fabs appear to exert their effects via a different domain of IgE-Fc.

$\alpha\epsilon$ Fab2,  $\alpha\epsilon$ Fab3 and  $\alpha\epsilon$ Fab13 bind the C $\epsilon$ 2 domains with almost the same affinity as they bind IgE-Fc, suggesting that IgE-Fc(3-4) has only a peripheral role in the binding of these  $\alpha\epsilon$ Fabs. The data suggest that  $\alpha\epsilon$ Fab12 and  $\alpha\epsilon$ Fab18, however, bind to the C $\epsilon$ 2-C $\epsilon$ 3 interface. The five  $\alpha\epsilon$ Fabs were primarily selected for their apparently different effects on the IgE-Fc/CD23 interaction (Section 5.2.2). CD23 binds to the C $\epsilon$ 3 domain very close to the C $\epsilon$ 3-C $\epsilon$ 4 interface, consequently, these  $\alpha\epsilon$ Fabs do not elicit their effects on the IgE-Fc/CD23 interaction by binding at, or adjacent to, the CD23 binding sites. Although the  $\alpha\epsilon$ Fabs do not bind at the CD23 binding sites, steric inhibition of one CD23 binding site is still possible since IgE-Fc

exists predominantly in a bent asymmetric structure in solution and consequently the C $\epsilon$ 2 domains come into close proximity with the C $\epsilon$ 3 domain of one chain. IgE-Fc, however can exist in extended, or partly extended conformations: a $\epsilon$ Fab1 binds to IgE-Fc and stabilises a conformation of IgE-Fc in which the C $\epsilon$ 2 domains are unbent [81] (Figure 6.1). If an a $\epsilon$ Fab stabilises an extended conformation of IgE-Fc in which the C $\epsilon$ 2 domains are no longer bent against the C $\epsilon$ 3 domain of one chain, IgE-Fc/CD23 inhibition would likely be allosteric in nature.

FRET assays, in which acceptor and donor fluorophores are attached to the C $\epsilon$ 2 and C $\epsilon$ 4 domains, have previously been used to determine the extent of IgE-Fc extension in solution [73, 74, 75, 81, 82]. Intramolecular FRET studies performed in this chapter indicated that the a $\epsilon$ Fab2:IgE-Fc complex is extended, the a $\epsilon$ Fab13:IgE-Fc complex is partially extended and a $\epsilon$ Fab12:IgE-Fc complex is partly unbent (Figure 6.22). If, as the data suggests, a $\epsilon$ Fab2:IgE-Fc and a $\epsilon$ Fab13:IgE-Fc complexes are mostly extended, it is unlikely that they could sterically interfere with CD23 binding (Figure 6.22). SPR experiments performed in Chapter 4 suggested that a $\epsilon$ Fab2 and a $\epsilon$ Fab13 are inhibitors of the IgE-Fc/CD23 interaction (Section 5.2.2). In light of the experiments performed in this chapter we suggest that the apparent inhibition is mediated by allosteric processes. However, further inhibition assays with appropriate controls for unmodulated IgE/CD23 binding are required to confirm that these a $\epsilon$ Fabs inhibit the IgE/CD23 interaction.

The intramolecular FRET data suggest that the binding of a $\epsilon$ Fab2, a $\epsilon$ Fab12 and a $\epsilon$ Fab13 are associated with a shift in the conformational equilibrium of IgE-Fc. C $\epsilon$ 2 domain extension is a large conformational change and could potentially affect IgE-Fc/receptor interactions in a variety of ways. At present it is unknown if and how the changes in C $\epsilon$ 2 domain extension, associated with the binding of these three a $\epsilon$ Fabs, affect IgE-Fc/receptor interactions. Changes in the C $\epsilon$ 2-C $\epsilon$ 3 interdomain angle could affect the C $\epsilon$ 3-C $\epsilon$ 4 interdomain angle, which is known to be important in the binding of both receptors to IgE-Fc [71, 72, 18]. Furthermore, the unbending of IgE-Fc induced by the a $\epsilon$ Fab1/IgE-Fc interaction prevents the binding of sFc $\epsilon$ R1 $\alpha$ , as the newly adopted position of the C $\epsilon$ 2 domain pair blocks the receptor binding site. If, as the data suggest, a $\epsilon$ Fab13:IgE-Fc is partially un-

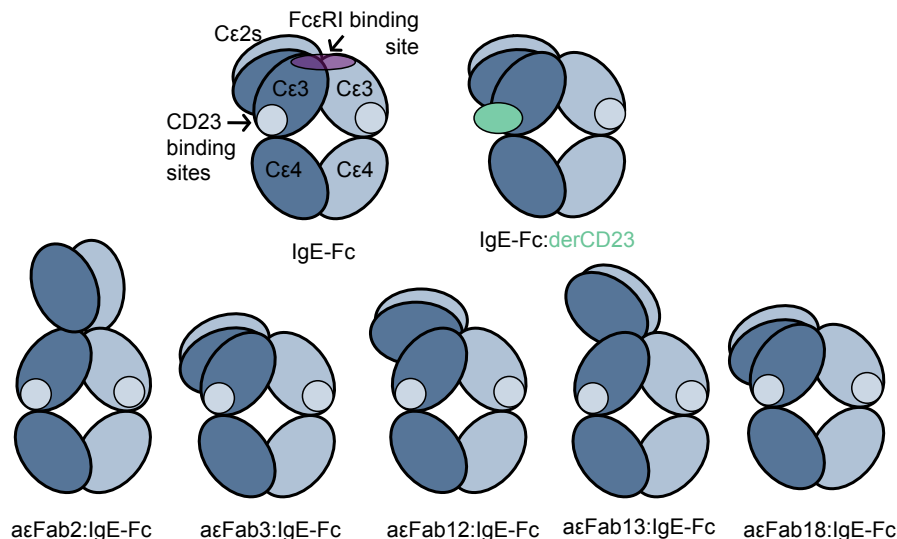


Figure 6.22: **Intramolecular FRET studies suggested that the binding of some of the  $\alpha\epsilon$ Fabs results in IgE-Fc unbending.** IgE-Fc exists primarily in an asymmetrically bent conformation [73, 74, 71, 75]. IgE-Fc retains an asymmetrically bent conformation when bound to derCD23 [75, 95]. Intramolecular FRET studies indicated that IgE-Fc also retains an asymmetric bent conformation when bound to  $\alpha\epsilon$ Fab3 and  $\alpha\epsilon$ Fab18. The intramolecular FRET data suggested that  $\alpha\epsilon$ Fab2 binds the C $\epsilon$ 2 domains IgE-Fc and  $\alpha\epsilon$ Fab2:IgE-Fc is almost fully extended IgE-Fc, consequently there is a significant distance between the  $\alpha\epsilon$ Fab2 and CD23 binding sites. The intramolecular FRET data also suggested  $\alpha\epsilon$ Fab13:IgE-Fc is partially extended and  $\alpha\epsilon$ Fab12:IgE-Fc is partially unbent. The schematic models are not meant as accurate reflections of the exact degree of C $\epsilon$ 2 unbending and instead are non-quantitative representations of the relative degree of IgE-Fc extension as suggested by the intramolecular FRET data.

bent, the position of the C $\epsilon$ 2 domains could be partly responsible for the increase in off-rate of the IgE-Fc/sFc $\epsilon$ RI $\alpha$  interaction that was observed in Chapter 5 (Section 5.2.3).

In addition to C $\epsilon$ 2 domain extension, the C $\epsilon$ 3 domains of IgE-Fc can undergo significant conformational changes. The C $\epsilon$ 3 domains can move upon the C $\epsilon$ 3-C $\epsilon$ 4 hinge so that they are either further from, or closer to, one another, thereby adopting a range of ‘open’ and ‘closed’ conformations [77, 71, 72, 18, 81, 82] (Figure 6.2). Fc $\epsilon$ RI binds a specific ‘open’ conformation and CD23 binds a specific ‘closed’ conformation of IgE-Fc, consequently simultaneous receptor binding is not possible, and partly explains how  $\alpha\epsilon$ Fab1 [81] and Xolair Fab mutant 3 [82], which bind very open forms of IgE-Fc, inhibit receptor binding (Figure 6.2). Furthermore, the C $\epsilon$ 3 domain itself has a high level of intrinsic flexibility [78], which is believed to play a

role in the mutual allosteric inhibition of receptors [18] and the allosteric inhibition of derCD23 binding by  $\alpha\epsilon$ Fab1 (Section 3.2.5).

IgE-Fc's unusually high degree of conformational flexibility results in a complex energy landscape [81], which we suggest is reflected in the binding kinetics of the sFc $\epsilon$ RI $\alpha$ /IgE-Fc interaction. sFc $\epsilon$ RI $\alpha$  binds IgE-Fc with a 1:1 stoichiometry but data from SPR, stopped-flow intrinsic fluorescence studies and stopped-flow FRET are best described by triphasic models. The sFc $\epsilon$ RI $\alpha$ /IgE-Fc interaction is described in the literature as having sub-nanomolar affinity but the data presented here suggest that only around 30 % of the complexes exist in this strongly-bound state, and that the conformational heterogeneity of IgE-Fc results in the formation weakly-bound complexes. Consequently, the results suggest that at any one time in the human body, only 30 % of circulating IgE binds Fc $\epsilon$ RI on the surface of mast cells and basophils with the characteristic sub-nanomolar affinity. Defining healthy persons as having serum IgE at a concentration of 0.8 nM [198], if 100 % of serum IgE bound to Fc $\epsilon$ RI on the surface of effector cells with 100 pM affinity, the fractional saturation of Fc $\epsilon$ RI would be 89 %, as opposed to 70 % if only 30 % of the serum IgE bound with this affinity (assuming Fc $\epsilon$ RI concentrations are not mass limiting). Defining atopic persons as having serum IgE at a concentration of 2.5 nM [199], if 100 % of IgE bound to Fc $\epsilon$ RI on the surface of effector cells with 100 pM affinity, the occupancy of Fc $\epsilon$ RI would be 96 %, as opposed to 88 % if only 30 % of serum IgE bound with this affinity (assuming Fc $\epsilon$ RI concentrations are not mass limiting).

The kinetics for the interactions between IgE-Fc and  $\alpha\epsilon$ Fab12 and IgE-Fc and  $\alpha\epsilon$ Fab13, as determined by SPR, were also well described by a triphasic model. Both  $\alpha\epsilon$ Fab12 and  $\alpha\epsilon$ Fab13 bind IgE-Fc with 2:1 stoichiometries and we therefore propose that the observed multiphasic binding kinetics could be the result of IgE-Fc heterogeneity: in IgE-Fc's complex conformational landscape there are states that can bind  $\alpha\epsilon$ Fab12 (or  $\alpha\epsilon$ Fab13) weakly, and states that can bind  $\alpha\epsilon$ Fab12 (or  $\alpha\epsilon$ Fab13) strongly. Stopped-flow experiments, like those performed for the sFc $\epsilon$ RI $\alpha$ /IgE-Fc interaction, could establish whether multiphasic kinetics of the  $\alpha\epsilon$ Fab12/IgE-Fc and  $\alpha\epsilon$ Fab13/IgE-Fc interactions occur without potential artifacts of solid phase immobilisation.



# Chapter 7

## Modulation of the IgE/CD23 interaction by anti-IgE Fabs

### 7.1 Introduction

CD23 is expressed on the surface of B cells, various inflammatory cells and epithelial cells [16]. It is expressed as a trimer: three lectin domain heads are tethered to the cell surface by an  $\alpha$ -helical coiled-coil stalk (Figure 7.1.a) [17]. The stalk is susceptible to proteolysis by various endogenous and exogenous proteases, which results in the release of different soluble CD23 (sCD23) fragments that have different activities dependent on their oligomeric state [4]. The protease der p1 is found in the feces of the house dust mite *Dermatophagoides pteronyssinus* and cleaves membrane CD23 (mCD23) resulting in the release of monomeric sCD23 head domains (derCD23) (Figure 7.1) [20].

IgE-Fc binds sCD23 and mCD23 through interactions with the CD23 head domain. A single CD23 head domain binds a single C $\epsilon$ 3 domain of IgE-Fc and consequently a single molecule of IgE-Fc can bind two CD23 head domains [88] (Figure 7.1.b). Geometric and physical constraints mean that two CD23 heads from the same mCD23 molecule cannot bind the same IgE-Fc molecule, however one molecule of IgE could cross-link two molecules of mCD23, and one molecule of trimeric CD23 could bind two or even three molecules of IgE. The high avidity of the IgE/mCD23 interaction enhances the strength of the interaction and the binding of IgE to mCD23 has a  $K_D$  in the range of 1-10 nM [39].

Despite their symmetry, the affinities of the two different CD23 binding sites on

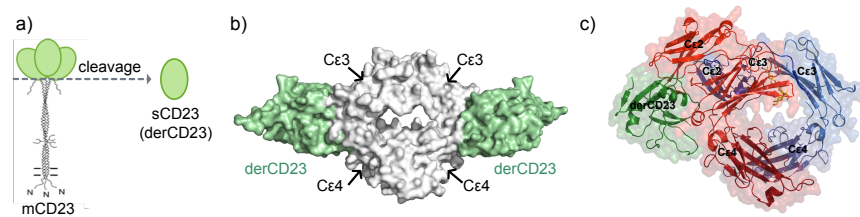


**Figure 7.1: Each C $\epsilon$ 3 domain of IgE-Fc can bind one CD23 head domain.** (a) A schematic representation of CD23. CD23 is expressed on the surface of various cells, including B cells, as a trimer (mCD23). Three soluble lectin head domains are tethered to the surface by an  $\alpha$ -helical coiled-coil stalk. Cleavage of the stalk by the der p1 protease results in the release of single soluble CD23 head domains called derCD23. (b) derCD23 (green) binds IgE-Fc(3-4) (white) with a 2:1 stoichiometry (PDB: 4EZM) [18]. (c) The crystal structure of IgE-Fc bound to a single molecule of derCD23 shows that IgE-Fc remains in an asymmetrically bent conformation when bound to derCD23 [95].

IgE-Fc are not equal: one has a  $K_D$  of around  $0.1 - 1 \mu\text{M}$  and the other has a  $K_D$  of around  $10 - 20 \mu\text{M}$  [88]. The variance is likely to be at least in part the result of IgE-Fc's conformational asymmetry [71, 72]. The structure of IgE-Fc bound to a single molecule of derCD23 has been solved and shows that IgE-Fc retains an asymmetrically bent conformation when bound to derCD23 (Figure 7.1.c) [18], which is also supported by intramolecular FRET data [75]. The derCD23 molecule is bound to the site closest to the C $\epsilon$ 2 domain pair and the C $\epsilon$ 3 domain to which it is bound is in the 'closed' conformation that is thought to be required for optimal CD23 binding [18]. The other CD23 binding site is unoccupied and this unbound C $\epsilon$ 3 domain is slightly more 'open'. One could suggest that the CD23 binding site furthest from the C $\epsilon$ 2 domains has the lower affinity, however this is speculation, and as of yet there is not enough evidence to convincingly assign the higher- and lower-affinity binding activities to particular CD23 binding sites of the structure.

The primary aim of this project is to generate  $\alpha$ Fabs that bind IgE-Fc and modulate the IgE-Fc/CD23 interaction allosterically. The binding of an allosteric modulator to one site of a macromolecule affects the functionality of another, often distal, site through changes in structure/dynamics. In the past a number of models have been employed to explain allosteric processes (Section 1.4). The ensemble view of allostery is comprehensive and been used to model a wide range observed allosteric phenomenon [111]. It is widely accepted that a protein exists as fluctua-

tion of structures around an average conformation, and that the different states of a protein exist in a conformational equilibrium [119, 120, 121]. The ensemble view of allostery suggests that the binding of an allosteric modulator causes a shift in the conformational ensemble of a protein that results in a change in the functionality of that protein (Section 1.4) [129]. An allosteric modulator that binds IgE-Fc may cause a shift in the conformational ensemble of IgE such that binding between CD23 is inhibited or enhanced.

Both orthosteric and allosteric modulators can mediate their effects on interactions in a number of ways (Figure 7.2). Enhancers shift the conformational equilibrium of the protein to which it binds towards the increased population of states that bind ligand with higher affinity. Allosteric inhibitors can either shift the conformational equilibrium of the protein to which it binds towards an the increased population of states that cannot bind ligand (Figure 7.2.a), or towards states that have a reduced affinity for ligand (Figure 7.2.b). Orthosteric inhibitors could inhibit interactions by binding at, or partially to, the ligand binding site, thereby spatially occluding simultaneous binding (Figure 7.2.c), or by binding close to the ligand binding site in such a way that results in non-optimal ligand binding (Figure 7.2.d).

Fc $\epsilon$ RI and Xolair<sup>®</sup> (Novartis) are known inhibitors of the IgE/CD23 interaction (Figure 7.3). Fc $\epsilon$ RI allosterically inhibits CD23, partly by stabilising a conformation of IgE-Fc with ‘open’ C $\epsilon$ 3 domains, which CD23 cannot bind [18]. Conversely, Xolair is an orthosteric inhibitor of the IgE/CD23 interaction: crystal structures of Xolair Fab and Xolair Fab mutant 3 bound to IgE-Fc show that CD23 and Xolair binding sites overlap (Figure 7.3). In Chapter 3 we demonstrated that a $\epsilon$ Fab1 also inhibits the binding of CD23 to IgE-Fc and suggested that it does so allosterically, by holding IgE-Fc in an ‘open’ conformation and by shifting key residues within the C $\epsilon$ 3 domains. There are, however, no reports of proteins that bind to IgE-Fc and enhance the interaction between IgE-Fc and CD23.

Previous chapters have described how five a $\epsilon$ Fabs, with seemingly different effects on IgE/receptor binding, were discovered, selected and purified. Unlike the other known IgE/CD23 modulators, which bind the C $\epsilon$ 3 domain of IgE-Fc, these a $\epsilon$ Fabs primarily bind the C $\epsilon$ 2 domains. In this chapter we show that the a $\epsilon$ Fabs

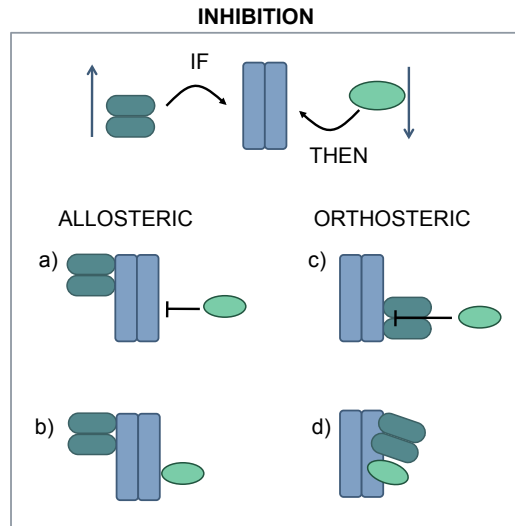


Figure 7.2: **A schematic representation of the different types of IgE/CD23 inhibition that are theoretically possible by  $\alpha\epsilon$ Fabs.** If increasing concentrations of  $\alpha\epsilon$ Fab cause a decrease in CD23 binding the  $\alpha\epsilon$ Fab is an inhibitor. Inhibition can be allosteric or orthosteric. An allosteric inhibitor could bind at a site distal to the CD23 binding site and inhibit the interaction by shifting IgE-Fc's conformational ensemble such that CD23-binding is less favourable. An allosteric inhibitor could shift the conformational ensemble of IgE such that states that can bind IgE-Fc are less populated (a) Alternatively, an allosteric inhibitor could cause a shift that stabilises transiently populated conformations that bind CD23 with a lower affinity (b). Orthosteric inhibitors could bind IgE at, or close to, the CD23 binding sites and prevent CD23 binding (c), or they may bind close to the CD23 binding site resulting in non-optimal binding of CD23 to its binding site and thereby reduce the affinity of the interaction (d).

have different enhancing and inhibitory effects on the interaction between IgE and CD23, and provide evidence that suggests they elicit some of these effects through allosteric mechanisms.

Using concentration-dependent binding assays, we show how each of the  $\alpha\epsilon$ Fabs affects the binding of IgE to mCD23 on the surface of B cells under equilibrium conditions. We then describe how we used SPR to investigate how the different  $\alpha\epsilon$ Fab:IgE-Fc complexes bind derCD23 compared to a control for unmodulated IgE-Fc/derCD23 binding. We determined the  $K_D$ , an indicator of the apparent affinity of an interaction, and the  $B_{max}$ , an indicator of the binding capacity, for the interactions between each of the five  $\alpha\epsilon$ Fab:IgE-Fc complexes and derCD23, and used these values to understand how the different  $\alpha\epsilon$ Fabs elicit their effects on the IgE-Fc/CD23 interaction (Section 2.6.5).

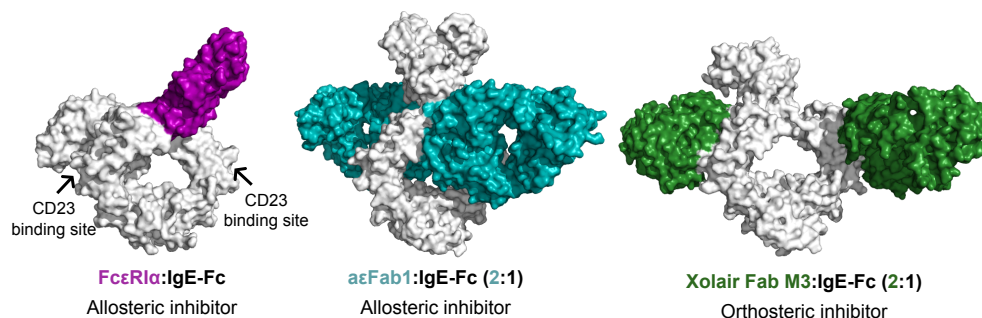


Figure 7.3: **FcεRI**, **αεFab1** and **Xolair<sup>®</sup>** bind **IgE-Fc** and inhibit the **IgE-Fc/CD23** interaction. The crystal structures of sFcεRIα:IgE-Fc [72], αεFab1:IgE-Fc (2:1) [81] and Xolair Fab mutant 3: IgE-Fc (2:1) [82]. IgE-Fc is shown as a white surface representation, and the CD23 inhibitors are shown as coloured surface representations.

## 7.2 Results

### 7.2.1 Modulation of the IgE/CD23 interaction on the surface of cells by αεFabs

Flow cytometry was used to measure the binding of a fluorescently-labeled IgE molecule (rIgE-A647) to CD23 expressed on the surface of RPMI 8866 cells in the presence of increasing concentrations of each of the αεFabs. The RPMI 8866 cell-line is a human B lymphocyte cell-line that expresses CD23 on its surface [161]. rIgE is a patient-derived full-length IgE antibody specific for the grass-pollen allergen Phl p7 [173]. For the purposes of this experiment rIgE was labeled with the Alexa Fluor 647 (A647) fluorophore (Thermo Fisher Scientific) using amine-coupling according to manufacturers instructions.

#### Experimental design

Preliminary experiments were performed to establish an appropriate working concentration of rIgE-A647. RPMI 8866 cells ( $1 \times 10^5$  cells per test) were incubated for one hour on ice with a titration of rIgE-A647 concentrations. The cell suspensions were subsequently washed to remove unbound rIgE-A647 and the fluorescence intensity of at least  $5 \times 10^3$  single live cells per test was measured using flow cytometry (Figure 7.4.a).

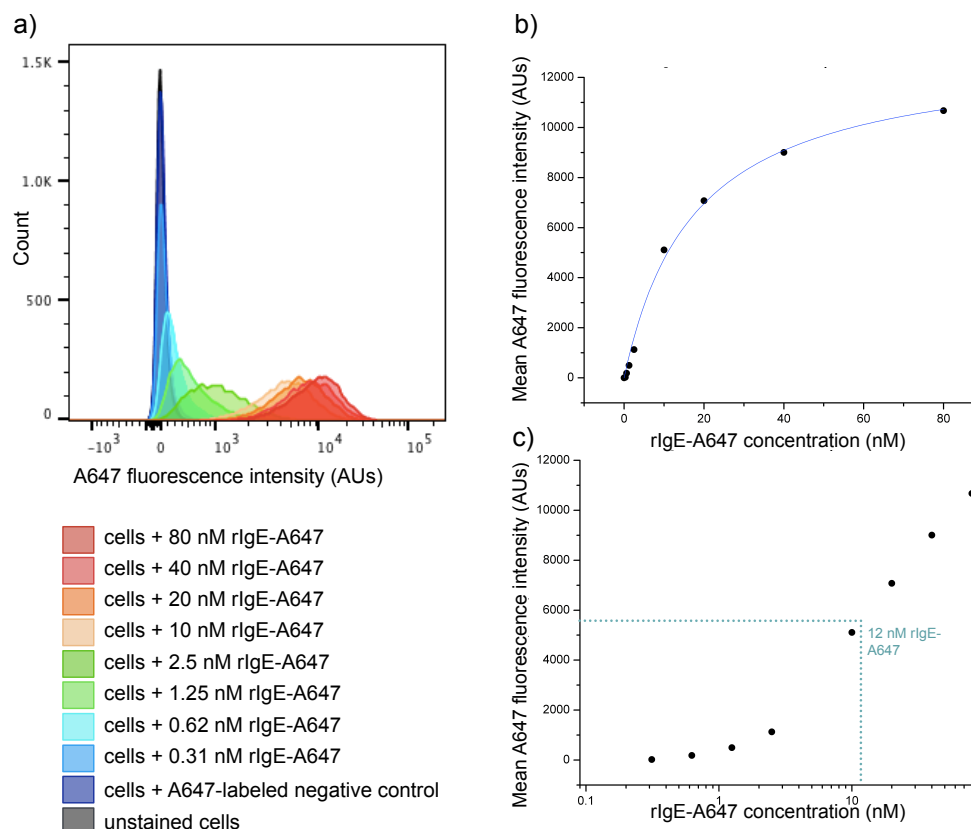


**Figure 7.4: rIgE-A647 binds to mCD23 with nanomolar binding affinity.** Preliminary experiments were performed to determine the appropriate working concentration of a fluorescently-labeled (A647) full length IgE (rIgE) for the concentration-dependent  $\alpha$ Fab studies. RPMI 8866 cells expressing mCD23 were incubated at 4 °C for one hour with varying concentrations of rIgE-A647. The cells were washed twice with wash buffer (Section 2.7.2) and the A647 fluorescence of single live cells was read using flow cytometry (a). The mean A647 fluorescence intensity (MFI) of each test sample was plotted as a function of rIgE-A647 concentration, and the data were fit using a one-to-one model (Section 2.6.4) (b). The  $K_D$  was estimated to be about 18 nM. At 12 nM rIgE-A647 the binding was in the linear range of the dose-response curve (c).

The mean A647 fluorescence intensity A647-MFI per cell was used as a measure of binding of rIgE-A647 to membrane CD23 (mCD23): higher A647-MFI values indicated a greater level of binding. The A647-MFI of a single cell suspension incubated with an A647-labeled antibody lacking specific CD23-binding activity was used to determine the non-specific background A647 fluorescence level. The A647-MFI values were plotted as a function of rIgE-A647 concentration to establish a saturation curve for the binding of rIgE-A647 to mCD23 (Figure 7.4.b). The data were fit to a one-to-one binding model (Section 2.6.4) and the  $K_D$  of the interaction

was approximated as 18 nM. 12 nM rIgE-A647 was chosen as a suitable working concentration of rIgE-A647 as it is close to the determined  $K_D$  of the interaction and the A647-MFI of RPMI 8866 cells incubated with rIgE-A647 at this concentration was in the linear range of the dose-response (Figure 7.4.b). Positive and negative modulation would therefore be observable under these conditions.

IgE-Fc has two CD23 binding sites, one with a  $K_D$  around 1  $\mu\text{M}$  and the other with a  $K_D$  around 10-20  $\mu\text{M}$  [88] (Section 6.2.3). CD23 exists as a trimer on the surface of cells and through the avidity effect the IgE/mCD23 interaction can reach low nanomolar binding affinity. The concentration of mCD23 in each test was estimated to be <0.3 nM, and therefore 12 nM rIgE-A647 the only observable binding was the binding between one molecule of rIgE-Fc and two molecules of CD23 (Figure 7.5.a). Accordingly, any effect on the A647-MFI as a result of increasing aεFab concentration could be a consequence of an impact on one or both of the CD23 binding sites. For example, an orthosteric or allosteric inhibitor that eliminated only one of the two CD23 binding sites could still, in theory, achieve 100 % inhibition of the rIgE-A647 binding signal at saturating concentrations, because at 12 nM rIgE-A647 will not show appreciable binding to a single CD23 molecule ( $K_D \sim 1 \mu\text{M}$ ).

The aεFabs were incubated with rIgE-A647 and RPMI 8866 cells on ice for one hour at final concentrations of 0 – 80 nM, using a two fold-dilution series (Section 2.7.2). Given the  $K_D$  values of the two different aεFab binding sites (high picomolar and low nanomolar) and the working concentration of rIgE-A647 (12 nM), it was assumed that only the higher-affinity site reached saturation in these experiments and that the lower-affinity aεFab site remained mostly unoccupied. In the previous chapter the  $K_D$  values of the lower affinity aεFab sites were determined to range from 170 nM to 800 nM. The fractional saturation of an interaction can be estimated using Equation 7.1. The fractional saturation of the second aεFab binding sites were estimated to range from 9-32 % at 80 nM.

$$\text{fractional saturation} = \frac{[\text{ligand}]}{[\text{ligand}] + K_D} \quad (7.1)$$

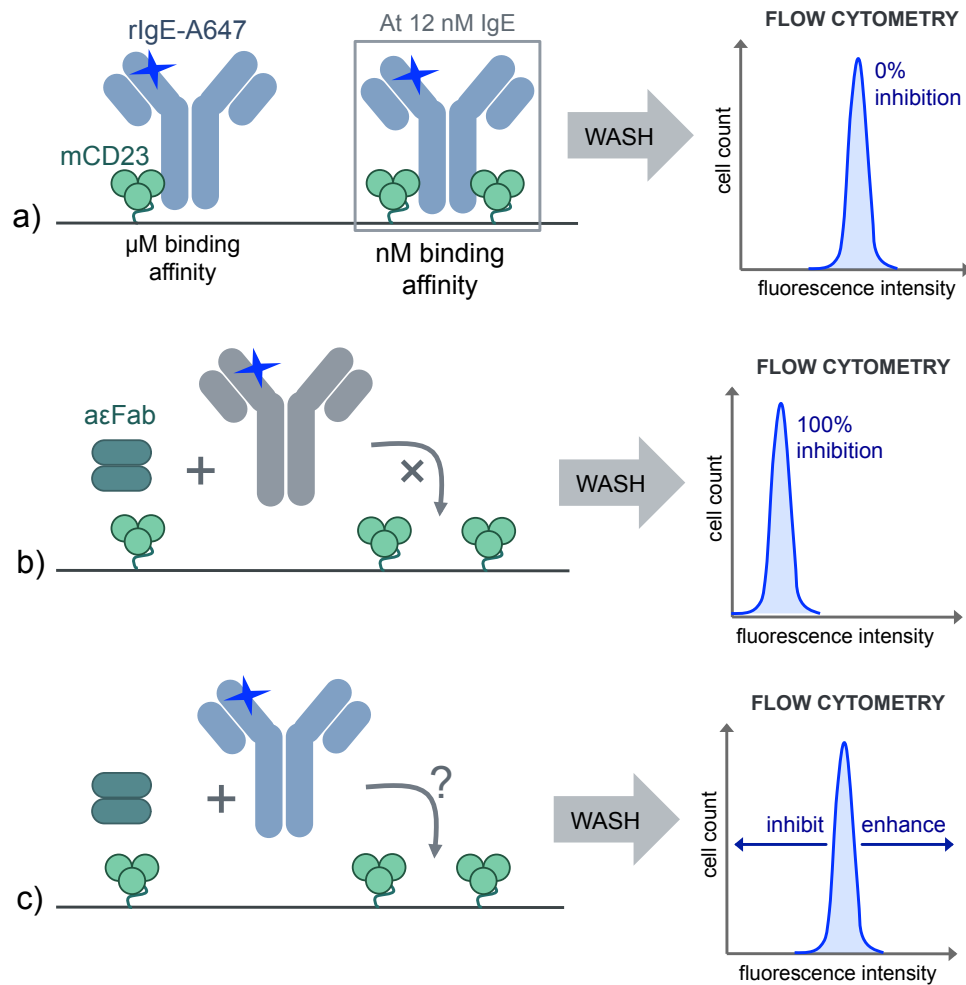


Figure 7.5: **Schematic representation of the rIgE-A647/mCD23 binding assays.** (a) A full-length IgE antibody (rIgE) was fluorescently-labeled with A647 (Thermo Fisher Scientific). rIgE-A647 was incubated with RPMI 8866 cells expressing mCD23 for one hour on ice. The cell suspensions were washed with wash buffer twice to remove unbound material. The A647 fluorescence of single live cells was measured using flow cytometry on a BD FACSCanto II (BD Biosciences). Binding of one rIgE molecule to one mCD23 molecule has a micromolar binding affinity, whereas the binding of one rIgE molecule to two mCD23 molecules has a nanomolar binding affinity. Accordingly, only the binding of one rIgE-A647 molecule to two mCD23 molecules occurs at 12 nM rIgE-A647. The A647 fluorescence intensity observed for this interaction was defined as 0 % inhibition. (b) The A647 fluorescence intensities of single RPMI 8866 cells incubated with an A647-labeled negative control and 80 nM of the different aεFabs, and was used to define 100 % inhibition. (c) The different aεFabs were incubated with rIgE-A647 and RPMI 8866 cells at various concentrations (80 - 0 nM) and their effect on the A647 fluorescence intensity of single live cells was measured using flow cytometry.

The experiments were performed to identify both positive and negative effects of the aεFabs on the IgE/CD23 interaction. Despite this, experimental results are



expressed in terms of percentage inhibition. 0 % inhibition, or more accurately 0 % modulation of the rIgE-A647/mCD23 interaction was established as the A647-MFI when the aεFab concentration was 0 nM (Figure 7.5.a). 100 % inhibition was defined as the A647-MFI when 80 nM of aεFab was incubated with RPMI 8866 cells in the absence of rIgE-A647, but in the presence of an A647-labeled antibody with no specific CD23-binding activity (Figure 7.5.b). An inhibiting effect is presented as a reduction in A647-MFI, and the difference in this MFI from the A647-MFI at 0 % is expressed a percentage of the difference between MFIs defined as 0 and 100 % inhibition. No enhancing effects were observed, but an enhancing effect would have manifested itself as an A647-MFI value greater than that observed for the 0 % data points.

### **Control experiments**

Two controls were performed for each experiment. The first control was performed to check that RPMI 8866 mCD23 expression levels were similar for each biological replicate. MHM6-FITC (Dako) is a fluorescently-labeled (FITC) antibody that binds specifically to CD23. MHM6-FITC was incubated on ice for one hour with RPMI 8866 cells, the cells were subsequently washed and the FITC fluorescence of single live cells was measured using flow cytometry. The MFI for background FITC fluorescence was determined by incubating RPMI 8866 cells with a FITC-labeled antibody lacking specific CD23-binding activity (Figure 7.6).

A positive control was also performed, in which Xolair Fab mutant 3 was incubated with rIgE-A647 and RPMI 8866 cells at the same concentrations as the aεFabs. Xolair Fab mutant 3 binds to IgE with nanomolar binding affinity and orthosterically inhibits the IgE/CD23 interaction [82]. The plot of A647-fluorescence inhibition as a function of Xolair Fab mutant 3 concentration showed a dose-dependent inhibition of the IgE/mCD23 interaction. The data were fit in Origin (OriginLab) to a dose-response sigmoidal equation and indicated that at saturating conditions Xolair Fab mutant 3 completely inhibited the IgE/mCD23 interaction (Figure 7.7). Although Xolair Fab mutant 3, a known orthosteric inhibitor of the IgE/CD23 interaction, achieved 100 % inhibition at saturating concentrations, there are circumstances in which inhibitors that elicit their effect by completely

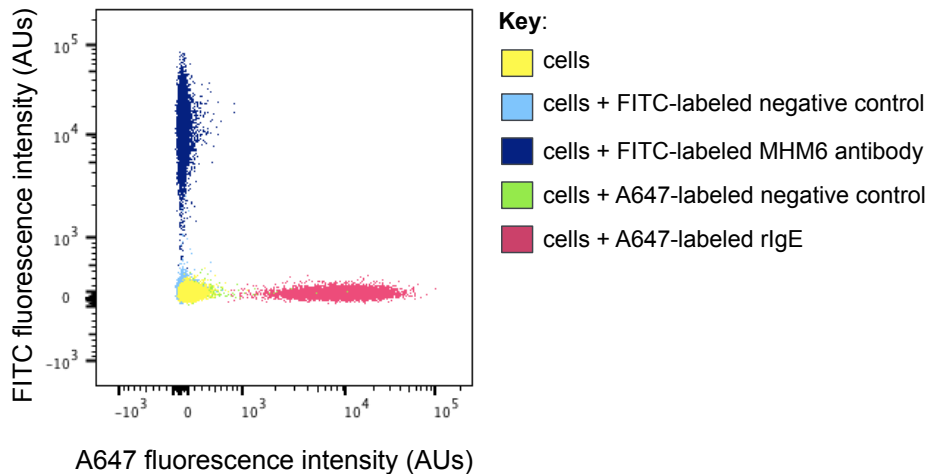


Figure 7.6: **The FITC-labeled MHM6-monoclonal antibody (Dako) indicated the levels of mCD23 expression on RPMI 8866 cells.** RPMI 8866 cells incubated with only buffer did not show fluorescence in the A647 or FITC channels. RPMI 8866 cells incubated with FITC-MHM6, an anti-CD23 antibody, showed fluorescence in the FITC channel, indicating the binding of the antibody to the surface of the cells. RPMI 8866 cells incubated with a FITC-labeled antibody lacking specific CD23 binding activity did not give fluorescence in the FITC channel, indicating that FITC-MHM6 bound to mCD23 on the cell surface specifically, and the FITC fluorescence intensity therefore gave an indication of the level of CD23 expression on the surface of the RPMI 8866 cells.

eliminating a binding site may not achieve 100 % inhibition at saturating conditions. For example, if a molecule exists in a range of conformations, some of which cannot bind inhibitor, the inhibitor cannot ever bind 100 % of the molecules and therefore cannot achieve 100 % inhibition.

### Concentration-dependent effects of the different $\alpha$ Fabs

Each  $\alpha$ Fab titration experiment was performed on three separate days. Saturation of the first  $\alpha$ Fab3 and  $\alpha$ Fab18 binding sites did not have any concentration-dependent inhibitory effects on the A647-MFI, suggesting that the binding of these  $\alpha$ Fabs to IgE had no effect on the amount of rIgE-A647/mCD23 binding at equilibrium (Figure 7.8.a). This experiment, however, could not differentiate between whether the binding of  $\alpha$ Fab3 (or  $\alpha$ Fab18) to IgE had no effect on either CD23 binding site or if, for example, one binding site was enhanced and one was inhibited. Repeated experiments were performed for the highest and lowest concentrations of  $\alpha$ Fab3 and the Wilcoxon Sum Rank tests 2.8.2 [166] indicated there was no sig-

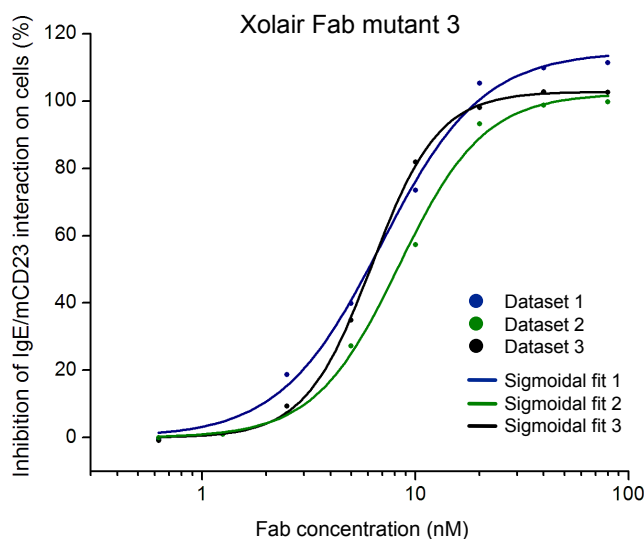


Figure 7.7: **Xolair Fab mutant 3, a Fab that binds to IgE and orthosterically inhibits CD23 binding, showed concentration-dependent inhibition of the rIgE-A647/CD23 interaction on the surface of RPMI 8866 cells.** RPMI cells, expressing mCD23, were incubated on ice for one hour with 12 nM rIgE-A647 and with increasing concentrations of Xolair Fab mutant 3. The cells were washed twice with buffer and the fluorescence of single live cells was read by flow cytometry. Reduction in MFI of the single cell suspensions was assumed to result from inhibition of the rIgE-A647/mCD23 interaction. 0 % inhibition was defined as the MFI in the absence of Xolair Fab mutant 3. 100 % inhibition was defined as the MFI in the absence of rIgE-A647, but in the presence of 80 nM Xolair Fab mutant 3 and an A647-labeled antibody with no specific CD23 binding activity.

nificant difference in the level of inhibition when 0.125 nM and 80 nM  $\alpha$ Fab3 were added to the incubations (Figure 7.8.b).

The results of the titration experiments showed that  $\alpha$ Fab2,  $\alpha$ Fab12 and  $\alpha$ Fab13 had concentration-dependent inhibitory effects on the A647-MFI, suggesting that they inhibited the interaction between IgE-A647 and mCD23 at equilibrium. Although  $\alpha$ Fab12 inhibited IgE/mCD23 binding in these cell-based assays, in Chapter 5 we observed that  $\alpha$ Fab12 appeared to enhance the affinity of the interaction between IgE-Fc and the high-affinity CD23 binding site in SPR experiments (Section 5.2.2). This apparent contrast in results will be discussed in greater depth later in the chapter. Plots of percentage inhibition of the IgE/mCD23 interaction versus  $\alpha$ Fab concentration were fit to a sigmoidal model in Origin (OriginLab) and suggested that the  $\alpha$ Fabs could achieve maximal inhibition of between 30-50 % (Figure 7.9, Table 7.1 and Appendix A.10). Repeated experiments were performed

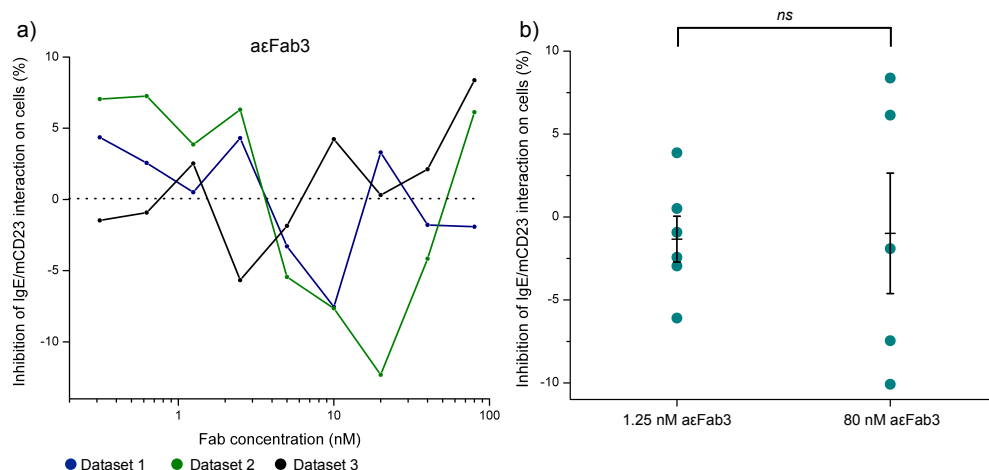


Figure 7.8: **aεFab3** showed no dose-dependent inhibition of the **rIgE-A647/CD23** interaction on the surface of **RPMI 8866** cells. RPMI 8866 cells expressing mCD23 were incubated for one hour on ice with rIgE-A647 at a final concentration of 12 nM and increasing concentrations of aεFab3. The cells were washed twice with buffer and then the A647 fluorescence of single live cells was measured using flow cytometry. (a) The A647-MFI was compared to the MFI of RPMI 8866 cells incubated with 12 nM rIgE-A647 in the absence of any aεFab (0 % inhibition) and the MFI of RPMI 8866 cells incubated in the presence of 80 nM aεFab3 in the presence of an A647-labeled antibody with no CD23-specific binding activity (100 % inhibition). The difference in the MFI in relation to these two MFI values indicated the percentage of rIgE-A647/mCD23 perturbation. (b) Five different measurements were taken of the RPMI 8866 cells incubated with 12 nM rIgE-Fc and aεFab3 at either 1.25 nM and or 80 nM. Wilcoxon sum rank tests [166] indicated there is no significant difference between the mean average level of inhibition of the two populations. The bars represent the means and the standard error of the means.

for the highest and lowest concentrations of aεFab2 and aεFab13, and the Wilcoxon sum rank tests [166] indicated the level of inhibition of the IgE/mCD23 achieved upon the addition of 80 nM aεFab was statistically significant (Figure 7.10).

As briefly discussed, there are certain conditions in which inhibitors that eliminate binding sites cannot achieve 100 % inhibition. IgE-Fc exists as a complex conformational ensemble and it is conceivable that each of the aεFabs can only bind a percentage of the available IgE-Fc and therefore cannot achieve 100 % inhibition at saturating conditions. Moreover, the binding of an allosteric inhibitor to IgE may result in a shift in IgE's conformational ensemble towards, but not completely to, conformations of IgE that cannot bind CD23. Alternatively, fractional maximal inhibition could occur through negative cooperativity (Section 1.4): if the

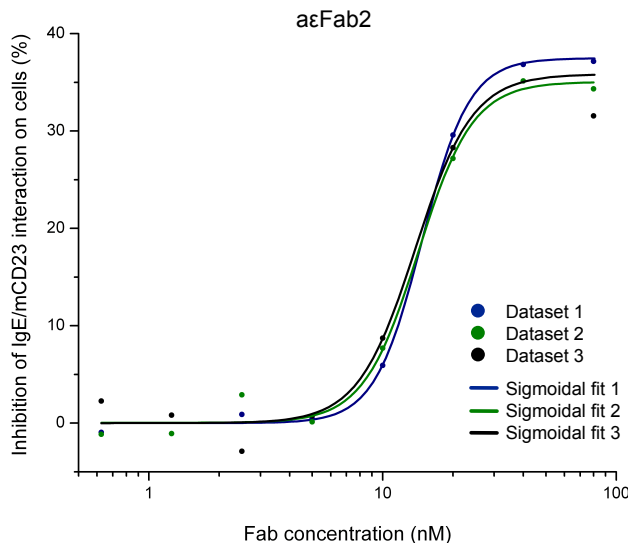


Figure 7.9: **aεFab2** showed concentration-dependent inhibition of the **rIgE-A647/CD23** interaction on the surface of RPMI 8866 cells. RPMI cells, expressing mCD23, were incubated on ice for one hour with 12 nM rIgE-A647 and increasing concentrations of aεFab2. The cells were washed twice with buffer and the fluorescence of single live cells was read by flow cytometry. Reduction in MFI of the single cell suspensions was assumed to result from inhibition of the rIgE-A647/mCD23 interaction. 0 % inhibition was defined as the MFI in the absence of Xolair Fab mutant 3. 100 % inhibition was defined as the MFI in the absence of rIgE-A647, but in the presence of 80 nM Xolair Fab mutant 3 and an A647-labeled antibody with no specific CD23 binding activity.

aεFab-bound IgE was still capable of binding CD23, but at a low affinity, such that the equilibrium levels of mCD23-engaged IgE were reduced. Such an effect can be mediated both allosterically and orthosterically (Figure 7.2. b and d).

In cases where both CD23 and aεFab can simultaneously bind IgE, CD23 may also affect the affinity of the aεFab:IgE interaction. In Chapter 5 we saw that derCD23 binding induced the accelerated dissociation of the aεFab13:IgE-Fc (1:1) complex (Section 5.2.2).

Based upon the estimated affinities of the two aεFab binding sites on IgE-Fc, the concentrations of aεFab used in these experiments were sufficient to saturate only the higher-affinity aεFab binding site. Since the observed inhibition of the IgE/mCD23 interaction by aεFab2, aεFab12 and aεFab13 reaches a maximum upon addition of  $\sim 30$  nM aεFab, it appears that occupation of only one aεFab binding site on IgE-Fc is necessary for the observed inhibition.

<b>Maximum inhibition of IgE/mCD23 interaction (%)</b>	
	<b>mean (<math>\pm</math> standard deviation)</b>
<b>aεFab2</b>	36 $\pm$ 1
<b>aεFab3</b>	-
<b>aεFab12</b>	33 $\pm$ 1
<b>aεFab13</b>	49 $\pm$ 1
<b>aεFab18</b>	-
<b>Xolair Fab mutant 3</b>	106 $\pm$ 6

Table 7.1: **Maximum inhibition of the IgE/CD23 interaction on the surface of RPMI 8866 cells under saturating conditions of different aεFabs.** RPMI cells, expressing mCD23, were incubated on ice for one hour with 12 nM rIgE-A647 and increasing concentrations of different aεFabs. The cells were washed twice with buffer and the fluorescence of single live cells was read by flow cytometry. Reduction in MFI of the single cell suspensions was assumed to result from inhibition of the rIgE-A647/mCD23 interaction. 0 % inhibition was defined as the MFI in the absence of Xolair Fab mutant 3. 100 % inhibition was defined as the MFI in the absence of rIgE-A647, but in the presence of 80 nM aεFab and an A647-labeled antibody with no specific CD23 binding activity. The percentage inhibition was plot as a function of the log of aεFab concentration and the data were fit to a sigmoidal binding model. The maximal inhibition was indicated by the upper plateau of each curve, when the lower plateau asymptoted to 0 % inhibition. The mean average of the maximum inhibition was determined from three biological repeats. aεFab3 and aεFab18 showed no concentration-dependent inhibition.

## 7.2.2 SPR investigations into the binding of derCD23 to different aεFab:IgE-Fc complexes

The cell-based binding assays described the effect of a single aεFab molecule on the binding of IgE to two molecules of CD23 under equilibrium conditions. These assays, however, could not resolve the observed effects in terms of the two different CD23 binding sites (Figure 7.11), nor could they be used to differentiate between inhibition as a result of change in the affinity of the interaction or inhibition as a result of elimination of binding sites (Figure 7.2). Understanding both of these details would help to uncover how the aεFabs elicit their modulating effects, and the latter may indicate whether any allosteric processes are involved.

Two sets of experiments were performed to ascertain the effect of binding of each of the aεFabs to IgE-Fc on the binding of derCD23 to IgE-Fc in terms of apparent

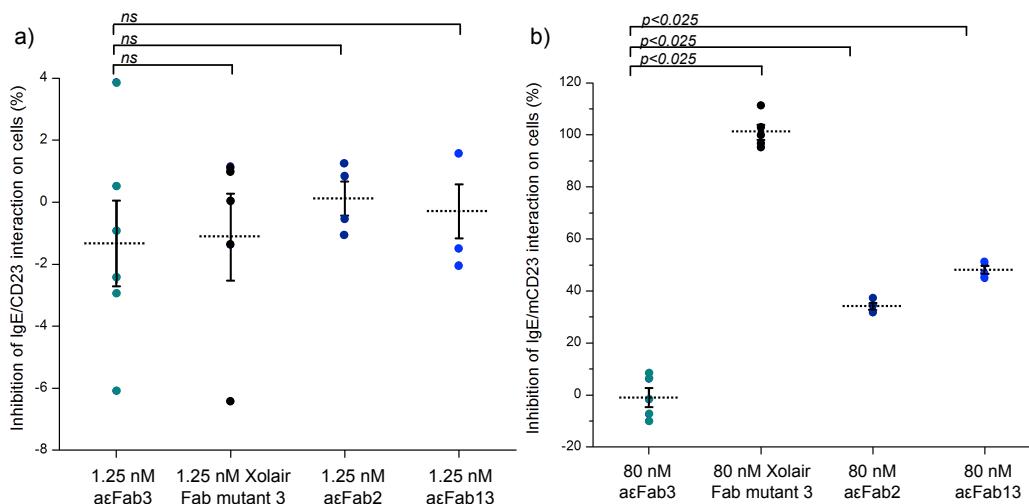


Figure 7.10: **The concentration-dependent inhibition of the rIgE-A647/CD23 interaction on the surface of RPMI 8866 cells by aεFab2 and aεFab13 is statistically significant.** Five different tests were performed to determine fluorescence of RPMI 8866 cells incubated with 12 nM rIgE-Fc and different aεFabs at either 1.25 nM and or 80 nM. (a) Wilcoxon ranked sum tests [166] indicated there is no significant difference between the mean average inhibition for cells incubated with 1.25 nM aεFab2, aεFab13 or Xolair Fab mutant 3, and 1.25 nM aεFab3, which is known to have no inhibiting effect. However, (b) Wilcoxon ranked sum tests [166] indicated the difference between the mean average inhibition for cells incubated with 80 nM aεFab2, aεFab13 or Xolair Fab mutant 3, and 80 nM aεFab3 is significant. The bars represent the means and the standard errors of the means.

affinity ( $K_D$ ) and occupancy ( $B_{max}$ ). The first set of experiments looked at the binding of a single molecule of derCD23 to an aεFab:IgE-Fc (1:1) complex, and the second looked at the binding of single molecule of derCD23 to an aεFab:IgE-Fc (2:1) complex. Both types of complex were captured on the surface of a SPR sensor chip via the interaction between aεFab and a Fab-specific goat-anti-rabbit F(ab')<sub>2</sub> (Jackson ImmunoResearch) (Figure 7.12.a and b). The goat-anti-rabbit surface was immobilised at a relatively low density ( $\sim 400$  RUs), using amine-coupling (Section 2.6.2), to ensure the aεFab/IgE-Fc interactions in the first set of experiments, and the IgE-Fc/derCD23 interactions in both sets of experiments, were monovalent. There were two main reasons for investigating the effect on the aεFabs on the higher ( $\sim 1 \mu\text{M}$ ) derCD23 binding activity rather than the the higher and the lower ( $\sim 10 \mu\text{M}$ ) derCD23 binding activities. Firstly, the difference in affinity between the two sites is relatively small and it could therefore be difficult to attribute the two sets

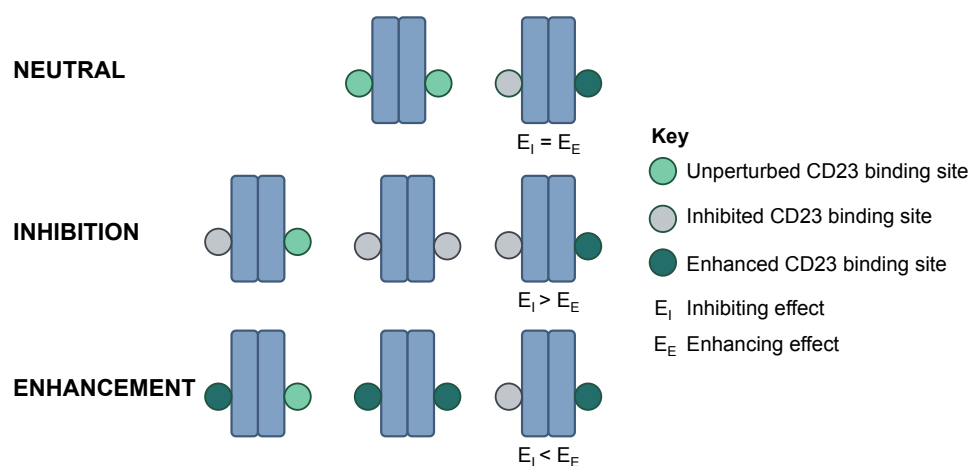


Figure 7.11: The equilibrium effect of the  $\alpha\epsilon$ Fabs on the interaction between 12 nM rIgE-A647 and CD23 on the surface of RPMI 8866 cells is a combination of the effects of each of the sites. In these assays an  $\alpha\epsilon$ Fab may have an inhibitory effect on the interaction, an enhancing effect of the interaction or no effect at all at equilibrium. However, the observed effects can be achieved in multiple ways by modulating the two CD23 binding sites differently.

of experimentally determined  $K_D$  and  $B_{max}$  values to the two different binding sites if the  $\alpha\epsilon$ Fabs alters these values. Secondly, determining the effect of the  $\alpha\epsilon$ Fabs on the  $K_D$  and  $B_{max}$  values of the 10  $\mu$ M binding site would require titrating derCD23 from high concentrations ( $\sim 100 \mu$ M), which would require significant quantities of derCD23.

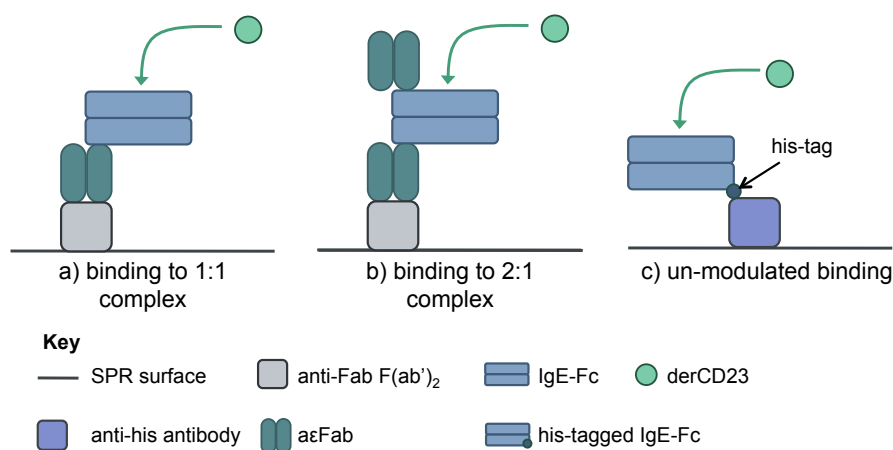


Figure 7.12: A schematic representation of the SPR experiments performed to assess the binding of derCD23 to the the higher-affinity binding site of different  $\alpha\epsilon$ Fab:IgE-Fc complexes.

A mock amine-coupled surface was used as a reference-subtraction surface in all SPR cycles. derCD23 was injected over the different  $\alpha\epsilon$ Fab:IgE-Fc complexes at



concentrations  $\leq 2 \mu\text{M}$ , at which only the higher-affinity derCD23 binding site is significantly occupied in an unmodulated IgE-Fc/derCD23 interaction. The SPR response during the steady-state of derCD23 binding to the different  $\alpha\epsilon\text{Fab}:\text{IgE-Fc}$  complexes was plot as a function of derCD23 concentration and fit using a one-to-one binding model (Section 2.6.4). The fits were used to determine the  $K_D$  and  $B_{\text{max}}$  values for the binding of a single molecule of derCD23 to an  $\alpha\epsilon\text{Fab}:\text{IgE-Fc}$  complex. These values were compared to the values derived for a control for the binding of derCD23 to IgE-Fc in the absence of  $\alpha\epsilon\text{Fab}$  (Figure 7.12.c).

Experiments similar to the first set of experiments were performed on the  $\alpha\epsilon\text{Fabs}$  in Chapter 5 except that the  $\alpha\epsilon\text{Fabs}$  had not been purified and they were performed in the absence of a control for unmodulated binding of a single molecule of derCD23 to IgE-Fc (Section 5.2.2). The production of anti-His-tagged IgE-Fc (Section 3.2.2) enabled these experiments to be performed alongside a control for an unmodulated derCD23/IgE-Fc interaction, and consequently the effects of the  $\alpha\epsilon\text{Fabs}$  could be defined as inhibitory or enhancing. An anti-histidine antibody (THE<sup>TM</sup> His tag mouse mAb, Genscript) was immobilised at a low density on an SPR surface using amine-coupling. His-tagged IgE-Fc was captured by the anti-His antibody and the same concentrations of derCD23 as injected over the  $\alpha\epsilon\text{Fab}:\text{IgE-Fc}$  surface were also injected over the anti-His:His-IgE-Fc complex as a control for unmodulated binding of derCD23 to IgE-Fc (Figure 7.12.c).

This experimental set-up can indicate different modes of modulation (inhibition versus enhancement) as well as different types of inhibition (Section 2.6.5) (Figure 7.2). If an  $\alpha\epsilon\text{Fab}$  sterically precludes the binding of derCD23 to its higher-affinity site (Figure 7.2.c) then there would be no increase in SPR response upon injection of derCD23, as derCD23 would be unable to bind to the  $\alpha\epsilon\text{Fab}:\text{IgE-Fc}$  complex. However, if the  $B_{\text{max}}$  of the derCD23/IgE-Fc interaction is reduced by the binding of an  $\alpha\epsilon\text{Fab}$  to IgE-Fc, it indicates that there are fewer derCD23 binding sites available as a result of allosteric modulation (Figure 7.2.a). Accordingly, these assays can differentiate between modulators that eliminate derCD23 binding sites allosterically and those that eliminate derCD23 binding sites orthosterically.

derCD23, however, may bind to an  $\alpha\epsilon\text{Fab}:\text{IgE-Fc}$  complex with the native capacity but with lower affinity (negative cooperativity (Section 1.4)). In which case,

the  $B_{\max}$  would be 100 % of the theoretical  $B_{\max}$  value, but the  $K_D$  of the interaction would be reduced. This assay is unable to distinguish whether an  $\alpha\epsilon$ Fab with this effect on derCD23 binding to IgE-Fc mediates the effect allosterically or orthosterically (Figure 7.2.b vs d).

### **derCD23 binding to $\alpha\epsilon$ Fab:IgE-Fc (1:1) complexes**

Firstly, to control for any nonspecific binding between the different  $\alpha\epsilon$ Fabs and derCD23, 100 nM of each of the purified  $\alpha\epsilon$ Fabs was injected for 180 s over the anti-rabbit-fab surface, followed by a 120 s injection of 2  $\mu$ M derCD23. There was no increase in SPR response upon injection of 2  $\mu$ M derCD23 over the different captured  $\alpha\epsilon$ Fabs (data not shown), indicating derCD23 does not bind appreciably to any of the  $\alpha\epsilon$ Fabs.

20 nM of each of the purified  $\alpha\epsilon$ Fabs were separately injected for 180 s over the anti-rabbit-Fab surface and 75 nM IgE-Fc was injected for 180 s over the captured  $\alpha\epsilon$ Fab resulting in the formation of captured  $\alpha\epsilon$ Fab:IgE-Fc (1:1) complexes. A two-fold dilution series of derCD23, starting at 2  $\mu$ M, was injected for 120 s over the  $\alpha\epsilon$ Fab:IgE-Fc (1:1) complex (Figure 7.13.a). The binding of derCD23 to each of the  $\alpha\epsilon$ Fab:IgE-Fc complexes reached steady-state during the time-course of each derCD23 injection (Figure 7.13.b and Appendix A.11). The  $K_D$  and  $B_{\max}$  values for the binding of a single molecule of derCD23 to His-tagged IgE-Fc were established by the binding of the same derCD23 titration to captured histidine-tagged IgE-Fc (Figure 7.14). The anti-rabbit-Fab surface was regenerated by two 60 s pulses of 10 mM glycine pH 1.7 and one 30 s pulse of 5 mM NaOH.

The  $B_{\max}$  of the control interaction was around 100 % of the theoretical  $B_{\max}$  for the binding of one molecule of derCD23 to IgE-Fc, indicating the experiment had been correctly set up to interrogate the binding of derCD23 to just one site on to IgE-Fc. The  $K_D$  of the interaction was  $\sim 0.7$   $\mu$ M.

Two of the  $\alpha\epsilon$ Fab:IgE-Fc (1:1) complexes,  $\alpha\epsilon$ Fab3:IgE-Fc (1:1) and  $\alpha\epsilon$ Fab13:IgE-Fc (1:1) also had  $B_{\max}$  values around 100 % of the theoretical  $B_{\max}$  value and had  $K_D$  values close to the control. This suggested that the binding of a single molecule of  $\alpha\epsilon$ Fab3, or a single molecule of  $\alpha\epsilon$ Fab13, to IgE-Fc did not affect the binding of derCD23 to the 1  $\mu$ M derCD23 binding site (Figure 7.15.a). The binding of

aεFab2, aεFab12 and aεFab18 to IgE-Fc, however, did modulate the binding of one molecule of derCD23 to IgE-Fc (Figure 7.15.a). aεFab2 appeared to inhibit the interaction (via negative cooperativity), aεFab12 appeared to enhance it (positive cooperativity), and aεFab18 appeared to have a mixed effect.

We plan to perform additional experimental repeats to verify the sometimes subtle effects of the various aεFabs that were observed. Experimental repeats are particularly important in assays where materials are highly variable, such as in cellular experiments. The number of variables that contribute to protein-only assays, like this, are comparatively very low. The variables in biophysical assays using purified proteins include protein concentration and the harder-to-quantitate protein quality. Variations in protein concentration, through errors in absorbance measurements or pipetting, for example, would affect the  $K_D$  and  $B_{max}$  values calculated from this set of experiments, and therefore statistical analysis of repeated measurements is necessary for a greater level of confidence in the results. Whilst the values themselves may be affected by concentration errors, the general trends in these observables, and the relation of the observables to the control, would not be effected by such variations since the injections were from the same closed vials of purified IgE-Fc and derCD23 for all SPR cycles. Indeed, we observe the same general trends in  $K_D$  and  $B_{max}$  in the same type of experiments performed in Chapter 5 with unpurified aεFabs.

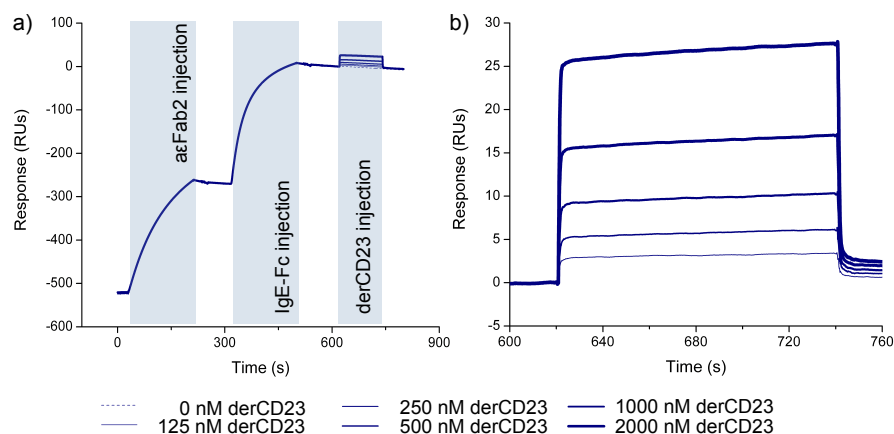


Figure 7.13: **Example sensorgrams from SPR experiments performed to investigate the binding of derCD23 to aεFab-bound IgE-Fc (1:1) complexes.** (a) Purified aεFab (aεFab2 here) was injected over a Fab-specific goat-anti-rabbit F(ab')<sub>2</sub> sensor surface. IgE-Fc bound the captured aεFab and derCD23 was injected over the aεFab2:IgE-Fc (1:1) complex. Binding was observed as an increase in SPR response. (b) The response when 0 nM derCD23 was injected over the aεFab2:IgE-Fc complex was subtracted from the response when derCD23 was injected over the complex at increasing concentrations. This subtraction eliminated changes in response that occurred as a result of dissociation of aεFab2:IgE-Fc from the anti-rabbit surface, as well as changes as a result of IgE-Fc dissociation from aεFab2.

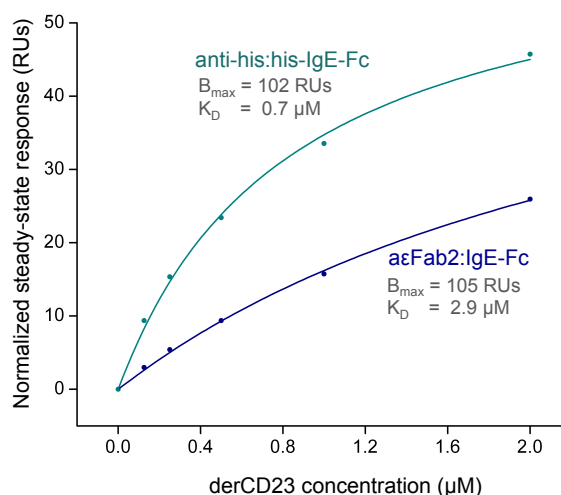


Figure 7.14: **Binding plots for the interaction between derCD23 and His-IgE-Fc (green) and derCD23 and the aεFab2:IgE-Fc (1:1) complex (blue).** The binding of derCD23 was measured as an increase in SPR response. The steady-state response values (circles) were determined from an average of 5 s of the steady-state response. The data were fit (lines) using a single binding site model. The steady-state response was normalized such that the maximum response for the binding of IgE-Fc to aεFab was 360 RUs. aεFab2-bound IgE-Fc shows a reduced affinity for the binding of derCD23 compared to His-IgE-Fc.

**derCD23 binding to  $\alpha$ Fab:IgE-Fc (2:1) complexes**

In order to investigate the binding of one molecule of derCD23 to IgE-Fc pre-complexed with two identical  $\alpha$ Fabs it was first necessary to generate the  $\alpha$ Fab:IgE-Fc (2:1) complexes. Protein G purified  $\alpha$ Fabs were incubated at 4°C overnight with IgE-Fc at a 2:1 molar ratio. An additional 10 % molar excess of each  $\alpha$ Fab was also added to ensure the full occupation of all  $\alpha$ Fab binding sites on the IgE-Fc molecules.

After incubation, each of the  $\alpha$ Fab:IgE-Fc (2:1) complex solutions were run down a Superdex 200 preparative SEC column (GE Healthcare) to purify the  $\alpha$ Fab:IgE-Fc (2:1) complex from potential contaminants such as unbound  $\alpha$ Fab, unbound IgE-Fc or 1:1 complexes. The  $\alpha$ Fab:IgE-Fc (2:1) complexes were eluted in 25 mM Tris-HCl, 125 mM NaCl pH 7.4, and appeared as the main peak in the chromatograms (data not shown). Aliquots of the main peak fractions were run down a G3000SWxl analytical HPLC SEC column (Tosoh) in 20 mM sodium phosphate, 50 mM sodium chloride buffer, pH 7.4 to determine their purity. HPLC analysis indicated that each of the  $\alpha$ Fab:IgE-Fc (2:1) complexes contained a very small percentage of contaminant in the form of un-complexed  $\alpha$ Fab (Figure 7.16 and Appendix A.12).

The purified  $\alpha$ Fab:IgE-Fc (2:1) complexes were injected for 180 s over the Fab-specific goat-anti-rabbit F(ab')<sub>2</sub> sensor chip surface at a concentration equating to 100 nM IgE-Fc, and increasing concentrations of derCD23 were injected for 120 s over the captured 2:1 complex (Figure 7.17 and Appendix A.13). Due to the intrinsic dissociation of the  $\alpha$ Fab:IgE-Fc (2:1) complexes, a small percentage of the derCD23 may actually have bound IgE-Fc that was bound to only a single molecule of  $\alpha$ Fab. The binding of derCD23 to each  $\alpha$ Fab:IgE-Fc (2:1) complex reached a steady-state during the time-course of each derCD23 injection (Figure 7.17.b). The  $K_D$  and  $B_{max}$  values for the unmodulated binding of one molecule of derCD23 to His-tagged IgE-Fc were established by injecting of the same derCD23 titration over captured histidine-tagged IgE-Fc (Figure 7.18).

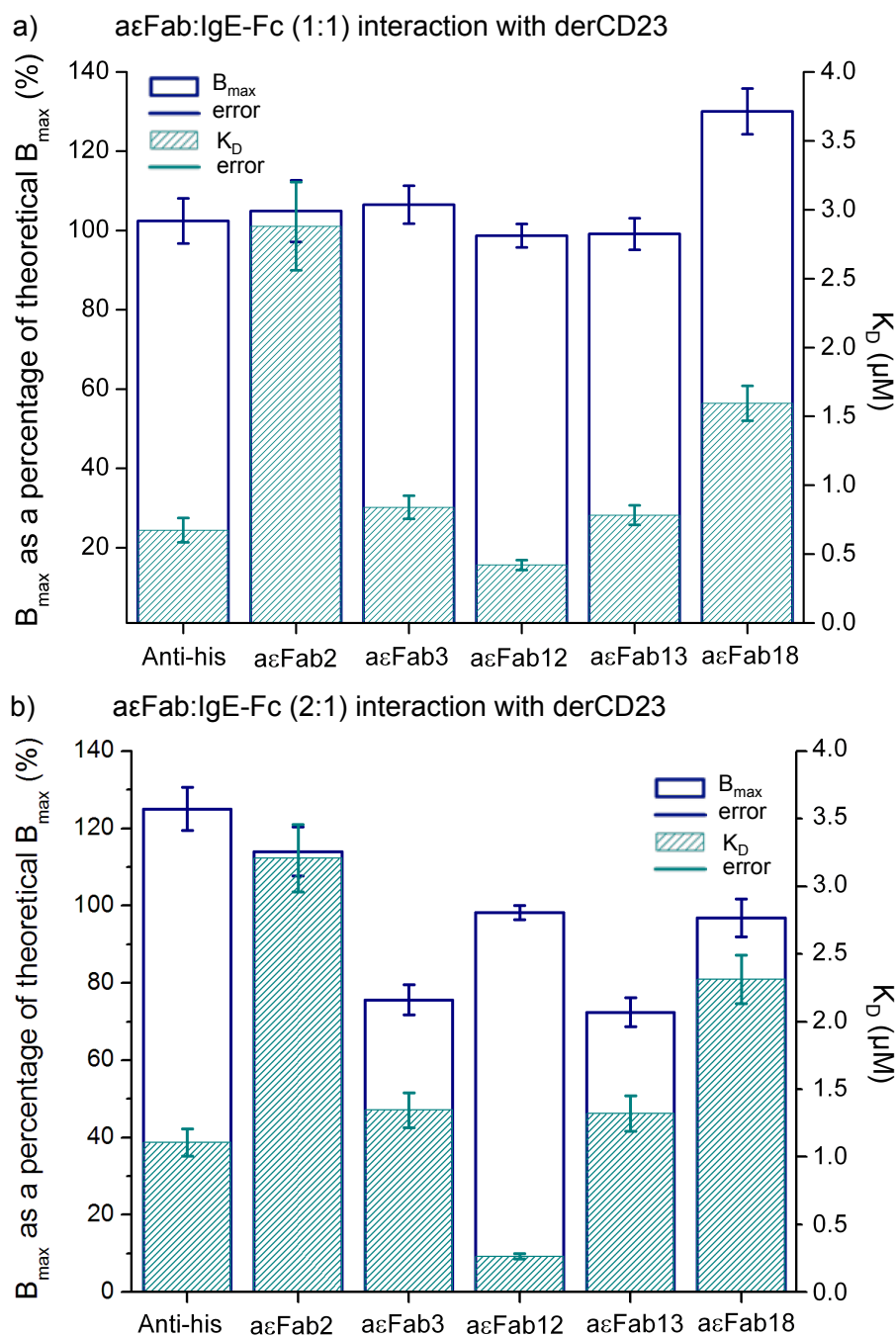


Figure 7.15: Histograms shown the dissociation constants ( $K_D$ ) and  $B_{\max}$  values for the binding of derCD23 to aεFab:IgE-Fc complexes as determined by SPR. The steady-state binding responses for the binding of 0-2  $\mu\text{M}$  of derCD23 to (a) captured aεFab:IgE-Fc (1:1) complexes and (b) captured aεFab:IgE-Fc (2:1) complexes, were plotted as a function of derCD23 concentration. The data were fit using a one-to-one binding model to determine the  $K_D$  and  $B_{\max}$  values. The  $B_{\max}$  values are expressed as a percentage of the theoretical  $B_{\max}$  values for the binding of one molecule of derCD23 to one molecule of IgE-Fc. The same experiments and analysis was performed the binding of derCD23 to captured-His-IgE-Fc as a control for unmodulated derCD23 binding to IgE-Fc. The error bars indicate the errors associated with the fit of the data.

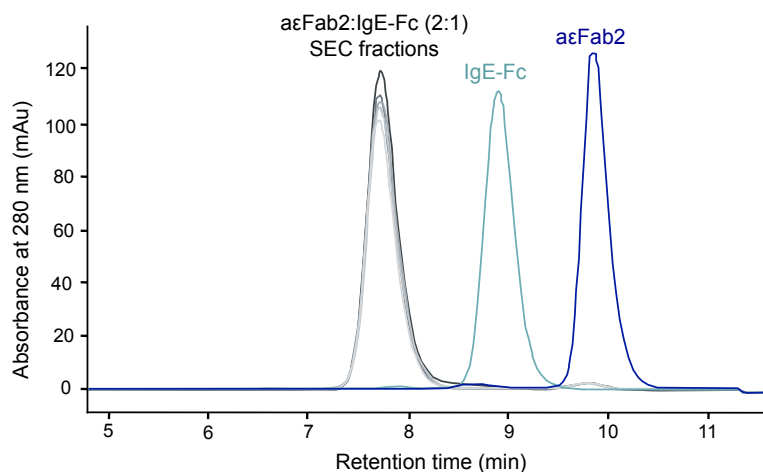


Figure 7.16: **Analytical HPLC SEC analysis of  $\alpha\epsilon$ Fab2:IgE-Fc (2:1) complex preparative SEC fractions.**  $\alpha\epsilon$ Fab2, IgE-Fc and peak fractions from SEC of the  $\alpha\epsilon$ Fab2:IgE-Fc (2:1) complex were run down a G3000SWxl analytical HPLC SEC column (Tosoh) in 20 mM sodium phosphate 50 mM sodium chloride buffer pH 7.4. The results suggest that the SEC fractions contain  $\alpha\epsilon$ Fab2:IgE-Fc (2:1) complex with a very small proportion of unbound  $\alpha\epsilon$ Fab2.

The experiments were performed with concentrations of derCD23 expected to result in significant occupation of the higher-affinity derCD23 site of the control His-tagged IgE-Fc only. However, the  $B_{\max}$  for the binding of derCD23 to His-tagged IgE-Fc was calculated to be around 125 % of the theoretical  $B_{\max}$  value, suggesting that under these experimental conditions the second derCD23 site was partially occupied. The  $K_D$  of the interaction was determined to be 1  $\mu$ M, which is the expected  $K_D$  for the binding of derCD23 to the higher-affinity site of IgE-Fc (Figure 7.15.b). It is immediately obvious from the binding curves (Figure 7.18) that none of the  $\alpha\epsilon$ Fab:IgE-Fc (2:1) complexes had the same binding profile as the control, indicating that in each case the binding of two  $\alpha\epsilon$ Fabs to IgE-Fc modulated the IgE-Fc/derCD23 interaction. As with the previous set of experiments that investigated the binding of derCD23 to 1:1  $\alpha\epsilon$ Fab:IgE-Fc complexes, we plan to perform additional experimental repeats to verify and statistically analyse the results.

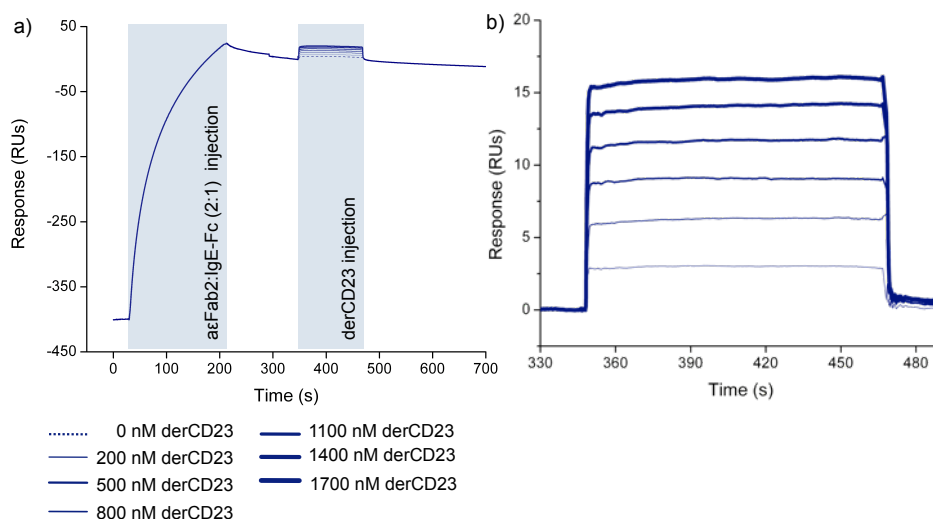


Figure 7.17: **Example sensorgrams from SPR experiments performed to investigate the binding of derCD23 to aεFab2:IgE-Fc (2:1) complexes (here the aεFab2:IgE-Fc (2:1) complex).** (a) The purified aεFab2:IgE-Fc (2:1) complex was captured on the surface of a sensor chip by a Fab-specific goat-anti-rabbit F(ab')<sub>2</sub>. derCD23 was injected over the complex and binding was observed as an increase in SPR response. (b) The response when 0 μM derCD23 was injected over the complex at increasing concentrations. This subtraction eliminated changes in response that occurred as a result of aεFab2:IgE-Fc (2:1) complex dissociation, and the dissociation of the complex from the surface.



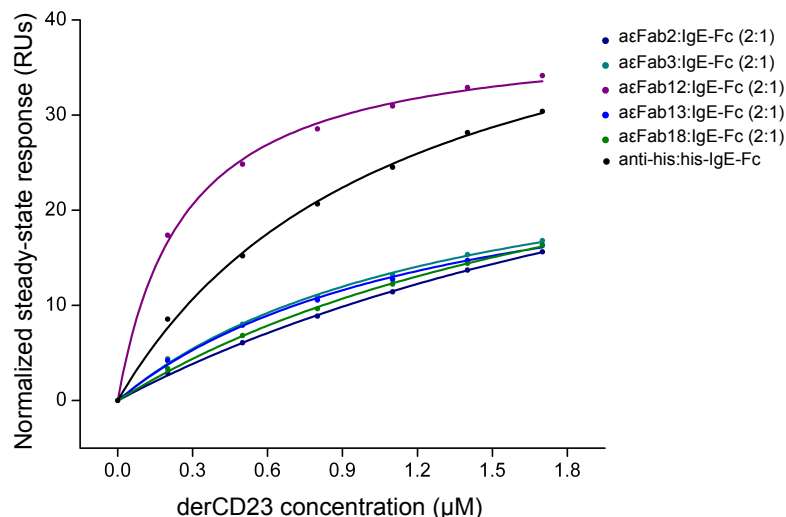


Figure 7.18: **Binding curves for the interactions between derCD23 and His-IgE-Fc and between derCD23 and  $\alpha\epsilon$ Fab:IgE-Fc (2:1) complexes.** The binding of derCD23 to either His-IgE-Fc captured on an anti-his tag antibody (Genscript) surface, or  $\alpha\epsilon$ Fab:IgE-Fc (2:1) captured on an a Fab-specific goat-anti-rabbit  $F(ab')_2$  (Jackson ImmunoResearch) surface, was measured as an increase in SPR response. The steady-state binding values (circles) were determined from an average of 5 s of response recorded during the steady-state binding of derCD23 to IgE-Fc. The data were fit (lines) using a single-site binding model. The steady-state response normalised so that the maximum binding of complex to the anti-Fab surface was equivalent of 400 RUs of IgE-Fc binding.

### 7.2.3 Models for how each $\alpha\epsilon$ Fab modulates the interaction between IgE and CD23

The results of the SPR experiments were examined in conjunction with the cell-based binding assays to build models for how each of the  $\alpha\epsilon$ Fabs modulate the interaction between IgE and CD23 (Figure 7.19). The cell-based assays investigated the effect that saturation of the first  $\alpha\epsilon$ Fab binding site had on the binding of IgE to membrane CD23 and was sensitive to effects on either CD23 binding sites. The SPR experiments, however, investigated how saturation of one or both  $\alpha\epsilon$ Fab binding sites affected the binding of derCD23 to the higher-affinity site of IgE-Fc only. Because one assay looked at the effect of the  $\alpha\epsilon$ Fabs on just one CD23 binding site and the other investigated the effects on either CD23 binding site, comparing the results allowed us to speculate how the second CD23 binding site was affected by the binding of each of the  $\alpha\epsilon$ Fabs. In some cases the results of the

two assays were in good agreement and the effect of  $\alpha\epsilon$ Fab binding on the IgE/CD23 interaction could be described by a simple model. In other cases the effect of an  $\alpha\epsilon$ Fab in the SPR experiments was not matched by the effect observed in the cell-binding experiments. In such cases it was necessary to invoke a more complicated mechanism to rationalise both results. In these latter cases, the models are more speculative, and it is possible that in fact the differences that were observed between the two results of the two assays are not simply a consequence of their differential sensitivities to effects of the two CD23 binding sites on IgE. These differences may also be the result of variations in the two assays such as the use of IgE versus IgE-Fc or mCD23 versus derCD23.

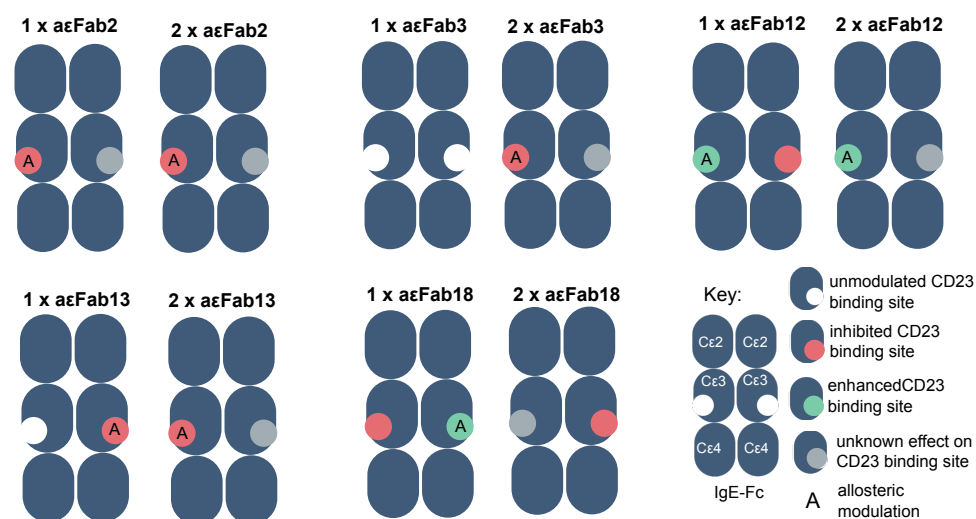


Figure 7.19: **Schematic representations of the proposed models for the affect of each  $\alpha\epsilon$ Fab on the IgE/CD23 interaction.** The left-hand side CD23 binding site represents the higher-affinity binding site, whereas the right-hand side CD23 binding site represents the lower-affinity binding site.

### The $\alpha\epsilon$ Fab2 model

The binding of 0 - 2  $\mu$ M derCD23 to  $\alpha\epsilon$ Fab2:IgE-Fc had an increased  $K_D$  compared to the control interaction, which did not increase further upon binding of a second  $\alpha\epsilon$ Fab2 molecule to IgE-Fc (Figure 7.15). It is possible that the higher-affinity CD23 site was blocked and the lower affinity activity that was observed was the result of derCD23 binding to an enhanced lower-affinity site (positive cooperativity with respect to the lower-affinity CD23 site). Two molecules of derCD23, however,

appeared able to bind to the  $\alpha\epsilon$ Fab2:IgE-Fc (2:1) complex, indicating that even when IgE-Fc is bound to two molecules of  $\alpha\epsilon$ Fab2, the two CD23 binding sites are both still available. We therefore attribute the increase in  $K_D$  to a reduction in the affinity of the higher-affinity site (negative cooperativity with respect to the higher-affinity CD23 site), rather than the abolition of the higher-affinity site and the enhancement of the lower-affinity site. The cell-based assay data also indicate that  $\alpha\epsilon$ Fab2 inhibits the interaction between IgE and CD23. The assay showed around a 30 % reduction in the binding of IgE to CD23 expressed on the surface of RPMI 8866 cells when incubated with  $\alpha\epsilon$ Fab2 under equilibrium conditions (Figures 7.9, 7.10 and Table 7.1), and this inhibition reached a maximum under conditions required to saturate the first  $\alpha\epsilon$ Fab2 binding site of IgE. It is therefore proposed that one molecule of  $\alpha\epsilon$ Fab2 inhibits the interaction between IgE-Fc and CD23 by reducing the affinity of the higher-affinity CD23 binding site. Evidence suggests that  $\alpha\epsilon$ Fab2 binds to the C $\epsilon$ 2 domains of IgE-Fc and that the  $\alpha\epsilon$ Fab2:IgE-Fc complex is extended (Section 6.2.5 and Section 6.2.4). Consequently we propose that  $\alpha\epsilon$ Fab2 acts as an allosteric inhibitor of the IgE/CD23 interaction, as  $\alpha\epsilon$ Fab2-bound to IgE-Fc would be unlikely to sterically interfere with the binding of CD23 (Figure 6.22).

### **The $\alpha\epsilon$ Fab3 model**

The binding of 0 - 2  $\mu$ M derCD23 to the  $\alpha\epsilon$ Fab3:IgE-Fc (1:1) complex had a binding profile comparable to the control interaction (Figure 7.15.a) indicating that the binding of the first  $\alpha\epsilon$ Fab3 molecule to IgE-Fc does not perturb the binding of derCD23 to the higher-affinity CD23 binding site on IgE-Fc. Similarly, saturation of the first  $\alpha\epsilon$ Fab3 binding site on IgE did not result in any change in the level of binding of IgE to CD23 on the surface of RPMI 8866 cells at equilibrium (Figure 7.8). The binding of 0 - 1.7  $\mu$ M derCD23 to the  $\alpha\epsilon$ Fab3:IgE-Fc (2:1) complex did, however, have a  $B_{\max}$  value around 75 % the value of the theoretical  $B_{\max}$  for the binding of one derCD23 molecule to IgE-Fc (Figure 7.15.a). The reduction in  $B_{\max}$  suggests that when IgE-Fc is bound to two molecules of  $\alpha\epsilon$ Fab3, the higher-affinity CD23 binding site is still available, but over the entire population the number of binding sites has been reduced. We therefore suggest that the binding of one

molecule of  $\alpha\epsilon$ Fab3 to IgE-Fc does not modulate the interaction between IgE and CD23, however the binding of a second  $\alpha\epsilon$ Fab3 molecule inhibits the binding of derCD23 to the higher-affinity binding site by shifting the conformational equilibrium of IgE-Fc such that states that cannot bind  $\alpha\epsilon$ Fab3 become more populated.

### **The $\alpha\epsilon$ Fab12 model**

The  $K_D$  for the binding of 0 - 2  $\mu$ M derCD23 to the  $\alpha\epsilon$ Fab12:IgE-Fc (1:1) complex was reduced compared to the control interaction, and it was further reduced by the binding of a second  $\alpha\epsilon$ Fab12 molecule to IgE-Fc (Figure 7.15). These results indicate positive cooperativity: that the binding of  $\alpha\epsilon$ Fab12 to IgE-Fc enhances the affinity of the higher-affinity derCD23 binding site. In the second set of SPR interactions, which investigated the effect of two molecules of  $\alpha\epsilon$ Fab on the binding of derCD23 to the higher-affinity binding site, the control interaction had a  $B_{\max}$  in excess of 100 % of the theoretical  $B_{\max}$  for the binding of a single derCD23 to IgE-Fc. This suggests that the concentrations of derCD23 that were used in these experiments was sufficient to give partial, but observable, binding to the lower-affinity binding site. Nevertheless, the  $B_{\max}$  of the interaction between derCD23 and the  $\alpha\epsilon$ Fab12:IgE-Fc (2:1) complex was around 100 % of the theoretical  $B_{\max}$  value, indicating that the binding of the second derCD23 site was inhibited by the presence of  $\alpha\epsilon$ Fab12 (Figure 7.15.b).

In the cell-based binding assays, increasing concentrations of  $\alpha\epsilon$ Fab12 resulted in about a 30 % reduction of binding between IgE and CD23 expressed on the surface of RPMI 8866 cells (Table 7.1), which may be attributed to the inhibition of the second CD23 binding site that was observed in the SPR experiments. It is proposed, therefore, that  $\alpha\epsilon$ Fab12 binds to IgE-Fc and acts as a positive allosteric modulator of the higher-affinity CD23 binding site, but that it inhibits the binding to the lower-affinity CD23 site. It is not possible to ascertain exactly how the second site is inhibited from this data: it could be allosterically or sterically inhibited.  $\alpha\epsilon$ Fab12 is thought to bind to the C $\epsilon$ 2-C $\epsilon$ 3 domain interface and evidence suggests that  $\alpha\epsilon$ Fab12:IgE-Fc is partially unbent. Depending on the degree of C $\epsilon$ 2 extension, overlap between a single  $\alpha\epsilon$ Fab12 molecule and a single CD23 head domain is possible, and therefore  $\alpha\epsilon$ Fab12 may potentially inhibit the lower-affinity binding

site orthosterically. X-ray crystallographic data will help to clarify if the lower-affinity derCD23 binding site is sterically inhibited by the the binding of  $\alpha\epsilon$ Fab12.

### **The $\alpha\epsilon$ Fab13 model**

Similar to  $\alpha\epsilon$ Fab3, the binding of 0 - 2  $\mu$ M derCD23 to the  $\alpha\epsilon$ Fab3:IgE-Fc (1:1) had a binding profile comparable to the control interaction (Figure 7.15.a) and the binding of 0 - 1.7  $\mu$ M derCD23 to the  $\alpha\epsilon$ Fab13:IgE-Fc (2:1) complex had a  $B_{\max}$  around 70 % of the theoretical  $B_{\max}$  for the binding of one derCD23 molecule to IgE-Fc (Figure 7.15.b). Saturation of the first  $\alpha\epsilon$ Fab13 binding site on IgE, however, resulted in a decrease of  $\sim$ 50 % in the binding of IgE to CD23 on the surface of RPMI 8866 cells under equilibrium conditions (Figure 7.10 and Table 7.1). Since the cell-binding assay is sensitive to effects on either CD23 binding site, it is possible that the inhibition that was observed upon saturation of only the first  $\alpha\epsilon$ Fab13 binding site was the consequence of inhibition of the second CD23 binding site only. Accordingly, it is proposed that the binding of one molecule of  $\alpha\epsilon$ Fab13 to IgE-Fc does not modulate the higher-affinity CD23 binding site on IgE, but that it does inhibit the lower-affinity CD23 binding site. The binding of a second molecule of  $\alpha\epsilon$ Fab13 to IgE-Fc, however, allosterically reduces the number of available derCD23 binding sites. Evidence suggests that  $\alpha\epsilon$ Fab13 binds the C $\epsilon$ 2 domains of IgE-Fc and  $\alpha\epsilon$ Fab13:IgE-Fc is partly extended (Section 6.2.5 and Section 6.2.4). Consequently,  $\alpha\epsilon$ Fab13 would be unlikely to sterically interfere with the binding of CD23 to the C $\epsilon$ 3 domain near the C $\epsilon$ 3-C $\epsilon$ 4 interface (Figure 6.22). Accordingly, inhibition of the lower-affinity CD23 binding site is also likely to be allosteric.

### **The $\alpha\epsilon$ Fab18 model**

The binding of 0 - 2  $\mu$ M of derCD23 to the  $\alpha\epsilon$ Fab18:IgE-Fc (1:1) complex had a  $B_{\max}$  that was  $\sim$ 130 % of the theoretical  $B_{\max}$  for the binding of derCD23 to IgE-Fc with a 1:1 stoichiometry (Figure 7.15.a), which suggests that the lower-affinity CD23 binding site was partially occupied. The contribution from the binding of a second derCD23 molecule to IgE-Fc made it difficult to establish the effects that the

binding of a single molecule of  $\alpha\epsilon$ Fab18 had on the higher-affinity derCD23 binding site, it did, however, indicate that  $\alpha\epsilon$ Fab18 enhanced the affinity of the lower-affinity derCD23 binding site (positivity cooperativity with respect to the lower-affinity derCD23 binding site). The cell-based binding studies showed that the binding of one molecule of  $\alpha\epsilon$ Fab18 to IgE had no effect on the levels of IgE binding to CD23 on the surface of RPMI 8866 cells under equilibrium conditions. This suggests that  $\alpha\epsilon$ Fab18 probably had an inhibitory effect on the higher-affinity CD23 binding site, which counteracted the enhancement of the lower-affinity site. The binding of 0 - 1.7  $\mu$ M derCD23 to the  $\alpha\epsilon$ Fab18:IgE-Fc (2:1) had an increased  $K_D$  compared to the control interaction (Figure 7.15.b), suggesting it had an inhibiting effect on the binding of derCD23 to the higher-affinity binding site. It is proposed, therefore, that the binding of one molecule of  $\alpha\epsilon$ Fab18 to IgE reduces the affinity of the higher-affinity CD23 binding site, but acts as a positive allosteric modulator of the lower-affinity CD23 binding site. The mechanism by which the binding of a second  $\alpha\epsilon$ Fab18 molecule to IgE-Fc elicits its inhibitory effect is unknown.

#### **derCD23-induced accelerated dissociation of $\alpha\epsilon$ Fab13 from IgE-Fc.**

The negative cooperative phenomenon of derCD23-induced accelerated dissociation of an  $\alpha\epsilon$ Fab13:IgE-Fc (1:1) complex was previously described in Chapter 5. Accelerated dissociation of other IgE-Fc complexes have previously been described (Section 1.3.5). DARPin E2.79 has been shown to induce the accelerated dissociation of IgE-Fc from Fc $\epsilon$ RI [109] and in Chapter 3 it was described how derCD23 induced the accelerated dissociation of  $\alpha\epsilon$ Fab1 from IgE-Fc. DARPin E2.79 has been proposed to induce accelerated dissociation via a facilitated dissociation mechanism, in which DARPin E2.79 binds several attachment points at the Fc $\epsilon$ RI binding site that become available during the normal dissociation process, and thereby increases the intrinsic rate of dissociation. It has also been proposed, by the same laboratory, that Xolair acts to accelerate dissociation of IgE:Fc $\epsilon$ RI complexes by facilitated dissociation [108]. However, these conclusions were based upon crystal structures of DARPin E2.79 and Xolair Fab bound to a constrained IgE-Fc(3-4) construct held in a 'closed' conformation [109]. Davies *et al.* have suggested that accelerated dissociation of Xolair actually occurs via an allosteric mechanism [82],

and in Chapter 3 we suggested that derCD23 induces the accelerated dissociation of the  $\alpha\epsilon$ Fab1:IgE-Fc (1:1) complex via allosteric processes involving conformational changes within the C $\epsilon$ 3 domains of IgE.

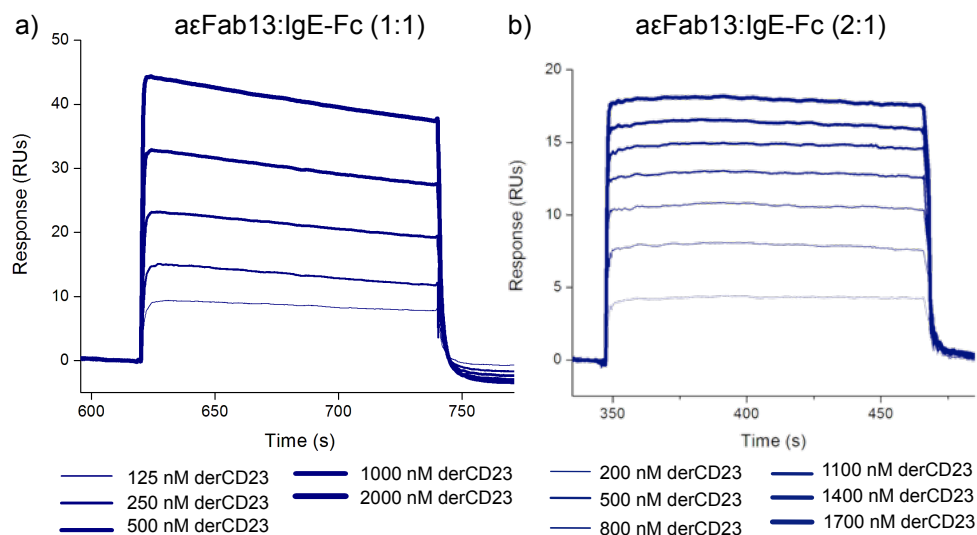


**Figure 7.20: derCD23-induced accelerated dissociation of  $\alpha\epsilon$ Fab13 from IgE-Fc occurs when  $\alpha\epsilon$ Fab13 is in a 1:1 complex with IgE-Fc but not a 2:1 complex.** The double-reference subtracted SPR sensorgrams of derCD23 binding to (a) captured  $\alpha\epsilon$ Fab13:IgE-Fc (1:1) complex and (b) captured  $\alpha\epsilon$ Fab13:IgE-Fc (2:1) complex. derCD23 binds to the  $\alpha\epsilon$ Fab13:IgE-Fc (1:1) complex resulting in an increase in signal, but during the derCD23 injection, the response falls, indicating a drop in mass at the surface from the accelerated dissociation of the  $\alpha\epsilon$ Fab13:IgE-Fc (1:1) complex. derCD23-induced accelerated dissociation of the  $\alpha\epsilon$ Fab13:IgE-Fc (2:1) complex does not occur.

The SPR experiments that were performed with purified  $\alpha\epsilon$ Fab13 described in this chapter also show that derCD23 induced the accelerated dissociation of  $\alpha\epsilon$ Fab13 from IgE-Fc, but only when  $\alpha\epsilon$ Fab13 was present in a 1:1 complex (Figure 7.20). When derCD23 bound to the  $\alpha\epsilon$ Fab:IgE-Fc (2:1) complex it did not induce accelerated dissociation. At present we do not know the exact binding site of  $\alpha\epsilon$ Fab13, but evidence suggests that  $\alpha\epsilon$ Fab13 binds to the C $\epsilon$ 2 domains of IgE-Fc and  $\alpha\epsilon$ Fab13:IgE-Fc is partly extended (Section 6.2.5 and Section 6.2.4). Given that the derCD23 binding sites are located in the C $\epsilon$ 3 domains close to the the C $\epsilon$ 3-C $\epsilon$ 4 interface, it is unlikely that the  $\alpha\epsilon$ Fab13 and derCD23 binding sites share any partial overlap required to induced accelerated dissociation by a facilitated dissociation mechanism. We therefore propose that derCD23 induced dissociation of the  $\alpha\epsilon$ Fab:IgE-Fc (1:1) is allosterically driven. The fact that derCD23 does not induce

accelerated dissociation of the 2:1 complex further suggests that the phenomenon described here is not mediated by facilitated dissociation. The same attachment points would presumably become available to derCD23 during the dissociation of both the 1:1 and 2:1 complexes, and so one would expect accelerated dissociation of both complexes could occur. Whereas it is plausible that the binding of two  $\alpha$ Fab13 molecules to IgE-Fc, as opposed to one, prevents the dynamic processes required for allosterically-mediated accelerated dissociation of the complex upon binding derCD23.

### 7.3 Discussion

The ultimate aim of this project is to identify allosteric modulators of the IgE/CD23 interaction, and through their characterisation gain insights into the mechanisms of allostery in IgE. Five  $\alpha$ Fabs were selected for their ability to bind IgE-Fc and their apparent ability to modulate IgE-receptor interactions in different ways. The aim of the work presented in this chapter was to determine the effects of the  $\alpha$ Fabs on the IgE/CD23 interaction compared to suitable controls for unmodulated interaction, and to ascertain whether the  $\alpha$ Fabs mediated any enhancing or inhibitory effects through allosteric processes.

Determining the exact effect of the  $\alpha$ Fabs on the IgE/CD23 interaction is complicated by the fact that IgE-Fc has two CD23 binding sites of different affinities (Section 1.2.3). The SPR experiments that were performed were designed to try to understand how each of the  $\alpha$ Fabs affects the higher-affinity CD23 binding site. In some instances the combination of SPR and cell-based experiments provided insights into how the  $\alpha$ Fabs may modulate the lower-affinity site.

The cell-based binding assays investigated the effect of saturation of a single  $\alpha$ Fab binding site on IgE-Fc on the interaction between IgE and CD23 expressed on the surface of a B lymphocyte cell-line under equilibrium conditions. Three  $\alpha$ Fabs inhibited the interaction, with a maximal level of inhibition around 30-50 %. None of the  $\alpha$ Fabs enhanced the binding between IgE and mCD23 under equilibrium conditions at the concentrations tested. These experiments explored the effect of  $\alpha$ Fab on IgE bound to mCD23 with a 1:2 stoichiometry. To deconvolute the



effects of the two different CD23 binding sites, SPR experiments were performed to investigate the binding of derCD23 to the higher-affinity binding site of IgE-Fc in complex with one and two molecules of  $\alpha\epsilon$ Fab. By determining the  $K_D$  and  $B_{\max}$  values of the interaction between derCD23 and the different  $\alpha\epsilon$ Fab:IgE-Fc complexes it was possible to determine the effect of the  $\alpha\epsilon$ Fabs on the higher-affinity derCD23 site. Using the SPR data in combination with the cell-based assay data, intramolecular FRET data and C $\epsilon$ 2 binding data, models for how each of the  $\alpha\epsilon$ Fabs affects the IgE/CD23 interaction were generated

The cell-based assays indicated that  $\alpha\epsilon$ Fab2,  $\alpha\epsilon$ Fab12 and  $\alpha\epsilon$ Fab13 inhibit the interaction between IgE and CD23, and the SPR studies suggest that the  $\alpha\epsilon$ Fabs achieve inhibition differently by affecting the two CD23 binding sites differentially.  $\alpha\epsilon$ Fab2, for example, appears to reduce the affinity of the higher-affinity binding site, whereas  $\alpha\epsilon$ Fab12 appears to simultaneously enhance the higher-affinity CD23 binding site and inhibit the lower-affinity site.

The results suggest that the  $\alpha\epsilon$ Fabs mediate at least some of their effects through allosteric mechanisms (Figure 7.19). Additionally, the SPR studies indicate that derCD23-induced accelerated dissociation of  $\alpha\epsilon$ Fab13 from IgE-Fc is allosterically driven. These examples of allosteric modulation are unique compared to any other instances of allosteric modulation of IgE-Fc reported in the literature. Firstly, no other engineered modulators that have been reported in the literature bind IgE and allosterically modulate CD23 binding. Furthermore, all of the published work on allosteric modulation of IgE-Fc to date, describes allosteric communication between two sites within a single C $\epsilon$ 3 domain [18, 81]. The  $\alpha\epsilon$ Fabs described here bind to the C $\epsilon$ 2 domains of IgE-Fc (Section 6.2.5) and in some cases allosterically communicate with the CD23 binding sites located near to the C $\epsilon$ 3-C $\epsilon$ 4 interface of the C $\epsilon$ 3 domains. This suggests that receptor binding can be allosterically modulated over relatively long distances and between different domains of IgE-Fc.

It is important to note that the models that have been proposed were based upon the assumption that the effect of one  $\alpha\epsilon$ Fab on the binding of a single CD23 head to the higher-affinity site of full-length IgE in the context of the cellular assays is the same as the effect of binding of derCD23 to the higher-affinity site of IgE-Fc

in the SPR assays. Because the SPR experiments were only sensitive to changes in the higher-affinity site, whereas the cell-binding assays were sensitive to changes in either CD23 binding site, the assumption was made in some cases in order to infer the effect that an  $\alpha$ Fab had on the second binding site, so as to reconcile the observations from the two different experiments. For example, saturation of the first  $\alpha$ Fab13 site reduced the level of mCD23-bound IgE at equilibrium by  $\sim 50\%$  in the cell assays. Whereas results from SPR experiments suggest that the saturation of the first  $\alpha$ Fab13 binding site had no effect on the binding of CD23 to its higher-affinity site. These two results could be explained if the inhibition observed in the cell-based assay was the result of negatively affecting the lower-affinity CD23 binding site as opposed to higher-affinity CD23 binding site.

Differences in IgE-Fc's environments in the SPR and cell-based experiments may, however, affect the functional outcome of a perturbation in each experiment. The exact effect a modulator has when it binds to its target depends upon the position of the ensemble equilibrium of the target at that time, and this can be altered by numerous factors (Section 1.4). For example, even if all other experimental conditions were identical, the position of the equilibrium of the ensemble of  $\alpha$ Fab-bound IgE-Fc in the context of full length IgE (as used in the cell-binding experiments), may be different from the position of the equilibrium ensemble of  $\alpha$ Fab-bound IgE-Fc. Consequently, the most populated of  $\alpha$ Fab-bound IgE-Fc under the two distinct conditions may be different, and therefore the weighted functional outcome of the ensemble may not be the same in the two different conditions. In this way, an allosteric modulator could have opposing effects under different conditions (Section 1.4).

Understanding exactly how the  $\alpha$ Fabs modulate the binding of the lower-affinity CD23 site may help to validate the models. The effects of the lower-affinity site may be better understood by performing the SPR experiments at higher concentrations of derCD23 that saturate both the higher-affinity and lower-affinity binding sites. However, this requires working at high micromolar concentrations of derCD23, and therefore requires significant quantities of derCD23. Furthermore, unambiguously attributing the two sets of  $K_D$  and  $B_{\max}$  values to the two different binding sites may not be possible if these values are perturbed by the presence of

aεFab.

Comparisons of X-ray crystallographic structures of the various aεFab:IgE-Fc complexes with those of derCD23-bound IgE-Fc could also help validate the models and may help to understand the mechanisms by which some of these aεFabs appear to allosterically modulate the IgE/CD23 interaction. Similar comparisons of the aεFab1:IgE-Fc (2:1) structure and derCD23:IgE-Fc (2:1) structure performed in Chapter 3 suggested an allosteric mechanism by which aεFab1 inhibits derCD23 binding.

X-ray crystallographic data, however, may not definitively reveal the mechanisms by which the aεFabs modulate CD23 binding. X-ray crystallographic structures are generally an average static structure of the protein or complex ensemble [200]. Allosteric modulators may shift the conformational ensembles of molecules towards states to different extents. The modulator-favoured state would only be well represented by the average crystal structure if the shift resulted in the majority of molecules existing in this state. aεFab3 and aεFab13 appear to act to allosterically reduce the number of available derCD23 binding sites by around 25-30 %. If this represents a scenario in which the binding of aεFab13 or aεFab3 to IgE-Fc shifts the conformational ensemble of IgE so that only 25-30 % of the molecules in the ensemble have non-viable higher-affinity binding sites, the average crystal structure may not represent these states. Additionally, structural averaging itself can result artifacts that do not represent reality and therefore may be misleading when trying to determine the mechanism by which a modulator works [200].

Whereas X-ray crystallography is often unable to directly probe the dynamic ensembles of proteins, NMR spectroscopy can. NMR can be used to determine the ensemble model for a protein structure, although generally these are not believed to be fully representative of the true solution-based equilibrium because the software used to derive the models biases the structures towards homogeneity [201]. NMR spectroscopy can however be used look at changes in dynamic processes in a protein on a wide range of timescales upon addition of increasing amounts of modulator. Such studies would help to understand dynamic changes that occur in IgE-Fc upon addition of the different aεFabs, and in this way could help to understand their allosteric mechanisms. Unfortunately, even IgE-Fc alone is a very challenging

NMR target: it has a relatively high molecular mass (72 kDa) and because of its complicated disulphide chemistry it is expressed in mammalian and insect cell-lines. Accordingly, no NMR data on full-length IgE-Fc has been published to date, however the McDonnell laboratory has recently produced isotopically-labeled IgE-Fc in a mammalian expression system, and solution-state studies are currently underway.

# Chapter 8

## Discussion

The interactions between IgE and its receptors, Fc $\epsilon$ RI and CD23, are central to many immunological mechanisms that initiate and propagate allergic disease (Section 1.1.1). Consequently, numerous studies have been performed in order to understand the biophysical and structural basis of IgE/receptor interactions (Section 1.2). It has emerged that the Fc region of IgE, which binds to the receptors, is highly dynamic and that its conformational versatility is central to the specificity and affinity of IgE/receptor interactions (Section 1.2). In the last few years it has been demonstrated through X-ray crystallographic structures of IgE-Fc complexes combined with kinetic and thermodynamic data, that receptor binding to IgE-Fc can be modulated from distal sites through conformational changes (Section 1.3). A rigid-body motion of the C $\epsilon$ 3 domains of IgE-Fc upon the C $\epsilon$ 4 domain pair has been implicated in the mutual allosteric inhibition of CD23 and Fc $\epsilon$ RI binding [18], as well as the allosteric inhibition of Fc $\epsilon$ RI binding by the therapeutic monoclonal antibody Xolair [82], and an engineered Fab ( $\alpha\epsilon$ Fab1) [81]. An even more dramatic rigid-body movement in which the the C $\epsilon$ 2 domains extend from a bent conformation, has been suggested to occur in solution, and the crystal structure of IgE-Fc bound to  $\alpha\epsilon$ Fab1 shows IgE-Fc in an almost fully and symmetric conformation, which is incapable of binding Fc $\epsilon$ RI [81].

The ensemble model of allostery posits that allosteric perturbations redistribute the population of species within the conformational ensemble of a protein [129] (Section 1.4.1). Accordingly, by learning more about the conformational ensemble of IgE-Fc, and the receptor-binding capabilities of the different IgE-Fc conformers, we may uncover more about the range of conformational changes that can occur

in IgE-Fc and that are involved in allosteric modulation of receptor-binding. Ultimately this may provide insights that prove to be useful in the development of novel therapeutics for allergy and asthma. This study set out to discover more about the allosteric processes of IgE that modulate binding to one of its two principal receptors, CD23, through either positive or negative cooperativity. We hypothesised that by investigating the impact of anti-IgE Fabs/IgE interactions on CD23 binding, we may learn more about the conformational ensemble of IgE-Fc and how it can be perturbed to alter the functionality of IgE.

Initially the study investigated the allosteric modulation of the IgE/CD23 interaction by phage display-derived  $\alpha$ εFab1, and the results from binding assays and structural comparisons described novel IgE/receptor interaction behaviours. Through a similar approach with different antibodies it was thought that more could be learnt about the dynamic properties of IgE and how this relates to receptor binding. Using UCB's Core Antibody Discovery Process, we aimed to identify new antibodies that bind to IgE-Fc and modulate the IgE/CD23 interaction preferentially through allosteric processes.

UCB's Core Antibody Discovery Process [148] is a single B cell technology (Section 4.1). Single B cell technologies involve the direct amplification, from individual B cells, of heavy and light variable region DNAs [176]. These technologies therefore circumnavigate the problems associated with the loss of original light and heavy chain pairings that are often encountered in display technologies (Section 4.1). For the first time, UCB's Core Antibody Discovery Process was used to screen the immune repertoire of three IgE-Fc immunised rabbits for antibodies that bind to IgE-Fc and modulate the IgE/CD23 interaction.

The process successfully generated antibodies that interact with IgE-Fc with high affinities (Section 5.2.1), are sequentially diverse (Section 4.2.3) and have a range of effects on the IgE/CD23 interaction (Section 5.2.2). Five antibodies were eventually chosen for further biophysical characterisation after initial selection using a homogeneous fluorescence-based assay (Section 4.2.1) and further selection using SPR (Section 4.2.4 and Chapter 5). When expressed as Fabs, the five selected antibodies bound to IgE-Fc with sub-nanomolar to nanomolar affinities; stronger than the IgE-Fc/ $\alpha$ εFab1 interaction [81]. In addition, the SPR sensorgrams of IgE-

Fc binding to the  $\alpha$ Fabs had different kinetic profiles (Section 6.2.2), indicating that the discovery process had successfully selected for diverse high-affinity IgE-Fc binders.

The second round of antibody screening involved another homogeneous-based assay that was used to identify antibodies that increase or decrease IgE-Fc/derCD23 binding, by analysing changes in associated fluorescence (Section 4.2.2). The secondary screen had several limitations, in particular there was a problem with fluorescence quenching: a component of the cell culture supernatant quenched the fluorescence from the labeled derCD23, which necessitated significant dilution of the supernatants (Section 4.2.2). The reduction in antibody concentration consequently reduced the signal-to-noise ratio and therefore made meaningful interpretation of single data points difficult. It is possible that the quenching was fluorophore-specific and consequently may be avoided using a different fluorescent label. Alternatively, the problem may be circumnavigated using a label-free screening technique.

Despite the lack of a stringent control for unperturbed binding, and problems with fluorescence quenching during the secondary screening process (Section 4.2.2), SPR studies of derCD23 binding to  $\alpha$ Fab:IgE-Fc complexes, indicated that the antibody discovery process had successfully identified five  $\alpha$ Fabs that have different effects on the IgE-Fc/CD23 interaction (Section 7.2.2).  $\alpha$ Fab12, for example, was shown to enhance the interaction between IgE-Fc and derCD23, whereas  $\alpha$ Fab3 was shown to inhibit it. Moreover, the impact of  $\alpha$ Fab binding on the affinity and availability of the CD23 binding sites was different for each of the  $\alpha$ Fabs, which was reflected in the SPR-determined  $K_D$  and  $B_{\max}$  values, respectively.

It should be noted, however, that despite picking some of the antibodies that scored the lowest in the secondary screen, none of the 25 antibodies that were initially tested for their effect on the IgE/CD23 interaction using SPR, completely inhibited the interaction (Section 4.2.4). Competitive inhibitors may have existed in the screening population but did not give significantly lower signals because of the described limitations and insensitivity of the secondary screen, and through chance were not selected. There does also seem to have been some intrinsic bias in the discovery process, since all five of the final selected antibodies bind to the

C $\epsilon$ 2 domains of IgE-Fc rather than the C $\epsilon$ 3 domains to which CD23 binds (Section 6.2.5). The reasons for this bias remain unclear, but the differences between rabbit IgE-Fc and human IgE-Fc (N265Q, N371Q), with which the immunisations were performed, is likely to shape the antibody repertoire and may be a contributing factor. Sequence alignments of rabbit IgE-Fc and human IgE-Fc (N265Q, N371Q) domains indicated that the C $\epsilon$ 2 domains share the least homology, which may render them more immunogenic (Appendix A.14).

SPR experiments investigating the binding of sub-fragments of IgE-Fc to each of the a $\epsilon$ Fabs suggested that the binding sites of the five selected a $\epsilon$ Fabs are completely, or at least predominately, located in the C $\epsilon$ 2 domains of IgE-Fc (Section 6.2.5). Subsequent SPR and cell-based binding assays went on to identify the effects of the a $\epsilon$ Fabs on the IgE/CD23 interaction (Section 7.2.2), and combining these data and the results from intramolecular FRET experiments (Section 6.2.4), indicated that the a $\epsilon$ Fabs can allosterically modulate receptor binding by binding to the C $\epsilon$ 2 domains, and do so in a variety of ways. Saturation of the first a $\epsilon$ Fab2 binding site appears to result in the extension of IgE-Fc and a shift towards conformations with reduced affinity for CD23. Saturation of both a $\epsilon$ Fab3 binding sites, however, is not associated with IgE-Fc extension and reduces the number of available CD23 binding sites.

Differences in the data collected from the other a $\epsilon$ Fabs in the SPR and cell-based binding assays, were likely to be, at least in part, because the SPR experiments were only sensitive to effects on the higher-affinity CD23 binding site, whereas the cell-based assays were sensitive to effects on either of the two CD23 binding sites (Chapter 7). This difference in the experiments allowed us to infer the effect of a $\epsilon$ Fab on the lower-affinity CD23 binding site. In some cases complicated models were invoked to rationalise the results from the two experiments. The interpretation of the data may, however, be complicated by other differences in the two types of experiment, for example the distinct environments of IgE-Fc. Such differences may affect the position of IgE-Fc's conformational equilibrium differentially and therefore the models require verification. Nevertheless, to the best of our knowledge the results indicate that this project is the first study to successfully select for allosteric modulators of the CD23/IgE interaction.



It is hoped that these newly generated aεFabs will reveal more about how changes in IgE-Fc dynamics affect the interactions between IgE and its receptors, which play pivotal roles in allergic disease (Section 1.1.1). Even in the early stages of their characterisation, these aεFabs and aεFab1, have provided new insights into IgE-Fc's dynamic behaviour and the allosteric regulation of receptor binding, as summarised below.

### **Intra-domain motions may contribute towards allosteric mechanisms of IgE/CD23 inhibition**

SPR and cell-based assays performed under equilibrium conditions showed that aεFab1 is a potent inhibitor of the IgE/CD23 interaction. A comparison of the structures of IgE-Fc(3-4) bound to derCD23 (PDB: 4EZM [18]), and IgE-Fc bound to aεFab1 (PDB: 4J4P [81]), showed that the CD23 and aεFab1 binding sites are non-overlapping and that their binding sites are spatially distinct (Section 3.2.5). To our knowledge, this is the first demonstration of allosteric inhibition of the IgE/CD23 interaction by an engineered protein. The naturally occurring IgE receptor, FcεRI, is known to allosterically prevent the binding of IgE to CD23, at least in part, by stabilising an 'open' IgE conformation in which the Cε3 domains are further apart from one another than in the 'closed' IgE-Fc conformation, thought to be necessary for CD23 binding (Section 1.3.1) [18]. aεFab1 stabilises an even more 'open' conformation of IgE-Fc [81], and the results from comparisons of the derCD23:IgE-Fc(3-4) complex and aεFab1:IgE-Fc complex similarly indicated that the rigid-body motion of the Cε3 domains upon the Cε4 domain pair may also in part be responsible for preventing the interaction between IgE-Fc and CD23.

Whereas it has previously been suggested that conformational changes within the intrinsically flexible Cε3 domains of IgE-Fc may play a role in the allosteric inhibition of IgE/CD23 interactions by FcεRI [18], the results from the comparison of aεFab1-bound IgE-Fc and derCD23-bound IgE-Fc structures explicitly show significant conformational differences within the Cε3 domains that may affect the coordination of the CD23 binding sites (Section 3.2.5). Additionally, negative cooperativity between the CD23 and aεFab1 binding sites was reduced in IgE-Fc with internally rigidified Cε3 domains (Section 3.2.6), further supporting the role of

intra-domain C $\epsilon$ 3 conformational changes in the allosteric inhibition of IgE/CD23 interactions by  $\alpha\epsilon$ Fab1. Whereas conformational changes associated with allostery in IgE-Fc have largely been realised in terms of large-scale motions, this finding reinforces that smaller dynamic changes may play significant roles, and their potential contributions to allostery in IgE should not be ignored.

Unfortunately, the comparison of static structures does not reveal even smaller-scale dynamic processes that may also play an important role in the allosteric inhibition of the CD23/IgE interaction by  $\alpha\epsilon$ Fab1 (Section 1.4.1). The binding of  $\alpha\epsilon$ Fab1 may change the amplitude and frequency of thermal fluctuations in IgE-Fc that disfavour the binding of CD23 (Section 1.4). Thermodynamic binding studies using isothermal calorimetry, for example, may indicate if entropic changes are involved in the allosteric inhibition of IgE/CD23 interactions by  $\alpha\epsilon$ Fab1. Molecular dynamic simulations may also prove to be useful in pinpointing the residues and regions of IgE-Fc that are most susceptible to dynamic changes upon the binding of  $\alpha\epsilon$ Fab1, and that may affect CD23 binding [175, 137].

### **Free IgE-Fc is heterogeneous in solution**

X-ray crystallographic structures of various IgE-ligand complexes show IgE-Fc can adopt a range of conformations (Section 1.2.1). Intramolecular FRET studies, in which a donor and acceptor pair were attached to the N and C termini of IgE-Fc, also indicate that bent IgE-Fc can extend partially or fully when incubated with Xolair Fab mutant 3 [82] and  $\alpha\epsilon$ Fab1 [81], respectively. Although IgE-Fc can adopt these various conformations in the presence of ligand, relatively little is known about what conformations free IgE-Fc experiences. Structures of IgE-Fc(3-4) determined from different crystal forms indicate that IgE-Fc(3-4) does not require a stabilising ligand to populate a range of ‘open’ and ‘closed’ conformations [77]. However, the C $\epsilon$ 2 domain pair is thought to limit this rigid-body motion [72], and consequently the results of these experiments do not report on whether IgE-Fc spends significant time in a range of ‘open’ and ‘closed’ conformations. Molecular dynamic simulations suggest that IgE-Fc can transiently populate extended conformations, and the C $\epsilon$ 2 domains may even ‘flip’ from one side of the molecule to the other, but that it exists predominantly in a bent asymmetric conformation,

as supported by intramolecular FRET data [81]. Work from our laboratory, in conjunction with work undertaken in this this project, provides further evidence to suggest that free IgE-Fc populates various conformations and that this has important implications for receptor binding.

As part of this project, a His-tagged IgE-Fc construct was generated (Section 3.2.2). This construct was captured on an anti-His-tag sensor chip surface to allow the straightforward deconvolution of  $B_{\max}$  and  $K_D$  values for IgE-Fc in SPR binding studies. Using this approach, it was found that only  $\sim 30\%$  of IgE-Fc in solution is capable of binding sFc $\epsilon$ RI $\alpha$  with the sub-nanomolar affinity that is often reported in the literature, and the remaining IgE-Fc binds sFc $\epsilon$ RI $\alpha$  with  $\sim 20$  nM or low micromolar affinities, accounting for the multiphasic kinetics of IgE-Fc/sFc $\epsilon$ RI $\alpha$  interaction. Multiphasic kinetics of the IgE-Fc/sFc $\epsilon$ RI $\alpha$  interaction were also evident in stopped-flow intrinsic fluorescence experiments and suggested an induced fit conformational change occurred after the initial binding event. Stopped-flow FRET studies of the IgE-Fc/sFc $\epsilon$ RI $\alpha$  also indicated that IgE-Fc could experience these different conformations even when in complex with Fc $\epsilon$ RI. Two of the  $\alpha\epsilon$ Fabs generated during this project,  $\alpha\epsilon$ Fab12 and  $\alpha\epsilon$ Fab13, bind IgE-Fc with a 2:1 stoichiometry, yet they interact with IgE-Fc with triphasic binding kinetics, which may also be indicative of IgE-Fc's heterogeneous conformational character (Section 6.2.3).

In collaboration with Dr Simon Ameer-Beg (KCL), our group is in the early stages of trying to understand more about the heterogeneity of IgE-Fc using single molecule FRET. Conventional FRET methods look at the statistical distribution of observables over a large number of molecules in a sample, whereas single molecule FRET observes individual molecules. Consequently, single molecule FRET can avoid ensemble averaging and can allow for the study of specific homogeneous populations within a heterogeneous sample [202]. Single molecule FRET experiments of IgE-Fc may be able to determine the distributions of various intermolecular distances and the relative populations of different IgE-Fc states. Initially the group aims to perform single molecule FRET experiments to determine C $\epsilon$ 2-C $\epsilon$ 4 distances in single IgE-Fc molecules and thereby ascertain the distribution of various extended states within the IgE-Fc population.

**The link between IgE-Fc extension and Fc $\epsilon$ RI inhibition is not binary**

Fc $\epsilon$ RI binds to the most bent and compact conformation of IgE-Fc so far observed [87, 75] (Section 1.2.2). The striking extension of IgE-Fc's C $\epsilon$ 2 domain pair, which occurs upon the binding of a $\epsilon$ Fab1, prevents Fc $\epsilon$ RI from binding (Section 1.3.3) [81]. Using intramolecular FRET, the binding of a $\epsilon$ Fab2, a $\epsilon$ Fab12 and a $\epsilon$ Fab13 to IgE-Fc were shown to be associated with various degrees of C $\epsilon$ 2 domain extension (Section 6.2.4). The binding of a $\epsilon$ Fab2 to IgE-Fc resulted in comparable levels of FRET inhibition to a $\epsilon$ Fab1, indicating that a $\epsilon$ Fab2 stabilises a conformation of IgE-Fc that is nearly fully extended. In Chapter 5, SPR experiments indicated that a $\epsilon$ Fab2 does not inhibit the IgE-Fc/Fc $\epsilon$ RI interaction (Section 5.2.3). Together, these results demonstrate that extension of the C $\epsilon$ 2 domains of IgE-Fc does not necessarily result in the inhibition of Fc $\epsilon$ RI binding. IgE-Fc may adopt a variety of extended conformations that differ in the arrangement of the C $\epsilon$ 2-C $\epsilon$ 3 linker region and the rotation of the C $\epsilon$ 2 domains, both of which may affect Fc $\epsilon$ RI binding (Section 1.3.3). The structure of the a $\epsilon$ Fab2:IgE-Fc complex may reveal a new extended conformation of IgE-Fc and elucidate why it does not prevent Fc $\epsilon$ RI binding. These findings highlight that although 'open', 'closed', 'bent' and 'extended' can be useful descriptors of IgE-Fc structure, each term encompasses a whole range of conformations and receptor-binding behaviours.

**Long-range allostery can occur in IgE**

To date, the handful of modulators known to affect IgE/receptor interactions allosterically have all been shown to bind to the C $\epsilon$ 3 domains, to which the receptors also bind. In this study, however, we have generated Fabs that bind to the C $\epsilon$ 2 domains of IgE-Fc and allosterically modulate CD23 binding, which occurs near the C $\epsilon$ 3-C $\epsilon$ 4 domains interfaces. This allosteric regulation is occurring over the longest distance observed in IgE-Fc to date, and indicates that allosteric communication can occur between two sites in IgE that are separated by significant distances and across different domains.

**derCD23 can allosterically accelerate the dissociation of IgE-Fc complexes**

A Designed Ankarin Repeat Protein, DARPin E2\_79, and Xolair have both been shown to accelerate the dissociation of IgE/Fc $\epsilon$ RI complexes [109, 110, 108] (Section 1.3.5). Xolair only mediates accelerated dissociation at concentrations far in excess of prescribed dosages and therefore it is not part of the mechanism through which it operates therapeutically. Instead, Xolair, the only anti-IgE-therapeutic antibody currently licenced for the treatment of allergic disease, primarily works by binding free IgE-Fc in the serum and by consequently affecting the levels of IgE-Fc bound to Fc $\epsilon$ RI on the surface of mast cells, basophils and dendritic cells (Section 1.1.2). Because of the very slow dissociation rate of the IgE/Fc $\epsilon$ RI interaction, IgE-Fc:Fc $\epsilon$ RI complexes can persist on the surface of these effector cells for weeks, resulting in long-term sensitisation (Section 1.1.1 and Section 1.2.2). While the levels of free IgE and IgE on the surface of basophils drops within days of Xolair treatment, the levels of IgE on mast cells remain higher for longer [108]. Accordingly, a drug that could bind to IgE-Fc in complex with Fc $\epsilon$ RI and destabilise the IgE-Fc/Fc $\epsilon$ RI complex could rapidly reduce the level of mast cell sensitisation and may have a more immediate therapeutic effect.

Evidence suggests that the benefit of Xolair may be limited by IgE-dependent homeostatic mechanisms that respond to the decline in receptor-bound IgE upon treatment [35, 55, 58, 37, 203, 204]. Pennington *et al.* have proposed that a drug capable of disrupting the IgE-receptor interactions may be used in combination with drug-resistant IgE variants to effectively replace the native IgE on effector cells [108]. One possibility is to engineer a variant of Xolair with an enhanced disruptive capability such that it could rapidly remove native IgE from effector cells at therapeutic concentrations, providing that, like Xolair, the variant did not have the propensity to form large immune complexes [205, 206, 207]. Accordingly, understanding what drives accelerated dissociation of IgE-Fc-ligand complexes may be beneficial in the design of novel drugs that harness this phenomenon.

The negative cooperative phenomenon of accelerated dissociation can be steric or allosteric. Facilitated dissociation is a process in which a competitor increases the

native rate of complex dissociation by engaging ligand attachment points during the dissociation process, thereby invoking atomic overlap. DARPin E2\_79- and Xolair-mediated accelerated dissociation of IgE-Fc/Fc $\epsilon$ RI complexes have been suggested to operate via facilitated dissociation [109, 108]. The conclusions were, however, based in part upon structural data from constrained IgE-Fc(3-4) complexes, in which IgE-Fc was held in a ‘closed’ conformation. The crystal structure of IgE-Fc bound to Xolair Fab mutant 3, in conjunction with SPR data, suggests that the Xolair Fab allosterically mediates accelerated dissociation of IgE/Fc $\epsilon$ RI complexes (Section 1.3.5).

In this study we discovered two new examples of accelerated dissociation of IgE-Fc complexes, and reported, for the first time, receptor-mediated accelerated dissociation of IgE-Fc complexes. SPR experiments showed that derCD23 bound to a $\epsilon$ Fab1:IgE-Fc (1:1) and a $\epsilon$ Fab13:IgE-Fc (1:1) complexes, and accelerated their dissociation (Section 3.2.3 and Section 7.2.3).

Crystal structures of the a $\epsilon$ Fab1:IgE-Fc (2:1) and derCD23:IgE-Fc(3-4) (2:1) complexes clearly show that the a $\epsilon$ Fab1 and CD23 binding sites are distinct and the binding of the two ligands to IgE-Fc is spatially separated, which suggests that derCD23 mediated accelerated dissociation of a $\epsilon$ Fab1:IgE-Fc is an allosteric process (Section 3.2.5). At present there is no crystal structure available for IgE-Fc bound to a $\epsilon$ Fab13, but the results of SPR experiments investigating the binding of different IgE-Fc sub-fragments to a $\epsilon$ Fab13 indicate that a $\epsilon$ Fab13 binding sites are located in the C $\epsilon$ 2 domains of IgE-Fc, far from the CD23 binding sites at the C $\epsilon$ 3-C $\epsilon$ 4 domain interface (Section 6.2.5). Consequently derCD23-mediated accelerated dissociation of a $\epsilon$ Fab13:IgE-Fc (1:1) complexes cannot occur through a facilitated dissociation mechanism. It is possible that derCD23-mediated accelerated dissociation of a $\epsilon$ Fab13:IgE-Fc (1:1) complexes is the result of atomic overlap between a $\epsilon$ Fab13 and derCD23 bound to IgE-Fc, however, intramolecular FRET data suggests that a $\epsilon$ Fab13 binds partially extended C $\epsilon$ 2 domains (Section 6.2.4). A partially extended conformation of IgE-Fc would have an increased distance between the C $\epsilon$ 2 and C $\epsilon$ 3 domains and therefore atomic overlap of a $\epsilon$ Fab13 and CD23 is unlikely. Furthermore, derCD23 was able to bind the a $\epsilon$ Fab13:IgE-Fc (2:1) complex but was unable to accelerate its dissociation at the tested concen-

trations (Section 7.2.3); if the phenomenon was sterically driven then it is unlikely that the stoichiometry of the complex should be influential. Structural data may help to determine if derCD23 does actually act to accelerate the dissociation of  $\alpha\epsilon$ Fab13:IgE-Fc via an allosteric mechanism.

Regardless of the mechanism of derCD23-mediated accelerated dissociation of  $\alpha\epsilon$ Fab13:IgE-Fc complexes, the studies of  $\alpha\epsilon$ Fab1 demonstrate that accelerated dissociation of IgE-Fc complexes can be mediated allosterically (Section 3.2.5). Although not directly comparable, understanding more about the way derCD23 allosterically induces the accelerated dissociation of  $\alpha\epsilon$ Fab1:IgE-Fc may indicate ways of destabilising IgE:Fc $\epsilon$ RI complexes allosterically. derCD23-mediated accelerated dissociation of  $\alpha\epsilon$ Fab1:IgE-Fc was reduced by stabilising the C $\epsilon$ 3 domains of IgE-Fc (Section 3.2.6), indicating that changes within the C $\epsilon$ 3 domains themselves contribute to destabilisation of the  $\alpha\epsilon$ Fab1:IgE-Fc complex. Perhaps, intra-domain changes may also play a role in the accelerated dissociation of IgE:Fc $\epsilon$ RI complexes.

## General implications

Because the IgE/Fc $\epsilon$ RI interaction occurs over an extended and largely flat interface, and because the interaction has such a high affinity, it was suggested that it was unlikely that the interactions could be inhibited by a small molecule drug and IgE was deemed ‘undruggable’ [208]. The findings from this research provide new insights into the highly dynamic nature of IgE and sheds light on novel mechanisms and properties that can affect its allosteric behaviour. Accordingly, we propose that IgE is in fact druggable; that instead of targeting the receptor-binding sites of IgE-Fc directly, small molecule drugs binding distal to them could inhibit receptor interactions through changes in IgE conformation and/or dynamics.

An understanding of how antibodies allosterically modulate IgE-receptor interactions may allow the design of small molecules with similar related effects. Antibodies that stabilise IgE in biologically relevant conformations could be used to hold IgE in transiently populated conformations during fragment screening and crystallography [209]. Such approaches may identify novel, perhaps normally inaccessible, binding sites on IgE that could be used in the development of small

molecules drugs for allergy and asthma.

IgE-Fc's conformational plasticity could be key in the design of novel allosteric therapeutics for allergy and asthma, but how does the immune system itself benefit from the evolution of such a highly dynamic structure? Allosteric regulation of IgE-Fc is already known to be crucial in preventing simultaneous engagement of both Fc $\epsilon$ RI and CD23, which would result in systemic anaphylaxis [18]. Additionally, it has been suggested that the bent conformation of IgE-Fc bound to Fc $\epsilon$ RI aids allergen cross-linking on the surface of mast cells, basophils and antigen presenting cells, whereas C $\epsilon$ 2 domain extension may facilitate the capture of allergen in the context of the B cell receptor [81]. It could also be that IgE-Fc's conformational diversity may play a role in tuning IgE-mediated immune responses.

Any conformationally-dependent functionality of IgE, such as the binding of IgE to Fc $\epsilon$ RI or CD23, is dependent on the position of IgE's conformational equilibrium and can be perturbed by changes in conditions. For example, shifting the equilibrium towards conformations that can bind Fc $\epsilon$ RI, or bind Fc $\epsilon$ RI with a higher affinity, will result in increased binding of IgE to Fc $\epsilon$ RI on the surface of effector cells. Whereas shifting the equilibrium towards conformations that cannot bind Fc $\epsilon$ RI, or those with lower affinities for the receptor, will result in less binding of IgE to Fc $\epsilon$ RI on the surface of effector cells. By existing in a range of different conformations with different Fc $\epsilon$ RI binding affinities, perturbing the equilibrium can 'tune' the amount of Fc $\epsilon$ RI-bound IgE on the surface of the effector cells at any one time. Tuneability allows a system to adapt to change and being able to adapt to change is crucial in the immune system, where a lack of response or an over-response to change can be fatal. The high-affinity IgE/Fc $\epsilon$ RI interaction on the surface of mast cells and basophils results in long-term sensitisation of these potent effector cells. Whilst this may be beneficial for a rapid response to a parasitic infection, it is the rapid release of inflammatory mediators by mast cells in response to otherwise innocuous antigens that triggers allergic reactions and can cause anaphylaxis. It is possible that IgE-Fc heterogeneity provides IgE with the tools to adapt to its environment, in order to prevent under- or over-reaction. For example, a shift towards conformations with high affinity for Fc $\epsilon$ RI may increase the local concentration of mast cells coated with antigen-specific IgE during a par-



asitic infection. Or to avoid anaphylaxis, a shift towards weakly-bound IgE:FcεRI complexes may accelerate the dissociation of IgE from FcεRI on the surface of mast cells.

This logic may apply to any conformationally-dependent function of IgE including binding to CD23. IgE/CD23 interactions have been implicated in various immunological roles including IgE-homoeostasis, although the exact mechanisms through which CD23 can prompt both up- and down-regulation of IgE are disputed, perhaps conformational dynamism of IgE-Fc may be involved in fine-tuning these processes.

Additionally, the role of allostery in IgE-Fc may extend beyond the scope of IgE/receptor interactions. IgE-Fc is joined to two Fab regions via links with the two Cε2 domains. Traditionally antigen-binding and receptor-binding/signalling have been treated as strictly distinct functionalities of the Fab and Fc regions of antibodies, respectively. There is now growing evidence that suggests the whole immunoglobulin should be considered in regards to both of these activities [210]. Antigen binding at the variable domains must somehow be communicated to the rest of the molecule to initiate signalling events. For example, antigen cross-linking of IgE on the surface of a mast cell is in some way relayed to the Fc region, which through its interaction with FcεRI triggers intracellular signalling cascades required for mast cell activation and degranulation. Similarly, binding of allergen to the Fab regions of IgE-B cell receptors must in some way be transmitted to the intracellular signalling machinery in order to initiate the signalling required for B cell proliferation or antigen internalisation. Furthermore, various studies have shown that the constant region of an immunoglobulin can affect the affinity and specificity of the variable regions [210].

Exactly how the antigen binding events are transduced to intracellular signalling domains and constant regions, and the mechanisms through which the constant regions affect antigen binding, remain obscure. It is certainly possible, however, that conformational changes provide a method of bidirectional communication. The binding of antigen to antibody is thought to require a degree of structural flexibility at the variable domains, and perhaps the conformational changes associated with the binding event are transmitted via allosteric processes to the necessary

signalling domains [210]. For example, it has been proposed that the binding of antigen leads to conformational changes in the constant region of the B cell receptor that then promotes oligomerisation, clustering and consequently signalling [211]. In this present study we show that perturbations can indeed be allosterically communicated across different domains of IgE. Perhaps the conformational flexibility of IgE-Fc does not simply provide IgE with the tools to fine-tune the outcomes of IgE-receptor interactions, but it may also provide a vital means of communicating the antigen binding and signalling events that fuel the allergic response.

### **Further studies**

The data presented in this thesis suggest that the  $\alpha\epsilon$ Fabs that have been generated elicit their effects on CD23 binding, at least in part, through allosteric processes. X-ray crystallographic structures of IgE-Fc bound to the different  $\alpha\epsilon$ Fabs would establish whether their binding sites are indeed within the C $\epsilon$ 2 domains and therefore distal from the CD23 binding sites. By overlaying the crystal structures of the  $\alpha\epsilon$ Fab:IgE-Fc complexes with structures of IgE-Fc bound to derCD23, we may also determine if the binding of each of the  $\alpha\epsilon$ Fabs and derCD23 is in fact spatially distinct.

X-ray structures will not only map the  $\alpha\epsilon$ Fab binding sites, but will reveal conformational changes associated with the binding of the different  $\alpha\epsilon$ Fabs. Crystallisation trials of  $\alpha\epsilon$ Fab:IgE-Fc complexes with 1:1 and 2:1 stoichiometries have been set up. We have grown crystals for the 2:1 complex of  $\alpha\epsilon$ Fab2:IgE-Fc and we have collected some diffraction data from these crystals at the Diamond Light Source (Harwell, UK). The data were scaled to 4.4 Å resolution and some progress has been made in structural determination. We have obtained a partial solution comprised of two  $\alpha\epsilon$ Fab2 molecules and the C $\epsilon$ 2 domain pair using molecular replacement (Figure 8.1). At present, the model does not contain the C $\epsilon$ 3 and C $\epsilon$ 4 domains. In addition to solving the complete structure, we are currently trying to optimise the crystallisation and cryoprotectant conditions to obtain higher resolution data.

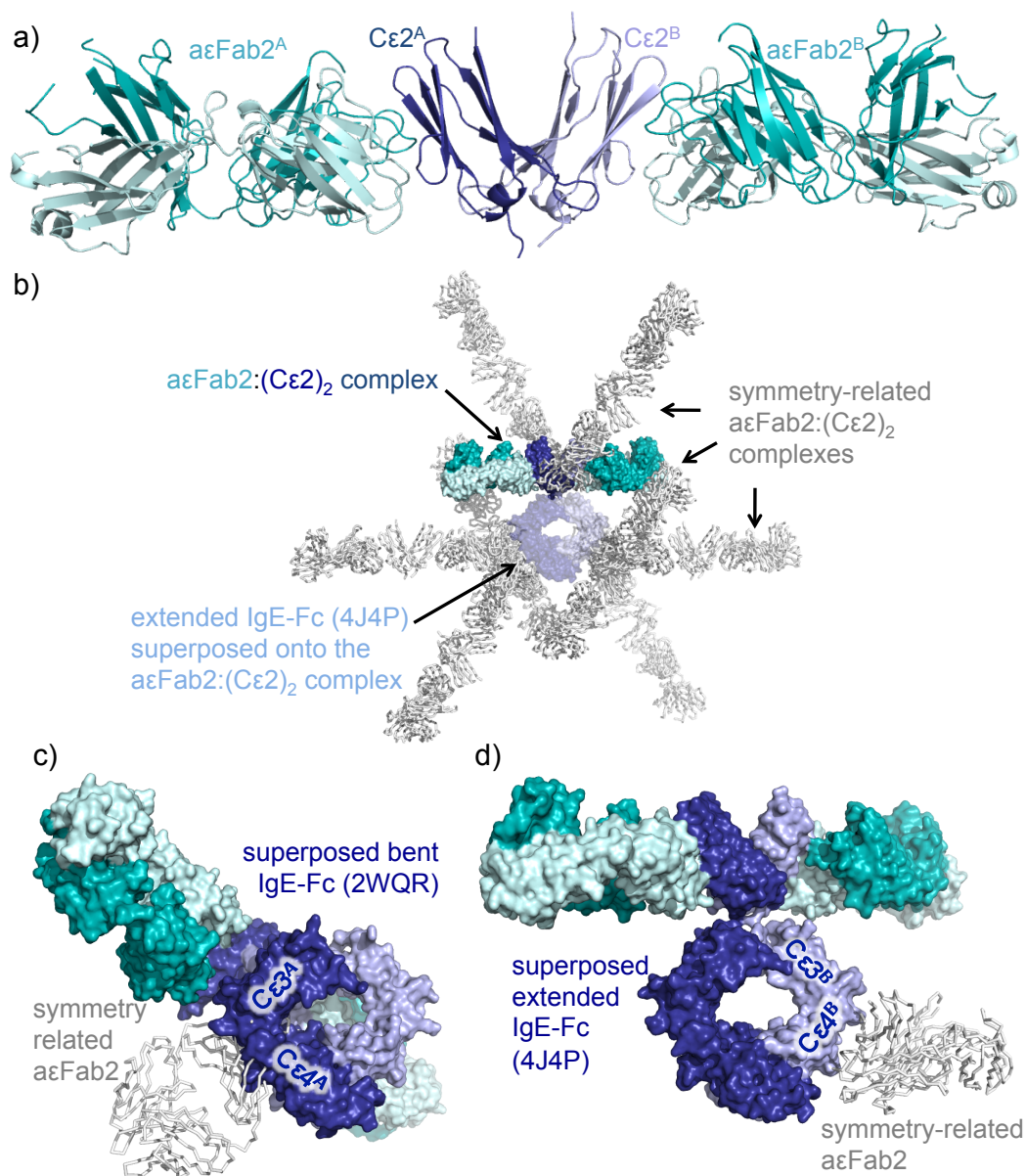


Figure 8.1: **A partially-solved crystal structure of the aεFab2:IgE-Fc (2:1) complex.** (a) The partially-solved crystal structure of the aεFab2:IgE-Fc (2:1) complex. The data were collected at the Diamond Light Source (Harwell, UK) and were scaled to 4.4 Å. The partial solution, comprising two aεFab2 molecules and the Cε2 domain pair, shows that each aεFab2 binds a single Cε2 domain. (b) The partial solution does not contain the Cε3 and Cε4 domains, but there is sufficient space in the crystal lattice to accommodate the remainder of the IgE-Fc molecule. Superposition of an extended IgE-Fc (4J4P) on the Cε2 domain pair of the partial solution, demonstrates how the lattice could accommodate the Cε3 and Cε4 domains of an extended IgE-Fc molecule. (c) Superposition of the bent IgE-Fc structure (2WQR) on the Cε2 domain pair of the partial solution shows that a bent IgE-Fc molecule would significantly clash with a symmetry-related aεFab2 molecule. (d) Superposition of an extended IgE-Fc structure (4J4P) on the Cε2 domain pair of the partial solution shows that this particular extended conformation of IgE-Fc would clash with a symmetry-related aεFab2 molecule.

Although the structure of the  $\alpha\epsilon$ Fab2:IgE-Fc (2:1) complex has not been fully solved, the data validate the findings reported in this thesis that relate to the binding of  $\alpha\epsilon$ Fab2 to IgE-Fc. The partial solution shows two molecules of  $\alpha\epsilon$ Fab2 bound to the C $\epsilon$ 2 domain pair of IgE-Fc (Figure 8.1.a). From the crystal packing, we can see sufficient space in the lattice for the C $\epsilon$ 3 and C $\epsilon$ 4 domains of IgE-Fc (Figure 8.1.b). Bent IgE-Fc (PDB: 2WQR) superposed on the C $\epsilon$ 2 domain pair of the partial solution is incompatible with the crystal lattice as there is extensive atomic overlap between one C $\epsilon$ 3 domain and a symmetry-related  $\alpha\epsilon$ Fab2 molecule (Figure 8.1.c). Extended IgE-Fc (IgE-Fc bound to  $\alpha\epsilon$ Fab1, PDB: 4J4P) superposed on the C $\epsilon$ 2 domain pair of the partial solution fits better into the space of the crystal lattice, but still clashes with a symmetry-related  $\alpha\epsilon$ Fab2 molecule (Figure 8.1.d). It is therefore likely that the  $\alpha\epsilon$ Fab2:IgE-Fc (2:1) complex is extended, but that it adopts a distinct conformation from the extended  $\alpha\epsilon$ Fab1-bound structure. An extended and twisted conformation would fit into the space in the crystal lattice and the flexibility of the C $\epsilon$ 2-C $\epsilon$ 3 linker-region could accommodate this.

It is necessary to solve the rest of the  $\alpha\epsilon$ Fab2:IgE-Fc (2:1) crystal structure to determine how extended the conformation is and if it is indeed twisted. Solving and refining the complete structure will also reveal any conformational differences between apo and  $\alpha\epsilon$ Fab2-bound IgE-Fc that may contribute towards the allosteric inhibition of CD23 binding. We hope to obtain diffraction data for all of the other  $\alpha\epsilon$ Fab complexes and that the structures of these complexes will describe conformations of IgE-Fc distinct from any that have already been observed. Consequently, we will reveal dynamic processes that occur within IgE-Fc that have not yet been described.

Whilst X-ray crystallography may reveal rigid-body domain movements and residue shifts involved in allosteric communication, it generally does not report changes in dynamics that may also contribute towards allosteric mechanisms. NMR spectroscopy provides information about protein structure, dynamics and thermodynamics and has been fundamental in the understanding of the allosteric regulation of many proteins [111]. NMR spectroscopy can report on dynamic processes that occur in proteins on a range of different timescales, and fast internal motions can be used as proxy for conformational entropy [212]. In collaboration with UCB,

the McDonnell laboratory has produced sufficient amounts of isotopically-labeled IgE-Fc for NMR spectroscopy experiments, but before the dynamics of IgE-Fc can be studied, the difficult task of protein assignment must be completed. Until then we hope to use isothermal calorimetry to characterise the thermodynamics of the interactions between IgE-Fc and its receptors in the presence and absence of each of the  $\alpha$ Fabs. In this way we intend to establish if binding of  $\alpha$ Fab to IgE-Fc is associated with changes in entropy that affect how it binds to its receptors, CD23 and Fc $\epsilon$ RI.

Further binding studies may help to verify the effects that the different  $\alpha$ Fabs have on the IgE/CD23 interaction. Upon generation of sufficient quantities of derCD23, we plan to perform SPR studies investigating the effect of each of the  $\alpha$ Fabs on the binding of two molecules of derCD23 to IgE-Fc. As described in Chapter 7's discussion, this experiment has potential limitations but it may provide insights into how each of the  $\alpha$ Fabs affects the IgE/CD23 interaction. To verify the results of the cell-binding assays we also plan to look at the effect of each of the  $\alpha$ Fabs on the IgE/CD23 interaction in a different homogeneous assay, for example using time-resolved FRET (TR-FRET) experiments. In addition to looking at the effect of the  $\alpha$ Fabs on the interaction between IgE and CD23, we are planning on performing SPR experiments to investigate modulation of the IgE/Fc $\epsilon$ RI interaction more closely.

Although the findings of this study show that derCD23 can accelerate the dissociation of IgE-Fc from  $\alpha$ Fab1 and  $\alpha$ Fab13, we have not investigated the ability of the  $\alpha$ Fabs to accelerate the dissociation of IgE:receptor complexes. To determine if any of the  $\alpha$ Fabs can mediate accelerated dissociation of IgE:CD23 complexes we will perform flow cytometry to detect any decrease in cell-associated fluorescence upon addition of each  $\alpha$ Fab to RPMI 8866 cells that have been pre-incubated with fluorescently-labeled IgE. Performing similar experiments using a rat basophil cell-line that expresses human sFc $\epsilon$ RI $\alpha$  will also indicate whether the  $\alpha$ Fabs can accelerate the dissociation of IgE from Fc $\epsilon$ RI. If any of the  $\alpha$ Fabs do mediate the accelerated dissociation of IgE/receptor interactions, crystal structures of the  $\alpha$ Fab:IgE-Fc complexes are likely to reveal mechanistic details of this potentially practicable phenomenon.

Furthermore, we hope to establish whether the effects of the  $\alpha\epsilon$ Fabs that we have observed in SPR and cell-based assays actually translate to the modulation of IgE-receptor functions. IgE-allergen complexes bind to CD23 on the surface of B cells and are internalised, processed and presented to  $T_H2$  cells in a process known as facilitated antigen presentation. This process results in the activation and propagation of a  $T_H2$  allergic response (Section 1.1.1). We plan to use the facilitated antigen binding (FAB) assay to obtain an indirect readout of the antigen presenting capacity of B cells to T cells in the presence and absence of the different  $\alpha\epsilon$ Fabs. The FAB assay uses flow cytometry to detect the amount of binding of allergen:IgE complexes to CD23 on the surface of B cells, and although it does not directly measure antigen presentation to T cells it has been shown to be representative of this process [213].

The findings of this study also indicate that IgE-Fc: $\alpha\epsilon$ Fab3 and IgE-Fc: $\alpha\epsilon$ Fab13 complexes bind Fc $\epsilon$ RI with a lower affinity (Section 5.2.3). We would like to determine what effect these  $\alpha\epsilon$ Fabs have on the level of mast cell degranulation. Using a rat mast cell-line, transfected with alpha chain of human Fc $\epsilon$ RI, we intend to investigate any potential differences in the amount of degranulation that occurs upon incubation with allergen-specific IgE (rIgE) and subsequent allergen (Phl p7) challenge, in the presence and absence of the  $\alpha\epsilon$ Fabs [214, 215].

IgE/CD23 and IgE/Fc $\epsilon$ RI interactions are also thought to be important in initiated cell-mediated killing of infected and foreign cells during parasitic infections (Section 1.1.1). We intend to perform experiments using flow cytometry to ascertain any potential effect that each of the  $\alpha\epsilon$ Fabs may have on antibody-dependent tumour cell killing by cytotoxicity and phagocytosis. Tumour target cells are fluorescently-labeled and mixed with effector cells and a tumour antigen-specific IgE. Following incubation, the effector cells are stained with a different fluorescently-conjugated antibody and dead cells are labeled with propidium iodide. The three different fluorescent stains can be differentiated by flow cytometry and the dead and phagocytosed tumour cells can be counted [216].

## Concluding remarks

IgE and its receptors, Fc $\epsilon$ RI and CD23, are central molecules in the mechanisms of allergic disease. Using UCB's Core Antibody Discovery Process we have successfully generated a small panel of  $\alpha$ Fabs that bind IgE-Fc with high affinities and that allosterically modulate the interaction between IgE and CD23. We have characterised how each of the  $\alpha$ Fabs binds IgE-Fc, and using SPR and cell-based assays we have also characterised how each  $\alpha$ Fab affects the IgE/CD23 interaction. Our findings provide further evidence that IgE-Fc is conformationally heterogeneous and that IgE/receptor interactions can be perturbed by the manipulation of IgE-Fc's conformational ensemble. We emphasise that IgE-Fc is highly amenable to allosteric regulation as a result of its conformational plasticity, and consequently understanding allostery in IgE-Fc is fundamental to understanding how IgE mediates allergic disease.

We propose that small-scale intra-domain movements, as well as larger-scale rigid-body motions, contribute towards allosteric mechanisms in IgE. For the first time, we provide evidence that allosteric communication can occur between different domains of IgE-Fc, which raises the question of the biological role of long-range allostery in IgE. In addition we show that accelerated dissociation of IgE-Fc complexes can be allosterically driven. Understanding the mechanisms of accelerated dissociation of IgE-Fc complexes may provide insights into how to disrupt pre-existing IgE/receptor interactions, which may be a novel way of targeting IgE in the design of therapeutics for asthma and allergy.

Using X-ray crystallography we hope to determine the structural basis of the allosterically-mediated accelerated dissociation of  $\alpha$ Fab13:IgE-Fc complexes by CD23, as well as the structural basis of the allosteric modulation of IgE/CD23 interaction by the  $\alpha$ Fabs. Crystallisation trials of the  $\alpha$ Fab:IgE-Fc complexes were recently set up and are already looking promising: we have collected data for an  $\alpha$ Fab2:IgE-Fc complex and they appear to describe a new conformation of IgE-Fc.

Allosteric perturbations may involve conformational changes anywhere on the dynamic continuum and may even be manifested as changes in the frequency and

amplitude of very fast thermal fluctuations. Whilst X-ray crystallography can be used to describe rigid-body movements and intra-domain motions in atomic detail, NMR spectroscopy can study dynamic processes that occur on a wide range of timescales. Producing isotopically-labeled IgE-Fc for NMR studies has been difficult because it is usually expressed in mammalian or insect cell-lines as a consequence of its complicated glycosylation and disulphide chemistry. The McDonnell laboratory, however, has recently produced sufficient amounts of isotopically-labeled IgE-Fc for NMR spectroscopy experiments. Using a combination of X-ray crystallography and NMR we will reveal the allosteric mechanisms by which the  $\alpha$ Fabs modulate IgE/CD23 binding, and in doing so discover the range of dynamic processes that occur in IgE and which are fundamental to its role in allergy and asthma.



# Appendix

## A.1 IgE-Fc protein sequence

232  
VASRDFTPPTVKILQSSCDGGGHFPPTIQLLCLVSGYTPGTIQITWLEDGQVMDVDLSTASTTQEG  
ELASTQSELTLSQKHWSDRITYTCQVTYQGHTFEDSTKKCADSN<sup>329</sup>PRGVSAYLSRPSFDLFIRKSPT<sup>333</sup>  
ITCLVVDLAPSKGTVQLTWSRASGKPVNHSTRKEEKQRNGTLTSTLPVGTDRDWIEGETYQCRVT  
THPHLPRALMRSTTKTSGPRAA<sup>437</sup>PEVYAFATPEWPGSRDKRTLACLIQNFMPEDISVQWLHNEVQ<sup>443</sup>  
LPDARHSTTQPRKTKGSGFFVFSRLEVTRAWEQKDEFICRAVHEAASPSQTVQRAVS<sup>542</sup>VNPGK

Figure 1: **The protein sequence of a single IgE-Fc chain (N265Q, N371Q background)**. The C $\epsilon$ 2 domain is in green (residues 232-239), the C $\epsilon$ 3 domain is in black (residues 333-437) and the C $\epsilon$ 4 domain is in blue (residues 443-542).

## A.2 SPR analysis of the interaction between IgE-Fc and unpurified $\alpha$ Fabs

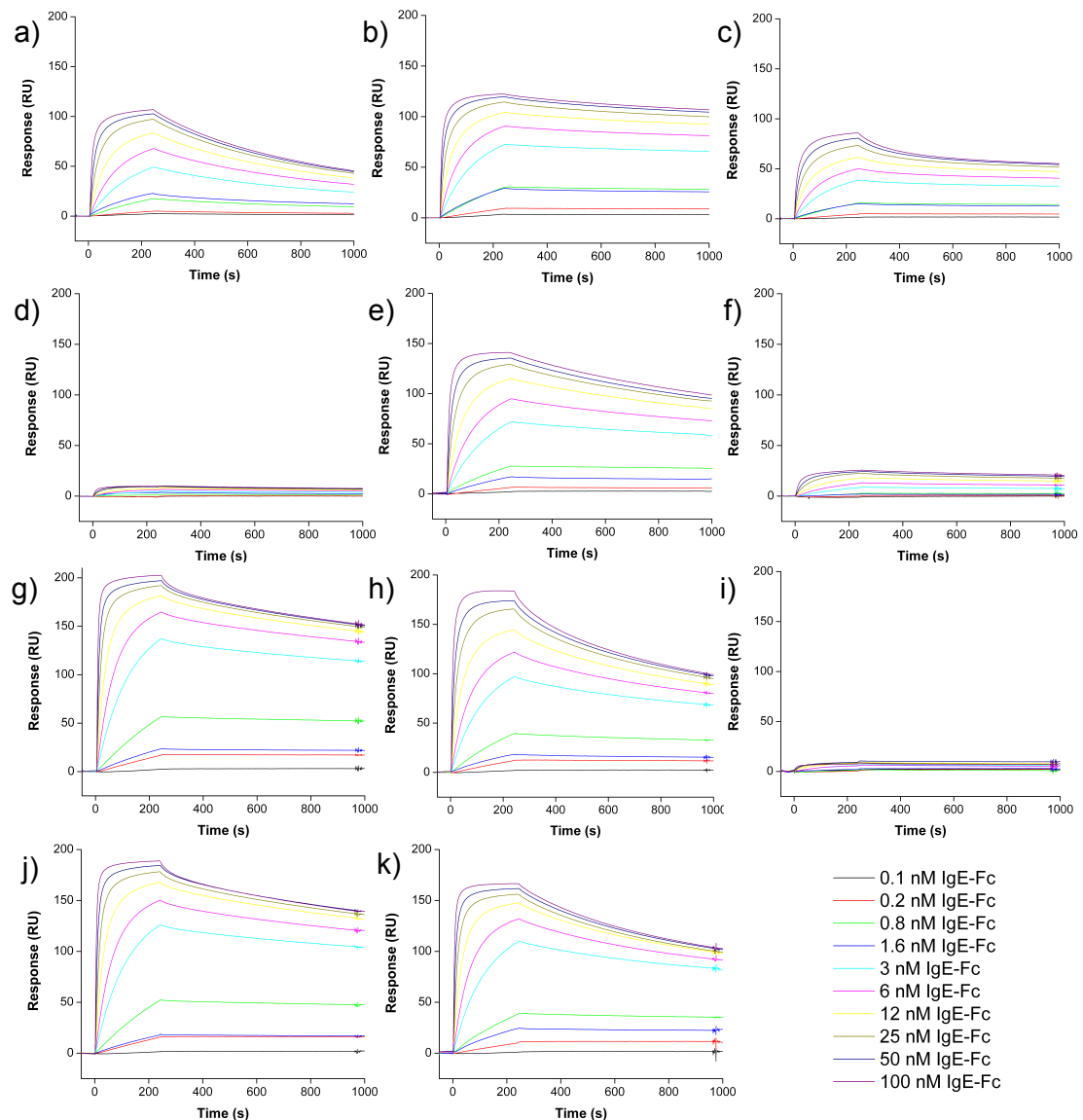


Figure 2: **Reference-subtracted sensorgrams from SPR experiments investigating the binding of IgE-Fc to  $\alpha$ Fabs in transient transfection supernatant.** Transient supernatants containing  $\alpha$ Fabs were injected over a Fab-specific goat anti-rabbit F(ab')<sub>2</sub>. IgE-Fc was injected over the captured  $\alpha$ Fab and binding was observed as a change in SPR response. In each case the response for the binding of 0 nM IgE-Fc to the respective  $\alpha$ Fab was subtracted to eliminate changes in response as a result of dissociation of  $\alpha$ Fab from the anti-rabbit-Fab surface. The sensorgrams have not been normalised for  $\alpha$ Fab capture levels. (a)  $\alpha$ Fab3, (b)  $\alpha$ Fab4, (c)  $\alpha$ Fab5, (d)  $\alpha$ Fab6, (e)  $\alpha$ Fab7, (f)  $\alpha$ Fab9, (g)  $\alpha$ Fab12, (h)  $\alpha$ Fab13, (i)  $\alpha$ Fab14, (j)  $\alpha$ Fab17, (k)  $\alpha$ Fab18

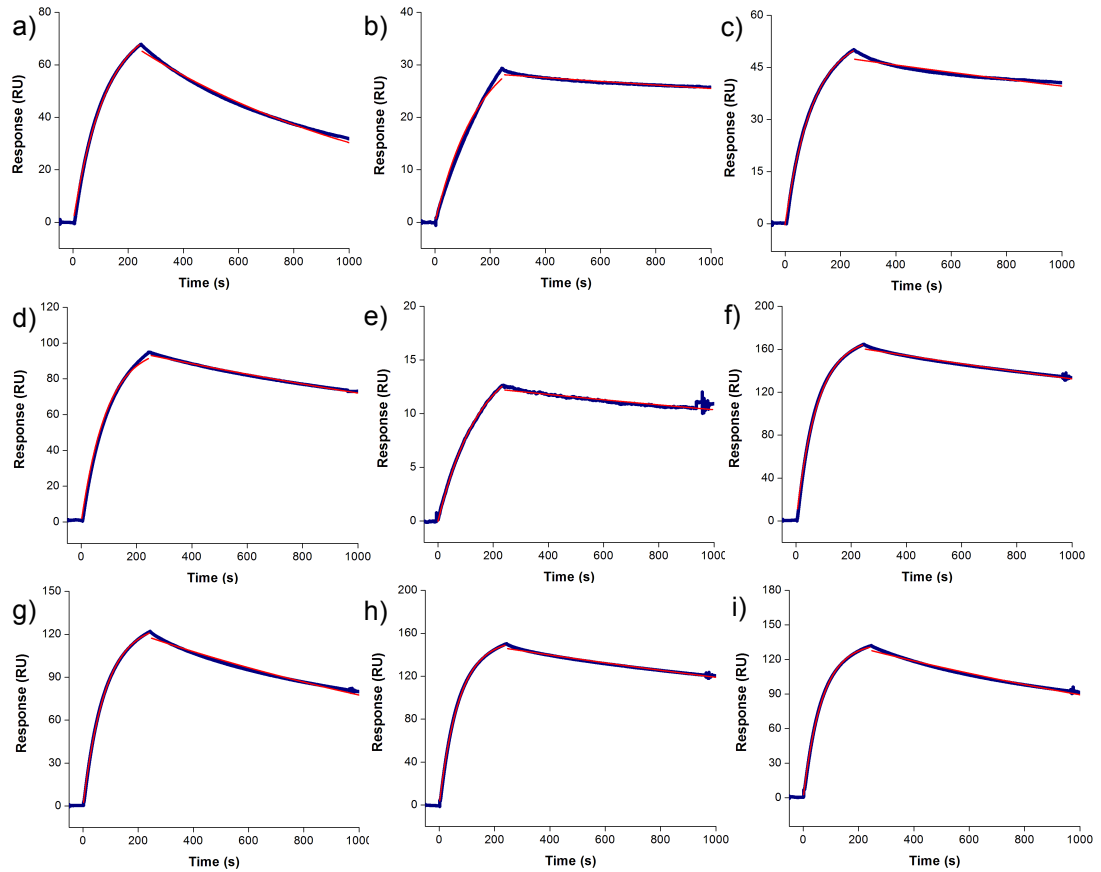


Figure 3: **Fitting the kinetic data for the interaction between IgE-Fc and aεFabs in transient transfection supernatant.** A Single  $k_{\text{off}}$  and  $k_{\text{on}}$  model was used to fit SPR data for the binding of 6 nM IgE-Fc to captured aεFab. The data is shown in blue and the fits are shown in red. (a) aεFab3,  $k_{\text{on}} = 1.4 \times 10^6 \text{ M}^{-1}\text{s}^{-1}$ ,  $k_{\text{off}} = 9.9 \times 10^{-4} \text{ s}^{-1}$ , (b) aεFab4,  $k_{\text{on}} = 1.1 \times 10^6 \text{ M}^{-1}\text{s}^{-1}$ ,  $k_{\text{off}} = 1.7 \times 10^{-4} \text{ s}^{-1}$ , (c) aεFab5,  $k_{\text{on}} = 1.6 \times 10^6 \text{ M}^{-1}\text{s}^{-1}$ ,  $k_{\text{off}} = 4.9 \times 10^{-4} \text{ s}^{-1}$ , (d) aεFab7,  $k_{\text{on}} = 2.0 \times 10^6 \text{ M}^{-1}\text{s}^{-1}$ ,  $k_{\text{off}} = 2.7 \times 10^{-4} \text{ s}^{-1}$ , (e) aεFab9,  $k_{\text{on}} = 1.1 \times 10^6 \text{ M}^{-1}\text{s}^{-1}$ ,  $k_{\text{off}} = 2.4 \times 10^{-4} \text{ s}^{-1}$ , (f) aεFab12,  $k_{\text{on}} = 2.3 \times 10^6 \text{ M}^{-1}\text{s}^{-1}$ ,  $k_{\text{off}} = 2.4 \times 10^{-4} \text{ s}^{-1}$ , (g) aεFab13,  $k_{\text{on}} = 8.4 \times 10^5 \text{ M}^{-1}\text{s}^{-1}$ ,  $k_{\text{off}} = 6.4 \times 10^{-4} \text{ s}^{-1}$ , (h) aεFab17,  $k_{\text{on}} = 2.7 \times 10^6 \text{ M}^{-1}\text{s}^{-1}$ ,  $k_{\text{off}} = 2.4 \times 10^{-4} \text{ s}^{-1}$ , (i) aεFab18,  $k_{\text{on}} = 1.7 \times 10^6 \text{ M}^{-1}\text{s}^{-1}$ ,  $k_{\text{off}} = 6.3 \times 10^{-4} \text{ s}^{-1}$ .

### A.3 SPR analysis of the interactions between derCD23 and IgE-Fc bound to unpurified $\alpha\epsilon$ Fabs

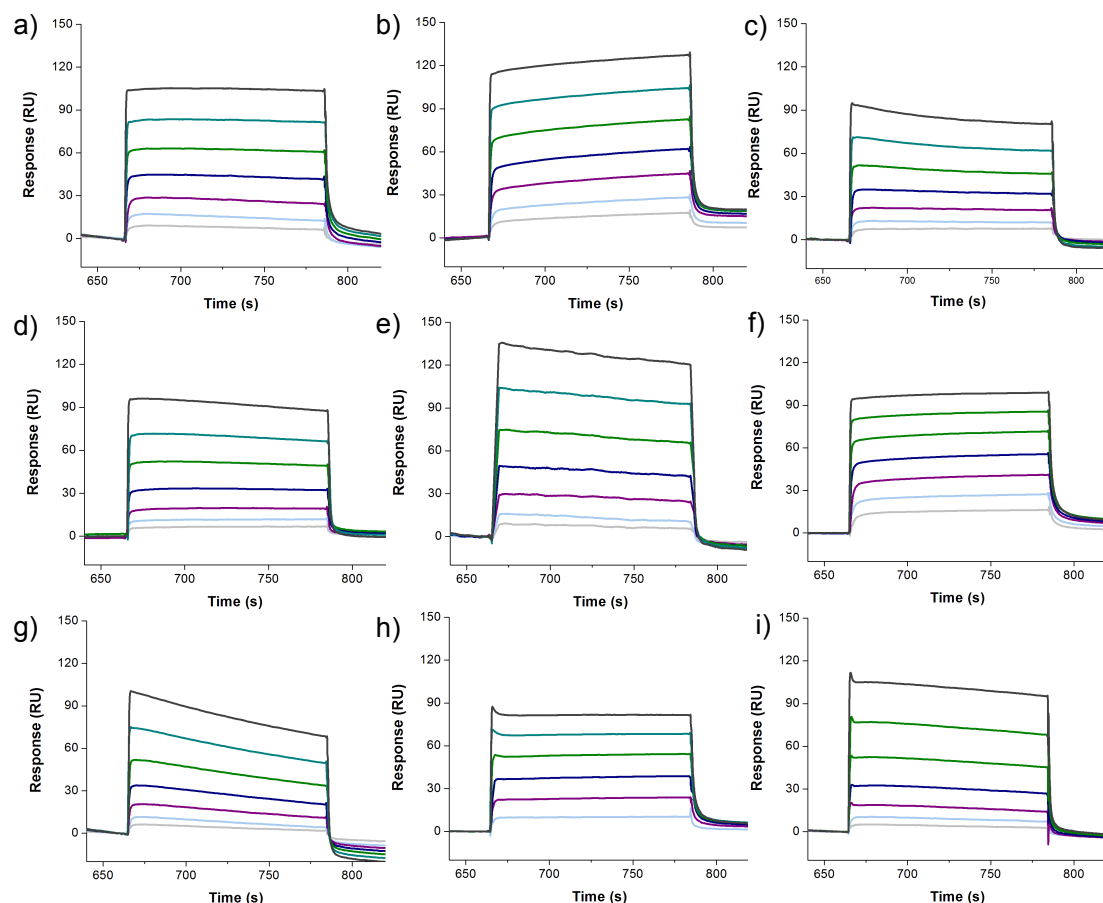


Figure 4: **Reference-subtracted sensorgrams from SPR experiments investigating the binding of derCD23 to  $\alpha\epsilon$ Fab-bound IgE-Fc.** Transient supernatants containing  $\alpha\epsilon$ Fabs were injected over a Fab-specific goat anti-rabbit  $F(ab')_2$ . IgE-Fc was injected over the captured  $\alpha\epsilon$ Fab. derCD23 was then injected over the  $\alpha\epsilon$ Fab:IgE-Fc (1:1) complex at various concentrations (grey - 0.78 nM, light blue - 156 nM, purple - 312 nM, navy - 625 nM, green - 1250 nM, cyan - 2500 nM, black - 5000 nM) and binding was observed as a change in SPR response. IgE-Fc was injected over the captured  $\alpha\epsilon$ Fab at various concentrations, and binding was observed as a change in SPR response. In each case the response for the binding of 0 nM derCD23 to the respective  $\alpha\epsilon$ Fab:IgE-Fc complex was subtracted to eliminate changes in response as a result of dissociation of  $\alpha\epsilon$ Fab from the anti-rabbit-Fab surface and IgE-Fc from the  $\alpha\epsilon$ Fab. The sensorgrams for the binding of derCD23 have been normalised such that the maximum response for the binding of IgE-Fc to  $\alpha\epsilon$ Fab was 450 RU. (a)  $\alpha\epsilon$ Fab3, (b)  $\alpha\epsilon$ Fab4, (c)  $\alpha\epsilon$ Fab5, (d)  $\alpha\epsilon$ Fab7, (e)  $\alpha\epsilon$ Fab9, (f)  $\alpha\epsilon$ Fab12, (g)  $\alpha\epsilon$ Fab13, (h)  $\alpha\epsilon$ Fab17, (i)  $\alpha\epsilon$ Fab18.

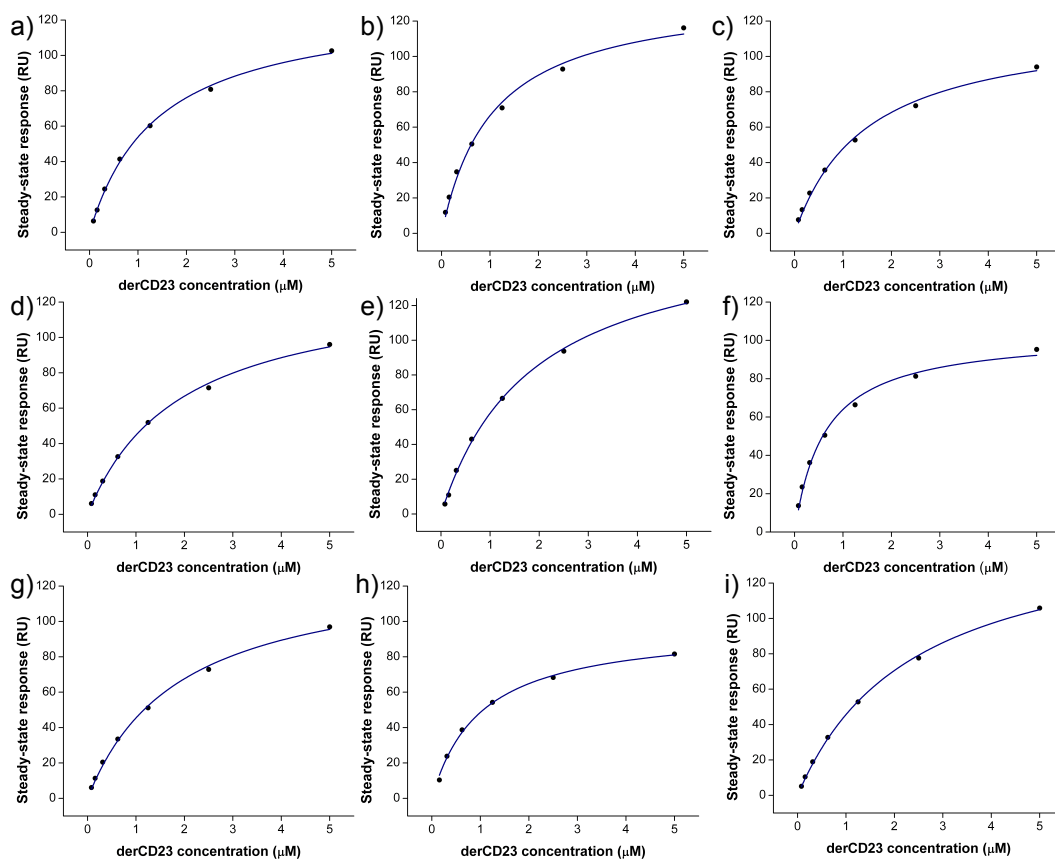


Figure 5: **Binding curves for the interactions between derCD23 and  $\alpha\epsilon$ Fab-bound IgE-Fc.** The data were generated from SPR experiments in which derCD23 binding to captured  $\alpha\epsilon$ Fab:IgE-Fc (1:1) complexes was measured as a change in response. The steady-state response was averaged from 5 s of the steady-state binding data (circle) and fit (lines) using a one-to-one binding model. The steady-state binding data had been normalised such that the maximum response for binding of IgE-Fc to  $\alpha\epsilon$ Fab was 450 RU. (a)  $\alpha\epsilon$ Fab3,  $K_D = 1.4 \mu\text{M}$ ,  $B_{\text{max}} = 130$  RU. (b)  $\alpha\epsilon$ Fab4,  $K_D = 1.1 \mu\text{M}$ ,  $B_{\text{max}} = 138$  RU. (c)  $\alpha\epsilon$ Fab5,  $K_D = 1.4 \mu\text{M}$ ,  $B_{\text{max}} = 118$  RU. (d)  $\alpha\epsilon$ Fab7,  $K_D = 1.9 \mu\text{M}$ ,  $B_{\text{max}} = 133$  RU. (e)  $\alpha\epsilon$ Fab9,  $K_D = 1.4 \mu\text{M}$ ,  $B_{\text{max}} = 130$  RU. (f)  $\alpha\epsilon$ Fab12,  $K_D = 0.6 \mu\text{M}$ ,  $B_{\text{max}} = 105$  RU. (g)  $\alpha\epsilon$ Fab13,  $K_D = 1.9 \mu\text{M}$ ,  $B_{\text{max}} = 133$  RU. (h)  $\alpha\epsilon$ Fab17,  $K_D = 1.0 \mu\text{M}$ ,  $B_{\text{max}} = 97$  RU. (i)  $\alpha\epsilon$ Fab18,  $K_D = 2.4 \mu\text{M}$ ,  $B_{\text{max}} = 156$  RU.

## A.4 SPR analysis of the interactions between Fc $\epsilon$ RI $\alpha$ and IgE-Fc bound to unpurified $\alpha\epsilon$ Fabs

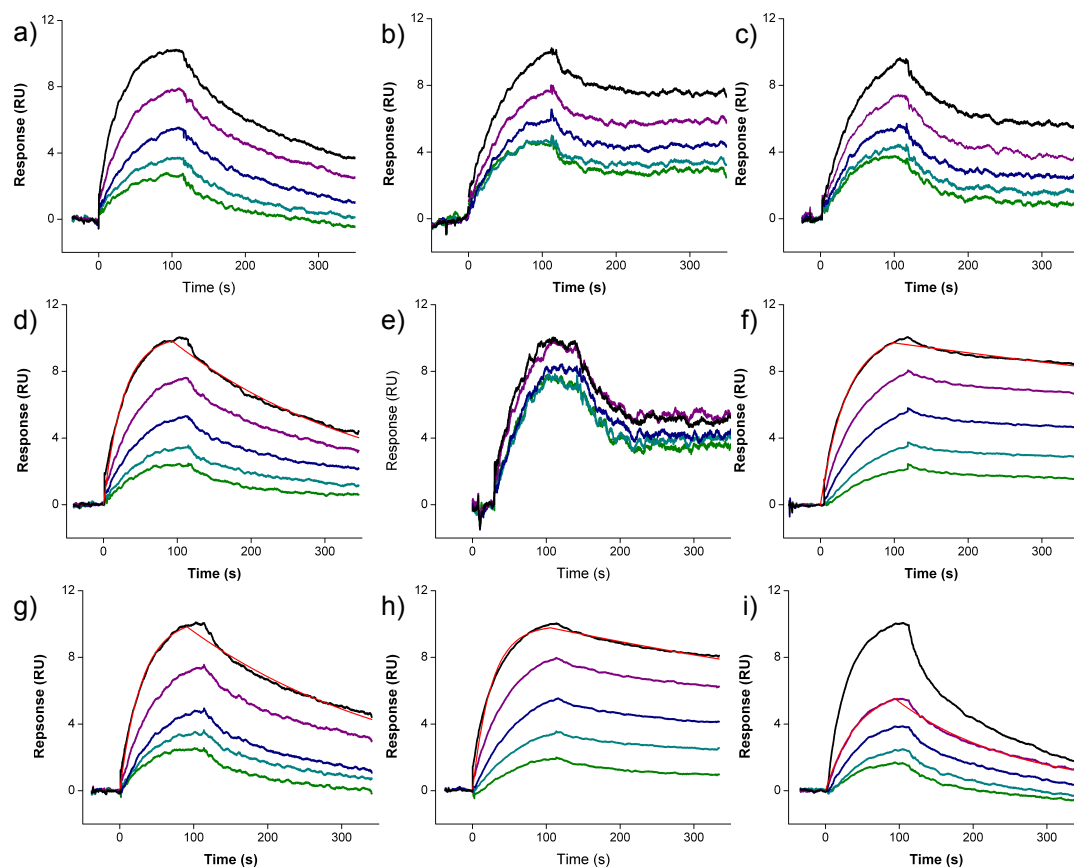


Figure 6: **Reference-subtracted sensorgrams from SPR experiments investigating the binding of sFc $\epsilon$ RI $\alpha$  to  $\alpha\epsilon$ Fab-bound IgE-Fc.** Transient supernatants containing  $\alpha\epsilon$ Fabs were injected over a Fab-specific goat anti-rabbit F(ab')<sub>2</sub>. IgE-Fc was injected over the captured  $\alpha\epsilon$ Fab. derCD23 was then injected over the  $\alpha\epsilon$ Fab:IgE-Fc (1:1) complex at various concentrations (green - 3.13 nM, cyan - 6.25 nM, navy - 12.5 nM, purple - 25 nM, black - 50 nM) and binding was observed as a change in SPR response. In each case the response for the binding of 0 nM sFc $\epsilon$ RI $\alpha$  to the respective  $\alpha\epsilon$ Fab:IgE-Fc complex was subtracted to eliminate changes in response as a result of dissociation of  $\alpha\epsilon$ Fab from the anti-rabbit-Fab surface and IgE-Fc from the  $\alpha\epsilon$ Fab. The data have been normalised to give a maximal response for the binding of 50 nM sFc $\epsilon$ RI $\alpha$  of 10 RU. (a)  $\alpha\epsilon$ Fab3, (b)  $\alpha\epsilon$ Fab4, (c)  $\alpha\epsilon$ Fab5, (d)  $\alpha\epsilon$ Fab7, (e)  $\alpha\epsilon$ Fab9, (f)  $\alpha\epsilon$ Fab12, (g)  $\alpha\epsilon$ Fab13, (h)  $\alpha\epsilon$ Fab17, (i)  $\alpha\epsilon$ Fab18. Single  $k_{\text{off}}$  and  $k_{\text{on}}$  kinetic fits of the data for the binding of 50 nM sFc $\epsilon$ RI $\alpha$  (or 25 nM in the case of  $\alpha\epsilon$ Fab18) are shown in red where applicable (Section 5.2.3).  $\alpha\epsilon$ Fab7  $k_{\text{off}} = 3.5 \times 10^{-3} \text{ s}^{-1}$   $k_{\text{on}} = 6.8 \times 10^5 \text{ s}^{-1}\text{M}^{-1}$ ,  $\alpha\epsilon$ Fab12  $k_{\text{off}} = 6.9 \times 10^{-4} \text{ s}^{-1}$   $k_{\text{on}} = 5.9 \times 10^5 \text{ s}^{-1}\text{M}^{-1}$ ,  $\alpha\epsilon$ Fab13  $k_{\text{off}} = 5.7 \times 10^{-3} \text{ s}^{-1}$   $k_{\text{on}} = 8.3 \times 10^5 \text{ s}^{-1}\text{M}^{-1}$ ,  $\alpha\epsilon$ Fab17  $k_{\text{off}} = 9.9 \times 10^{-4} \text{ s}^{-1}$   $k_{\text{on}} = 5.4 \times 10^5 \text{ s}^{-1}\text{M}^{-1}$ ,  $\alpha\epsilon$ Fab18  $k_{\text{off}} = 4.8 \times 10^{-3} \text{ s}^{-1}$   $k_{\text{on}} = 7.4 \times 10^5 \text{ s}^{-1}\text{M}^{-1}$

## A.5 SPR analysis to investigate $\alpha\epsilon$ Fab competition

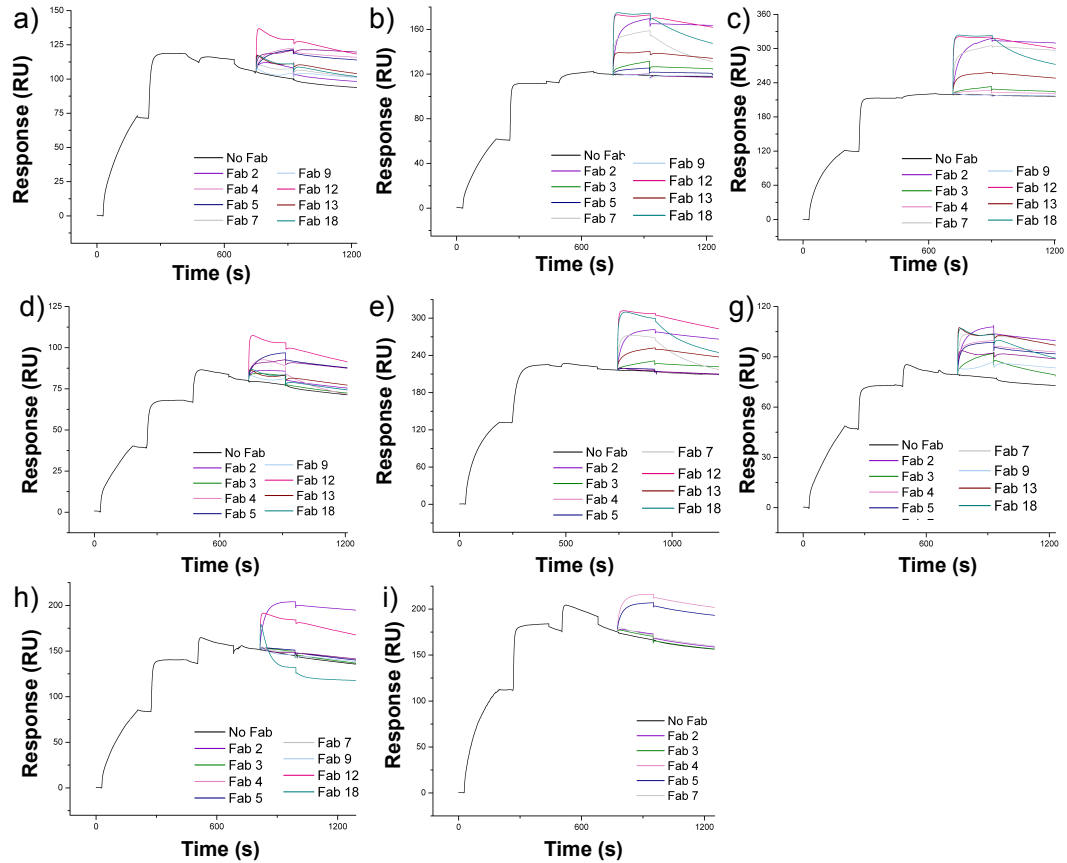


Figure 7: **SPR analysis to investigate  $\alpha\epsilon$ Fab competition.**  $\alpha\epsilon$ Ab, in transiently transfected supernatant, was captured by immobilised IgG-Fc-specific goat-anti-rabbit F(ab')<sub>2</sub> (Jackson ImmunoResearch). IgE-Fc was injected over the captured  $\alpha\epsilon$ Ab to generate an  $\alpha\epsilon$ Ab:IgE-Fc: $\alpha\epsilon$ Fab (1:1:1) complex. Other  $\alpha\epsilon$ Fabs, in transiently transfected supernatant were then injected over the complex and the binding was measured as a change in SPR response. (a)  $\alpha\epsilon$ Ab3:IgE-Fc: $\alpha\epsilon$ Fab3, (b)  $\alpha\epsilon$ Ab4:IgE-Fc: $\alpha\epsilon$ Fab4, (c)  $\alpha\epsilon$ Ab5:IgE-Fc: $\alpha\epsilon$ Fab5, (d)  $\alpha\epsilon$ Ab7:IgE-Fc: $\alpha\epsilon$ Fab7, (e)  $\alpha\epsilon$ Ab9:IgE-Fc: $\alpha\epsilon$ Fab9, (f)  $\alpha\epsilon$ Ab12:IgE-Fc: $\alpha\epsilon$ Fab12, (g)  $\alpha\epsilon$ Ab13:IgE-Fc: $\alpha\epsilon$ Fab13, (h)  $\alpha\epsilon$ Ab18:IgE-Fc: $\alpha\epsilon$ Fab18.

## A.6 Investigating the stoichiometry of the $\alpha\epsilon$ Fab/IgE-Fc interactions

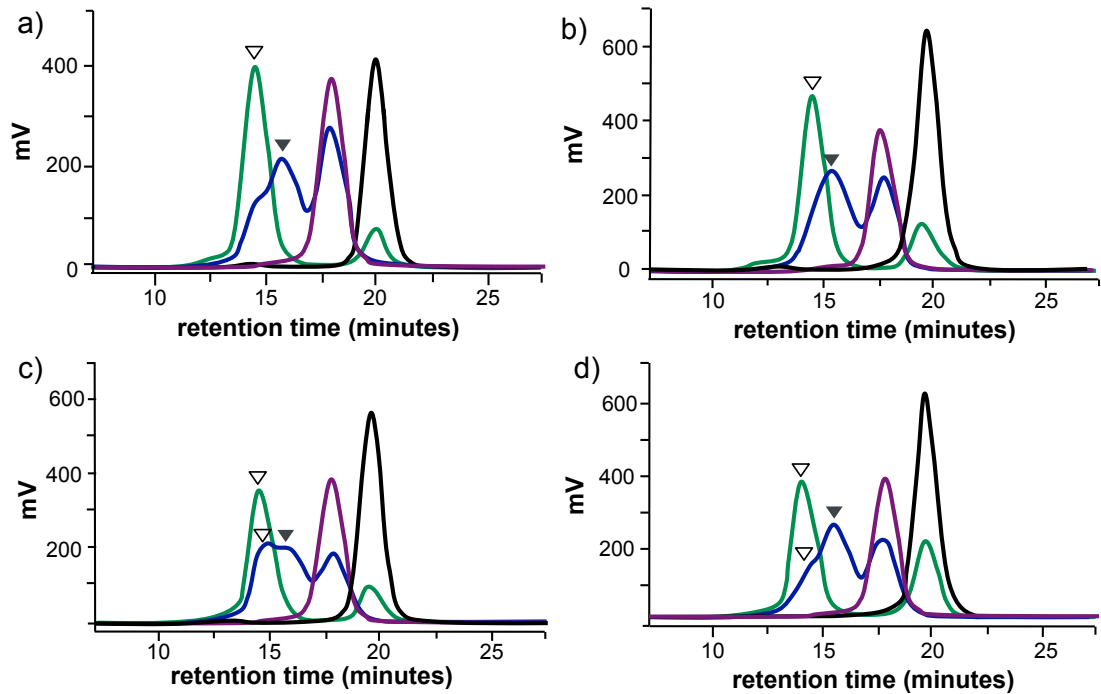


Figure 8: **Size exclusion chromatograms for each  $\alpha\epsilon$ Fab, IgE-Fc and  $\alpha\epsilon$ Fab:IgE-Fc complexes.** Purified  $\alpha\epsilon$ Fab was incubated with purified IgE-Fc overnight at 4 °C at 1:2.4 (blue) and 2.4:1 molar ratios (green). The mixture samples,  $\alpha\epsilon$ Fab alone (black), and purified IgE-Fc (purple), were run down a Superdex S200 10x30 GL SEC column (GE Healthcare) in PBS, pH 7.4. The results suggest the formation of 1:1 (filled triangle) and 2:1  $\alpha\epsilon$ Fab:IgE-Fc complexes (empty triangle) for each  $\alpha\epsilon$ Fab. (a)  $\alpha\epsilon$ Fab3, (b)  $\alpha\epsilon$ Fab12, (c)  $\alpha\epsilon$ Fab13, (d)  $\alpha\epsilon$ Fab18.



## A.7 SPR analysis of the interaction between IgE-Fc and purified $\alpha\epsilon$ Fabs

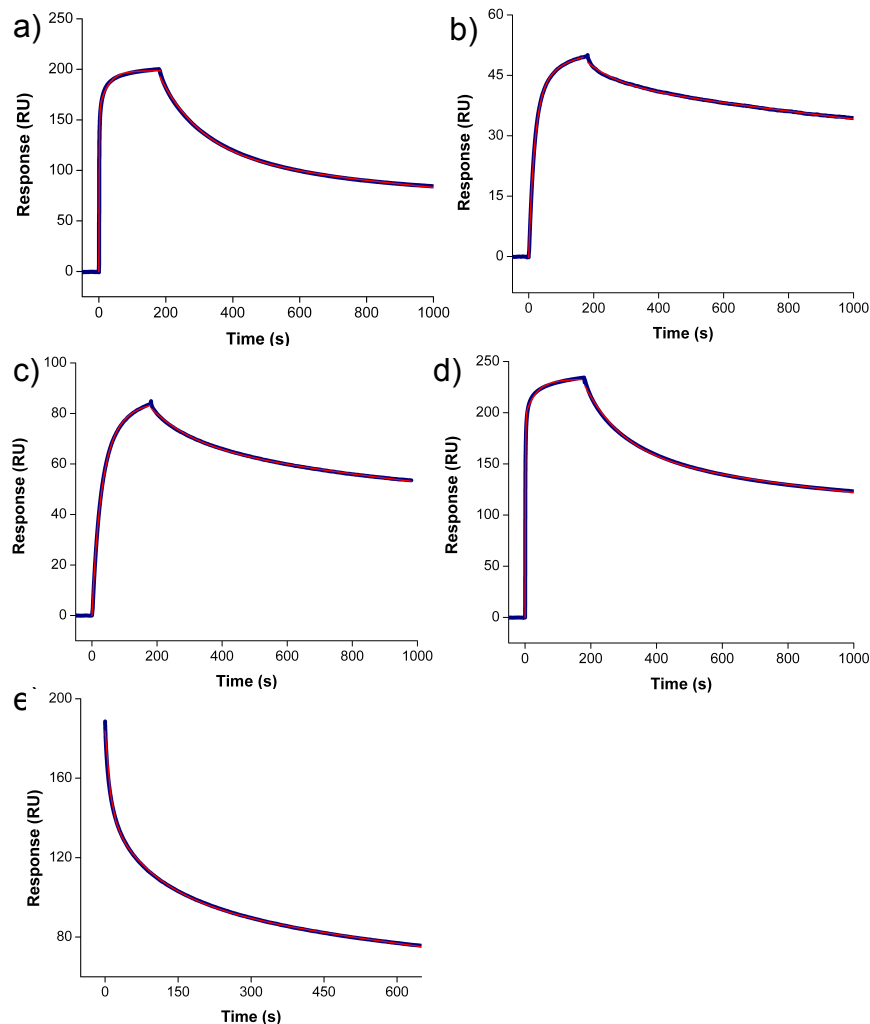


Figure 9: **Fitting the kinetic data for the interaction between IgE-Fc and purified  $\alpha\epsilon$ Fabs.** Purified  $\alpha\epsilon$ Fabs were injected over a Fab-specific goat anti-rabbit  $F(ab')_2$ . IgE-Fc was injected over the captured  $\alpha\epsilon$ Fab at various concentrations, and binding was observed as a change in SPR response (shown here). The data (blue) were fit using double  $k_{off}$  and double  $k_{on}$  models (red) (a-d) and the dissociation of  $2 \mu\text{M}$  IgE-Fc from  $\alpha\epsilon$ Fab13 was fit to a triple  $k_{off}$  model (e). (a)  $2 \mu\text{M}$  IgE-Fc to  $\alpha\epsilon$ Fab3,  $k_{off1} = 3.7 \times 10^{-4} \text{ s}^{-1}$ ,  $k_{off2} = 7.6 \times 10^{-3} \text{ s}^{-1}$ ,  $k_{on1} = 4.8 \times 10^5 \text{ M}^{-1} \text{ s}^{-1}$ ,  $k_{on2} = 1.9 \times 10^4 \text{ M}^{-1} \text{ s}^{-1}$ . (b)  $8 \text{ nM}$  IgE-Fc  $\alpha\epsilon$ Fab12,  $k_{off1} = 1.5 \times 10^{-4} \text{ s}^{-1}$ ,  $k_{off2} = 6.5 \times 10^{-3} \text{ s}^{-1}$ ,  $k_{on1} = 6.9 \times 10^5 \text{ M}^{-1} \text{ s}^{-1}$ ,  $k_{on2} = 8.2 \times 10^3 \text{ M}^{-1} \text{ s}^{-1}$ . (c)  $8 \text{ nM}$  IgE-Fc to  $\alpha\epsilon$ Fab13,  $k_{off1} = 2.8 \times 10^{-4} \text{ s}^{-1}$ ,  $k_{off2} = 7.9 \times 10^{-3} \text{ s}^{-1}$ ,  $k_{on1} = 2.2 \times 10^6 \text{ M}^{-1} \text{ s}^{-1}$ ,  $k_{on2} = 4.7 \times 10^3 \text{ M}^{-1} \text{ s}^{-1}$ . (d)  $2 \mu\text{M}$  IgE-Fc to  $\alpha\epsilon$ Fab18,  $k_{off1} = 3.0 \times 10^{-4} \text{ s}^{-1}$ ,  $k_{off2} = 8.2 \times 10^{-3} \text{ s}^{-1}$ ,  $k_{on1} = 4.6 \times 10^5 \text{ M}^{-1} \text{ s}^{-1}$ ,  $k_{on2} = 1.0 \times 10^4 \text{ M}^{-1} \text{ s}^{-1}$ . (e) The dissociation of  $2 \mu\text{M}$  IgE-Fc from  $\alpha\epsilon$ Fab13 is well described by a triphasic model for dissociation.

## A.8 Repeat SPR experiment for the binding of IgE-Fc (3-4) to $\alpha\epsilon$ Fab12

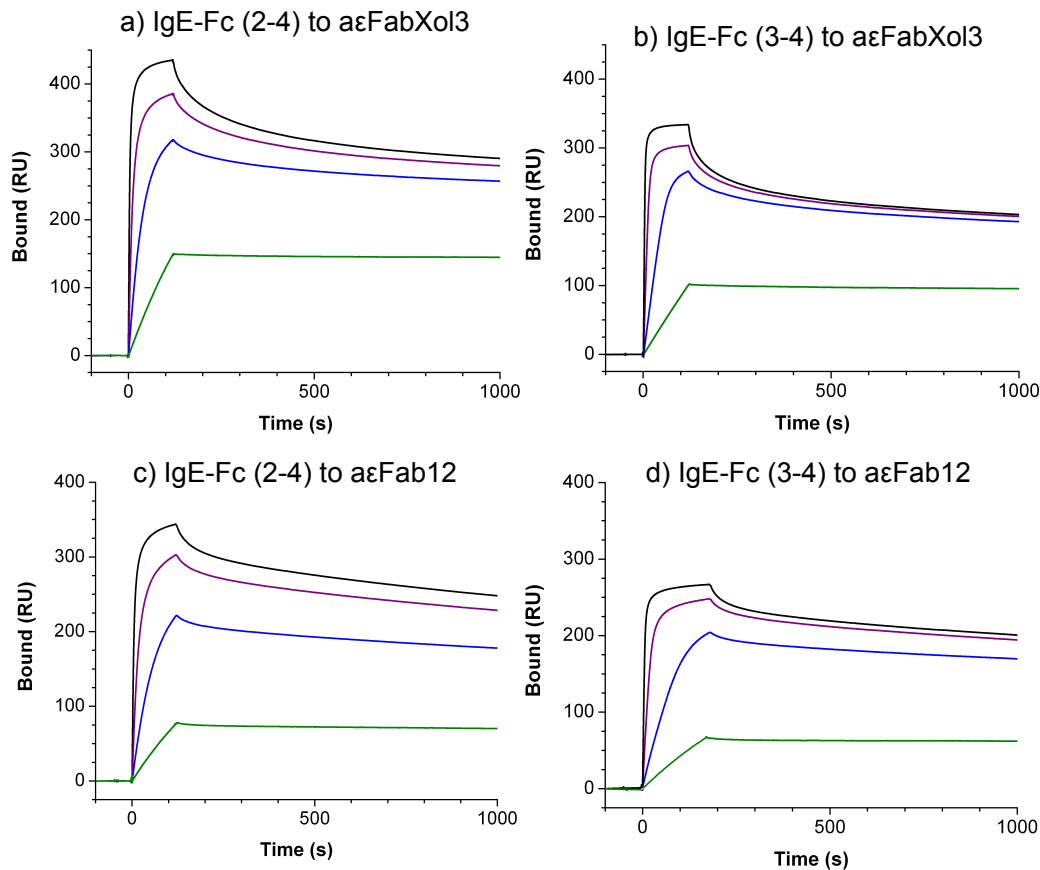


Figure 10: **IgE-Fc (3-4) binds  $\alpha\epsilon$ Fab12 in a repeated SPR binding experiment.** Double reference-subtracted sensorgrams for the binding of full length IgE-Fc to Xolair Fab Mutant 3 ( $\alpha\epsilon$ FabXol3) and  $\alpha\epsilon$ Fab12 are shown in (a) and (c), respectively. IgE-Fc was injected over the surfaces at concentrations of 200 nM (black), 50 nM (purple), 12.5 nM (blue), 3.1 nM (green). Double reference-subtracted sensorgrams for the binding of IgE-Fc (3-4) to Xolair Fab Mutant 3 and  $\alpha\epsilon$ Fab12 are shown in (b) and (d), respectively. IgE-Fc (3-4) was injected over the surfaces at concentrations of 200 nM (black), 50 nM (purple), 12.5 nM (blue), 3.1 nM (green). The sensorgrams have not been normalised for the difference in mass between IgE-Fc and IgE-Fc (3-4). Here, Xolair Fab Mutant 3 is a positive control for binding to IgE-Fc (3-4): X-ray crystallography shows the symmetrical Xolair Fab Mutant 3 binding sites are centred on the C $\epsilon$ 3 domains of IgE-Fc [82]. Xolair Fab mutant 3 was immobilised onto the sensor surface using amine coupling.  $\alpha\epsilon$ Fab12 was captured by a goat anti-rabbit-Fab surface. Both  $\alpha\epsilon$ Fab12 and Xolair Fab Mutant 3 were present at densities of approximately 400 RU.

## A.9 Repeat SPR experiment for the binding of the C $\epsilon$ 2 dimer to $\alpha\epsilon$ Fab12

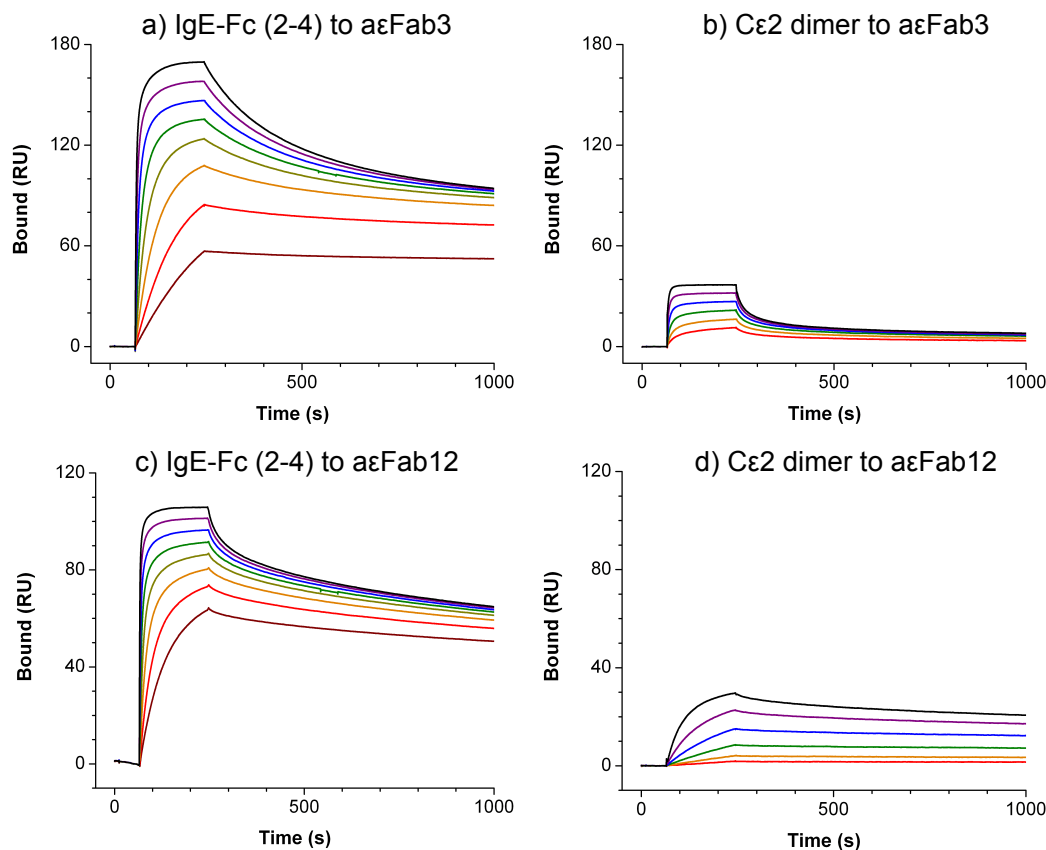


Figure 11: **The C $\epsilon$ 2 dimer binds  $\alpha\epsilon$ Fab12 in a repeated SPR binding experiment.**  $\alpha\epsilon$ Fab3 and  $\alpha\epsilon$ Fab12 were immobilised on separate sensor surfaces using amine coupling at densities below 400 RU. Double-reference subtracted sensorgrams for the binding of full length IgE-Fc to  $\alpha\epsilon$ Fab3 and  $\alpha\epsilon$ Fab12 surfaces are shown in (a) and (c), respectively. Full length IgE-Fc was injected over the surfaces at concentrations of 100 nM (black), 50 nM (purple), 25 nM (blue), 12.5 nM (green), 6.25 nM (olive), 3.13 nM (orange), 1.56 nM (red) and 0.78 nM (brown). Double-reference subtracted sensorgrams for the binding of the C $\epsilon$ 2 domain pair of IgE-Fc to  $\alpha\epsilon$ Fab3 and  $\alpha\epsilon$ Fab12 surfaces are shown in (b) and (d), respectively. The C $\epsilon$ 2 dimer was injected over the surfaces at concentrations of 4,000 nM (black), 2,000 nM (purple), 1,000 nM (blue), 500 nM (green), 250 nM (orange) and 125 nM (red). The sensorgrams have not been normalised for the difference in mass between IgE-Fc and the C $\epsilon$ 2 dimer.

## A.10 IgE/mCD23 inhibition assays

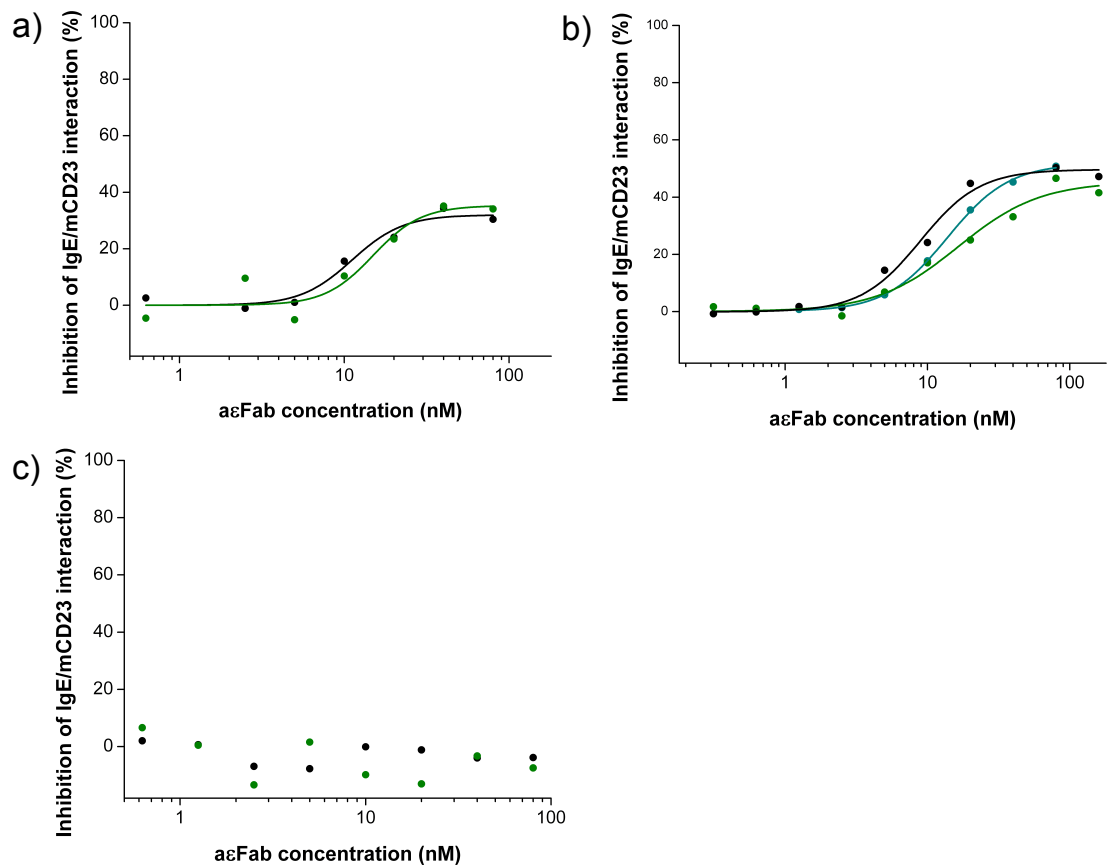


Figure 12: **IgE/mCD23 inhibition assays.** RPMI cells, expressing mCD23, were incubated on ice for one hour with 12 nM rIgE-A647 and increasing concentrations of each aεFab. The cells were washed twice with buffer and the fluorescence of single live cells was read by flow cytometry. Reduction in MFI was assumed to be the result of inhibition of the rIgE-A647/mCD23 interaction. The experiments were performed two or three times for each aεFab, and the results of these repeats are given in different colours. The data were fit to four parametric logistic curves where applicable. Concentration-dependent inhibition was observed for aεFab12 and aεFab13, but not for aεFab18.

## A.11 SPR experiments investigating the binding of derCD23 to $\alpha\epsilon$ Fab:IgE-Fc (1:1) complexes

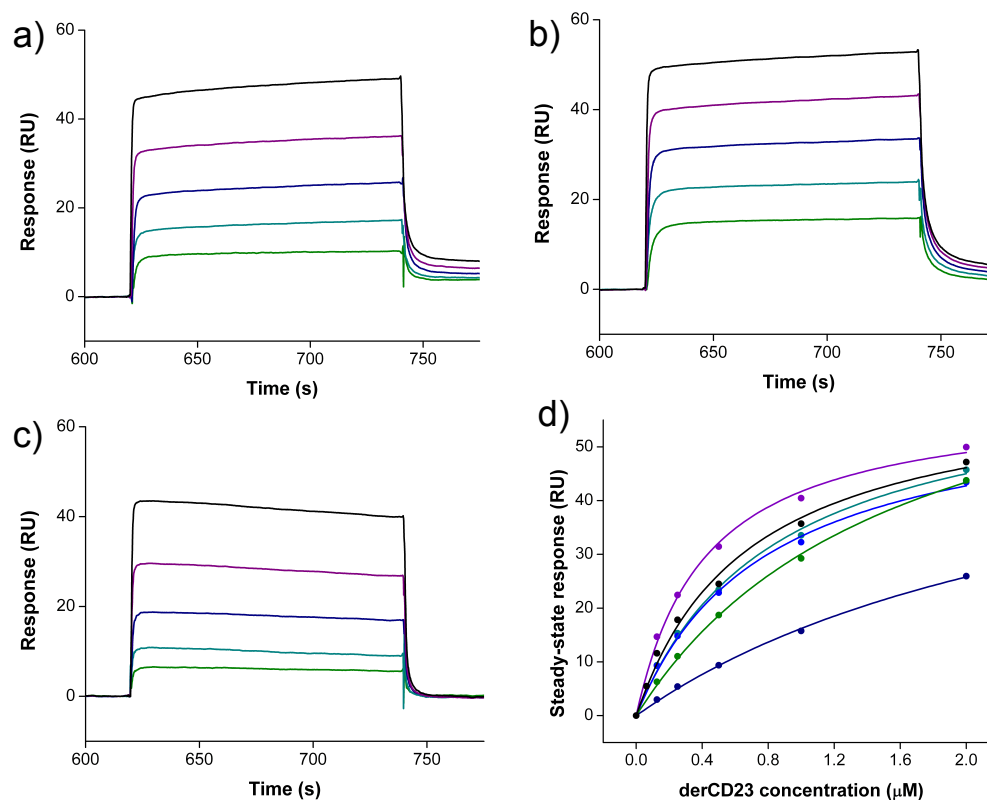


Figure 13: **SPR experiments investigating the binding of derCD23 to  $\alpha\epsilon$ Fab:IgE-Fc (1:1) complexes.** Purified  $\alpha\epsilon$ Fabs were injected over a Fab-specific goat anti-rabbit F(ab')<sub>2</sub>. IgE-Fc was injected over the captured  $\alpha\epsilon$ Fab. derCD23 was then injected over the  $\alpha\epsilon$ Fab:IgE-Fc (1:1) complex at various concentrations (green - 125 nM, cyan- 250 nM, navy - 500 nM, purple 1000 nM, black - 2000 nM) and binding was observed as a change in SPR response. The double-subtracted sensorgrams for the binding of derCD23 (a-c) have been normalised such that the maximum response for the binding of IgE-Fc to  $\alpha\epsilon$ Fab was 360 RU. (a)  $\alpha\epsilon$ Fab3, (b)  $\alpha\epsilon$ Fab12, (c)  $\alpha\epsilon$ Fab18. (d) The various steady-state responses for the binding of derCD23 to the different  $\alpha\epsilon$ Fab1:IgE-Fc (1:1) complexes (dots) were fit (lines) using a single binding site model, as was the steady-state binding responses for the same derCD23 concentrations binding to anti-histidine captured His-IgE-Fc. The steady state binding responses in all cases were normalised for the binding of 360 RU of IgE-Fc (or His-IgE-Fc). Black - anti-histidine bound His-IgE-Fc, navy -  $\alpha\epsilon$ Fab2:IgE-Fc, cyan -  $\alpha\epsilon$ Fab3:IgE-Fc, purple -  $\alpha\epsilon$ Fab12:IgE-Fc, blue -  $\alpha\epsilon$ Fab13:IgE-Fc, green -  $\alpha\epsilon$ Fab18:IgE-Fc.

## A.12 Analytical HPLC SEC analysis of $\alpha\epsilon$ Fab:IgE-Fc (2:1) complex preparative SEC fractions

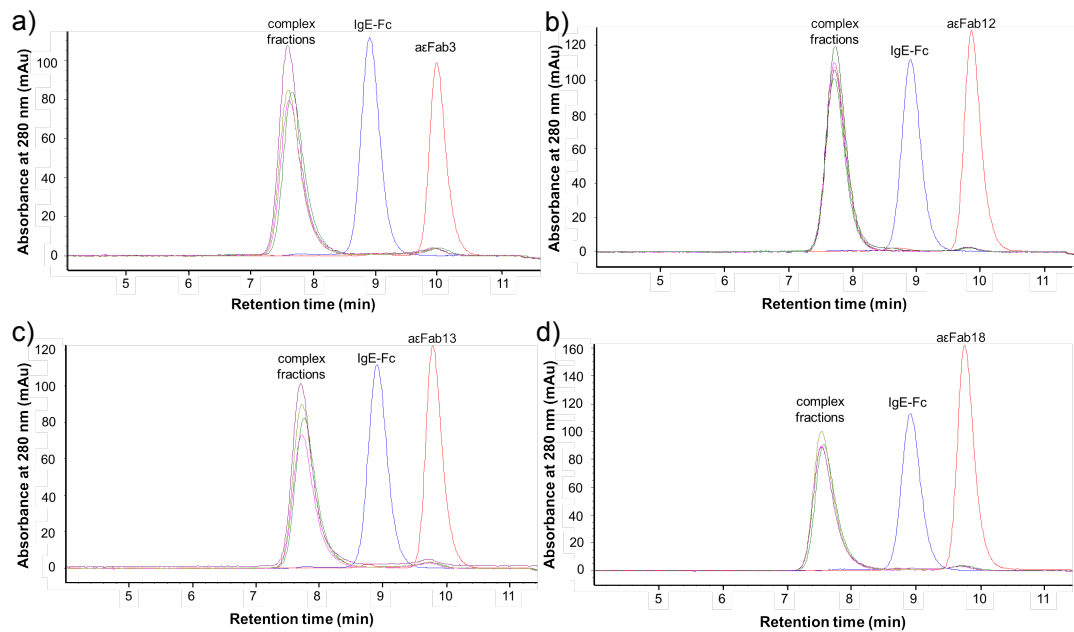


Figure 14: **Analytical HPLC SEC analysis of  $\alpha\epsilon$ Fab:IgE-Fc (2:1) complex preparative SEC fractions.** Each  $\alpha\epsilon$ Fab, IgE-Fc and peak fractions from each SEC of the  $\alpha\epsilon$ Fab2:IgE-Fc (2:1) complex were run down a G3000SWxl analytical HPLC SEC column (Tosoh) in 20 mM sodium phosphate 50 mM sodium chloride buffer pH 7.4. The results suggest that the SEC fractions contain the  $\alpha\epsilon$ Fab:IgE-Fc (2:1) complexes with a very small proportion of unbound  $\alpha\epsilon$ Fab

## A.13 SPR experiments investigating the binding of derCD23 to $\alpha\epsilon$ Fab:IgE-Fc (2:1) complexes

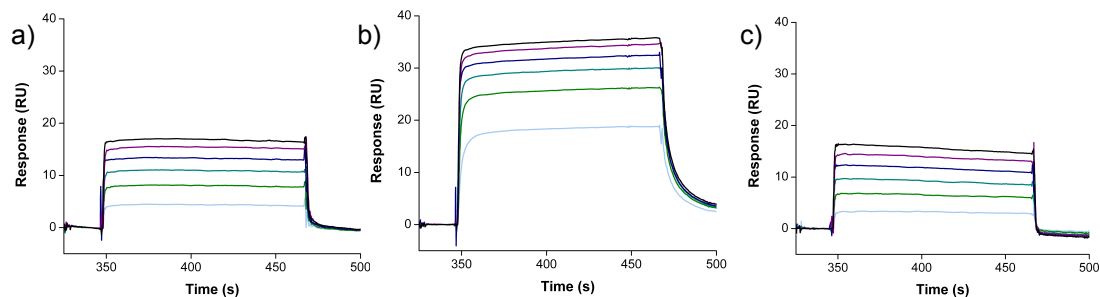


Figure 15: **Double-subtracted SPR sensorgrams for the binding of derCD23 to  $\alpha\epsilon$ Fab:IgE-Fc (2:1) complexes.** Purified  $\alpha\epsilon$ Fab:IgE-Fc (2:1) complexes were injected over a Fab-specific goat anti-rabbit F(ab')<sub>2</sub>. derCD23 was then injected over the  $\alpha\epsilon$ Fab:IgE-Fc (2:1) complexes at various concentrations (light blue - 200 nM, green - 500 nM, cyan - 800 nM, navy - 1100 nM, purple 1400 nM, black - 1700 nM) and binding was observed as a change in SPR response. The sensorgrams have been normalised such that the maximum response for the binding of IgE-Fc to  $\alpha\epsilon$ Fab was 400 RU. (a)  $\alpha\epsilon$ Fab3, (b)  $\alpha\epsilon$ Fab12, (c)  $\alpha\epsilon$ Fab18.

## A.14 Protein sequence alignment of human and rabbit IgE-Fc

Human	1	DIVASRDFTPPTVKILQSSCDGGGHFPPTIQLLCLVSGYTPGTIQITWLE	50
Rabbit	1	FQACSVSFTPPAVRLFHSSCDPRENDTYTVQLLCLISGYTPGDIEVTWLW	50
Human	51	DGQVMDVDL--STASTTQEGELASTQSELTLSQKHWSLDRITYTCQVTYQG	98
Rabbit	51	DGQ-KDPNMF SITAQPRQEGKLASTHSELNITQGEWASKRTYTCRVAYQG	99
Human	99	HTFEDSTKKCADSNPRGV SAYLSRSPFDL FIRKSPTITCLVVDLAPSKG	148
Rabbit	100	ELFEAHARECTDYEPRGVSTYLSSPSPLDLYVHKSPKLTCLVVDLASEEG	149
Human	149	TVQLTWSRASGKPVNHSTRKEEKQRNGTLT VTSTL PVGTRDWIEGETYQC	198
Rabbit	150	-VSLVWSRDSGKPVDPDPWKS DKQFNATV IIRSTLPVDAQDWIDGEIFKC	198
Human	199	RVTHPHLPRALMRSTTKTSGPRAAPEVYAFATPEW-PGSRDKRTLACLIQ	247
Rabbit	199	TVTHPDLPTAIVRSISK AQGKRAAPEVHLFTPPEEDQGSRDQLTLTCLVQ	248
Human	248	NFMPEDISVQWLHNEVQLP DARHSTQPRKTKGSG--FFVFSRLEVTRAE	295
Rabbit	249	NFFPADIFVDWLRNGQHMPSGQQSTTEPRLAGGSNQTYFVFSRLEVSRAD	298
Human	296	WEQKDEFICRAVHEAASPSQTVQRAVSVNPGK	327
Rabbit	299	WEQNIPFTCRVVHEAVTDTRTLTKTVSKRPGK	330

b)

	Length	Identical residues		Similar residues		Gaps		Score
		number	%	number	%	number	%	
<b>Cε2</b>	102	54	52.9	69	67.6	3	2.9	276.5
<b>Cε3</b>	105	61	38.1	76	72.4	1	1.0	324.0
<b>Cε4</b>	108	58	53.7	72	66.7	3	2.8	292.5

Figure 16: **Protein sequence alignment of human and rabbit (*Oryctolagus cuniculus*) IgE-Fc.** Protein sequence alignment was performed using the online tool EMBOSS Needle [217] with default settings (BLOSUM 62 matrix). a) Alignment of rabbit IgE-Fc protein sequence with the sequence of the human IgE-Fc (N265Q, N371Q) construct. A line between aligned residues indicates that they are identical, two dots between aligned residues indicates that they are similar, one dot indicates the residues are not similar and gaps are represented by white space. b) The different IgE-Fc domains (defined in A.1) of human and rabbit IgE-Fc were also aligned separately. The sequence alignment of the human and rabbit Cε2 domains gave the lowest score, indicating that they are the least homologous domains of IgE-Fc.



# Bibliography

- [1] C. A. Janeway, P. J. Travers, M. Walport, and M. Shlomick. *Immunobiology, 5th Edition*. Garland Science, New York, USA, 2001.
- [2] B. A. Wurzburg and T. S. Jardetzky. Structural insights into the interactions between human IgE and its high affinity receptor FcεRI. *Mol. Immunol.*, 38(14):1063–1072, May 2002.
- [3] D. Dombrowicz and M. Capron. Eosinophils, allergy and parasites. *Curr. Opin. Immunol.*, 13(6):716–720, Dec 2001.
- [4] H. J. Gould and B. J. Sutton. IgE in allergy and asthma today. *Nat. Rev. Immunol.*, 8(3):205–217, Mar 2008.
- [5] R. Pawankar, G. Walker Canonica, S. T. Holgate, and R.F Lockett. *White Book on Allergy 2011-2012 Executive Summary*. World Allergy Organization, Milwaukee, Wisconsin, USA, 2011.
- [6] World Health Organisation. The WHO bronchial asthma fact sheet, fact sheet number 206. <http://www.who.int/mediacentre/factsheets/fs206/en/>.
- [7] Allergy UK. Allergy UK Websites, Medications. <http://www.allergyuk.org/the-management-of-allergy/allergy-medications>.
- [8] A. Durham, I. M. Adcock, and O. Tliba. Steroid resistance in severe asthma: current mechanisms and future treatment. *Curr. Pharm. Des.*, 17(7):674–684, 2011.
- [9] Allergy UK. Allergy UK Websites, Statistics. <https://www.allergyuk.org/allergy-statistics/allergy-statistics>.
- [10] I. T. Harvima, F. Levi-Schaffer, P. Draber, S. Friedman, I. Polakovicova, B. F. Gibbs, U. Blank, G. Nilsson, and M. Maurer. Molecular targets on mast cells and basophils for novel therapies. *J. Allergy Clin. Immunol.*, 134(3):530–544, Sep 2014.
- [11] M. J. Holtzman. Drug development for asthma. *Am. J. Respir. Cell Mol. Biol.*, 29(2):163–171, Aug 2003.
- [12] K. Ishizaka, T. Ishizaka, and M. M. Hornbrook. Physico-chemical properties of human reaginic antibody. IV. Presence of a unique immunoglobulin as a carrier of reaginic activity. *J. Immunol.*, 97(1):75–85, Jul 1966.

- [13] T. A. Waldman, W. Strober, and R. M. Blaese. Variations in the metabolism of immunoglobulins measured by turnover rates. In Merler. E, editor, *Immunoglobulins*, chapter 15, pages 33–51. National Academy of Science, Washington, USA, 1970.
- [14] J. P. Kinet. The high-affinity IgE receptor (Fc epsilon RI): from physiology to pathology. *Annu. Rev. Immunol.*, 17:931–972, 1999.
- [15] S. Kraft and J. P. Kinet. New developments in FcepsilonRI regulation, function and inhibition. *Nat. Rev. Immunol.*, 7(5):365–378, May 2007.
- [16] M. Acharya, G. Borland, A. L. Edkins, L. M. Maclellan, J. Matheson, B. W. Ozanne, and W. Cushley. CD23/FcεRII: molecular multi-tasking. *Clin. Exp. Immunol.*, 162(1):12–23, Oct 2010.
- [17] J. Y. Bonnefoy, S. Lecoanet-Henchoz, J. F. Gauchat, P. Graber, J. P. Aubry, P. Jeannin, and C. Plater-Zyberk. Structure and functions of CD23. *Int. Rev. Immunol.*, 16(1-2):113–128, 1997.
- [18] B. Dhaliwal, D. Yuan, M. O. Pang, A. J. Henry, K. Cain, A. Oxbrow, S. M. Fabiane, A. J. Beavil, J. M. McDonnell, H. J. Gould, and B. J. Sutton. Crystal structure of IgE bound to its B-cell receptor CD23 reveals a mechanism of reciprocal allosteric inhibition with high affinity receptor FcεRI. *Proc. Natl. Acad. Sci. U.S.A.*, 109(31):12686–12691, Jul 2012.
- [19] M. Letellier, M. Sarfati, and G. Delespesse. Mechanisms of formation of IgE-binding factors (soluble CD23)–I. Fc epsilon R II bearing B cells generate IgE-binding factors of different molecular weights. *Mol. Immunol.*, 26(12):1105–1112, Dec 1989.
- [20] O. Schulz, B. J. Sutton, R. L. Beavil, J. Shi, H. F. Sewell, H. J. Gould, P. Laing, and F. Shakib. Cleavage of the low-affinity receptor for human IgE (CD23) by a mite cysteine protease: nature of the cleaved fragment in relation to the structure and function of CD23. *Eur. J. Immunol.*, 27(3):584–588, Mar 1997.
- [21] S. J. Galli, J. R. Gordon, and B. K. Wershil. Cytokine production by mast cells and basophils. *Curr. Opin. Immunol.*, 3(6):865–872, Dec 1991.
- [22] G. C. Mudde, I. G. Reischul, N. Corvaia, A. Hren, and E. M. Poellabauer. Antigen presentation in allergic sensitization. *Immunol. Cell Biol.*, 74(2):167–173, Apr 1996.
- [23] U. Pirron, T. Schlunck, J. C. Prinz, and E. P. Rieber. IgE-dependent antigen focusing by human B lymphocytes is mediated by the low-affinity receptor for IgE. *Eur. J. Immunol.*, 20(7):1547–1551, Jul 1990.
- [24] S. N. Karagiannis, J. K. Warrack, K. H. Jennings, P. R. Murdock, G. Christie, K. Moulder, B. J. Sutton, and H. J. Gould. Endocytosis and recycling of the complex between CD23 and HLA-DR in human B cells. *Immunology*, 103(3):319–331, Jul 2001.

- [25] F. Carlsson, F. Hjelm, D. H. Conrad, and B. Heyman. IgE enhances specific antibody and T-cell responses in mice overexpressing CD23. *Scand. J. Immunol.*, 66(2-3):261–270, 2007.
- [26] G. C. Mudde, R. Bheekha, and C. A. Bruijnzeel-Koomen. Consequences of IgE/CD23-mediated antigen presentation in allergy. *Immunol. Today*, 16(8):380–383, Aug 1995.
- [27] A. Capron, J. P. Dessaint, M. Capron, M. Joseph, J. C. Ameisen, and A. B. Tonnel. From parasites to allergy: a second receptor for IgE. *Immunol. Today*, 7(1):15–18, Jan 1986.
- [28] S. N. Karagiannis, Q. Wang, N. East, F. Burke, S. Riffard, M. G. Bracher, R. G. Thompson, S. R. Durham, L. B. Schwartz, F. R. Balkwill, and H. J. Gould. Activity of human monocytes in IgE antibody-dependent surveillance and killing of ovarian tumor cells. *Eur. J. Immunol.*, 33(4):1030–1040, Apr 2003.
- [29] S. Palaniyandi, E. Tomei, Z. Li, D. H. Conrad, and X. Zhu. CD23-dependent transcytosis of IgE and immune complex across the polarized human respiratory epithelial cells. *J. Immunol.*, 186(6):3484–3496, Mar 2011.
- [30] D. Kaiserlian, A. Lachaux, I. Grosjean, P. Graber, and J. Y. Bonnefoy. Intestinal epithelial cells express the CD23/Fc epsilon RII molecule: enhanced expression in enteropathies. *Immunology*, 80(1):90–95, Sep 1993.
- [31] M. Zhou, D. Du, K. Zhao, and C. Zheng. In vivo intranasal anti-CD23 treatment inhibits allergic responses in a murine model of allergic rhinitis. *J. Mol. Histol.*, 44(3):327–338, Jun 2013.
- [32] Y. Tu, S. Salim, J. Bourgeois, V. Di Leo, E. J. Irvine, J. K. Marshall, and M. H. Perdue. CD23-mediated IgE transport across human intestinal epithelium: inhibition by blocking sites of translation or binding. *Gastroenterology*, 129(3):928–940, Sep 2005.
- [33] H. Li, A. Nowak-Wegrzyn, Z. Charlop-Powers, W. Shreffler, M. Chehade, S. Thomas, G. Roda, S. Dahan, K. Sperber, and M. C. Berin. Transcytosis of IgE-antigen complexes by CD23a in human intestinal epithelial cells and its role in food allergy. *Gastroenterology*, 131(1):47–58, Jul 2006.
- [34] M. Sarfati, E. Rector, M. Rubio-Trujillo, K. Wong, A. H. Schon, and G. Delespesse. In vitro synthesis of IgE by human lymphocytes. III. IgE-potentiating activity of culture supernatants from Epstein-Barr virus (EBV) transformed B cells. *Immunology*, 53(2):207–214, Oct 1984.
- [35] J. P. Aubry, S. Pochon, P. Graber, K. U. Jansen, and J. Y. Bonnefoy. CD21 is a ligand for CD23 and regulates IgE production. *Nature*, 358(6386):505–507, Aug 1992.
- [36] N. McCloskey, J. Hunt, R. L. Bevil, M. R. Jutton, G. J. Grundy, E. Girardi, S. M. Fabiane, D. J. Fear, D. H. Conrad, B. J. Sutton, and H. J. Gould.

- Soluble CD23 monomers inhibit and oligomers stimulate IGE synthesis in human B cells. *J. Biol. Chem.*, 282(33):24083–24091, Aug 2007.
- [37] A. M. Cooper, P. S. Hobson, M. R. Jutton, M. W. Kao, B. Drung, B. Schmidt, D. J. Fear, A. J. Beavil, J. M. McDonnell, B. J. Sutton, and H. J. Gould. Soluble CD23 controls IgE synthesis and homeostasis in human B cells. *J. Immunol.*, 188(7):3199–3207, Apr 2012.
- [38] T. Roberts and E. C. Snow. Cutting edge: recruitment of the CD19/CD21 coreceptor to B cell antigen receptor is required for antigen-mediated expression of Bcl-2 by resting and cycling hen egg lysozyme transgenic B cells. *J. Immunol.*, 162(8):4377–4380, Apr 1999.
- [39] R. G. Hibbert, P. Teriete, G. J. Grundy, R. L. Beavil, R. Reljic, V. M. Holers, J. P. Hannan, B. J. Sutton, H. J. Gould, and J. M. McDonnell. The structure of human CD23 and its interactions with IgE and CD21. *J. Exp. Med.*, 202(6):751–760, Sep 2005.
- [40] P. Yu, M. Kosco-Vilbois, M. Richards, G. Kohler, and M. C. Lamers. Negative feedback regulation of IgE synthesis by murine CD23. *Nature*, 369(6483):753–756, Jun 1994.
- [41] A. Stief, G. Texido, G. Sansig, H. Eibel, G. Le Gros, and H. van der Putten. Mice deficient in CD23 reveal its modulatory role in IgE production but no role in T and B cell development. *J. Immunol.*, 152(7):3378–3390, Apr 1994.
- [42] M. Payet and D. H. Conrad. IgE regulation in CD23 knockout and transgenic mice. *Allergy*, 54(11):1125–1129, Nov 1999.
- [43] G. Lewis, E. Rapsomaniki, T. Bouriez, T. Crockford, H. Ferry, R. Rigby, T. Vyse, T. Lambe, and R. Cornall. Hyper IgE in New Zealand black mice due to a dominant-negative CD23 mutation. *Immunogenetics*, 56(8):564–571, Nov 2004.
- [44] J. W. Ford, J. L. Sturgill, and D. H. Conrad. 129/SvJ mice have mutated CD23 and hyper IgE. *Cell. Immunol.*, 254(2):124–134, 2009.
- [45] M. Sarfati and G. Delespesse. Possible role of human lymphocyte receptor for IgE (CD23) or its soluble fragments in the in vitro synthesis of human IgE. *J. Immunol.*, 141(7):2195–2199, Oct 1988.
- [46] E. Sherr, E. Macy, H. Kimata, M. Gilly, and A. Saxon. Binding the low affinity Fc epsilon R on B cells suppresses ongoing human IgE synthesis. *J. Immunol.*, 142(2):481–489, Jan 1989.
- [47] J. Y. Bonnefoy, J. Shields, and J. J. Mermod. Inhibition of human interleukin 4-induced IgE synthesis by a subset of anti-CD23/Fc epsilon RII monoclonal antibodies. *Eur. J. Immunol.*, 20(1):139–144, Jan 1990.
- [48] M. Wakai, P. Pasley, Z. M. Stoeber, D. N. Posnett, R. Brooks, S. Hashimoto, and N. Chiorazzi. Anti-CD23 monoclonal antibodies: comparisons of epitope

- specificities and modulating capacities for IgE binding and production. *Hybridoma*, 12(1):25–43, Feb 1993.
- [49] L. Flores-Romo, J. Shields, Y. Humbert, P. Graber, J. P. Aubry, J. F. Gauchat, G. Ayala, B. Allet, M. Chavez, and H. Bazin. Inhibition of an in vivo antigen-specific IgE response by antibodies to CD23. *Science*, 261(5124):1038–1041, Aug 1993.
- [50] G. Dasic, P. Juillard, P. Graber, S. Herren, T. Angell, R. Knowles, J. Y. Bonnefoy, M. H. Kosco-Vilbois, and Y. Chvatchko. Critical role of CD23 in allergen-induced bronchoconstriction in a murine model of allergic asthma. *Eur. J. Immunol.*, 29(9):2957–2967, Sep 1999.
- [51] A. Haczku, K. Takeda, E. Hamelmann, J. Loader, A. Joetham, I. Redai, C. G. Irvin, J. J. Lee, H. Kikutani, D. Conrad, and E. W. Gelfand. CD23 exhibits negative regulatory effects on allergic sensitization and airway hyperresponsiveness. *Am. J. Respir. Crit. Care Med.*, 161(3 Pt 1):952–960, Mar 2000.
- [52] L. J. Rosenwasser, W. W. Busse, R. G. Lizambri, T. A. Olejnik, and M. C. Totoritis. Allergic asthma and an anti-CD23 mAb (IDEC-152): results of a phase I, single-dose, dose-escalating clinical trial. *J. Allergy Clin. Immunol.*, 112(3):563–570, Sep 2003.
- [53] W. Busse, J. Corren, B. Q. Lanier, M. McAlary, A. Fowler-Taylor, G. D. Cioppa, A. van As, and N. Gupta. Omalizumab, anti-IgE recombinant humanized monoclonal antibody, for the treatment of severe allergic asthma. *J. Allergy Clin. Immunol.*, 108(2):184–190, Aug 2001.
- [54] S. Holgate, T. Casale, S. Wenzel, J. Bousquet, Y. Deniz, and C. Reisner. The anti-inflammatory effects of omalizumab confirm the central role of IgE in allergic inflammation. *J. Allergy Clin. Immunol.*, 115(3):459–465, Mar 2005.
- [55] D. W. MacGlashan, B. S. Bochner, D. C. Adelman, P. M. Jardieu, A. Togias, J. McKenzie-White, S. A. Sterbinsky, R. G. Hamilton, and L. M. Lichtenstein. Down-regulation of Fc(epsilon)RI expression on human basophils during in vivo treatment of atopic patients with anti-IgE antibody. *J. Immunol.*, 158(3):1438–1445, Feb 1997.
- [56] L. A. Beck, G. V. Marcotte, D. MacGlashan, A. Togias, and S. Saini. Omalizumab-induced reductions in mast cell Fc epsilon RI expression and function. *J. Allergy Clin. Immunol.*, 114(3):527–530, Sep 2004.
- [57] H. Lin, K. M. Boesel, D. T. Griffith, C. Prussin, B. Foster, F. A. Romero, R. Townley, and T. B. Casale. Omalizumab rapidly decreases nasal allergic response and Fc epsilon RI on basophils. *J. Allergy Clin. Immunol.*, 113(2):297–302, Feb 2004.

- [58] C. Prussin, D. T. Griffith, K. M. Boesel, H. Lin, B. Foster, and T. B. Casale. Omalizumab treatment downregulates dendritic cell FcεRI expression. *J. Allergy Clin. Immunol.*, 112(6):1147–1154, Dec 2003.
- [59] J. A. Poole, J. Meng, M. Reff, M. C. Spellman, and L. J. Rosenwasser. Anti-CD23 monoclonal antibody, lumiliximab, inhibited allergen-induced responses in antigen-presenting cells and T cells from atopic subjects. *J. Allergy Clin. Immunol.*, 116(4):780–788, Oct 2005.
- [60] L. J. Rosenwasser, J. Meng, M. A. Chan, N. M. Gigliotti, and B. E. May. The role of CD23 in IgE dependent signaling: implications from pharmacogenetics. *Trans. Am. Clin. Climatol. Assoc.*, 122:27–33, 2011.
- [61] M. Stocks. Intrabodies as drug discovery tools and therapeutics. *Curr Opin Chem Biol*, 9(4):359–365, Aug 2005.
- [62] Clinical supply chain logistics of small molecules vs. biologics - A provider's perspective. [http://www.fisherclinicalservices.com/wp-content/uploads/2014/03/KB-0016\\_Clinical\\_Supply\\_Chain\\_Logistics.pdf](http://www.fisherclinicalservices.com/wp-content/uploads/2014/03/KB-0016_Clinical_Supply_Chain_Logistics.pdf).
- [63] R. G. Werner. Economic aspects of commercial manufacture of biopharmaceuticals. *J. Biotechnol.*, 113(1-3):171–182, Sep 2004.
- [64] B. Kelley. Industrialization of mAb production technology: the bioprocessing industry at a crossroads. *MAbs*, 1(5):443–452, 2009.
- [65] A. Nechansky and R. Kircheis. Immunogenicity of therapeutics: a matter of efficacy and safety. *Expert Opin Drug Discov*, 5(11):1067–1079, Nov 2010.
- [66] J. Stanely. In C. L Esperti, editor, *Essentials of Immunology and Serology*. Delmar, New York, USA, 2002.
- [67] M. A. Tabrizi, C. M. Tseng, and L. K. Roskos. Elimination mechanisms of therapeutic monoclonal antibodies. *Drug Discov. Today*, 11(1-2):81–88, Jan 2006.
- [68] Xolair FDA Alert 2/2007. <http://www.fda.gov/Drugs/DrugSafety/ucm162905.htm>.
- [69] J. C. Fuller, N. J. Burgoyne, and R. M. Jackson. Predicting druggable binding sites at the protein-protein interface. *Drug Discov. Today*, 14(3-4):155–161, Feb 2009.
- [70] H. Hwang, T. Vreven, J. Janin, and Z. Weng. Protein-protein docking benchmark version 4.0. *Proteins*, 78(15):3111–3114, Nov 2010.
- [71] T. Wan, R. L. Beavil, S. M. Fabiane, A. J. Beavil, M. K. Sohi, M. Keown, R. J. Young, A. J. Henry, R. J. Owens, H. J. Gould, and B. J. Sutton. The crystal structure of IgE Fc reveals an asymmetrically bent conformation. *Nat. Immunol.*, 3(7):681–686, Jul 2002.

- [72] M. D. Holdom, A. M. Davies, J. E. Nettleship, S. C. Bagby, B. Dhaliwal, E. Girardi, J. Hunt, H. J. Gould, A. J. Beavil, J. M. McDonnell, R. J. Owens, and B. J. Sutton. Conformational changes in IgE contribute to its uniquely slow dissociation rate from receptor Fc epsilonRIalpha. *Nat. Struct. Mol. Biol.*, 18(5):571–576, May 2011.
- [73] D. Holowka and B. Baird. Structural studies on the membrane-bound immunoglobulin E (IgE)-receptor complex. 2. Mapping of distances between sites on IgE and the membrane surface. *Biochemistry*, 22(14):3475–3484, Jul 1983.
- [74] Y. Zheng, B. Shopes, D. Holowka, and B. Baird. Conformations of IgE bound to its receptor Fc epsilon RI and in solution. *Biochemistry*, 30(38):9125–9132, Sep 1991.
- [75] J. Hunt, A. H. Keeble, R. E. Dale, M. K. Corbett, R. L. Beavil, J. Levitt, M. J. Swann, K. Suhling, S. Ameer-Beg, B. J. Sutton, and A. J. Beavil. A fluorescent biosensor reveals conformational changes in human immunoglobulin E Fc: implications for mechanisms of receptor binding, inhibition, and allergen recognition. *J. Biol. Chem.*, 287(21):17459–17470, May 2012.
- [76] A. J. Beavil, R. J. Young, B. J. Sutton, and S. J. Perkins. Bent domain structure of recombinant human IgE-Fc in solution by X-ray and neutron scattering in conjunction with an automated curve fitting procedure. *Biochemistry*, 34(44):14449–14461, Nov 1995.
- [77] B. A. Wurzburg and T. S. Jardetzky. Conformational flexibility in immunoglobulin E-Fc 3-4 revealed in multiple crystal forms. *J. Mol. Biol.*, 393(1):176–190, Oct 2009.
- [78] N. E. Price, N. C. Price, S. M. Kelly, and J. M. McDonnell. The key role of protein flexibility in modulating IgE interactions. *J. Biol. Chem.*, 280(3):2324–2330, Jan 2005.
- [79] N. E. Harwood and J. M. McDonnell. The intrinsic flexibility of IgE and its role in binding Fc epsilon RI. *Biomed. Pharmacother.*, 61(1):61–67, Jan 2007.
- [80] S. Borthakur, G. Andrejeva, and J. M. McDonnell. Basis of the intrinsic flexibility of the Cε3 domain of IgE. *Biochemistry*, 50(21):4608–4614, May 2011.
- [81] N. Drinkwater, B. P. Cossins, A. H. Keeble, M. Wright, K. Cain, H. Hailu, A. Oxbrow, J. Delgado, L. K. Shuttleworth, M. W. Kao, J. M. McDonnell, A. J. Beavil, A. J. Henry, and B. J. Sutton. Human immunoglobulin E flexes between acutely bent and extended conformations. *Nat. Struct. Mol. Biol.*, 21(4):397–404, Apr 2014.
- [82] Anna Marie Davies, Elizabeth G. Allan, Anthony H. Keeble, Jean Delgado, Benjamin P Cossins, Alkistis N. Mitropoulou, Marie O.Y. Pang, Tom Ceska, Andrew J. Beavil, Graham Craggs, Marta Westwood, Alistair J. Henry,

- James M. McDonnell, and Brian J. Sutton. Allosteric mechanism of action of the therapeutic anti-ige antibody omalizumab. *Journal of Biological Chemistry*, 4 2017.
- [83] J. M. McDonnell, R. Calvert, R. L. Beavil, A. J. Beavil, A. J. Henry, B. J. Sutton, H. J. Gould, and D. Cowburn. The structure of the IgE Cepsilon2 domain and its role in stabilizing the complex with its high-affinity receptor FcepsilonRIalpha. *Nat. Struct. Biol.*, 8(5):437–441, May 2001.
- [84] K. Maenaka, P. A. van der Merwe, D. I. Stuart, E. Y. Jones, and P. Sondermann. The human low affinity Fc gamma receptors IIa, IIb, and III bind IgG with fast kinetics and distinct thermodynamic properties. *J. Biol. Chem.*, 276(48):44898–44904, Nov 2001.
- [85] B. J. Sutton and A. M. Davies. Structure and dynamics of IgE-receptor interactions: Fc epsilon RI and CD23/Fc epsilon RII. *Immunol. Rev.*, 268(1):222–235, Nov 2015.
- [86] S. C. Garman, B. A. Wurzburg, S. S. Tarchevskaya, J. P. Kinet, and T. S. Jardetzky. Structure of the Fc fragment of human IgE bound to its high-affinity receptor Fc epsilon RI alpha. *Nature*, 406(6793):259–266, Jul 2000.
- [87] S. C. Garman, S. Sechi, J. P. Kinet, and T. S. Jardetzky. The analysis of the human high affinity IgE receptor Fc epsilon RI alpha from multiple crystal forms. *J. Mol. Biol.*, 311(5):1049–1062, Aug 2001.
- [88] J. Shi, R. Ghirlando, R. L. Beavil, A. J. Beavil, M. B. Keown, R. J. Young, R. J. Owens, B. J. Sutton, and H. J. Gould. Interaction of the low-affinity receptor CD23/Fc epsilon RII lectin domain with the Fc epsilon 3-4 fragment of human immunoglobulin E. *Biochemistry*, 36(8):2112–2122, Feb 1997.
- [89] S. Borthakur, R. G. Hibbert, M. O. Pang, N. Yahya, H. J. Bax, M. W. Kao, A. M. Cooper, A. J. Beavil, B. J. Sutton, H. J. Gould, and J. M. McDonnell. Mapping of the CD23 binding site on immunoglobulin E (IgE) and allosteric control of the IgE-Fc epsilon RI interaction. *J. Biol. Chem.*, 287(37):31457–31461, Sep 2012.
- [90] S. L. Bowles, C. Jaeger, C. Ferrara, J. Fingerroth, M. Van De Venter, and V. Oosthuizen. Comparative binding of soluble fragments (derCD23, sCD23, and exCD23) of recombinant human CD23 to CD21 (SCR 1-2) and native IgE, and their effect on IgE regulation. *Cell. Immunol.*, 271(2):371–378, 2011.
- [91] S. E. Dierks, W. C. Bartlett, R. L. Edmeades, H. J. Gould, M. Rao, and D. H. Conrad. The oligomeric nature of the murine Fc epsilon RII/CD23. Implications for function. *J. Immunol.*, 150(6):2372–2382, Mar 1993.
- [92] B. H. Chen, C. Ma, T. H. Caven, Y. Chan-Li, A. Beavil, R. Beavil, H. Gould, and D. H. Conrad. Necessity of the stalk region for immunoglobulin E interaction with CD23. *Immunology*, 107(3):373–381, Nov 2002.



- [93] D. Yuan, A. H. Keeble, R. G. Hibbert, S. Fabiane, H. J. Gould, J. M. McDonnell, A. J. Beavil, B. J. Sutton, and B. Dhaliwal. Ca<sup>2+</sup>-dependent structural changes in the B-cell receptor CD23 increase its affinity for human immunoglobulin E. *J. Biol. Chem.*, 288(30):21667–21677, Jul 2013.
- [94] D. Vercelli, B. Helm, P. Marsh, E. Padlan, R. S. Geha, and H. Gould. The B-cell binding site on human immunoglobulin E. *Nature*, 338(6217):649–651, Apr 1989.
- [95] B. Dhaliwal, M. O. Pang, A. H. Keeble, L. K. James, H. J. Gould, J. M. McDonnell, B. J. Sutton, and A. J. Beavil. IgE binds asymmetrically to its B cell receptor CD23. *Sci Rep*, 7:45533, Mar 2017.
- [96] V. J. Hilser. Biochemistry. An ensemble view of allostery. *Science*, 327(5966):653–654, Feb 2010.
- [97] R. Nussinov, C. J. Tsai, and J. Liu. Principles of allosteric interactions in cell signaling. *J. Am. Chem. Soc.*, 136(51):17692–17701, Dec 2014.
- [98] R. Nussinov and C. J. Tsai. Allostery in disease and in drug discovery. *Cell*, 153(2):293–305, Apr 2013.
- [99] K. Gunasekaran, B. Ma, and R. Nussinov. Is allostery an intrinsic property of all dynamic proteins? *Proteins*, 57(3):433–443, Nov 2004.
- [100] A. E. Kelly, B. H. Chen, E. C. Woodward, and D. H. Conrad. Production of a chimeric form of CD23 that is oligomeric and blocks IgE binding to the Fc epsilonRI. *J. Immunol.*, 161(12):6696–6704, Dec 1998.
- [101] M. Suemura, H. Kikutani, K. Sugiyama, N. Uchibayashi, M. Aitani, T. Kuritani, E. L. Barsumian, A. Yamatodani, and T. Kishimoto. Significance of soluble Fc epsilon receptor II (sFc epsilon RII/CD23) in serum and possible application of sFc epsilon RII for the prevention of allergic reactions. *Allergy Proc*, 12(3):133–137, 1991.
- [102] G. J. Braunstahl, C. W. Chen, R. Maykut, P. Georgiou, G. Peachey, and J. Bruce. The eXpeRIence registry: the 'real-world' effectiveness of omalizumab in allergic asthma. *Respir Med*, 107(8):1141–1151, Aug 2013.
- [103] T. Lai, S. Wang, Z. Xu, C. Zhang, Y. Zhao, Y. Hu, C. Cao, S. Ying, Z. Chen, W. Li, B. Wu, and H. Shen. Corrigendum: Long-term efficacy and safety of omalizumab in patients with persistent uncontrolled allergic asthma: a systematic review and meta-analysis. *Sci Rep*, 5:9548, Aug 2015.
- [104] P. J. Lowe, S. Tannenbaum, A. Gautier, and P. Jimenez. Relationship between omalizumab pharmacokinetics, IgE pharmacodynamics and symptoms in patients with severe persistent allergic (IgE-mediated) asthma. *Br J Clin Pharmacol*, 68(1):61–76, Jul 2009.
- [105] J. D. Wright, H. M. Chu, C. H. Huang, C. Ma, T. W. Chang, and C. Lim. Structural and Physical Basis for Anti-IgE Therapy. *Sci Rep*, 5:11581, Jun 2015.

- [106] L. Zheng, B. Li, W. Qian, L. Zhao, Z. Cao, S. Shi, J. Gao, D. Zhang, S. Hou, J. Dai, H. Wang, and Y. Guo. Fine epitope mapping of humanized anti-IgE monoclonal antibody omalizumab. *Biochem. Biophys. Res. Commun.*, 375(4):619–622, Oct 2008.
- [107] R. K. Jensen, M. Plum, L. Tjerrild, T. Jakob, E. Spillner, and G. R. Andersen. Structure of the omalizumab Fab. *Acta Crystallogr F Struct Biol Commun*, 71(Pt 4):419–426, Apr 2015.
- [108] L. F. Pennington, S. Tarchevskaya, D. Brigger, K. Sathiyamoorthy, M. T. Graham, K. C. Nadeau, A. Eggel, and T. S. Jardetzky. Structural basis of omalizumab therapy and omalizumab-mediated IgE exchange. *Nat Commun*, 7:11610, 2016.
- [109] B. Kim, A. Eggel, S. S. Tarchevskaya, M. Vogel, H. Prinz, and T. S. Jardetzky. Accelerated disassembly of IgE-receptor complexes by a disruptive macromolecular inhibitor. *Nature*, 491(7425):613–617, Nov 2012.
- [110] A. Eggel, G. Baravalle, G. Hobi, B. Kim, P. Buschor, P. Forrer, J. S. Shin, M. Vogel, B. M. Stadler, C. A. Dahinden, and T. S. Jardetzky. Accelerated dissociation of IgE-F $\epsilon$ RI complexes by disruptive inhibitors actively desensitizes allergic effector cells. *J. Allergy Clin. Immunol.*, 133(6):1709–1719, Jun 2014.
- [111] H. N. Motlagh, J. O. Wrabl, J. Li, and V. J. Hilser. The ensemble nature of allostery. *Nature*, 508(7496):331–339, Apr 2014.
- [112] J. Monod, J. Wyman, and J. P. Changeux. On the nature of allosteric transitions: a plausible model. *J. Mol. Biol.*, 12:88–118, May 1965.
- [113] D. E. Koshland, G. Nemethy, and D. Filmer. Comparison of experimental binding data and theoretical models in proteins containing subunits. *Biochemistry*, 5(1):365–385, Jan 1966.
- [114] Q. Cui and M. Karplus. Allostery and cooperativity revisited. *Protein Sci.*, 17(8):1295–1307, Aug 2008.
- [115] M. F. Perutz. Stereochemistry of cooperative effects in haemoglobin. *Nature*, 228(5273):726–739, Nov 1970.
- [116] M. M. Silva, P. H. Rogers, and A. Arnone. A third quaternary structure of human hemoglobin A at 1.7-Å resolution. *J. Biol. Chem.*, 267(24):17248–17256, Aug 1992.
- [117] M. F. Colombo, D. C. Rau, and V. A. Parsegian. Protein solvation in allosteric regulation: a water effect on hemoglobin. *Science*, 256(5057):655–659, May 1992.
- [118] T. Yonetani and A. Tsuneshige. The global allostery model of hemoglobin: an allosteric mechanism involving homotropic and heterotropic interactions. *C. R. Biol.*, 326(6):523–532, Jun 2003.

- [119] C. M. Dobson and M. Karplus. Internal motion of proteins: nuclear magnetic resonance measurements and dynamic simulations. *Meth. Enzymol.*, 131:362–389, 1986.
- [120] H. Frauenfelder, S. G. Sligar, and P. G. Wolynes. The energy landscapes and motions of proteins. *Science*, 254(5038):1598–1603, Dec 1991.
- [121] O. Jardetzky. Protein dynamics and conformational transitions in allosteric proteins. *Prog. Biophys. Mol. Biol.*, 65(3):171–219, 1996.
- [122] R. Nussinov and P. G. Wolynes. A second molecular biology revolution? The energy landscapes of biomolecular function. *Phys Chem Chem Phys*, 16(14):6321–6322, Apr 2014.
- [123] S. Kumar, B. Ma, C. J. Tsai, N. Sinha, and R. Nussinov. Folding and binding cascades: dynamic landscapes and population shifts. *Protein Sci.*, 9(1):10–19, Jan 2000.
- [124] N. Popovych, S. Sun, R. H. Ebricht, and C. G. Kalodimos. Dynamically driven protein allostery. *Nat. Struct. Mol. Biol.*, 13(9):831–838, Sep 2006.
- [125] L. R. Masterson, A. Cembran, L. Shi, and G. Veglia. Allostery and binding cooperativity of the catalytic subunit of protein kinase A by NMR spectroscopy and molecular dynamics simulations. *Adv Protein Chem Struct Biol*, 87:363–389, 2012.
- [126] G. Veglia and A. Cembran. Role of conformational entropy in the activity and regulation of the catalytic subunit of protein kinase A. *FEBS J.*, 280(22):5608–5615, Nov 2013.
- [127] A. Cooper and D. T. Dryden. Allostery without conformational change. A plausible model. *Eur. Biophys. J.*, 11(2):103–109, 1984.
- [128] C. J. Tsai and R. Nussinov. A unified view of "how allostery works". *PLoS Comput. Biol.*, 10(2):e1003394, Feb 2014.
- [129] B. Ma, S. Kumar, C. J. Tsai, and R. Nussinov. Folding funnels and binding mechanisms. *Protein Eng.*, 12(9):713–720, Sep 1999.
- [130] V. J. Hilser, J. O. Wrabl, and H. N. Motlagh. Structural and energetic basis of allostery. *Annu Rev Biophys*, 41:585–609, 2012.
- [131] J. Zheng, D. R. Knighton, N. H. Xuong, S. S. Taylor, J. M. Sowadski, and L. F. Ten Eyck. Crystal structures of the myristylated catalytic subunit of cAMP-dependent protein kinase reveal open and closed conformations. *Protein Sci.*, 2(10):1559–1573, Oct 1993.
- [132] N. Narayana, S. Cox, X. Nguyen-huu, L. F. Ten Eyck, and S. S. Taylor. A binary complex of the catalytic subunit of cAMP-dependent protein kinase and adenosine further defines conformational flexibility. *Structure*, 5(7):921–935, Jul 1997.

- [133] Madhusudan, E. A. Trafny, N. H. Xuong, J. A. Adams, L. F. Ten Eyck, S. S. Taylor, and J. M. Sowadski. cAMP-dependent protein kinase: crystallographic insights into substrate recognition and phosphotransfer. *Protein Sci.*, 3(2):176–87, Feb 1994.
- [134] P. Akamine, W. J. Madhusudan, N. H. Xuong, L. F. Ten Eyck, and S. S. Taylor. Dynamic features of cAMP-dependent protein kinase revealed by apoenzyme crystal structure. *J Mol Bio*, 14(327):159–71, Mar 2003.
- [135] L. R. Masterson, A. Mascioni, N. J. Traaseth, S. S. Taylor, and G. Veglia. Allosteric cooperativity in protein kinase A. *Proc. Natl. Acad. Sci. U.S.A.*, 105(2):506–511, Jan 2008.
- [136] R. Nussinov. Introduction to Protein Ensembles and Allostery. *Chem. Rev.*, 116(11):6263–6266, Jun 2016.
- [137] M. Louet, C. Seifert, U. Hensen, and F. Grater. Dynamic Allostery of the Catabolite Activator Protein Revealed by Interatomic Forces. *PLoS Comput. Biol.*, 11(8):e1004358, Aug 2015.
- [138] C. M. Petit, J. Zhang, P. J. Sapienza, E. J. Fuentes, and A. L. Lee. Hidden dynamic allostery in a PDZ domain. *Proc. Natl. Acad. Sci. U.S.A.*, 106(43):18249–18254, Oct 2009.
- [139] J. Guo and H. X. Zhou. Protein Allostery and Conformational Dynamics. *Chem. Rev.*, 116(11):6503–6515, Jun 2016.
- [140] S. R. Tzeng and C. G. Kalodimos. Protein dynamics and allostery: an NMR view. *Curr. Opin. Struct. Biol.*, 21(1):62–67, Feb 2011.
- [141] S. Grutsch, S. Bruschweiler, and M. Tollinger. NMR Methods to Study Dynamic Allostery. *PLoS Comput. Biol.*, 12(3):e1004620, Mar 2016.
- [142] J. E. Nettleship, R. Assenberg, J. M. Diprose, N. Rahman-Huq, and R. J. Owens. Recent advances in the production of proteins in insect and mammalian cells for structural biology. *J. Struct. Biol.*, 172(1):55–65, Oct 2010.
- [143] A. Dutta, K. Saxena, H. Schwalbe, and J. Klein-Seetharaman. Isotope labeling in mammalian cells. *Methods Mol. Biol.*, 831:55–69, Jan 2012.
- [144] D. H. Jones, S. E. Cellitti, X. Hao, Q. Zhang, M. Jahnz, D. Summerer, P. G. Schultz, T. Uno, and B. H. Geierstanger. Site-specific labeling of proteins with NMR-active unnatural amino acids. *J. Biomol. NMR*, 46(1):89–100, Jan 2010.
- [145] A. Kuzmanic, N. S. Pannu, and B. Zagrovic. X-ray refinement significantly underestimates the level of microscopic heterogeneity in biomolecular crystals. *Nat Commun*, 5:3220, 2014.
- [146] S. Tickle, R. Adams, D. Brown, M. Griffiths, D. Lightwood, and L. Lawson. High-throughput screening for high affinity antibodies. *Journal of Laboratory Automation*, 14(5):304–307, Oct 2009.

- [147] A. M. Clargo, A. R. Hudson, W. Ndlovu, R. J. Wootton, L. A. Cremin, V. L. O'Dowd, C. R. Nowosad, D. O. Starkie, S. P. Shaw, J. E. Compson, D. P. White, B. MacKenzie, J. R. Snowden, L. E. Newnham, M. Wright, P. E. Stephens, M. R. Griffiths, A. D. Lawson, and D. J. Lightwood. The rapid generation of recombinant functional monoclonal antibodies from individual, antigen-specific bone marrow-derived plasma cells isolated using a novel fluorescence-based method. *MAbs*, 6(1):143–159, 2014.
- [148] S. Tickle, L. Howells, V. O'Dowd, D. Starkie, K. Whale, M. Saunders, D. Lee, and D. Lightwood. A fully automated primary screening system for the discovery of therapeutic antibodies directly from B cells. *J Biomol Screen*, 20(4):492–497, Apr 2015.
- [149] K Ikuta, M Takami, C W Kim, T Honjo, T Miyoshi, Y Tagaya, T Kawabe, and J Yodoi. Human lymphocyte Fc receptor for IgE: sequence homology of its cloned cDNA with animal lectins. *Proc.Natl.Acad.Sci.USA*, 84:819–823, 1987.
- [150] K. Cain, S. Peters, H. Hailu, B. Sweeney, P. Stephens, J. Heads, K. Sarkar, A. Ventom, C. Page, and A. Dickson. A CHO cell line engineered to express XBP1 and ERO1-L has increased levels of transient protein expression. *Biotechnol. Prog.*, 29(3):697–706, 2013.
- [151] Philip Anton Van Der Merwe. *Protein-Ligand Interactions: Hydrodynamics and Calorimetry*. Oxford University Press, New York, USA, 2001.
- [152] R. W. Glaser. Antigen-antibody binding and mass transport by convection and diffusion to a surface: a two-dimensional computer model of binding and dissociation kinetics. *Anal. Biochem.*, 213(1):152–161, Aug 1993.
- [153] P. Schuck and H. Zhao. The role of mass transport limitation and surface heterogeneity in the biophysical characterization of macromolecular binding processes by SPR biosensing. *Methods Mol. Biol.*, 627:15–54, 2010.
- [154] Biacore 3000 sensor surface handbook. <http://timothyspringer.org/files/tas/files/biacore3000-sensorsurface.pdf>.
- [155] R. B. M. Schasfoort and J. A Tudos. *Handbook of surface plasmon resonance*. Royal Society of Chemistry, Cambridge, UK, 2008.
- [156] Givan A L. *Flow Cytometry: First Principles*. Wiley-Liss, New York, USA, 2001.
- [157] Fluorescence Assisted Cell Sorting. <http://www.di.uq.edu.au/sparqfac>.
- [158] BD Introduction to flow cytometry: a learning guide. <http://www.bu.edu/flow-cytometry/files/2010/10/BD-Flow-Cytom-Learning-Guide.pdf>.
- [159] Abcam Introdction to flow cytometry. <http://www.abcam.com/protocols/introduction-to-flow-cytometry>.

- [160] J. Spidlen, W. Moore, D. Parks, M. Goldberg, C. Bray, P. Bierre, P. Gorombey, B. Hyun, M. Hubbard, S. Lange, R. Lefebvre, R. Leif, D. Novo, L. Ostruszka, A. Treister, J. Wood, R. F. Murphy, M. Roederer, D. Sudar, R. Zigon, and R. R. Brinkman. Data File Standard for Flow Cytometry, version FCS 3.1. *Cytometry A*, 77(1):97–100, Jan 2010.
- [161] I. Finegold, J. L. Fahey, and H. Granger. Synthesis of immunoglobulins by human cell lines in tissue culture. *J. Immunol.*, 99(5):839–848, Nov 1967.
- [162] A. J. Pope, U. M. Haupts, and K. J. Moore. Homogeneous fluorescence readouts for miniaturized high-throughput screening: theory and practice. *Drug Discov. Today*, 4(8):350–362, Aug 1999.
- [163] P. R. Selvin. Fluorescence resonance energy transfer. *Meth. Enzymol.*, 246:300–334, 1995.
- [164] J. Lakowicz. *Principles of fluorescence spectroscopy*. KluwerAcademic/Plenum, New York, USA, 1999.
- [165] T. Förster. Intermolecular energy migration and fluorescence. *Ann. Phys*, 437:55–75, 1948.
- [166] F. Wilcoxon. Individual comparisons of grouped data by ranking methods. *J. Econ. Entomol.*, 39:269, Apr 1946.
- [167] N. McCloskey, J. Hunt, R. L. Beavil, M. R. Jutton, G. J. Grundy, E. Girardi, S. M. Fabiane, D. J. Fear, D. H. Conrad, B. J. Sutton, and H. J. Gould. Soluble CD23 monomers inhibit and oligomers stimulate IGE synthesis in human B cells. *J. Biol. Chem.*, 282(33):24083–24091, Aug 2007.
- [168] T. Rehm, R. Huber, and T. A. Holak. Application of NMR in structural proteomics: screening for proteins amenable to structural analysis. *Structure*, 10(12):1613–1618, Dec 2002.
- [169] A. De Lean, P. J. Munson, and D. Rodbard. Multi-subsite receptors for multivalent ligands. Application to drugs, hormones, and neurotransmitters. *Mol. Pharmacol.*, 15(1):60–70, Jan 1979.
- [170] C. H. Powell-Jones, C. G. Thomas, and S. N. Nayfeh. Thyrotropin receptors in normal human thyroid. Nonclassical binding kinetics not explained by the negative cooperativity model. *J. Biol. Chem.*, 255(9):4001–4010, May 1980.
- [171] A. Goll, D. R. Ferry, and H. Glossmann. Target size analysis and molecular properties of Ca<sup>2+</sup> channels labelled with [3H]verapamil. *Eur. J. Biochem.*, 141(1):177–186, May 1984.
- [172] H. Prinz and J. Striessnig. Ligand-induced accelerated dissociation of (+)-cis-diltiazem from L-type Ca<sup>2+</sup> channels is simply explained by competition for individual attachment points. *J. Biol. Chem.*, 268(25):18580–18585, Sep 1993.

- [173] L. K. James, H. Bowen, R. A. Calvert, T. S. Dodev, M. H. Shamji, A. J. Beavil, J. M. McDonnell, S. R. Durham, and H. J. Gould. Allergen specificity of IgG(4)-expressing B cells in patients with grass pollen allergy undergoing immunotherapy. *J. Allergy Clin. Immunol.*, 130(3):663–670, Sep 2012.
- [174] Thomas Holder. Show Bumps Python Script. [https://pymolwiki.org/index.php/Show\\_bumps](https://pymolwiki.org/index.php/Show_bumps).
- [175] S. Hertig, N. R. Latorraca, and R. O. Dror. Revealing Atomic-Level Mechanisms of Protein Allostery with Molecular Dynamics Simulations. *PLoS Comput. Biol.*, 12(6):e1004746, Jun 2016.
- [176] T. Tiller. Single B cell antibody technologies. *N Biotechnol*, 28(5):453–457, Sep 2011.
- [177] G. Kohler and C. Milstein. Continuous cultures of fused cells secreting antibody of predefined specificity. *Nature*, 256(5517):495–497, Aug 1975.
- [178] G. Galfre, S. C. Howe, C. Milstein, G. W. Butcher, and J. C. Howard. Antibodies to major histocompatibility antigens produced by hybrid cell lines. *Nature*, 266(5602):550–552, Apr 1977.
- [179] X. Yu, P. A. McGraw, F. S. House, and J. E. Crowe. An optimized electrofusion-based protocol for generating virus-specific human monoclonal antibodies. *J. Immunol. Methods*, 336(2):142–151, Jul 2008.
- [180] H. R. Hoogenboom, A. P. de Bruine, S. E. Hufton, R. M. Hoet, J. W. Arends, and R. C. Roovers. Antibody phage display technology and its applications. *Immunotechnology*, 4(1):1–20, Jun 1998.
- [181] D. Lowe and L. Jermutus. Combinatorial protein biochemistry for therapeutics and proteomics. *Curr Pharm Biotechnol*, 5(1):17–27, Feb 2004.
- [182] W. P. Bowen and P. G. Wylie. Application of laser-scanning fluorescence microplate cytometry in high content screening. *Assay Drug Dev Technol*, 4(2):209–221, Apr 2006.
- [183] R. Lee, M. Tran, M. Nocerini, and M. Liang. A high-throughput hybridoma selection method using fluorometric microvolume assay technology. *J Biomol Screen*, 13(3):210–217, Mar 2008.
- [184] X. Liang, A. Teng, D. M. Braun, J. Felgner, Y. Wang, S. I. Baker, S. Chen, O. Zelphati, and P. L. Felgner. Transcriptionally active polymerase chain reaction (TAP): high throughput gene expression using genome sequence data. *J. Biol. Chem.*, 277(5):3593–3598, Feb 2002.
- [185] R. C. Edgar. MUSCLE: multiple sequence alignment with high accuracy and high throughput. *Nucleic Acids Res.*, 32(5):1792–1797, 2004.
- [186] R. Barbour and M. P. Bova. Combining label-free technologies: discovery in strength. *Bioanalysis*, 4(6):619–622, Mar 2012.

- [187] F. L. Graham, J. Smiley, W. C. Russell, and R. Nairn. Characteristics of a human cell line transformed by DNA from human adenovirus type 5. *J. Gen. Virol.*, 36(1):59–74, Jul 1977.
- [188] Swiss Institute of Bioinformatics. ExPASy Translate Tool. <http://web.expasy.org/translate/>.
- [189] M. Erntell, E. B. Myhre, U. Sjobring, and L. Bjorck. Streptococcal protein G has affinity for both Fab- and Fc-fragments of human IgG. *Mol. Immunol.*, 25(2):121–126, Feb 1988.
- [190] P. Di Tommaso, S. Moretti, I. Xenarios, M. Orobittg, A. Montanyola, J. M. Chang, J. F. Taly, and C. Notredame. T-Coffee: a web server for the multiple sequence alignment of protein and RNA sequences using structural information and homology extension. *Nucleic Acids Res.*, 39(Web Server issue):W13–17, Jul 2011.
- [191] M. R. Wilkins, E. Gasteiger, A. Bairoch, J. C. Sanchez, K. L. Williams, R. D. Appel, and D. F. Hochstrasser. Protein identification and analysis tools in the ExPASy server. *Methods Mol. Biol.*, 112:531–552, 1999.
- [192] D. Chelius, K. Jing, A. Lueras, D. S. Rehder, T. M. Dillon, A. Vizel, R. S. Rajan, T. Li, M. J. Treuheit, and P. V. Bondarenko. Formation of pyroglutamic acid from N-terminal glutamic acid in immunoglobulin gamma antibodies. *Anal. Chem.*, 78(7):2370–2376, Apr 2006.
- [193] Y. D. Liu, A. M. Goetze, R. B. Bass, and G. C. Flynn. N-terminal glutamate to pyroglutamate conversion in vivo for human IgG2 antibodies. *J. Biol. Chem.*, 286(13):11211–11217, Apr 2011.
- [194] W. Xu, Y. Peng, F. Wang, B. Paporello, D. Richardson, and H. Liu. Method to convert N-terminal glutamine to pyroglutamate for characterization of recombinant monoclonal antibodies. *Anal. Biochem.*, 436(1):10–12, May 2013.
- [195] E. S. Schulman. Development of a monoclonal anti-immunoglobulin E antibody (omalizumab) for the treatment of allergic respiratory disorders. *Am. J. Respir. Crit. Care Med.*, 164(8 Pt 2):6–11, Oct 2001.
- [196] A. J. Henry, J. P. Cook, J. M. McDonnell, G. A. Mackay, J. Shi, B. J. Sutton, and H. J. Gould. Participation of the N-terminal region of Cepsilon3 in the binding of human IgE to its high-affinity receptor FcepsilonRI. *Biochemistry*, 36(50):15568–15578, Dec 1997.
- [197] J. P. Cook, A. J. Henry, J. M. McDonnell, R. J. Owens, B. J. Sutton, and H. J. Gould. Identification of contact residues in the IgE binding site of human FcepsilonRIalpha. *Biochemistry*, 36(50):15579–15588, Dec 1997.
- [198] H. J. Gould, B. J. Sutton, A. J. Beavil, R. L. Beavil, N. McCloskey, H. A. Coker, D. Fear, and L. Smurthwaite. The biology of IGE and the basis of allergic disease. *Annu. Rev. Immunol.*, 21:579–628, 2003.



- [199] M. Amarasekera. Immunoglobulin E in health and disease. *Asia Pac Allergy*, 1(1):12–15, Apr 2011.
- [200] D. Kruschel and B. Zagrovic. Conformational averaging in structural biology: issues, challenges and computational solutions. *Mol Biosyst*, 5(12):1606–1616, Dec 2009.
- [201] Daniel M. Zuckerman. The ensemble protein database. <http://www.epdb.pitt.edu/>.
- [202] B. Schuler. Single-molecule FRET of protein structure and dynamics - a primer. *J Nanobiotechnology*, 11 Suppl 1:S2, 2013.
- [203] D. W. Macglashan and S. S. Saini. Omalizumab increases the intrinsic sensitivity of human basophils to IgE-mediated stimulation. *J. Allergy Clin. Immunol.*, 132(4):906–911, Oct 2013.
- [204] D. W. MacGlashan, J. H. Savage, R. A. Wood, and S. S. Saini. Suppression of the basophil response to allergen during treatment with omalizumab is dependent on 2 competing factors. *J. Allergy Clin. Immunol.*, 130(5):1130–1135, Nov 2012.
- [205] J. Liu, P. Lester, S. Builder, and S. J. Shire. Characterization of complex formation by humanized anti-IgE monoclonal antibody and monoclonal human IgE. *Biochemistry*, 34(33):10474–10482, Aug 1995.
- [206] J. A. Fox, T. E. Hotaling, C. Struble, J. Ruppel, D. J. Bates, and M. B. Schoenhoff. Tissue distribution and complex formation with IgE of an anti-IgE antibody after intravenous administration in cynomolgus monkeys. *J. Pharmacol. Exp. Ther.*, 279(2):1000–1008, Nov 1996.
- [207] C. L. Hsu, Y. Y. Shiung, B. L. Lin, H. Y. Chang, and T. W. Chang. Accumulated immune complexes of IgE and omalizumab trap allergens in an in vitro model. *Int. Immunopharmacol.*, 10(4):533–539, Apr 2010.
- [208] U. Bauer and A. L. Breeze. “ligandability” of drug targets: assessment of chemical tractability via experimental and in silico approaches. In Holenz. J, editor, *Lead generation: methods, strategies and case studies*, chapter 3. Wiley, Weinheim, Germany, 2016.
- [209] A. D. Lawson. Antibody-enabled small-molecule drug discovery. *Nat Rev Drug Discov*, 11(7):519–525, 06 2012.
- [210] M. Torres and A. Casadevall. The immunoglobulin constant region contributes to affinity and specificity. *Trends Immunol.*, 29(2):91–97, Feb 2008.
- [211] P. Tolar and S. K. Pierce. A conformation-induced oligomerization model for B cell receptor microclustering and signaling. *Curr. Top. Microbiol. Immunol.*, 340:155–169, 2010.

- [212] Z. Li, S. Raychaudhuri, and A. J. Wand. Insights into the local residual entropy of proteins provided by NMR relaxation. *Protein Sci.*, 5(12):2647–2650, Dec 1996.
- [213] P. A. Wachholz, N. K. Soni, S. J. Till, and S. R. Durham. Inhibition of allergen-IgE binding to B cells by IgG antibodies after grass pollen immunotherapy. *J. Allergy Clin. Immunol.*, 112(5):915–922, Nov 2003.
- [214] S. D. Demo, E. Masuda, A. B. Rossi, B. T. Thronset, A. L. Gerard, E. H. Chan, R. J. Armstrong, B. P. Fox, J. B. Lorens, D. G. Payan, R. H. Scheller, and J. M. Fisher. Quantitative measurement of mast cell degranulation using a novel flow cytometric annexin-V binding assay. *Cytometry*, 36(4):340–348, Aug 1999.
- [215] F. Marchand, S. Mecheri, L. Guilloux, B. Iannascoli, A. Weyer, and U. Blank. Human serum IgE-mediated mast cell degranulation shows poor correlation to allergen-specific IgE content. *Allergy*, 58(10):1037–1043, Oct 2003.
- [216] M. Bracher, H. J. Gould, B. J. Sutton, D. Dombrowicz, and S. N. Karagianis. Three-colour flow cytometric method to measure antibody-dependent tumour cell killing by cytotoxicity and phagocytosis. *J. Immunol. Methods*, 323(2):160–171, Jun 2007.
- [217] W. Li, A. Cowley, M. Uludag, T. Gur, H. McWilliam, S. Squizzato, Y. M. Park, N. Buso, and R. Lopez. The EMBL-EBI bioinformatics web and programmatic tools framework. *Nucleic Acids Res.*, 43(W1):W580–584, Jul 2015.